Lecture Notes in Engineering

Edited by C. A. Brebbia and S. A. Orszag

DFVLR 13

Nonlinear Dynamics of Transcritical Flows

Proceedings of a DFVLR International Colloquium
Bonn, Germany, March 26, 1984

Edited by
H. L. Jordan, H. Oertel, and K. Robert

Springer-Verlag
Berlin Heidelberg New York Tokyo

Lecture Notes in Engineering

The Springer-Verlag Lecture Notes provide rapid (approximately six months), refereed publication of topical items, longer than ordinary journal articles but shorter and less formal than most monographs and textbooks. They are published in an attractive yet economical format; authors or editors provide manuscripts typed to specifications, ready for photo-reproduction.

The Editorial Board

Lecture Notes in Engineering

Edited by C. A. Brebbia and S. A. Orszag

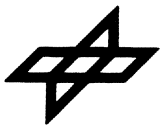

DFVLR 13

Nonlinear Dynamics of Transcritical Flows

Proceedings of a DFVLR International Colloquium
Bonn, Germany, March 26, 1984

Edited by
H. L. Jordan, H. Oertel, and K. Robert

Springer-Verlag
Berlin Heidelberg New York Tokyo

Editors
H. L. Jordan
DFVLR – Vorsitzender des Vorstands
Postfach 906058
D-5000 Köln 90/FRG

H. Oertel
DFVLR – Institut für Theoretische Strömungsmechanik
Bunsenstraße 10
D-3400 Göttingen/FRG

K. Robert
DFVLR – Stabsabteilung Programmvorbereitung
Postfach 906058
D-5000 Köln 90/FRG

ISBN-13: 978-3-540-15430-3 **e-ISBN-13: 978-3-642-82506-4**
DOI: 10.1007/978-3-642-82506-4

Binding: Lüderitz und Bauer, Berlin
2061/3020-543210

PREFACE

The German Aerospace Research Establishment (DFVLR) has initiated a new series of seminars concerning *fundamental problems in applied engineering sciences*. These seminars will be devoted to interdisciplinary topics related to the vast variety of DFVLR activities in the fields of *fluid mechanics, flight mechanics, guidance and control, materials and structures, non-nuclear energetics, communication technology, and remote sensing*.

The purpose of the series is twofold, namely, to bring modern ideas and techniques to the attention of the DFVLR in order to stimulate internal activities, and secondly, to promulgate DFVLR achievements within the international scientific/technical community. To this end, prominent speakers from Germany and other countries will be invited to join in a series of lectures and discussions on certain topics of mutual interest.

The first colloquium of this series dealt with the *dynamics of nonlinear systems*, especially in relation to its application to fluid mechanics, particularly in *transcritical flows*. Of special interest are questions concerning the formation of nonlinear three-dimensional structures in classical fluid mechanical stability problems, the physical process of transition to turbulence, and the appearance of chaotic solutions. The scope of lectures reaches from *self-organization in physical systems to structural stability of three-dimensional vortex patterns, the treatment of dissipative and conservative systems, the formation of nonlinear structures in the region of laminar-turbulent transition*, and *numerical simulation of cumulus cloud convection in meteorology*. The seminar should provide an insight into the extent to which theoretical findings in Nonlinear Dynamics apply to the comprehension of fluid-mechanical problems.

The following collection of articles consists of the revised versions of the lectures that were held. It has been supplemented by additional contributions in order to provide a more detailed insight. The book is intended as an introduction to various aspects of Nonlinear Dynamics and Fluid Mechanics. It does not present a review of the entire field but is rather meant to provide engineers and physicists with a first insight by means of some selected topics. We wish to express our thanks to L. Emme, K. Kosch, E. Kraft, E. Meiburg, B.L. Mügge, and D. Schlesinger for the preparation of the manuscript and the revision of the English text. We are also grateful to our publishers "Springer Verlag" for their outstanding cooperation in the printing of this book.

Köln-Porz, November 1984

Hermann L. JORDAN, Herbert OERTEL jr.
Klaus ROBERT

Experimental Mathematics

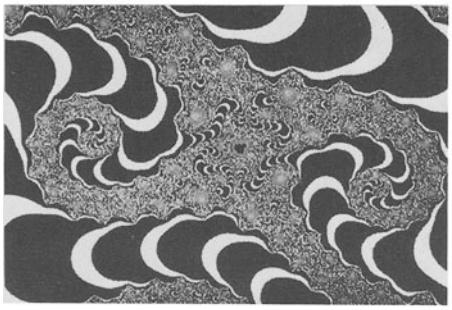

Boundaries of the Mandelbrot Set

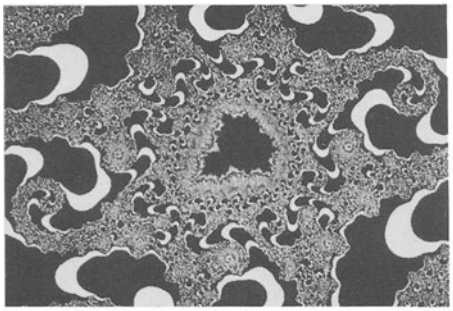

Detail

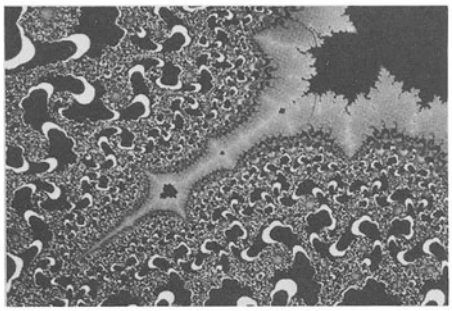

Quadratic Iteration

$x_i \rightarrow x_i^2+c \rightarrow x_{i+1}$

PEITGEN, RICHTER 1984

Fluid Mechanics

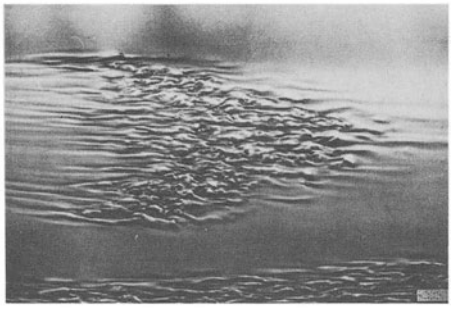

Turbulent Spot

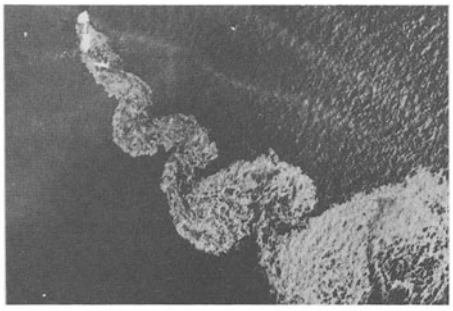

Wake of a Grounded Tankship

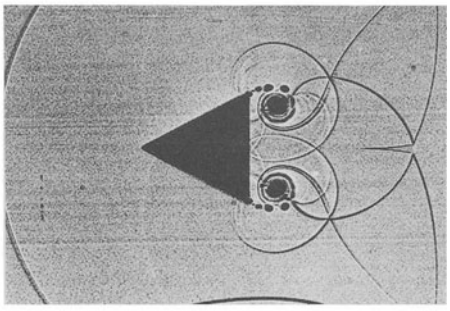

Diffraction of a Shock Wave

CANTWELL et al. 1978, NASA photograph 1976, SCHARDIN, OERTEL 1966

Fig. 1 NONLINEAR DYNAMICS

CONTRIBUTORS

ALLEN, G.A., jr.
Department of Aeronautics and Astronautics,
Stanford University, Stanford, CA 94305, USA

DALLMANN, U.
Institute for Theoretical Fluid Mechanics, DFVLR,
D-3400 Göttingen, Fed. Rep. Germany

HAKEN, H.
Institute for Theoretical Physics, University of Stuttgart,
D-7000 Stuttgart 80, Fed. Rep. Germany

KAHLERT, C.
Institute for Physical and Theoretical Chemistry, University
of Tübingen, D-7400 Tübingen 1, Fed. Rep. Germany

KLEISER, L.
Institute for Theoretical Fluid Mechanics, DFVLR,
D-3400 Göttingen, Fed. Rep. Germany

OERTEL, H., jr.
Institute for Theoretical Fluid Mechanics, DFVLR,
D-3400 Göttingen, Fed. Rep. Germany

ORSZAG, S.A.
Princeton University, Princeton, NJ 08540, USA

RÖSSLER, O.E.
Institute for Physical and Theoretical Chemistry, University
of Tübingen, D-7400 Tübingen 1, Fed. Rep. Germany

SCHUMANN, U.
Institute of Atmospheric Physics, DFVLR,
D-8031 Wessling, Fed. Rep. Germany

SREENIVASAN, K.R.
Mason Laboratory, Yale University, New Haven, CT 06520, USA

UEHLEKE, B.
Institute for Physical and Theoretical Chemistry, University
of Tübingen, D-7400 Tübingen 1, Fed. Rep. Germany

YAKHOT, V.
Department of Mathematics, Massachusetts Institute of Technology,
Cambridge, MA 02139, USA

CONTENTS

INTRODUCTION

NONLINEAR DYNAMICS

TEMPORAL AND SPATIAL STRUCTURES IN FLUID MECHANICS

H. OERTEL JR.

1. OVERVIEW

Fluid mechanical instabilities are the primary cause of well-organized structures of different characteristic wavelengths in a flow field. The key to a physical understanding of the laminar-turbulent transition process lies in understanding the temporal and spatial development and decay of these flow structures. In this volume, we will be concerned with selected examples of the formation of structures. In the fluid mechanical part, we will deal only with *transcritical flows*, i.e., flows across and beyond a critical state and therefore beyond one or more fluid mechanical instabilities. Figs. 1 and 2 portray transcritical flows. The first photograph of Fig. 2 shows a carbon dioxide jet in air, which is coming out of a round nozzle. The jet flow is laminar at first; however, after a characteristic length, it becomes unstable, forming vortex rings, and the transition to turbulence occurs, at which point a characteristic microscale structure becomes visible. A mixing layer allows us to observe a plane transcritical flow. Again it starts with a laminar shear flow, which becomes unstable and causes vortices with a spatially increasing flow amplitude. With increasing relative velocity of the upper and lower portions of the flow forming the shear layer, the transition to a turbulent flow takes place. The structure of the original fluid mechanical instability is preserved, but, as in the case of the free jet, a microscale structure is superimposed. The flame example shows the coupling of two instabilities of different wavelengths. Classical shear instabilities of a characteristic wavelength are shown in a satellite photograph of the earth's atmosphere.

The transition to chaotic motions occurs in quite different disciplines. Irregular quasi-stochastic motions in the mechanical three-body problem are well-known. Chaos can also be observed in electronic devices, nonlinear oscillators, and control systems. Chemical reactions and biological and sociological systems show chaotic behavior under special conditions.

The manifold examples of the temporal evolution of nonlinear systems and the study of the self-organization of these systems are the subject of HAKEN's theory of *SYNERGETICS*, [1 - 4]. It is shown here that the deterministic chaos is a dynamic characteristic of nonlinear systems. The starting point of the mathematical treatment is the discussion of the solution of simple nonlinear model equations. The mathematical and physical aspects are described for example in [5 - 14]. Quotations [15 - 20] focus on fluid mechanical applications, especially the transition to turbulent flow.

We have been discussing fluid mechanical *structures* without having previously defined the term. We have also applied the concept of structure in different ways. The spatial structures of fluid-mechanical instabilities have been mentioned, as well as the temporal structure in the phase space, coherent turbulent structures, and microscale structures. We use these terms as being synonymous with some unknown structural behavior of the fluid properties. A possible means of reaching a qualitative physical description of the flow field and a definition of structure is by investigating the singularities of the basic system of equations. The mathematical treatment leads through a Taylor series in the area around the critical points and makes possible a topological classification of the flow field. The *structure* is defined by the *critical points, saddle point, node, focus, center, and their separatrices*. It will be most significant to see how successfully one can apply the concept of spatial structures to the temporal dynamics of the three-dimensional fluid mechanical patterns. The prerequisite of that is that the temporal structure changes be independent of the frame of reference.

To further elucidate this issue, Fig. 3 presents a sketch of the periodic separation of vortices behind a cylinder in a uniform flow. The arrows point out the field of direction of the streak lines in the vortices that are floating away periodically. The observer, who is situated in a stationary frame of reference, can see that the two sets of vortex sheets have a mutual effect upon one another in the far wake. But the structure of the wake flow would look quite different to an observer moving along with the mean velocity of the center line. It is characterized by the set of saddle and focal points.

The central question as to the definition and qualitative description of temporal and spatial fluid mechanical formation of structures still remains unsolved. A universal variable transformation must be derived in such a way that within the transformed system the definition of structure is independent of the frame of reference. This requires a physical model in the four-dimensional domain of space and time. In the following articles in this book, some of the basic aspects will be demonstrated individually and new impulses, esepcially for the modelling of transcritical flows, will be examined. The volume begins with HAKEN's short survey

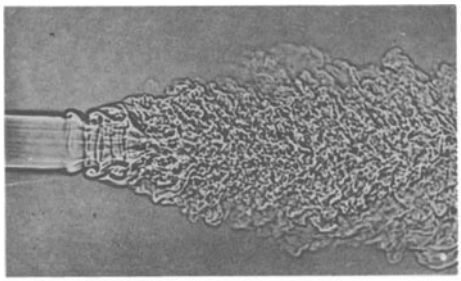

Jet

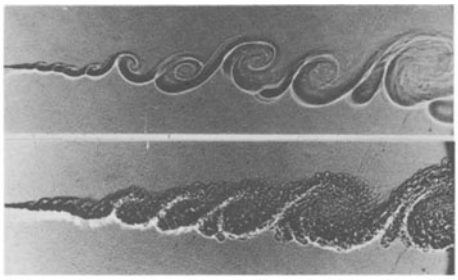

Mixing Layer

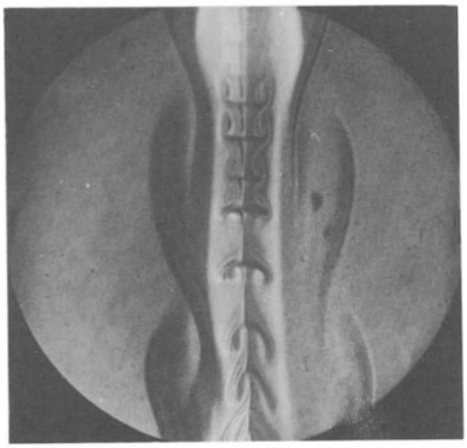

Flame

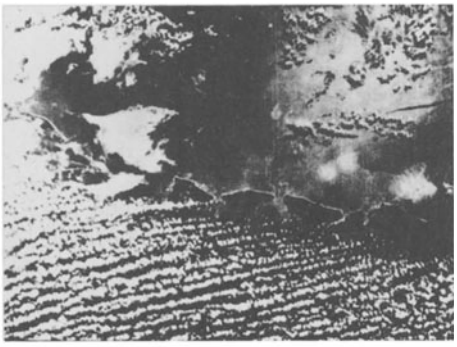

Shear Layer

LANDIS and SHAPIRO [21], BROWN and ROSHKO [22], EICKHOFF [23], SCORER [24]

Fig. 2 TRANSCRITICAL FLOWS

of the synergetic aspects of physical *self-organization*. Next follows the expansion of the classical model of the *RÖSSLER attractor*, a system of ordinay differential equations that produces a one-parameter family of invariant tori. SREENIVASAN's article on *Transitional and Turbulent Wakes* suggests new means of inter-relating the mathematical-physical findings of non-linear dynamical systems with regard to the interpretation of fluid mechanical findings in the transcritical regime. Then there follows a discussion of the fluid mechanical concept of structure, as well as a numerical simulation of transcritical and turbulent flows. The book concludes with examples of *meteorological applications*, in cumulus cloud convection.

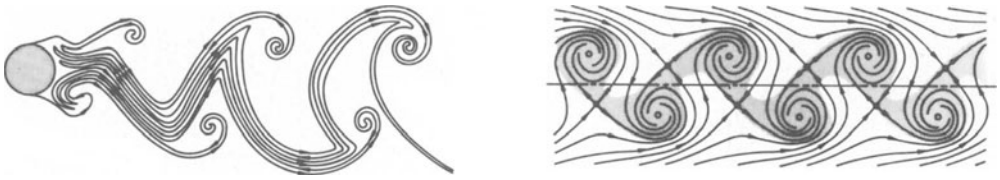

PERRY et al. [25], COLES [26]

Fig. 3 STRUCTURES OF WAKE FLOWS

2. NONLINEAR DYNAMICAL SYSTEMS

2.1 Basic Concepts

We will begin by explaining some concepts. We will discuss the temporal behavior of a fluid mechanical variable as the flow amplitude increases. The general outline in Fig. 4 begins with a measured oscillatory state in a wake flow. Steady states of motion and oscillations are called *attractors* because they attract neighboring states in the phase plot during transient processes. The phase plot of a steady motion shows a node. Any perturbation is damped and converges into one point. An oscillatory disturbance forms a focus in the phase plane. At a critical value of the flow amplitude, the steady state becomes unstable and periodic oscillations occur. A transition to a cycle can be observed in the phase plot. The Fourier analysis shows discrete lines in the power spectrum. The transition to a *chaotic attractor* is followed by quasi-stochastic non-periodic oscillations associated with a broad-band continual spectrum.

Since two calculated trajectories that start close together in the phase space will remain close together and move around a torus, as shown in Fig. 4, a single calculation can be used to predict the behavior of a group of trajectories that all start in the same neighborhood. So much for the attractor situation. Chaotic attractors are non-periodic and extremely sensitive to initial conditions, which leads to large and unpredictable change in the time-dependent long-range evolution of the system. The difference between two trajectories will generally grow exponentially with time, so that they rapidly lose any relation to one another that they have had previously. As a result of that, long-range computations and measurements in the regime of a chaotic attractor will be affected by small perturbations. Experimental noise, numerical errors, and especially

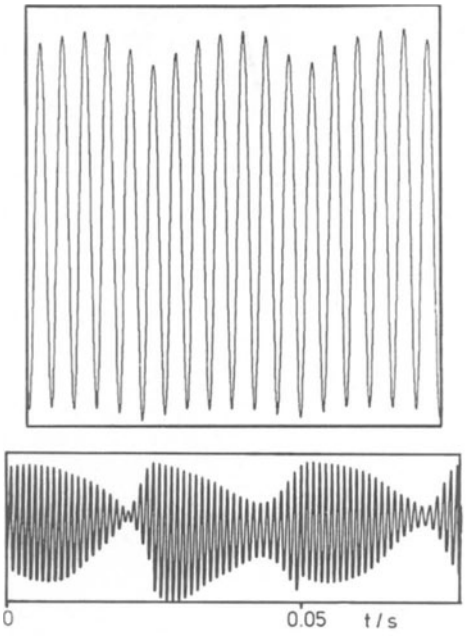

SREENIVASAN 1984

Measured Signals of Periodical Oscillations and Chaos

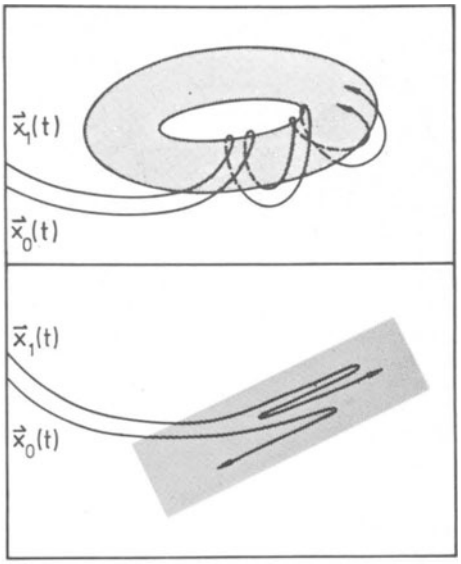

Torus, Chaotic Attractor

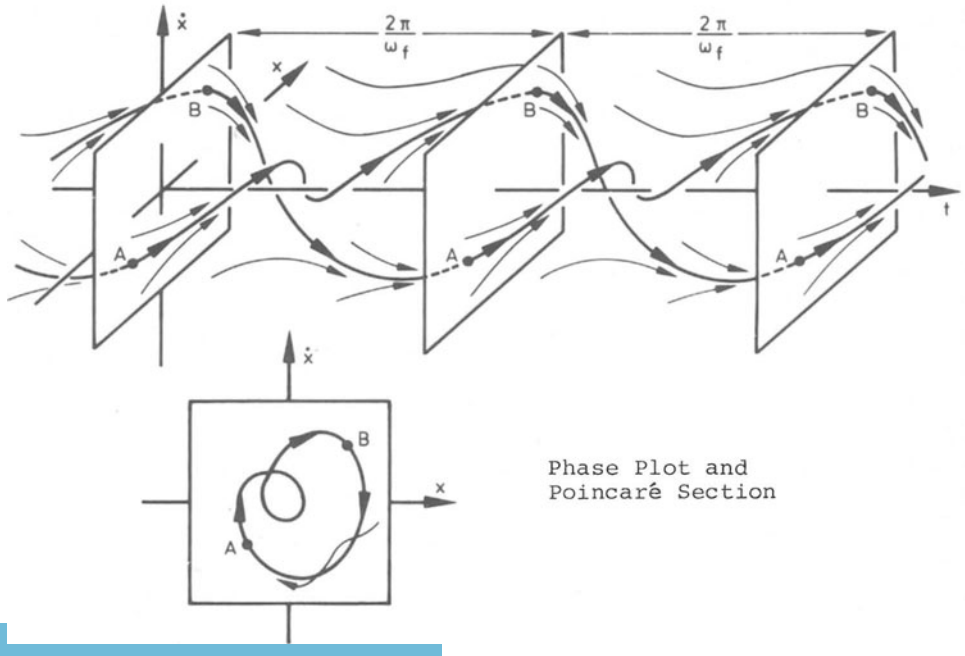

Phase Plot and Poincaré Section

Fig. 4 SIGNALS AND PHASE PLOTS

numerical dissipation produce a different pattern during each run. Such a system would be described as chaotic or irregular.

Now we ask how we can quantify the behavior of dynamical systems that have so far been described only qualitatively. The spectrum of *Lyapunov exponents* provides a partial classification scheme for dynamical systems that enables us to distinguish the different kinds of attractors, such as focus, cycle, torus, and chaotic attractor. If we consider the phase plots of Fig. 4, a chaotic attractor distinguishes itself in that two neighboring points in the phase space will initially diverge with time at an exponential rate $e^{\lambda t}$ with λ being the Lyapunov exponent. If $\lambda > 0$, the attractor is chaotic. If λ is negative, the attractor is stable. If we follow the introductory article by HAKEN [4], then the exponents can be determined by a linear stability analysis in the neighborhood of an attractor. For the one-dimensional case, λ can be determined analytically. In general, λ is obtained numerically by determining the following limit

$$\lambda = \lim_{t\to\infty} \sup \frac{1}{t} \ln |x^*(t)| \qquad (2.1)$$

The solution for the variable x(t) is expanded according to the perturbations x*(t) around the attractor. The limes superior guarantees that the largest rate of λ is chosen. For an n-dimensional system, a maximum of n characteristic Lyapunov exponents can be defined. This spectrum of Lyapunov numbers provides a partial classification scheme for dynamical systems.

In one dimension, there is only one stable fixed point, for which the Lyapunov exponent λ_1 is negative (-). In two dimensions, two attractors are stable: the focus $(\lambda_1,\lambda_2) = (-,-)$ and a limit cycle (-,0). In the case of a limit cycle, the Lyapunov exponent belonging to a motion x* transverse to the limit cycle is negative and therefore stable. The exponent of the tangential direction vanishes. Fig. 5 shows the simplest attractors in three dimensions: stable focus $(\lambda_1,\lambda_2,\lambda_3) = (-,-,-)$, stable limit cycle (-,-,0), and a stable torus (-,0,0). An attractor with the exponents (+,0,-) is considered to be a chaotic attractor. (+,+,0) may indicate an unstable limit cycle and (+,0,0) an unstable torus. Four-dimensional systems are of interest with regard to the time-dependent, three-dimensional spatial formation of structures in fluid mechanics. As regards chaotic behavior, they may be classified as (+,0,-,-) and (+,+,0,-) types. However, the structure of chaotic systems of four or more dimensions is completely unknown.

It is important to note that the *Lyapunov exponents* measure only the average local rate of divergence, thus revealing *nothing about the topology* of the given attractor. For example, both the Lorenz and Rössler attractors

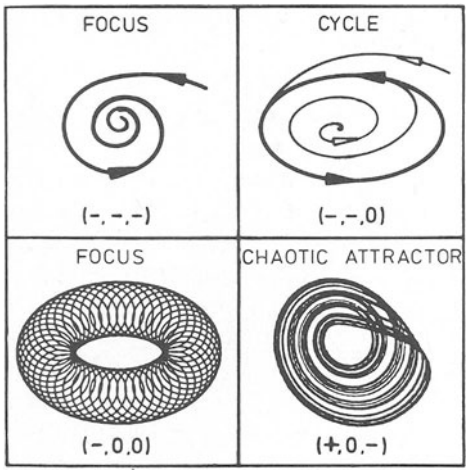

Fig. 5
LYAPUNOV EXPONENTS (λ_1, λ_2, λ_3)

described in chapters 2.2 and 2.3 are of type (+,0,-), yet they differ significantly in their stuctures. The Lorenz attractor contains a fixed point, this means a steady solution while the standard Rössler attractor does not.

We have so far been discussing qualitative changes of the *temporal behavior of dynamical systems*. Figs. 1 and 2 showed that the temporal formation of structures can be related to a *spatial structure*. It is therefore imperative that the *concept of structure* be expanded. Choosing the classical route of applied mathematics, we inquire about the singularities or *critical points* of an autonomous system of two differential equations:

$$\frac{dx}{dt} = f_1(x,y)$$
$$\frac{dy}{dt} = f_2(x,y) \qquad (2.2)$$

These are formed with the vectors of the velocity field $\vec{f}(x,y) = (f_1,f_2)$. The point $P_o(x_o,y_o)$, where $f_1(x,y) = f_2(x,y) = 0$ is called a *critical point*, at which *the direction is not defined, but the magnitude of the vector field can by all means be finite*. The bases of the classifications have been well-known for quite some time. They can be found, for example, in BLAQUIERRE [27]. The most typical cases of the real eigenvectors and corresponding eigenvalues are shown in Fig. 6 with the discriminant $\Delta = T^2-4D$, where the trace is $T = \partial f_1/\partial x|_o + \partial f_2/\partial y|_o$ and the Jacobian $D = \partial f_1/\partial x\ \partial f_2/\partial y|_o - \partial f_1/\partial y\ \partial f_2/\partial x|_o$

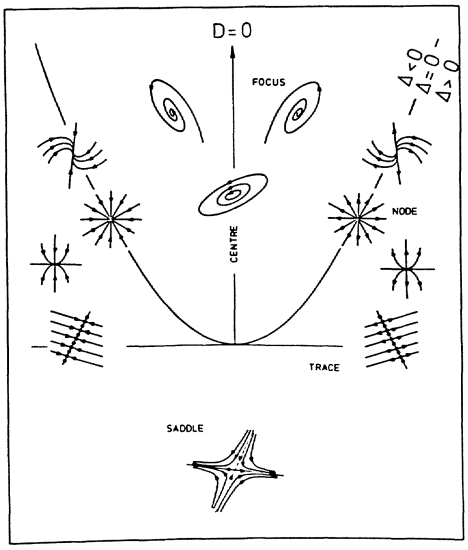

Two-Dimensional Critical Points

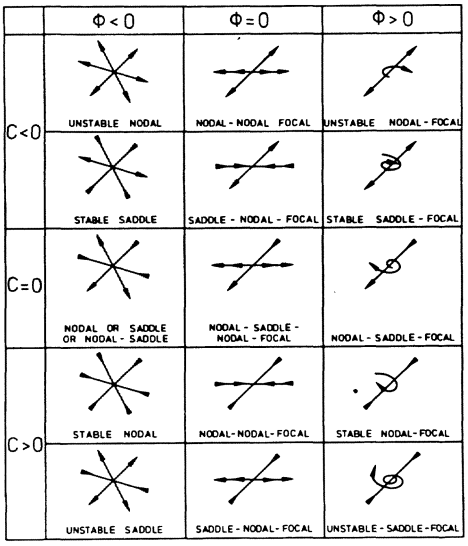

Three-Dimensional Critical Points

$D < 0$			Saddle
$D > 0$	$\Delta > 0$		Node
	$\Delta < 0$	$T \neq 0$	Focus
		$T = 0$	Center
$D = 0$	$\Delta = 0$	$T \neq 0$	degenerate Node
		$T = 0$	Center

D	Jacobian Determinant
T	Trace of the Jacobian
Δ	Discriminant
c	Product of Eigenvalues
$\phi < 0$	Real Eigenvalues
$\phi > 0$	Complex Eigenvalues

Fig. 6 CLASSIFICATIONS OF TWO- AND THREE-DIMENSIONAL CRITICAL POINTS

The *three-dimensional extension* is straightforward. We consider the three differential equations

$$\frac{dx}{dt} = f_1(x,y,z)$$

$$\frac{dy}{dt} = f_2(x,y,z) \qquad (2.3)$$

$$\frac{dz}{dt} = f_3(x,y,z)$$

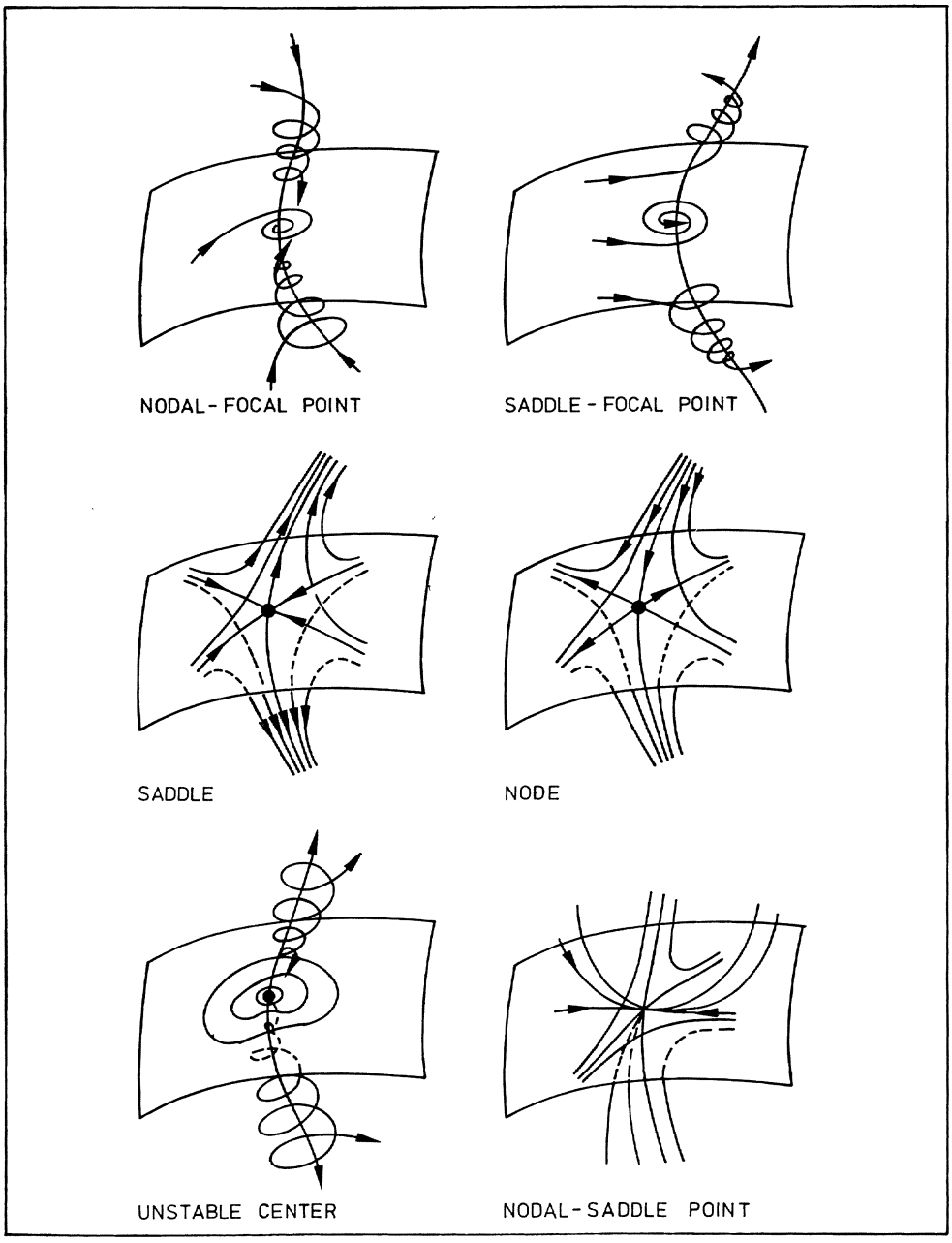

Three-Dimensional Critical Points

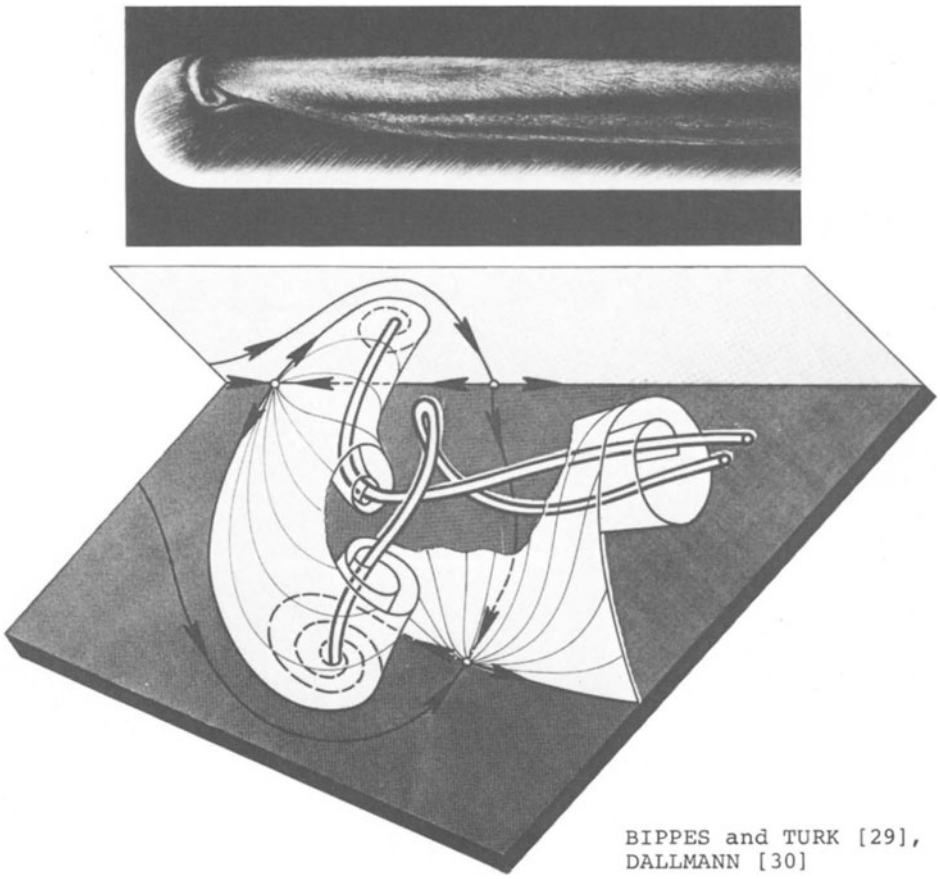

Fig. 7 TOPOLOGICAL STRUCTURE OF THE HEMISPHERE CYLINDER FLOW

Trajectories and critical points are considered in the three-dimensional phase space (x,y,z). The structures of the solutions are described by the boundary surfaces:

$$F_1 : f_1(x,y,z) = 0$$

$$F_2 : f_2(x,y,z) = 0 \qquad (2.4)$$

$$F_3 : f_3(x,y,z) = 0$$

The Jacobian will be replaced by $D(f_1,f_2,f_3)/D(x,y,z)$. Fig. 6 shows a tabular classification and a few examples of three-dimensional critical points. A summary of them is given by SIDERIADES [28].

The classification of the critical points of the basic system of equations allows a qualitative description of the *fluid mechanical formation of structures*. The structure is defined by the critical points and their connecting surfaces. For incompressible flows, a significant simplification occurs, since the trace of the Jacobian matrix is 0 because of the non-divergence of the velocity field. Thus focal and saddle points remain possible distinctive characteristics.

The contribution by DALLMANN will describe in further detail the mathematical principles of the classification of three-dimensional flow fields. As an introduction, we will discuss Fig. 7, which represents the incompressible three-dimensional flow around a hemisphere cylinder at 30° angle of attack. The photograph shows the wall-streamlines and a sketch of the flow field of a topologically possible structure, which has been reconstructed from those streamlines.

2.2 Scenarios to Chaos

Until now, we have been investigating how the structure of the solution of a given differential equation looks like. It is also possible to ask how this behavior varies as a parameter in the differential equation changes. Of particular interest is the study of the transition process from an equation with asymptotically stationary or periodic solutions to an equation with a chaotic attractor. ECKMANN [15] has introduced the term *scenario* for such transition processes. A first bifurcation may be followed by further bifurcations, and we may ask what happens when a certain sequence of bifurcations occurs. We will illustrate three important scenarios that have proved successful both theoretically and experimentally. The transition processes are often seen in connection with the transition to fluid mechanical *turbulence*. The "turbulence" described in the scenarios found is a simple form of temporal aperiodicity. So far, there are no known scenarios that describe the manifold *spatio-temporal structure* of fully developed turbulence. That corresponds to our comment in the previous chapter that the structure of chaotic systems of four dimensions is unknown.

The simplest *transition model* has been described by LANDAU. It proceeds from the observation that the developing turbulent flow is on a smaller and smaller scale. The irregular behavior of the flow is thus hypothesized to result from an infinite cascade of bifurcations. With each step, a new discrete frequency is added to the flow. The flows that LANDAU describes are not sensitive to initial conditions. Two trajectories that start close in the phase space remain close. Landau-type flow will yield sharp frequency peaks and their harmonics, while a system that is sensitive to initial conditions will yield a noiselike spectrum. We have already dis-

cussed that this is a distinctive characteristic of the transition to fluid mechanical turbulence.

The *RUELLE-TAKENS-NEWHOUSE Scenario* is the oldest one that fulfills the condition of having a chaotic limiting solution dependent on the initial conditions at large values of the flow parameters. After three Hopf bifurcations, chaos sets in suddenly. The initial state is a stationary solution of a differential equation. It loses stability if a parameter is changed. The steady state becomes oscillatory. The second bifurcation leads to a torus and the third one may lead to chaos.

It is known that the state following the third bifurcation is not necessarily unstable at all times. It can merely be asserted that chaotic behavior is possible after three Hopf bifurcations. The power spectrum of such a system is characterized by one, then two, and possibly three independent basic frequencies. When the third frequency appears, some broad-band noise will appear simultaneously if there is a strange attractor present. The experiments of SWINNEY and GOLLUB [18] demonstrate that the Fourier spectra of the classical Taylor-Couette and Rayleigh-Benard stability problems can be interpreted in the sense of the Ruelle-Takens-Newhouse scenario.

The third scenario, the *FEIGENBAUM sequence*, is quite different from the other two. The onset of chaos occurs by means of an infinite cascade of *periodic doublings* c_i. The series of bifurcations is also referred to as pitchfork bifurcations.

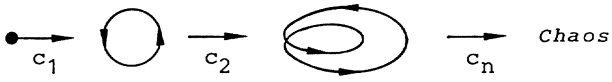

If subharmonic bifurcations are observed at parameters c_n and c_{n+1}, it is quite probable that the n-th subharmonic bifurcation occurs at

$$\lim_{n\to\infty} \frac{c_n - c_{n-1}}{c_{n+1} - c_n} = 4.6692 \qquad (2.5)$$

If three bifurcations have been observed, then a fourth one becomes more probable than the third had been, and so on. The spectral peaks of each of the subsequent bifurcations are in a ratio of about 6.6. At the accumulation point, aperiodic behavior can be observed, but *no broad-band spectrum*. What Feigenbaum predicts has been verified in thermal convection

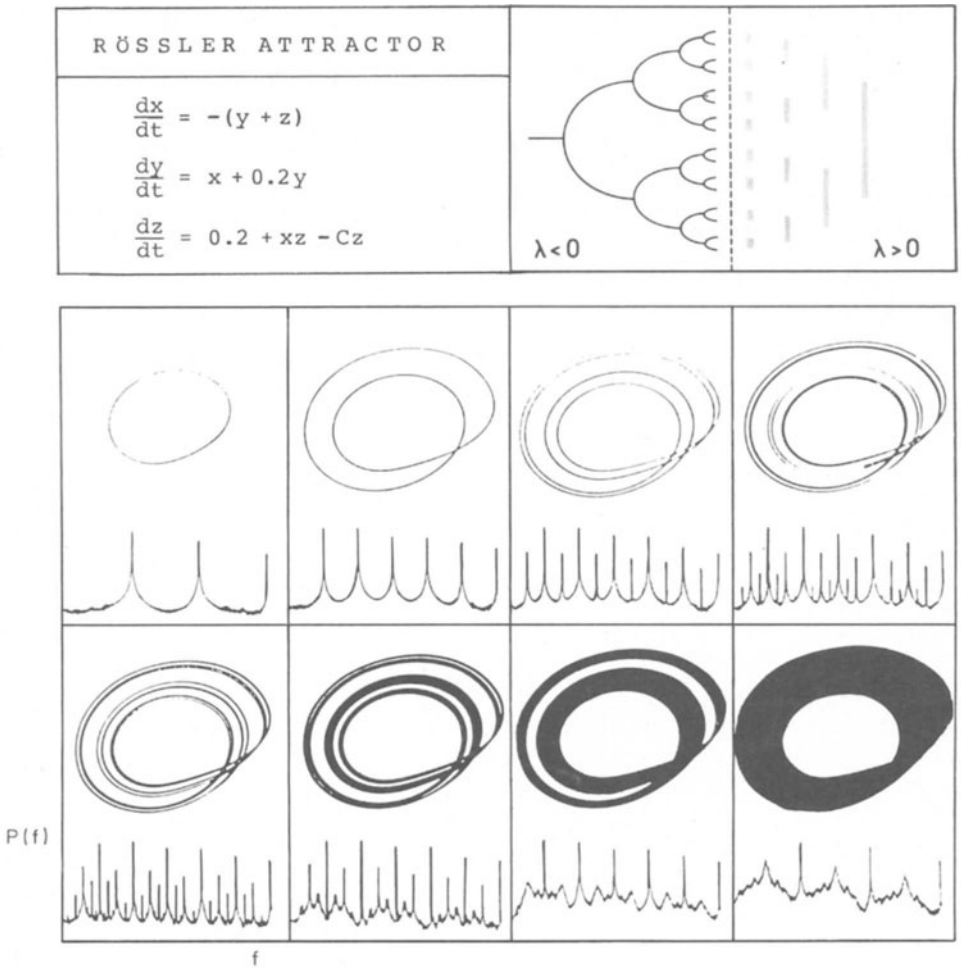

Fig. 8 RÖSSLER ATTRACTOR

experiments with liquid helium performed by LIBCHABER and MAURER [31]. We will take up this question once again in chapter 3.2 and show that the real convection transitions under normal conditions are considerably more complex, but show elements of the previously described scenarios.

The period doubling mechanism has been observed in several differential systems. The best-known example is the *RÖSSLER attractor* [32,33]. Fig. 8

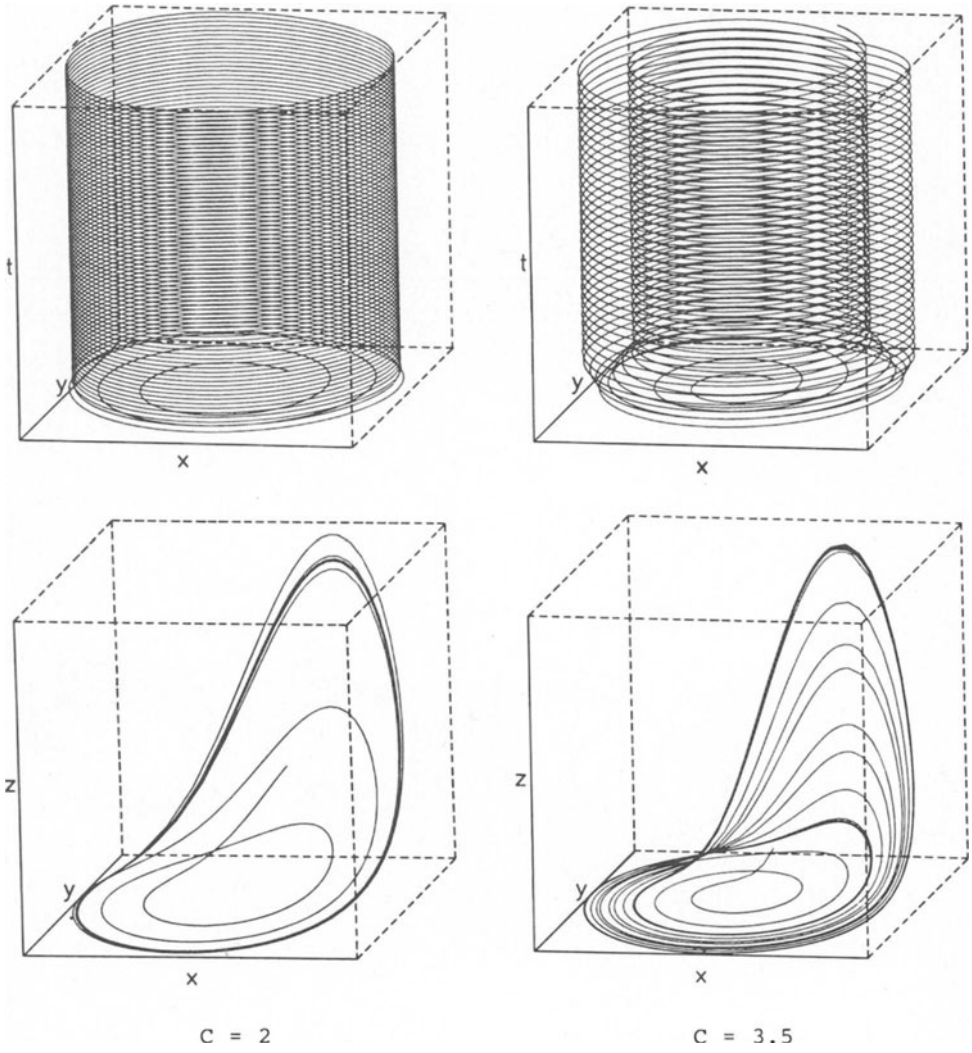

C = 2

Periodical Oscillations, Cycle

C = 3.5

Period Doubling

shows the basic ordinary nonlinear differential equations, the projections and the three-dimensional phase plots, the power spectral densities, and the bifurcation sequence. The bifurcation sequence begins with a limit cycle. Its first few period doubling bifurcations lead to sub-harmonic frequencies and the corresponding higher harmonics. The Lyapunov exponent is negative, which indicates an attractor. The doubling

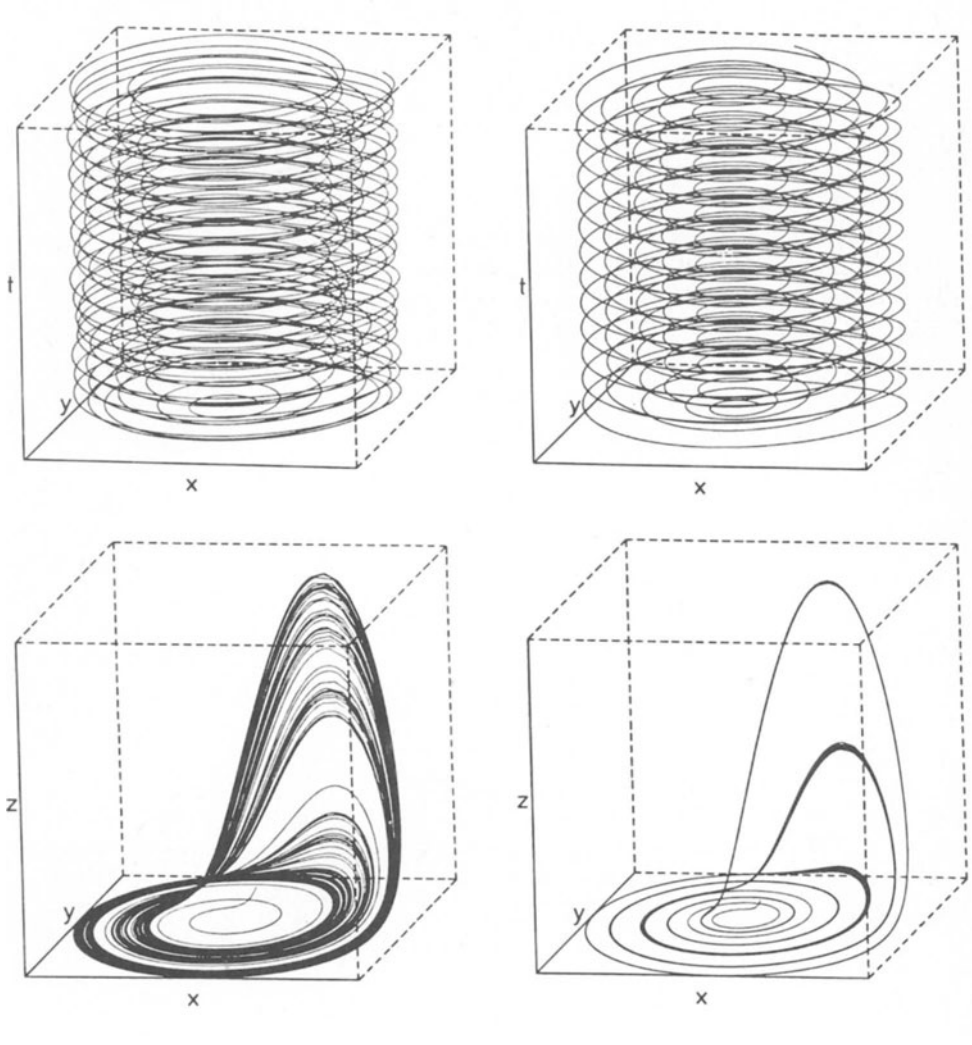

C = 4.3

Chaotic Bands

C = 6

Chaotic Attractor

process reaches an accumulation point at which the largest non-zero Lyapunov exponent becomes positive, which results in the exponential divergence of trajectories. Orbits remain confined to thin bands, which rejoin in pairs. A distinctive characteristic of this transition is the presence of sharp frequency components in the chaotic regime with the corresponding chaotic bands in the bifurcation diagram. Even at the asymptotic stage, when the trajectories fill out the complete Rössler attractor, the spec-

trum shows discrete peaks. The three-dimensional phase plots of the solutions complete the picture of the projections in Fig. 8.

It should be emphasized that we have presented a merely qualitative description of the transition to turbulence and have pointed out corresponding phenomena in the solution of simple nonlinear model equations in fluid mechanics. These observations are limited to analogies but do not allow the conclusion that the RÖSSLER equations, for example, are relevant with respect to fluid mechanics even though the phenomenon of period doubling can be observed in several transcritical flows.

The *POMEAU-MANNEVILLE-SCENARIO* takes into consideration another important characteristic, that of the transition to turbulence through intermittence. While the other two scenarios have been associated with Hopf and pitchfork bifurcations, this one is associated with a saddle node bifurcation, the collision of a stable and an unstable fixed point, which then both disappear into complex fixed points. The difficulty with this model lies in its lack of a quantitative statement about the critical bifurcation point, since the unstable fixed point that is going to collide with the stable fixed point may not be visible. POMEAU and MANNEVILLE [34,35] based their work on observations of the Lorenz system which we will deal with in chapter 2.3.

The intermittent transition to aperiodic behavior can be seen in many fluid-mechanical experiments. The article in this book by SREENIVASAN will provide us with a particularly impressive example. We have touched upon four scenarios. It seems certain that *there are many more routes to fluid mechanical chaos*.

2.3 Fluid Mechanical Model Equations

The picture of heuristically derived or mathematical scenarios to chaos will be broadened by two nonlinear model equations derived from the basic equations of fluid mechanics for convective heat transport, and for the propagation of perturbation waves. Both of the fluid mechanical model equation systems that are discussed here are valid in the vicinity of a critical bifurcation point, which superimposes an unstable flow upon a steady basic state.

The *LORENZ-model* [11] describes under severe approximations the periodical thermal convection in an infinite horizontal fluid layer heated from below. Below a critical temperature difference, heat conduction without convection sets in as the basic state. In the convective region, which is unstable, we expand the flow variables, the convective velocity u, and the temperature disturbance T into an infinite number of modes.

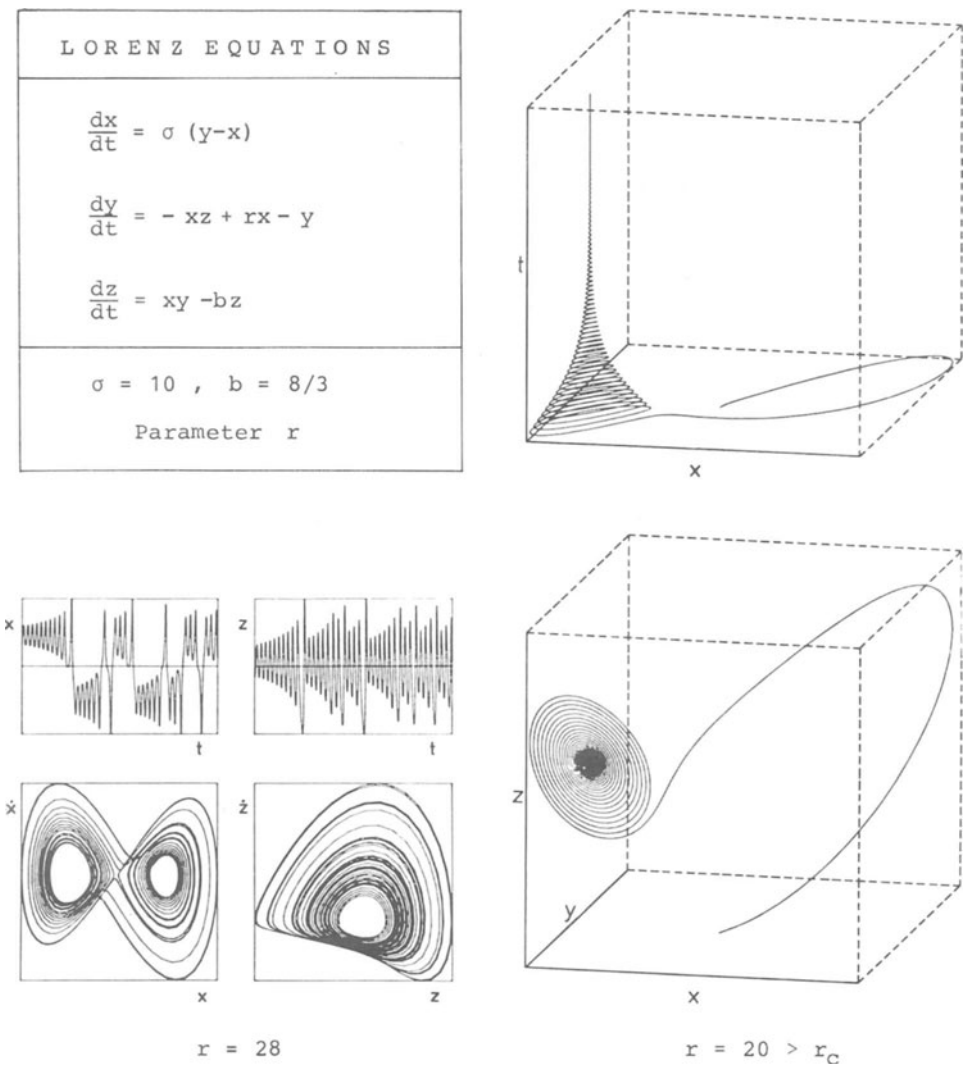

LORENZ [11]

Chaotic Regime and Projections of the Phase Plots

Damped Oscillations and Steady Solution, Focus

Fig. 9 LORENZ MODEL

$$u(x,z) = i \sum_{l,m=-\infty}^{\infty} \hat{u}(l,m)\exp(k_1 lx + m\pi_z) \qquad (2.6)$$

$$T(x,z) = i \sum_{l,m=-\infty}^{\infty} \hat{T}(l,m)\exp(k_1 lx + m\pi_z) \qquad (2.7)$$

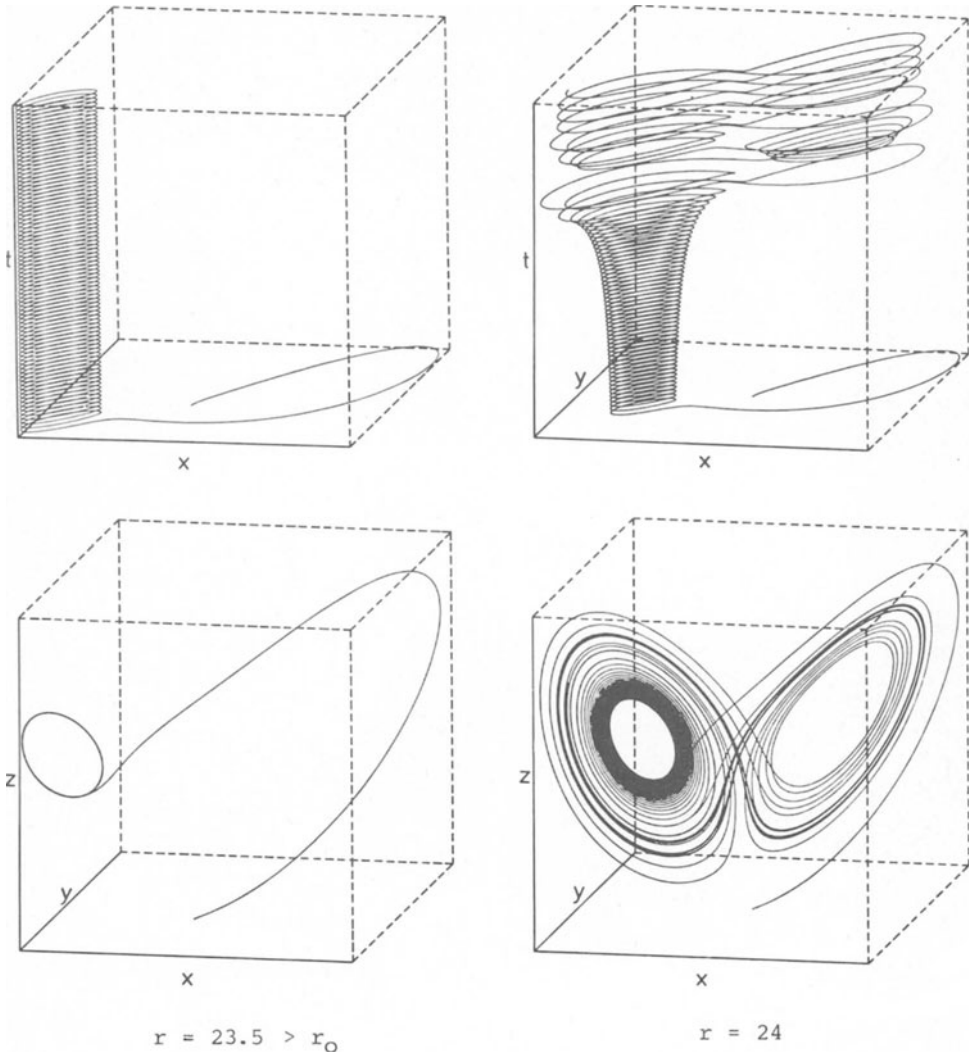

r = 23.5 > r_o

Periodical Oscillations, Cycle

r = 24

Transition to Aperiodical Oscillations

If we limit ourselves to the three most important Fourier modes of the perturbation values, then, after having inserted the Fourier expansion into the basic equations of fluid mechanics, with the assumption of the Boussinesq approximation we obtain the Lorenz equations for the amplitudes of the perturbation terms

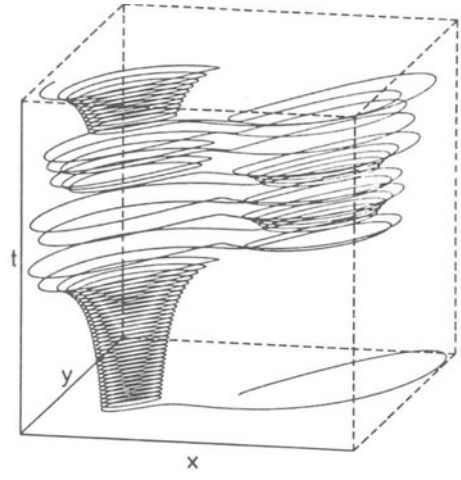

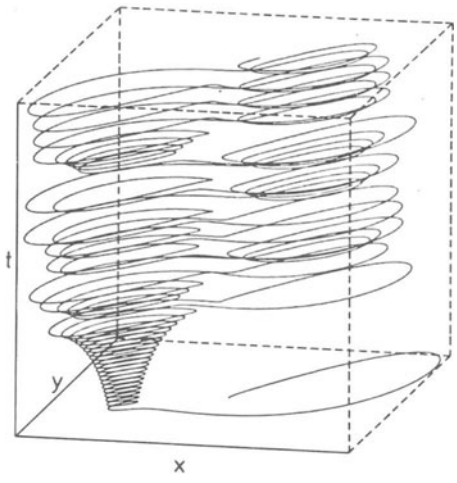

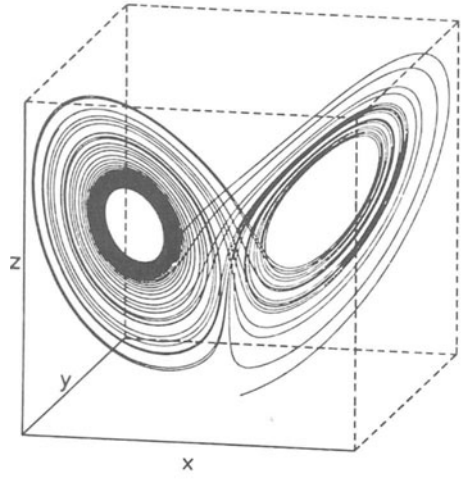

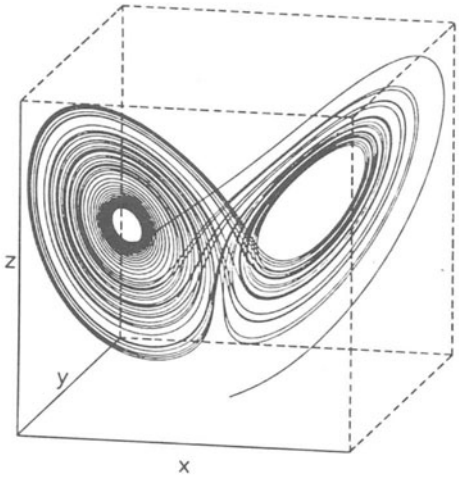

r = 24.5

r = 28 > r_{ca}

Intermittent Periodical and Aperiodical Oscillations

Chaotic Attractor

$$\frac{dx}{dt} = \sigma(y-x) \tag{2.8}$$

$$\frac{dy}{dt} = -xz + rx - y \tag{2.9}$$

$$\frac{dz}{dt} = xy - bz \tag{2.10}$$

A set of three coupled ordinary differential equations results $\hat{u}(1,1) \equiv x$ represents the fluid's angular velocity, $\hat{T}(1,1) \equiv y$ the horizontal temperature gradient, and $\hat{T}(0,2) \equiv z$ the vertical temperature gradient. The parameter σ stands for the Prandtl number of the medium, r is proportional to the Rayleigh number, the characteristic spatial dimension is given by the critical value at the bifurcation point $b = 4\pi^2/(\pi^2+k_1^2)$.

In Fig. 9 we follow the solutions of the Lorenz equations for constant values of σ and b with an increasing parameter r. Above a critical value of $r = r_c$, a stationary solution with a focus in the phase space sets in. Any perturbation around the steady state is damped through oscillations of decreasing amplitude. For values of r larger than a second critical bifurcation point r_0, the stationary solution is replaced by a periodic oscillation. We observe a cycle in the phase space. An intermittent transition regime of r follows, in which periodic and aperiodic oscillations alternate. For $r > r_{ca} \approx 24.74$, a chaotic attractor can be observed after a characteristic time. If we follow the numerical integration, the trajectory in the phase space winds around, first on one side and then on the other, without ever settling down to either periodic or stationary behavior. It cannot be predicted how the sequence of the cycles around the two centers in the phase space will look. The chaotic solutions of the Lorenz equations are, as is to be expected, very sensitive to initial data. If we follow two solutions that lie close to one another at the beginning, we see that their difference increases in such a way that the pattern of their aperiodic oscillations soon grows quite differently.

The Lorenz model was derived for the weakly nonlinear vicinity of the critical point at which the periodic convective flow sets in. We have discussed numerical solutions, all the way into the strongly nonlinear chaotic region. However, we may not expect that merely three Fourier modes of the expansion (2.6), (2.7) can reproduce the transition to turbulent convection. The Lorenz equations may claim merely to the qualitative description of possible convective transition phenomena that are characterized by the dominant modes of the perturbation terms. Chapter 3.2 will show that for a thorough treatment of the nonlinear transition mechanisms of thermal instabilities, the solution of the entire system of basic fluid-mechanical equations is requisite.

Up until now we have discussed the bifurcation to a stationary solution at a critical point of the stability problem in question. In many cases, the generation and continuation of perturbation waves have figured significantly. In Chapter 3, we will become acquainted with examples from laminar-turbulent transition in boundary layers and channel flows as well as in wake flows. The *GINZBURG-LANDAU* equation describes the weakly nonlinear temporal evolution of the complex amplitude A(x,t) of a wave instability in the vicinity of the critical bifurcation point.

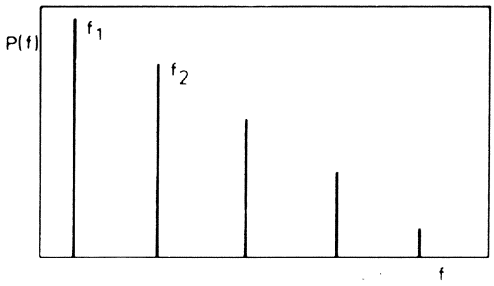

POWER SPECTRA OF A(o,t)

Initial Disturbances

$A(x,o) = 1 + 0.2 \cos kx$

$k = 0.55,\ 0.51,\ 0.48$

$c_o = 0.25$

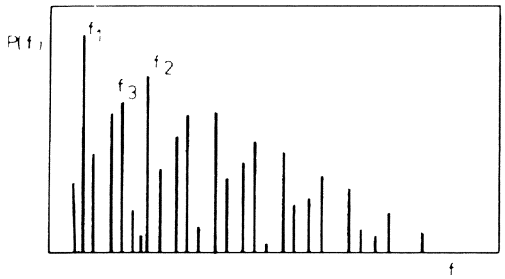

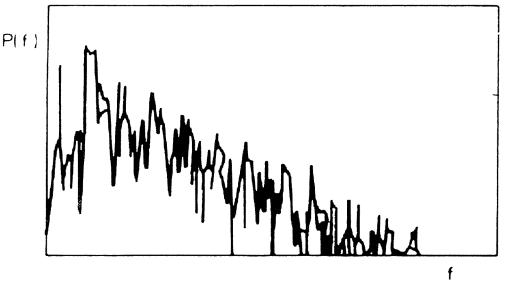

MOON et al. [36,37]

Fig. 10

STOKES SOLUTIONS OF THE GINZBURG-LANDAU EQUATION

$$i\frac{\partial A}{\partial t} + (1-iC_0)\frac{\partial^2 A}{\partial x^2} = iC_0 A - (1+iC_0)|A|^2 A \qquad (2.11)$$

The wave perturbation is of the form $\sim A(x,t)e^{i(kx-\omega t)}$; c_0 is a real parameter. We move along with the frame of reference, which is moving at the group velocity $\partial\omega/\partial k|_c$ at the critical point c. Time is scaled with $1/C_0$. Ginzburg-Landau equation is a partial differential equation for the increase in a perturbation amplitude, and can be derived from the Navier-Stokes equation within the framework of a stability analysis. We follow the work of MOON et al. [36] and discuss the Stokes solution of (2.11), $A(x,t) = e^{it}$, which is unstable to fluctuations of sideband wave numbers k. The complex amplitude of the wave is expanded into the spatial Fourier series

$$A(x,t) = \sum_{n=0}^{N-1} (a_n(t) + ib_n(t)\cos(nkx)) \qquad (2.12)$$

Qualitative changes in the behavior of the numerical phase space trajectories are presented in Fig. 10 for various wave numbers k in the form of power spectra.

Within the range of $0.6 < k < 1.31$, the motion is periodic and the power spectrum of A shows only one frequency f along with its harmonics, which decreases continuously with k. In the interval $0.52 < k < 0.6$, the flow becomes quasi-periodic with two independent frequencies f_1 and f_2 and the corresponding harmonics. As k decreases to less than 0.52, a third independent frequency f_3 is calculated. A detailed examination in the phase space shows that it is a matter of a three-torus motion. At $k = 0.49$, the motion of A(x,t) is abruptly reduced to a two-torus. The locking of the three-torus into a two-torus state is immediately followed by the onset of chaos with a broad power spectrum. The three-torus transition to a turbulent state has been observed in a Rayleigh-Bénard convection experiment by GOLLUB and BENSON [38]. Further examples, particularly in wake flows, will be discussed in this volume. The Ginzburg-Landau model leads beyond the Ruelle-Takens-Newhouse scenario with bifurcations from a limit cycle to a two-torus motion and then on to chaos. A three-frequency quasi-periodic motion is stable over a significant range of parameters. The subharmonic two-torus transition can also be observed in the case of the Ginzburg-Landau equation, if the sideband wave number is further decreased.

However, as in the case of the LORENZ model we cannot expect a weakly nonlinear expansion to correctly describe the fully nonlinear dynamics of disturbance waves in the transcritical regime.

3. TRANSCRITICAL FLOWS

3.1 Taylor Instabilities

After the basic concepts of nonlinear dynamics and of scenarios to chaos and turbulence have been provided, we will turn to the fluid mechanical stability problems that are referred to in the following articles. Serving as an introduction is the description of the classical *TAYLOR-COUETTE instabilities* in the gap between two cylinders, the outer cylinder being at rest while the inner cylinder rotates. When the diameter d of the gap is small, a linear Couette profile forms approximately, with an unstable velocity distribution in the centrifugal force field as the basic state.

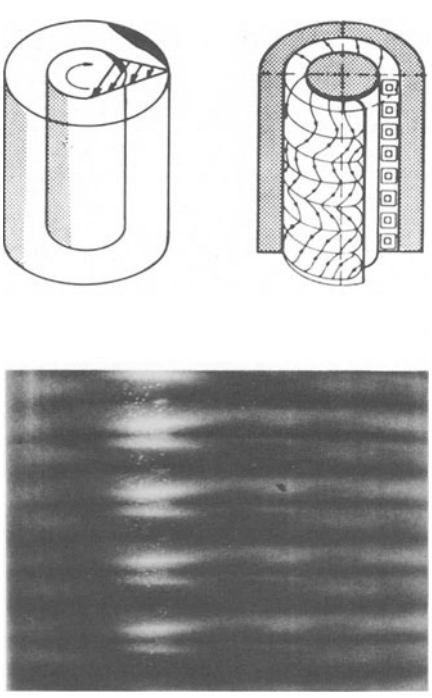

Principle Sketch and Photograph

OERTEL and BÜHLER [39]

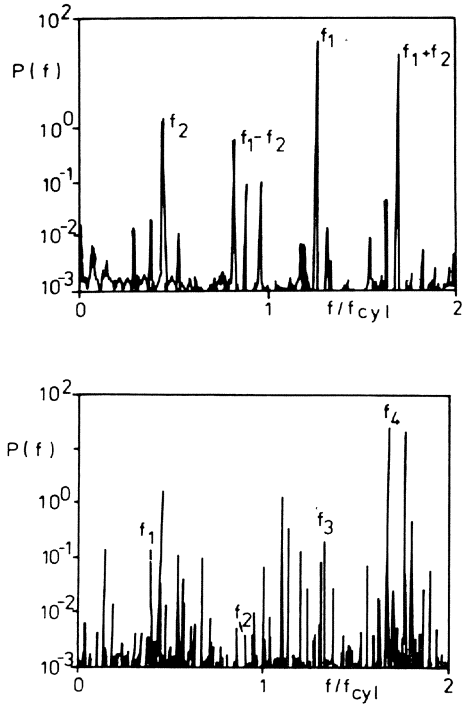

Power Spectra

SWINNEY and BRANDTSTÄDTER [40]

Fig. 11 TAYLOR INSTABILITIES

$$u_\varphi = Ar + B/r, \quad u_r = u_z = 0 \tag{3.1}$$

with the cylindrical co-ordinates r, φ, z. A and B are constants with values determined by the no-slip boundary conditions at the inner and outer cylinders r_i, r_o. The characteristic dimensionless parameter for this system, the Reynolds number, can be defined as $Re = r_i\omega(r_o-r_i)/\nu$. ω is the angular velocity of the inner cylinder and ν the kinematic viscosity. At a critical Reynolds number Re_c, the basic state becomes unstable. Horizontal toroidal vortices form, superimposed upon the azimuthal flow, as sketched in Fig. 11. With further increase in the Reynolds number, at a second critical value the rolls start to oscillate periodically. Azimuthal travelling waves form, superimposed on the toroidal vortices. When the rotation rate is further increased, a double period of oscillations with half of the basic frequency is a possible oscillatory state. This is the FEIGENBAUM period doubling mechanism. Recent experimental studies

show, however, that different stable modulation patterns can occur in the quasi-periodic regime, and that the frequency f_2 is different for different patterns. Fig. 11 shows the power spectrum at a Reynolds number ten times the critical value. f_{cyl} is the rotation rate of the Taylor instability at the critical Reynolds number Re_c. With further increasing Reynolds number, a quasi-periodic behavior with more than two characteristic frequencies can be observed. At $Re/Re_c = 12$, the diagram shows four independent frequencies with the corresponding higher harmonics. All of the other sharp peaks in the power spectra are linear combinations of the fundamental frequency components. This state can be interpreted as a transient state to the chaotic regime with a broad-band frequency spectrum. However, other transition sequences are possible, depending on the initial rotation rate and the gap between the cylinders. In the chaotic regime, the flow appears to be increasingly noisy, and at sufficiently large Reynolds numbers, the azimuthal waves disappear while the spatial vortex structure remains.

3.2 Rayleigh-Bénard Convection

Another standard type of transcritical stability problem is the Rayleigh-Bénard convection. A horizontal fluid layer that is heated from below will become unstable at a characteristic temperature difference. The basic state of the stability problem is now rendered by a linear vertical temperature profile. The dimensionless number that describes the convective heat transport is the Rayleigh number $Ra = (\alpha\ g\ \Delta T\ h_z^3)/(\nu\kappa)$, with the temperature difference ΔT between the horizontal boundaries and the height of the fluid layer h_z. If the Rayleigh number exceeds a certain critical value, convection rolls with periodic spatial expansion form between two solid horizontal walls. In a convection roll, the heated fluid, driven by buoyancy, moves upwards, cools down at the upper surface, and sinks once again. The principle sketch and the interferogram of Fig. 12 show the periodical succession of areas in a rectangular box where the fluid is moving upwards and downwards along the axes of the convection rolls. When the temperature difference in the Rayleigh-Bénard problem is increased, a spatial structural change can be observed at discrete Rayleigh numbers, thus differentiating it from the Taylor stability problem. DALLMANN's article in this book will qualitatively describe the topological structure with the critical points in the flow field. Under the assumption of the Boussinesq approximation (3.2),(3.3),(3.4), the *basic fluid mechanical equations* show that a further dimensionless number, the Prandtl number $Pr = \nu/\kappa$, determines the spatial structural change.

$$\nabla \cdot \vec{v} = 0 \tag{3.2}$$

$$\frac{1}{Pr}\left(\frac{\partial}{\partial t} + \vec{v} \cdot \nabla\right)\vec{v} = -\nabla p + \nabla^2 \vec{v} + Ra\,T\vec{e} \tag{3.3}$$

$$(\frac{\partial}{\partial t} + \vec{v} \cdot \nabla) T = \nabla^2 T \qquad (3.4)$$

In media with small Prandtl numbers, such as air or molten metal, the nonlinear inertia terms of the momentum equation (3.3) dominate. These are essentially responsible for the change in the number of cells in the convection box.

The transition to an oscillatory convective instability at a further critical Rayleigh number takes place quite analogously to the Taylor problem. This Rayleigh number also depends on the Prandtl number of the medium, as (3.3) shows. For media with small Prandtl numbers, a transition to a time-dependent flow can be expected at lower critical Rayleigh numbers. The theoretical and experimental frequency spectrum of Diagram 12 shows that the oscillations begin with a dominant frequency f_1. In a rectangular convection box, the *experiment in air* demonstrates the appearance of a second and a third oscillatory frequency. The quasi-periodic regime of the route to turbulent convection is thereby determined by the mode locking $kf_1+lf_2+mf_3$, with integers k, l, m', of the higher harmonics and their combination harmonics. The convection experiment further shows that at the Rayleigh number 52324, the oscillatory instability is again determined by the initial frequency f_1. With increasing Rayleigh number, there appear the subharmonics of f_1 and f_2, the period doubling mechanism, and the higher harmonic frequencies. So again we find all the individual phenomena of the nonlinear model equations of Chapter 2 in our convection experiment; but the transition to chaos appears much more complex in the quasi-periodic regime than the LORENZ model, for example, would predict. It should also be noted that at very high Rayleigh numbers, the discrete mode-locking of individual frequencies can still be measured exactly. The Rayleigh-Bénard experiment proves to have a variety of different routes to turbulence, depending on the geometry, the Prandtl number of the medium, and the rate of heating. We also observe two torus transitions in the quasi-periodic regime, with two frequencies $f_1 f_2$ or $f_1 f_3$ if the Prandtl number of the fluid is increased [42-51].

The numerical simulation of the Rayleigh-Bénard convection in the rectangular box shows, assuming symmetry in the center plane box, the onset of oscillatory convection with the experimental frequency f_1 and the corresponding harmonic frequencies. The calculated periodic variations in velocity and temperature are shown in Fig. 12, along with the corresponding phase plots at the onset of the oscillations and in the quasi-periodic regime. The calculation shows the subharmonic route to turbulence and the period doubling phenomena. At the Rayleigh number 39000, the calculation shows that first a characteristic time is needed before the subharmonic frequency sets in. The symmetry-breaking modes f_2 and f_3 cannot be calculated, because of the theoretical presuppositions. This indicates that although the model equations in Chapter 2 can describe individual phenome-

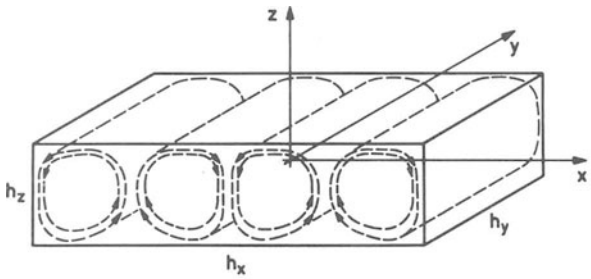

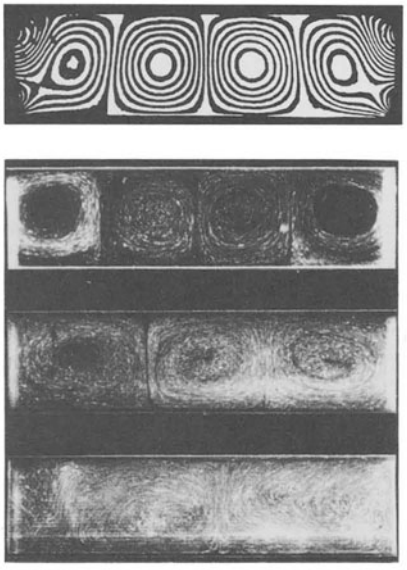

Spatial Structure

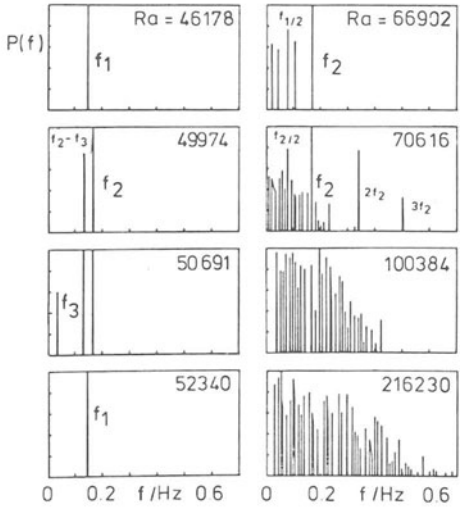

Experimental Power Spectra
OERTEL et al. [19,41-44]

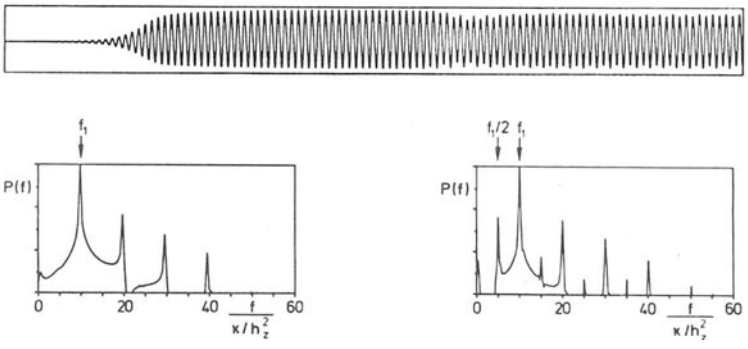

Signal and Theoretical Power Spectra, Ra = 39000, KESSLER [45-47]

Fig. 12 THERMAL CELLULAR CONVECTION

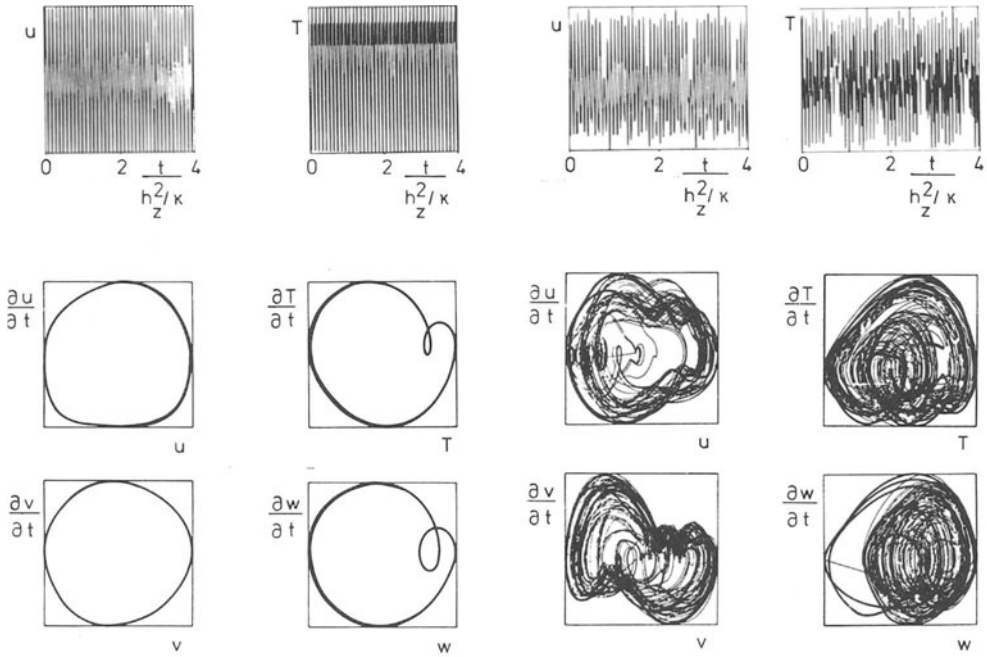

Ra = 38 000 Ra = 70 000

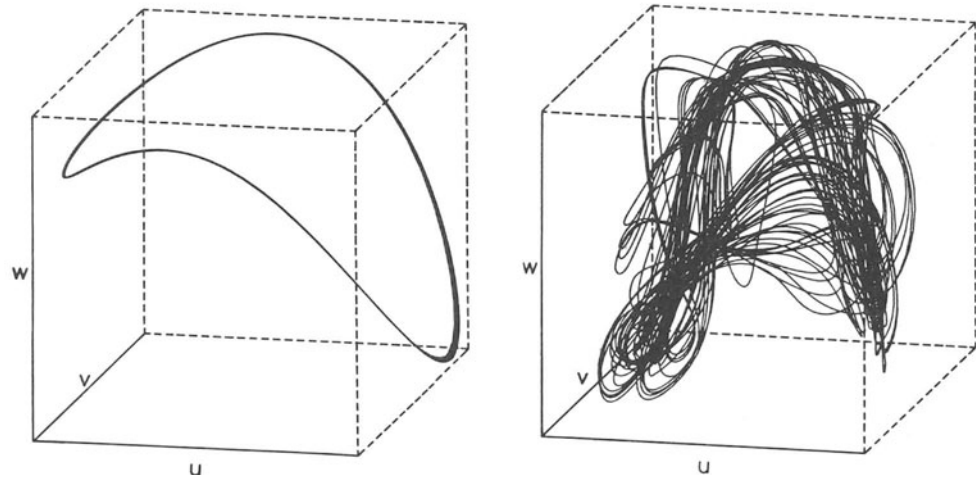

Numerical Simulation

na of the routes to turbulence, if we want to comprehend the transition processes in their full complexity, we must solve the set of equations (3.2) - (3.4) without any limiting presuppositions.

3.3 Transitions

Until now we have dealt with stability problems in which the stable basic state was replaced by a stationary, spatially periodic flow. At this point, we turn to wave instabilities in boundary layers and Poiseuille channel flows. We will attempt to provide merely a rough introduction to the article by KLEISER that appears in this volume. The instability in a boundary layer or a Poiseuille flow starts with the linear Tollmien-Schlichting waves (1), which move downstream with a characteristic phase velocity. The linear stability theory predicts a critical Reynolds number 5772 for a plane Poiseuille flow, with the Reynolds number $Re = u_{max}h/\nu$ describing the ratio of the nonlinear inertial force and the frictional force. Here, h is 1/2 the height of the channel, and u_{max} is the maximum velocity of the basic profile. A new phenomenon appears, in relation to the stability problems mentioned thus far; the onset of instability depends on the magnitude of the perturbation amplitude. The critical Reynolds number can fall down to 1000, if the amplitudes of the perturbation waves are very high. The further downstream development of the three-dimensional formation of structures in the transitional regime takes place in several steps. After about two Tollmien-Schlichting wavelengths, the variations in the u-components of the velocities show a characteristic spanwise periodic pattern called peak and valley (2). Further downstream, the amplitudes of variations increase further and the travelling Λ-vortex structure shown in Fig. 13 forms, which leads to the transition to a turbulent flow. This form of transition is also referred to as the K-type. In boundary layers as well as in Poiseuille flows, the transition can likewise be observed to have subharmonic Tollmien-Schlichting frequencies. A spatial staggered Λ-vortex pattern corresponds to this. The physical mechanism of the temporal and spatial formation of structures in the transitional regime is a *secondary shear instability* of the inflection point profiles, which are superimposed upon the basic profile. That is why a component of the shear vector is presented for the characterization of the spatial formation of structures. Further downstream in the flowfield, there are spikes (3), which can be observed in a fixed place in the measured and calculated velocity profile passing by. The spikes are brought about by high-shear layer inflection point profiles. Then come the turbulent spots (4) and the fully developed turbulent boundary layer or channel flows (5). The hierarchy of the nonlinear formation of structures following one after the other is completed by further subharmonic routes to turbulence, all determined according to the magnitude of the variations. The basic fluid mechanical equations for the transitions are expressed as follows, assuming incompressible flows:

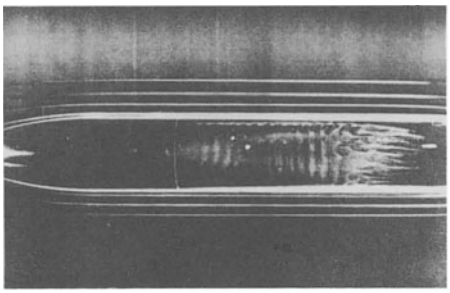

Boundary Layer

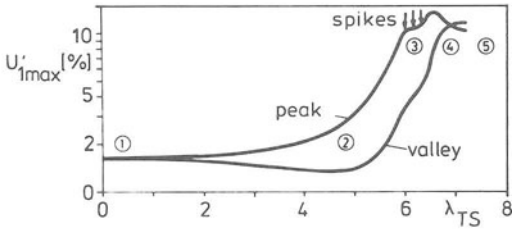

Poiseuille Flow

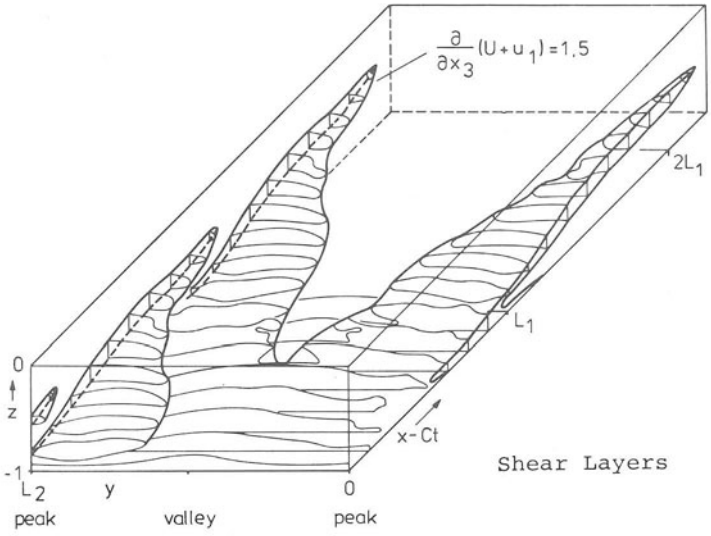

Shear Layers

BROWN [52], KLEISER [53,54]

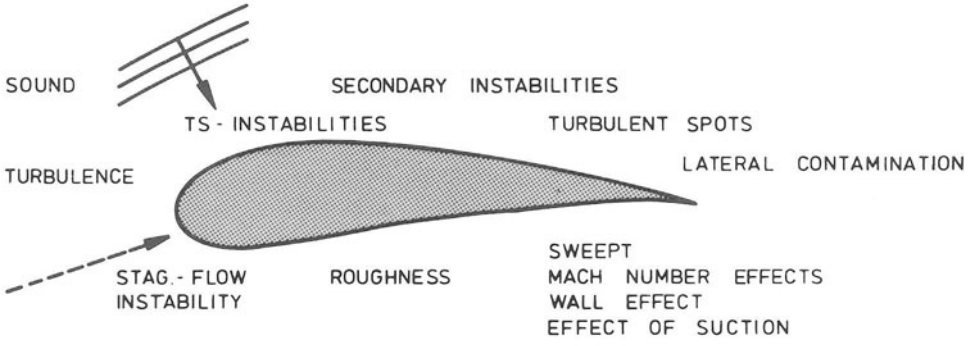

HERBERT and MORKOVIN [55]

Fig. 13 TRANSITIONS IN BOUNDARY LAYERS AND POISEUILLE FLOWS

$$\nabla \cdot \vec{v} = 0 \tag{3.5}$$

$$\frac{\partial \vec{v}}{\partial t} + (\vec{v} \cdot \nabla)\vec{v} = -\nabla p + \frac{1}{Re} \Delta \vec{v} \tag{3.6}$$

The sketch by HERBERT and MORKOVIN [55] shows that, in addition to mechanisms of transition that we have discussed so far, other parameters can be of great significance in practical applications. The free-stream turbulence, the influence of sound, surface roughness, curvature, wing sweep, suction, and wall temperature make some of the most important effects on transitions. It is of course in our best interest technologically to learn how to manipulate transition, since it is one of the keys to reducing drag. The prerequisite for such manipulation is the physical understanding of the temporal and spatial formation of structures in the transitional regime.

3.4 Wakes

If the profile of the *basic flow* exhibits a *point of inflection*, there then appears a new phenomenon of wave instabilities. Consider, for example, the wake flow behind a body. Areas of "absolute" and "convective" instability can be distinguished, in which the perturbation waves are amplified either both temporally and spatially or else only spatially. The differing areas of stability are separated by the surface, in which the group velocity of the perturbation is 0. KOCH [59], has introduced the idea of aerodynamic resonance for the self-excitation of the wake instability in the "absolutely" unstable region. In order to elucidate this somewhat, we will first discuss the result of the linear stability theory. For the perturbation waves in the wake flow, we make the expansion ~exp[ia(x-ct)] with a wave number a and phase velocity c. If c is complex, then we are dealing with a spatially periodic perturbation that is temporally amplified. The corresponding stability diagram is presented in Fig. 14 for three given time-averaged wake profiles. The unstable region is indicated by the dotted area. We have a spatially amplified instability if the wave number a is complex and the phase velocity c is real. If we follow the maximum of the amplification rate for various wake profiles, then we come to the resonance point at a dimensionless depth of $\sigma = 0.92$ for the assumed wake profile. For $\sigma > 0.92$, the stability problem is temporally and spatially amplified. An example for this is the variety in the temporal formation of structures in the transcritical regime, as SREENIVASAN describes in his article.

Although the wake stability problem is now included in textbooks, the nonlinear temporal-spatial formation of structures at transcritical Reynolds numbers is still not as well-known as in a boundary layer or in a Poiseuille flow. Experiments by PRANDTL [55] already show that for small Rey-

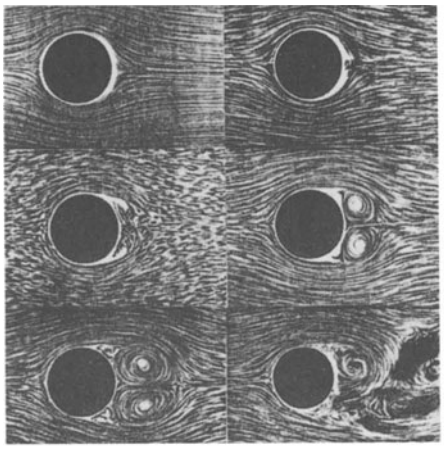

Cylinder Wake
PRANDTL [56]

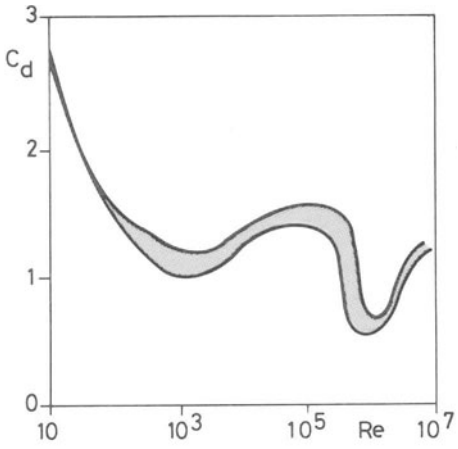

Drag Coefficient
MORKOVIN [57]

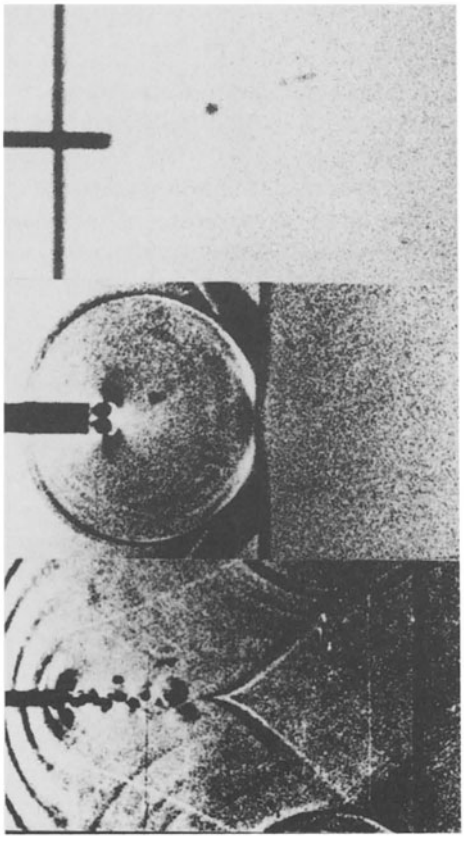

Shock Tube Experiment

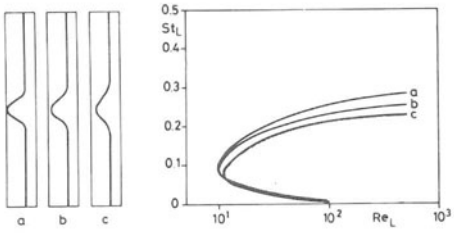

Stability Diagram

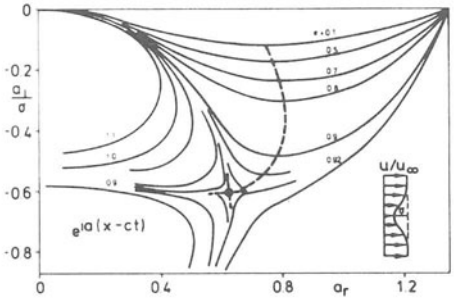

OERTEL [58], KOCH [59]

Spatial Amplification

Fig. 14 WAKES

nolds numbers, a stationary flow around a cylinder appears, which at Reynolds numbers greater than 5 is related to a stationary separation behind the cylinder. At the critical Reynolds number, which is between 30 and 40, the wake becomes unstable with respect to asymmetrical perturbations. As the Reynolds number is further increased, a periodic separation of the upper and lower boundary layers of the cylinder occurs. This is the classical Kármán vortex street. The experimental Fourier spectra obtained by SREENIVASAN show that the nonlinear temporal formation of structures is first characterized by two and then by three characteristic frequencies and their rational multiples. It then follows an intermittent state of a first appearance of chaos and a discrete power spectrum with four frequencies. At Reynolds numbers of about 150, there occurs the transition to a partially chaotic turbulent wake with a broad, slowly varying background of the power spectrum. The periodic spatial structure is preserved. Only the turbulent wake at Reynolds numbers larger than 10^5 with a homogeneous power spectrum shows a continuous wake. A drastic reduction in the drag coefficient c_D is related to this. The turbulent wake also grows unstable again and produces a new characteristic oscillation frequency of the newly-forming coherent turbulent structure at even higher Reynolds numbers. The temporal progression of the shock tube experiment of Fig. 14 shows that the separation of vortices is related to the formation of cylindrical pressure waves that influence the formation of structures in both the wake as well as the separating boundary layer. The entire flow field is coupled by the acoustic waves, which can lead to the appearance of acoustic resonance. Their interaction with the hydromechanical formation of structures is now a focus of research.

The fluid mechanical examples presented clearly demonstrate the complexity of the continuum mechanical transition to chaos in its dependence on differing initial and boundary conditions. For the description of the nonlinear evolution of fluid mechanical structures the model equations, discussed in the previous chapters, provide a valid solution only close to the onset of the primary instability. Nevertheless, the value of these model equations can be seen in their capability to describe characteristic details of the transition process at least qualitatively by means of simple numerical methods.

REFERENCES

[1] H. HAKEN: Synergetics, An Introduction, 3rd. ed., Springer, 1983.

[2] H. HAKEN: Cooperative Effects, Progress in Synergetics, North Holland, 1974.

[3] H. HAKEN: Cooperative Effects in Systems far from Thermal Equilibrium and in Non-physical System, Rev. Mod. Phys., 47, 67 (1975).

[4] H. HAKEN: Advanced Synergetics, Instability Hierarchies of Self-Organizing Systems and Devices, Springer, 1984.

[5] M.V. BERRY: Regular and Irregular Motion, Topics in Nonlinear Dynamics, American Institute of Physics Conference Proceedings Series, 46, 1978.

[6] P. COLLET, J.P. ECKMANN: Iterated Maps on the Interval as Dynamical Systems, Birkhäuser, 1980.

[7] O. GUREL, O.E. RÖSSLER: Bifurcation Theory and Applications in Scientific Disciplines, Annals of the New York Academy of Sciences, 316, 1979.

[8] R.H.G. HELLEMANN: Nonlinear Dynamics, Annals of the New York Academy of Sciences, 357, 1980.

[9] R.H.G. HELLEMANN: Self-Generated Chaotic Behavior in Nonlinear Mechanics, Fundamental Problems in Statistical Mechanics, North Holland, 1980.

[10] C.W. MORTON jr., L.E. REICHL, V.G. SZEBEHELY: Long-Time Prediction in Dynamics, John Wiley & Sons, 1983.

[11] E.N. LORENZ: Deterministic Nonperiodic Flow, J. Atmos. Sci., 20, 130 (1963).

[12] D. RUELLE: Dynamical Systems with Turbulent Behavior, Mathematical Problems in Theoretical Physics, Lecture Notes in Physics, 80, Springer, 1978.

[13] C. SPARROW: The Lorenz Equations: Bifurcations, Chaos and Strange Attractors, Applied Mathematical Sciences 41, Springer, 1982.

[14] N.J. ZABUSKY: Computational Synergetics and Mathematical Innovation, J. of Computational Physics, 43, 195-249 (1981).

[15] J.P. ECKMANN: Roads to Turbulence in Dissipative Dynamical Systems, Rev. Mod. Phys., 53, 643-645 (1981).

[16] D. RUELLE, F. TAKENS: On the Nature of Turbulence, Com. Math. Phys. 20, 167 (1971); 23, 343 (1971). J. of Computational Physics, 43, 195-249 (1981).

[17] B. SALTZMAN: Finite Amplitude Free Convection as an Initial Value Problem, J. Atmos. Sci., 19, 329 (1962).

[18] M.L. SWINNEY, J.P. GOLLUB: Hydrodynamic Instabilities and the Transition to Turbulence, Topics in Applied Physics, 45, Springer, 1981.

[19] J. ZIEREP, H. OERTEL jr., Convective Transport and Instability Phenomena, G. Braun, 1982.

[20] J.A. YORKE, E.D. YORKE: Chaotic Behavior and Fluid Dynamics, Topics in Applied Physics, 45, 77-95, Springer, 1981.

[21] M. VAN DYKE: An Album of Fluid Motion, 70, The Parabolic Press, 1982.

[22] G.L. BROWN, A. ROSHKO: On density effects and large structures in turbulent mixing layers, J. Fluid Mech., 64, 775-816, 1974.

[23] H. EICKHOFF, A. WINANDY: Visualization of Vortex Formation in Jet Diffusion and Flames, to appear: Combustion and Flame (1985).

[24] R. SCORER: Clouds of the World, Lothian, 1972.

[25] A.E. PERRY, M.S. CHONG, T.T. LIM: The Vortex-Shedding Process behind Two-Dimensional Bluff Bodies, J. Fluid Mech., 116, 77-90 (1982)

[26] D. COLES: Prospects for Useful Research on Coherent Structures in Turbulent Shear Flow, Proc. Indian Acad. Sci., 4, 2, 111-127 (1981).

[27] A. BLAQUIERE: Nonlinear System Analysis, Academic Press, 1966.

[28] L. SIDERIADES: Methods topologiques et applications, Annales télécommunication, 14, 8 (1959).

[29] H. BIPPES, M. TURK: Oil Flow Patterns of Separated Flow on a Hemisphere Cylinder at Incidence. DFVLR-FB 84-20, 1983.

[30] U. DALLMANN: Topological Structures of Three-Dimensional Vortex Flow Separation. AIAA-83-1935 (1983).

[31] A. LIBCHABER, J. MAURER: Une Experience de Rayleigh-Bénard de Geôme-trie Reduite; Multiplication, Accrochage et Demultiplication de Frequences, J. de Phys. (Paris) 41, C3, 51-56 (1980).
J. Phys. (Paris) 41, C3, 51 (1980).

[32] O.E. RÖSSLER: The Chaotic Hierarchy, Z. Naturforschung, 38a, 788-801 (1983).

[33] J. CRUTCHFIELD, D. FARMER, N. PACKARD, R. SHAW, G. JONES, R.J. DONNELY: Power Spectral Analysis of a Dynamical System, Phys. Lett., 76A, 1-4 (1980).

[34] Y. POMEAU, P. MANNEVILLE: Intermittent Transition to Turbulence in Dissipative Dynamical Systems, Commun. of Math. Phys., 74, 189-197 (1980).

[35] P. MANNEVILLE, Y. POMEAU: Different Ways to Turbulence in Dissipative Dynamical Systems, Physica 1D, 219-226 (1980).

[36] H.T. MOON, P. HUERRE, L.G. REDEKOPP: Transition to Chaos in the Ginzburg-Landau Equation, Physica 7D, 135-150, North-Holland Publishing Company, 1983.

[37] H.T. MOON, P. HUERRE, L.G. REDEKOPP: Three Frequency Motion and Chaos in the Ginzburg-Landau Equation, Phys. Rev. Lett. 49, 7, 458-460.

[38] J.P. GOLLUB, S.V. BENSON: Many Routes to Turbulent Convection, J. Fluid Mech. 100, 449-470, 1980.

[39] H. OERTEL jr., K. BÜHLER: in: Strömungsmechanische Instabilitäten, DFVLR-IB 221-83 A 01 (1983).

[40] H.L. SWINNEY, A. BRANDSTÄTER: A Strange Attractor: Chaos in the Couette-Taylor System, Preprints of the IUTAM Symposium on Turbulence and Chaotic Phenomena in Fluids, Kyoto, Japan, 26-33, 1983.

[41] H. OERTEL jr.: Thermal Instabilities, Adv. Space Res., 3, 5, 11-17 (1983).

[42] W. JÄGER, H. OERTEL jr.: Three-Dimensional Thermal Convection, DFVLR-IB 221-83 A 04 (1983).

[43] R. KESSLER, U. DALLMANN, H. OERTEL jr.: Nonlinear Transition in Rayleigh Benard Convection, Proceedings of the IUTAM Symposium on Turbulence and Chaotic Phenomena in Fluids (1983).

[44] H. OERTEL jr., K.R. KIRCHARTZ: Influence of Initial and Boundary Conditions of Benard Convection, Recent Developments in Theoretical and Experimental Fluid Mechanics, 355-366, Springer, 1979.

[45] R. KESSLER, H. OERTEL jr.: Nichtlineare Konvektion, ZAMM 63, T262-T264 (1983).

[46] R. KESSLER: Oszillatorische Konvektion, DFVLR-FB 84-14 (1984).

[47] R. KESSLER: Oscillatory convection in a rectangular box, submitted to J.F.M. (1984).

[48] S. FAUVE, A. LIBCHABER: Rayleigh-Bénard Experiment in a Low Prandtl Number Fluid, Mercury, Chaos in Order, ed. H. HAKEN, 25-35, Springer, 1984.

[49] J.P. GOLLUB, S.V. BENSON, J. STEINMAN: A Subharmonic Route to Turbulent Convection, Nonlinear Dynamics, ed. H.G. HELLEMAN, 22-27, New York Academy of Sciences, 1980.

[50] A. LIBCHABER, J. MAURER: Rayleigh-Bénard Experiment in Liquid Helium, Frequency Locking and the Onset of Turbulence, J. de Physique lettres, 40, 419-423 (1979).

[51] P. BERGE, M. DUBOIS, V. CROQUETTES: Approach to Rayleigh-Bénard Turbulent Convection in Differnt Geometries in Convective Transport and Instability Phenomena, ed. J. ZIEREP and H. OERTEL jr., 123-148, Braun-Verlag, 1982.

[52] F.N.M. BROWN: The Physical Model of Boundary Layer Transition, Proceedings of Ninth Midwestern Mechanics Conference, University of Wisconsin, Aug. 1965, pp.421-429.

[53] L. KLEISER, Spectral Simulations of Laminar-Turbulent Transition in Plane Poiseuille Flow and Comparison with Experiments, Springer Lecture Notes in Physics 170, 280-285 (1982).

[54] L. KLEISER, E. LAURIEN: Three-Dimensional Numerical Simulation of Laminar-Turbulent Transition and its Control by Periodic Disturbances, Proc. IUTAM Symposium on Laminar-Turbulent Transition, Novosibirsk, July 9-13, 1984 (Springer-Verlag, to appear).

[55] TH. HERBERT, M.V. MORKOVIN: Dialogue on Bridging Some Gaps in Stability and Transition Research, Laminar-Turbulent Transition, 47-72, Springer, 1980.

[56] W. TOLLMIEN, H. SCHLICHTING, H. GÖRTLER, F.W. RIEGELS, LUDWIG PRANDTL: Gesammelte Abhandlungen, Springer 1961.

[57] M.V. MORKOVIN: Flow Around Circular Cylinder - A Kaleidoscope of Challenging Fluid Phenomena, Proceedings ASME Symposium on Fully Separated Flows, 102-118, 1964.

[58] H. OERTEL jr.: Vortices in Wakes Induced by Shock Waves, Proceedings of the 14th International Symposium on Shock Tubes and Waves, Sydney, Australia, 293-300 (1983).

[59] W. KOCH: Local Instability Characteristics and Frequency Determination of Self-Excited Wake Flows. to appear in J. Sound Vibration 99 (1985).

SYNERGETICS

SELF-ORGANIZATION IN PHYSICS

H. HAKEN

1. INTRODUCTION

In my contribution, I shall present a small cross-section of a rather new field of interdisciplinary research called *"synergetics"*, HAKEN [1,2,3]. Emphasis will be laid on problems of fluid dynamics. In synergetics, we study the co-operation of individual parts of a system, which makes possible a self-organized formation of spatial, temporal, or functional structures on macroscopic scales. Systems studied so far belong to the fields of physics, electronics, mechanical and electrical engineering, chemistry, biology, and some "soft sciences". We shall ask whether or not there are general principles that govern self-organization irrespective of the nature of the individual subsystems, which may be electrons, molecules, photons, biological cells, or animals. In particular, we wish to develop an operational approach that will allow us to actually calculate the evolving structures (or "patterns"). The price we have to pay for the general validity of our approach is that we are limited to considering only such situations in which the state of a system undergoes qualitative macroscopic changes. Figures 1 and 2 provide us with some simple examples.

2. OUTLINE OF THE GENERAL APPROACH

The state of the system is described by a set of variables $q_1 \ldots q_n$, which we lump together into a state vector q. Since the processes generally depend on space and time, q also is a function of x and t. The following list gives a number of interpretations of the various components of q, and fields of applications:

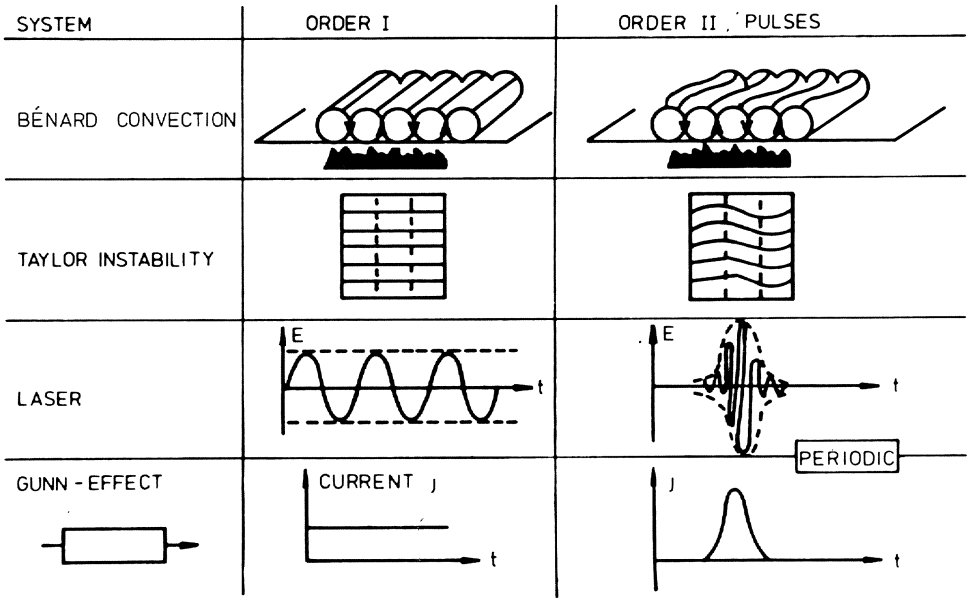

Fig. 1 Examples of self-organized formation of structures.
Row 1: *convection instability*
When a fluid layer is heated from below, beyond a critical temperature difference, a macroscopic motion in the form of rolls may start. With an even further increased temperature difference, oscillations may start.
Row 2: *Taylor instability.*
The liquid between two coaxial cylinders can follow the rotation of the inner cylinder by Couette flow, provided the rotation speed is small enough. Beyond a critical rotation speed, Taylor vortices are formed. If the rotation speed is even further increased, the Taylor vortices may start to oscillate.
Row 3: *laser light.*
When a laser is pumped only weakly, it acts like a lamp emitting incoherent wave tracks. Beyond a critical pump power, a coherent wave emerges. At still higher pump power, the coherent wave may decay into ultrashort regular pulses.
Row 4: *the Gunn instability.*
When a constant voltage is applied to a semiconductor sample, a dc current is generated. In some semiconductors, such as GaAs, pulsed currents can occur at an elevated voltage.

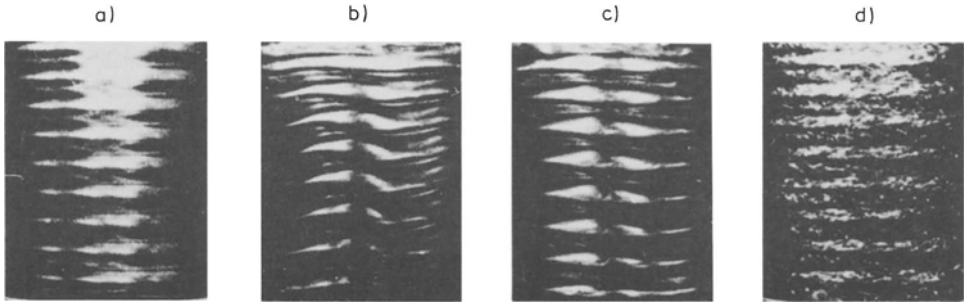

Fig. 2 Instability hierarchy of Taylor vortices ending in chaotic motion (weak turbulence) (according to H.L. SWINNEY, P.R. FENSTERMACHER and J.P. GOLLUP, in "Synergetics. A Workshop", ed. H. HAKEN, Springer Verlag, Berlin, Heidelberg, 1977, p.60).

numbers or densities	fluids, solidification
of atoms or molecules	chemical reactions
velocity fields	flames, lasers, plasmas
electromagnetic fields	electronic devices
electrons	solid state
firing rates of neurons	neural nets
numbers of specific cells	morphogenesis
monetary flows, etc.	economy
numbers of animals	ecology

The approach of synergetics rests on a number of "paradigms" (to use a word en vogue), namely:

a) evolution equations
b) instability
c) slaving
d) order parameters
e) formation of structures
f) instability hierarchies, chaos

3. A BRIEF OUTLINE OF THE MATHEMATICAL APPROACH

3.1 Evolution equations

These equations deal with the temporal evolution of q, i.e., we have to study $\dot{q} = N(q)$. The r.h.s. is a nonlinear function of the components q_j, e.g., q_1^2, $q_1 1_2$, etc.. The systems under consideration are dissipative, i.e., they contain equations of the form

$$\dot{q}_1 = -\gamma_1 q_1 + \ldots \tag{3.1}$$

They may contain transport terms describing

$$\begin{aligned} &\text{convection:} && v\nabla v, \quad v\text{: velocity} \\ &\text{diffusion:} && \nabla^2 q \equiv \Delta q \\ &\text{waves:} && \nabla^2 q \equiv \Delta q \end{aligned} \tag{3.2}$$

The systems are controlled from the outside, e.g., by changing the energy input. This control is described by control parameters, e.g., by α in the equation

$$\dot{q} = (\alpha - \gamma) q + \ldots \tag{3.3}$$

Finally, close to transition points fluctuations may play a decisive role. These fluctuations stem from fluctuating forces that represent the action of the microscopic "underworld" on the physical quantities q. Lumping all the different terms together, we are led to consider coupled nonlinear stochastic partial differential equations of the type

$$dq(x,t) = N(q,\nabla,x,\alpha,t)\,dt + dF \tag{3.4}$$

where we may use the Stratonovich calculus. Without fluctuations, the equations reduce to

$$\dot{q} = N(q,\nabla,x,\alpha,t) \tag{3.5}$$

Our following presentation will be based on (3.5), which includes, for example, the Navier-Stokes equations. For the general case, consult HAKEN [2].

3.2 Instability

We assume that we have found a solution of the nonlinear equations for given control parameters $\alpha = \alpha_0$. In practical cases such a solution may describe, for instance, a quiescent and homogeneous state, but our treatment may also include spatially inhomogeneous and oscillatory states. We

denote the corresponding solution by q_0. When we change the control parameter, that solution q_0 may lose its stability. To study the stability (or instability), we put

$$q(x,t,\alpha) = q_0(x,t,\alpha) + w(x,t,\alpha) \tag{3.6}$$

and insert it into (3.5). Assuming that w is a small quantity, we may linearize (3.5) and study the resulting equations of the form

$$\dot{w} = L(q_0(x,t),\nabla,x,\alpha)w, \quad w = w(t) \tag{3.7}$$

If L is independent of t, or depends on t periodically, or in a large class of systems depends on t in a quasiperiodic fashion, the solutions can be written in the form

$$w^{(j)}(t) = \exp(\lambda_j t)v^{(j)}(t) \tag{3.8}$$

where the vector v(x,t) is time-independent, time-periodic, or time- quasiperiodic. Thus the global temporal behaviour of w is determined by the exponential function in (3.8). We call those solutions whose real part of λ is positive, *unstable*, and those whose real part of λ is negative, *stable*. In order to solve the nonlinear equation (3.5), we make the hypothesis

$$q(x,t) = q_0(x,t,\Phi(t)) + \sum_j u_j(t)v^{(j)}(x,t,\Phi(t)) + \sum_k s_k(t)v^{(k)}(x,t,\Phi(t)) \tag{3.9}$$

(j and k run over the unstable and stable mode indices, respectively) where u_j and s_k are time-dependent, still unknown amplitudes, and Φ is a set of certain phase angles, in case we deal with quasiperiodic motion. For details, I refer the reader to HAKEN [2]. Here it may suffice to note that by inserting the hypothesis (3.9) into our original nonlinear equations (3.5), we find after some mathematical manipulations the following equations:

$$\dot{u}_j = \lambda_j u_j + N_j^{(u)}(u,\Phi,t,s) \tag{3.10}$$

$$\dot{s}_k = \lambda_k s_k + N_k^{(s)}(u,\Phi,t,s) \tag{3.11}$$

$$\dot{\Phi}_\ell = N_\ell^{(\Phi)}(u,\Phi,t,s) \tag{3.12}$$

Though in general one may not expect to simplify a problem by means of a transformation, the new equations (3.10)-(3.12) can be considerably sim-

plified when a system is close to instability points, where the real parts of some λ's change their sign from negative to positive.

3.3 The slaving principle

For the situations just mentioned we have derived the slaving principle for (stochastic) differential equations, HAKEN [2]. The slaving principle states that we may express the amplitudes s of the damped modes by means of u and ϕ at the same time, so that

$$s = f(u,\phi,t) \tag{3.13}$$

We shall call u and ϕ *order parameters*. We have studied numerous cases of dissipative systems and have found that in practically all of them there occur only few order parameters, while there are still very many slaved modes. As a consequence, we achieve an enormous reduction in the number of degrees of freedom, because we may express all damped modes s by the order parameters. In this way we obtain a closed set of equations of the form

$$\dot{u} = N(u,\phi,t) \tag{3.14}$$

$$\dot{\phi} = N'(u,\phi,t) \tag{3.15}$$

4. CLASSIFICATION OF ORDER PARAMETER EQUATIONS UNIVERSALITY CLASSES

To explain the essential features of the further approach, let us ignore the phase angles ϕ. As can be shown, close to transition points the order parameters u are small, so that N can be expanded into a Taylor series. Furthermore, due to symmetries, the resulting equations for u can be simplified and cast into a "normal form". The final equations may describe quite different systems. For example, the equation

$$\dot{u} = \lambda u - u^3 \tag{4.1}$$

describes a single mode laser close to the first threshold, roll formation in the convection instability, or formation of a chemical pattern. More complicated phenomena can be classified similarly.

5. FORMATION OF SPATIAL STRUCTURE
EXAMPLE OF A SINGLE ORDER PARAMTER

Let us start from a homogeneous, quiescent state, q_o. The hypothesis (3.9) then reduces to

$$q(x,t) = q_0 + u(t)v_u(x) + \sum_j s_j v_j(t) \qquad (5.1)$$

mode skeleton slaved modes

Because the amplitudes of the slaved modes are small compared to u (close to the transition point), the evolving pattern is determined by the mode skeleton $u(t)v_u(x)$. Figure 3 shows the temporal growth of u(t) according to eq.(4.1), and figure 4 shows the evolving pattern.

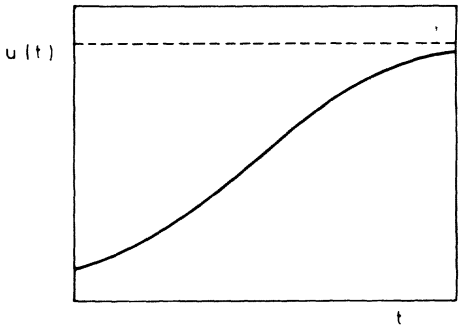

Fig. 3

Increase of u(t) towards its stationary state.

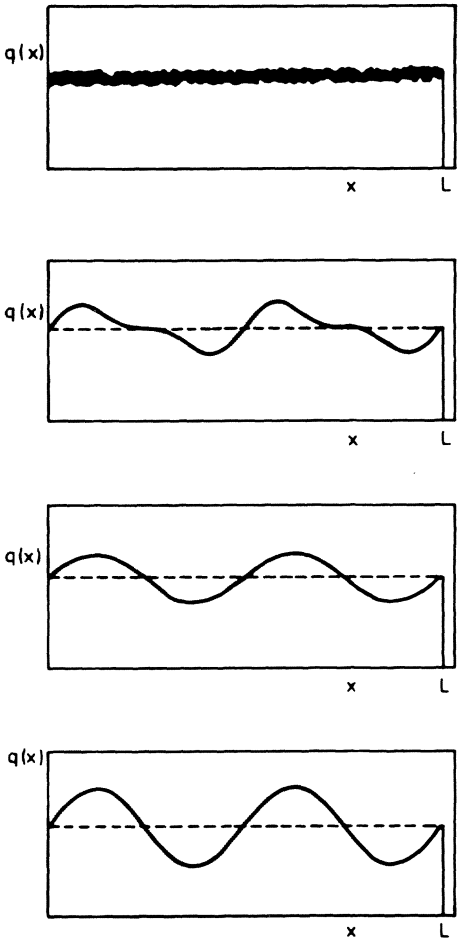

Fig. 4 Build-up of spatial patterns.

6. GENERALIZED GINZBURG-LANDAU EQUATIONS

When the dimensions of continuously extended systems are large compared to the fundamental length of developing patterns, the spectrum λ is practically continuous. In such a case, particular mathematical difficulties arise, since it is no longer possible to clearly distinguish between undamped and damped modes. A way out of this difficulty can be found when we resort to the formation of wave packets. This in turn necessitates that the order parameters, which we shall call ξ, depend not only on time but now also on space (in a slowly varying fashion). Therefore our hypothesis reads

$$q(x,t) = q_0 + \sum_{k_c} \xi_{k_c}(x,t) v_{k_c}(x) + \sum \text{ slaved modes} \tag{6.1}$$

where k_c runs over a discrete set of critical wave vectors at which the instabilities occur. For simplicity, let us again consider a case in which no phase angles occur, and let us from this point on be satisfied with an expansion of the nonlinear terms up to third order. The order parameter equations then aquire the form

$$\dot{\xi}_{k_c}(x,t) = \lambda_{k_c}(\nabla)\xi_{k_c}(x,t) + \sum_{k_1,k_2} A \ldots \xi_{k_1}\xi_{k_2} + \sum_{k_1,k_2,k_3} B \ldots \xi_{k_1}\xi_{k_2}\xi_{k_3} + F_{k_c} \tag{6.2}$$

I have called these equations, which I derived some time ago, "Generalized Ginzburg-Landau-equations", because they are strongly reminescent of the famous Ginzburg-Landau-equations. But two important distinctions should be noted. While the original Ginzburg-Landau-equations refer to a system in thermal equilibrium, my Generalized Ginzburg-Landau-equations refer to systems far from thermal equilibrium. Furthermore, the original Ginzburg-Landau-equations were derived in a heuristic fashion, whereas the Generalized Ginzburg-Landau-equations have been derived rigorously. Because of the double and triple sums, these equations are quite clumsy. However, under well justified assumptions, these equations can be simplified, as I have shown recently, HAKEN [2]. To this end, I define a new function

$$\Psi(x,t) = \sum_{k_c} \exp\{ik_c x\}\xi_{k_c}(x,t) \tag{6.3}$$

After a few elementary manipulations and under specific assumptions on λ, A and B, eq.(6.2) can be cast into the form

$$\dot{\Psi}(x,t) = (a+b(k_0^2-\nabla^2)^2)\Psi + a\Psi^2 + B\Psi^3 + F, \qquad (6.4)$$

where I have chosen an explicit example for $\lambda(k)$, which refers to the eigenvalues of the convection instability. We have solved this equation on a computer to study the temporal evolution of patterns, BESTEHORN & HAKEN [4]. Some typical results are shown in Figures 5 - 9.

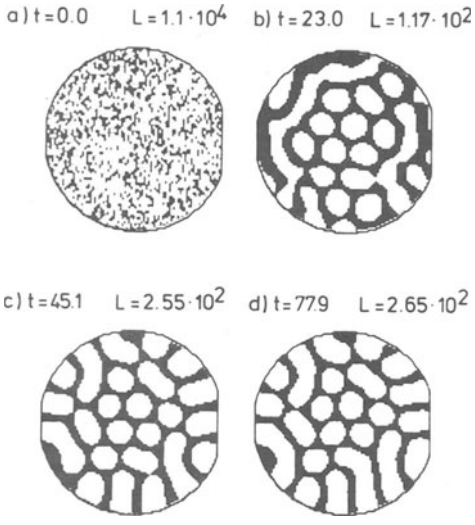

Fig. 5

Computer solution of eq. (6.4) for circular geometry. Starting from a random dot pattern, the parameters are chosen such that a hexagonal pattern is to be expected (according to M. BESTEHORN and H. HAKEN [4]).

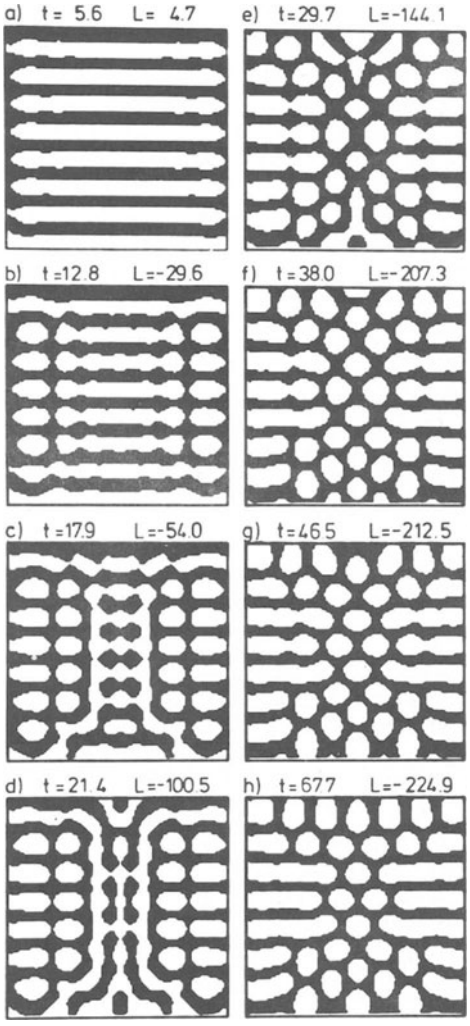

Fig. 6

Computer solution of eq. (6.4). As initial condition a roll pattern is given. The pattern evolves towards a mixed hexagonal and roll pattern. Time of evolution: first left row downwards, then right row downwards [4].

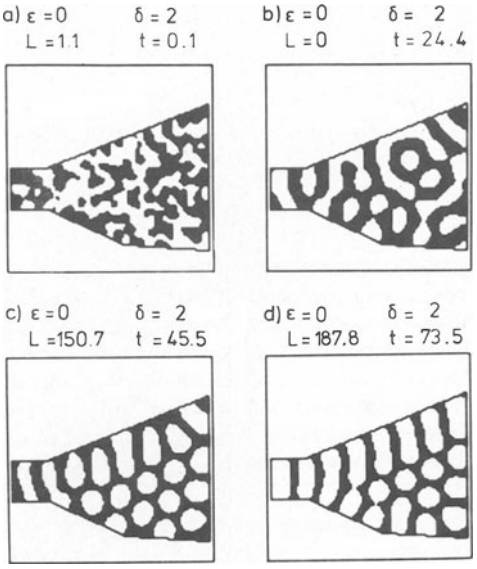

Fig. 7

Computer solution of eq. (6.4) for an odd geometry starting from a random initial state [4].

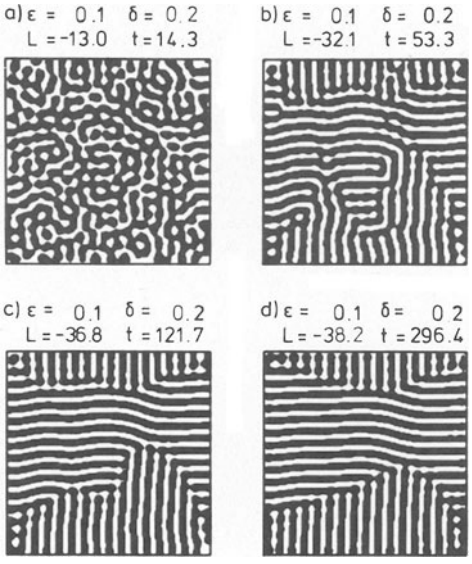

Fig. 8

This computer solution of eq. (6.4) describing the time evolution shows the coexistence of roll patterns [4].

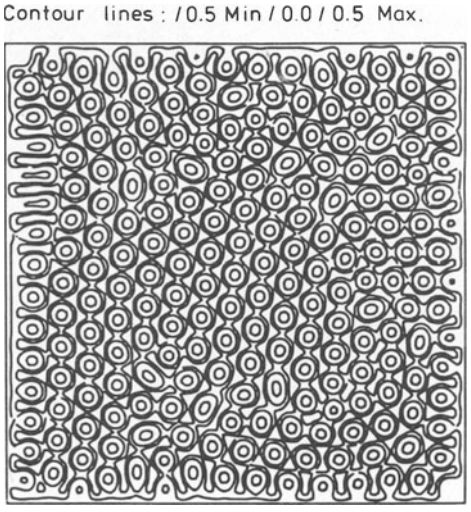

Fig. 9

Contour line plot of solution to eq. (6.4) for $t \to \infty$. The hexagonal pattern is clearly visible [4].

7 LOW-DIMENSIONAL ORDER PARAMETER EQUATIONS LEADING TO TEMPORAL STRUCTURES

When two real order parameters are present, and a control parameter is changed, a fixed point may bifurcate into a limit cycle (describing an oscillation at a fundamental frequency ω_1, see Figure 10). With α changed further, a third order parameter may occur and the limit cycle bifurcates into a torus describing quasiperiodic motion at fundamental frequencies ω_1, ω_2 (being irrational with respect to each other). If ω_1 and ω_2 are rational with respect to each other, some new limit cycle occurs (Figure 11).

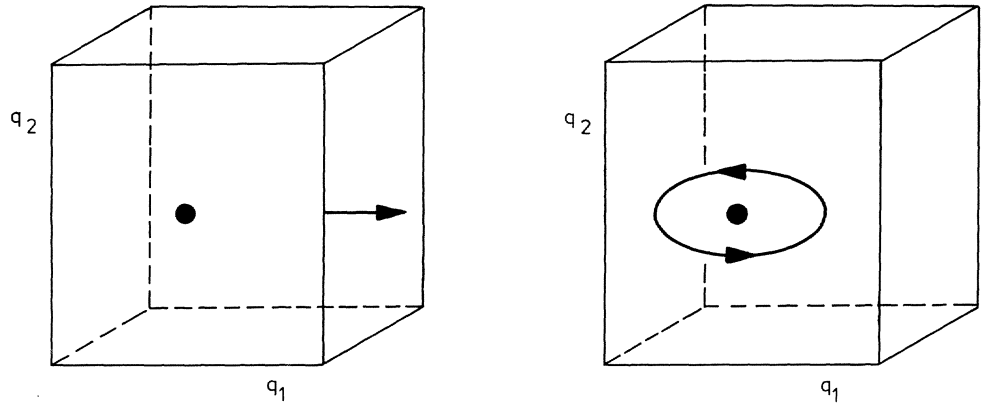

Fig. 10 Bifurcation of a stable fixed point to a limit cycle.

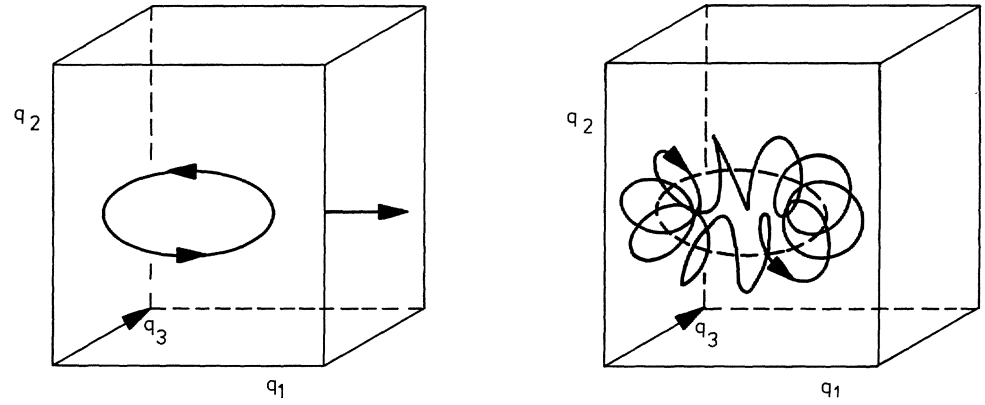

Fig. 11 Transition from the limit cycle to a limit cycle of a more complicated structure. If the corresponding two frequencies of the motions are irrational with respect to each other, the solid curve does not close but fills a torus.

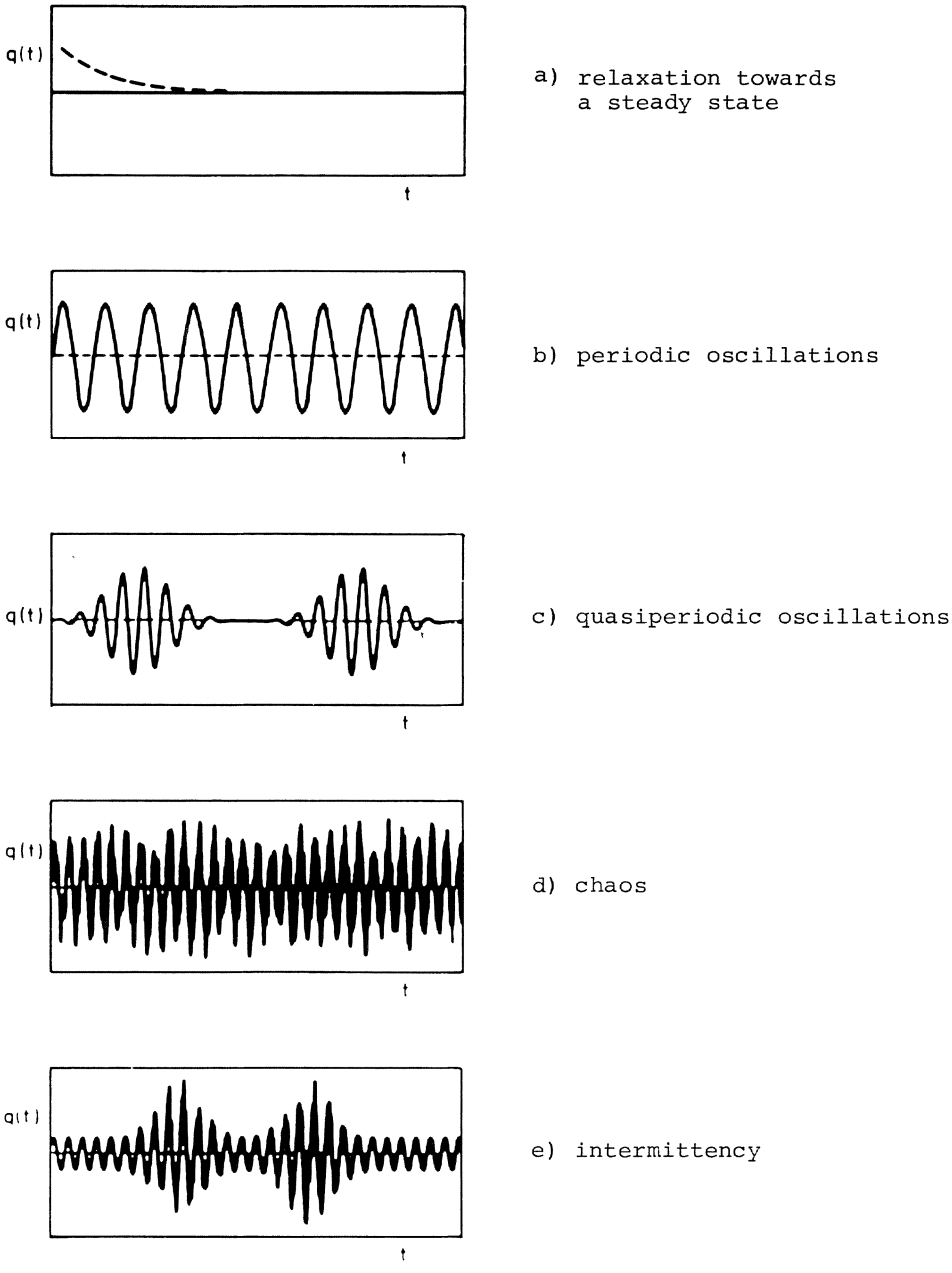

Fig. 12 Typical temporal patterns found in synergetic systems.

When α is changed further, the T_2-torus may become unstable. According to the "Ruelle-Takens picture" (RUELLE, TAKENS [5]), chaos, i.e., irregular motion, then occurs in the "generic case". According to my own analysis, HAKEN [2], the question of whether chaos occurs is not a problem of "genericity" but of measure.

As a consequence, a T_3-torus with three basic (irrational) frequencies ω_1, ω_2, ω_3 can occur as well. This explains why experimentally both phenomena, chaos or T_3 (or even T_4), are found (c.f. e.g. the contribution by SREENIVASAN to this volume). Figure 12 presents typical examples of temporal structures described by low-dimensional order parameter equations.

In conclusion, we mention that the various routes to chaos, e.g. the Ruelle-Takens picture or the period doubling sequence, can be understood within *low-dimensional* subspaces spanned by few order parameters. In the case of a strange attractor, only part of the subspace is "filled" by the trajectories, so that a fractional dimension may result.

8. SYNERGETICS, WHAT USE?

I hope that I was able to show in the foregoing how the mathematical approach of synergetics, of which I presented a skeleton, allows us to calculate evolving patterns, e.g., in fluid dynamics. In particular, the slaving principle and order parameter approach allow us to calculate the patterns directly "by hand", or at least to save considerable computer time. The whole method applies not only to space- and time-independent q_o's but also to q_o's with arbitrary space dependence and quasiperiodicity in time. But I think it is still more important that this approach provides us with new qualitative insights into the behaviour of complex systems.

Finally, the analogies between different systems at the order parameter level have proven most useful. For instance, in fluid dynamics LORENZ [6] demonstrated the possibility of chaos. In 1962 I derived the single-mode laser equations, and solved them for the steady state. Later (1975) I found that both types of equations can be easily transformed into each other, HAKEN [7]. I predicted as the immediate consequence the possibility of producing a new type of light: chaotic laser light. It was found recently, as were even various routes to it (see e.g. WEISS [8]). In this case, fluid dynamics has helped to find new phenomena in laser physics. I hope that in the future, fluid dynamics can profit in the same way from other fields by use of analogies at the order parameter level.

9. REFERENCES

[1] H. HAKEN: Synergetics. An Introduction. Nonequilibrium Phase Transitions and Self-Organization in Physics, Chemistry, and Biology. Third Revised and Enlarged Edition, Springer Verlag, Berlin, Heidelberg, New York, Tokyo (1983).

[2] H. HAKEN: Advanced Synergetics. Instability Hierarchies of Self-Organizing Systems and Devices. Springer Verlag, Berlin, Heidelberg, New York, Tokyo (1983).

[3] For a popularisation, see:
H. HAKEN: The Science of Structure. Synergetics. Van Nostrand Reinhold Comp., New York, Toronto, London (1984).

[4] M. BESTEHORN & H. HAKEN: Phys. Letters 99A, 6,7, (1983), p.265, and to be published.

[5] D. RUELLE, F. TAKENS: Commun. Math. Phys. 20, 167 (1971);
S. NEWHOUSE, D. RUELLE, F. TAKENS: Commun. Math. 64, 35 (1978).

[6] E.N. LORENZ: J. Atmospheric Sci. 20, 130 (1963); 20, 448 (1963).

[7] H. HAKEN: Phys. Letters 53A, 77 (1975).

[8] C.O. WEISS, A. GODONE, A. ÓLAFSSON: Phys. Rev. A28, 892 (1983).

NONLINEAR DYNAMICAL SYSTEMS

TORI AND CHAOS IN A SIMPLE C^1-SYSTEM

O.E. RÖSSLER, C. KAHLERT, B. UEHLEKE

1. INTRODUCTION

The world is a partial differential equation (P.D.E.) - to some approximation at least. The qualitative behavior of P.D.E.s, however, is potentially infinitely complex. It is therefore fortunate that some P.D.E.s behave precisely like ordinary differential equations (O.D.E.s) in some of their regimes. Two recent cases in point are the surprising discovery of *silent turbulence* by DALLMANN [1], and the successful analytic demonstration of constant-shape traveling chaotic waves in a boundary value problem of reaction-diffusion type, RÖSSLER & KAHLERT [2]. A third example is the new observation by SREENIVASAN [3] that turbulent vortex streets involve, with comparable probabilities, either hypertori of up to 50 dimensions or related hyperchaos of the same dimensionality (cf. RÖSSLER [4] for these notions).

These empirical findings provide sufficient motivation to present a new prototypic ordinary differential equation that (1) possesses solutions with similar properties and (2) is in principle completely tractable analytically.

2. THE EQUATION

Consider the following simple 3-variable autonomous dynamical system:

$$\begin{aligned} \dot{x} &= -y-z \\ \dot{y} &= x \\ \dot{z} &= a(1-|y|)-bz \end{aligned} \qquad (1)$$

The system consists of two linear half systems that differ only by the sign of one term (in the last line). The two half systems are glued together along a threshold plane (y = 0) in such a way that each trajectory continues smoothly (in a once differentiable, "C^1", fashion) across the divide.

3. SOME PICTURES

A first numerical simulation is presented in Fig. 1. It pertains to the special case of no damping (b = 0). In this case of zero divergence, volume in state space is strictly conserved. The initial condition chosen in the simulation is maximally close (just short of coinciding numerically) to one of the two steady states of the system - that on the left (at 0, 1, -1). This steady state is a saddle focus whose stable manifold is one-

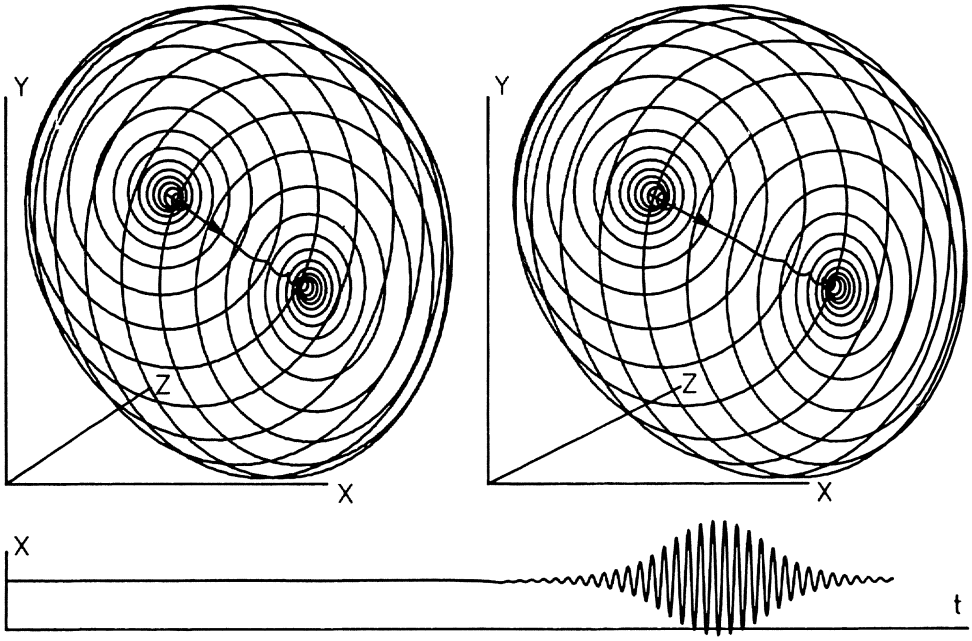

Fig. 1 A transient, maximum-amplitude recurrent trajectory in Eq. (1). Case of no damping (see text). Numerical simulation using a standard Runge-Kutta-Merson integration routine (maximum step error $10^{\ }$). Stereoplot (two different parallel projections) with one time-trace added (bottom). Parameters chosen: a = 0.1, b = 0. Initial conditions: x(0) = 0, y(0) = 1, z(0) = - 0.99999999999. Axes: -2 to 2 for x and y, -1 to 1 for z, 0 to 500 for t.

dimensional (a straight line emerging from the saddle). Therefore the trajectory (see arrow) at first virtually coincides with this straight line - until it reaches the separating plane (y = 0). Beyond that threshold, a spiralling motion of visible amplitude suddenly takes over in a smooth fashion. The reason for this transition is that the *mirror* saddle focus on the right (at 0, -1, 1), which punctures the same plane with its own one-dimensional manifold, which is unstable, does so at not quite the same point. The continuation of the original trajectory to the right therefore has a displaced axis to circle, so to speak. From then on, the trajectory expands along the 2-D stable manifold of the right-hand saddle until the vicinity of the first saddle (to the left) is reached again - and so forth. Such back and forth motions continue for quite a while until eventually the trajectory escapes to infinity. (In the present simulation, though, actually a more *inner* torus of the type to be described next was attended over many rounds - 61 per 10000 time units.)

A different type of qualitative behavior, applying at the same parameter values, is shown in Fig. 2. The trajectory now starts considerably more to the inside of the *onion* seen in Fig. 1. One sees that it never leaves the vicinity of a certain toroidal surface. The latter is apparently just one element of a one-parameter family of concentric invariant tori. In between this infinite number of tori, the results of KOLMOGOROV, ARNOLD, and MOSER on *weak* chaos (sandwiched in between a countable set of Hamiltonian tori, see MOSER [5], and ABRAHAM & MARSDEN [6]) can be expected to apply. If a is increased progressively up to $a_{crit} < 0.503$ (appropriate initial conditions are 1.68, 0, 0, respectively), eventually not even an infinitely thin *tube* (family of tori) of the same (*period one*) class survives, cf. ABRAHAM & MARSDEN [6]. The present system is probably the simplest continuous example of these *Hamiltonian* phenomena.

Proceeding now to small finite damping (b = 0.03), one finds the chaotic attractor of Fig. 3 for an appropriate window of initial conditions. The present attractor consists of a folded-over (and therefore partly MÖBIUS [7]) *band* that happens to be wrapped up twice. The chaos shown therefore is a modulation of an underlying period-4 process. Probably an infinite number of such chaotic attractors arise and disappear close to the limit b = 0 (cf. CHENCINER [8]).

If the damping is increased to a considerably higher value (b = 0.2), a simpler chaotic attractor of the same basic type is obtained: Fig. 4.

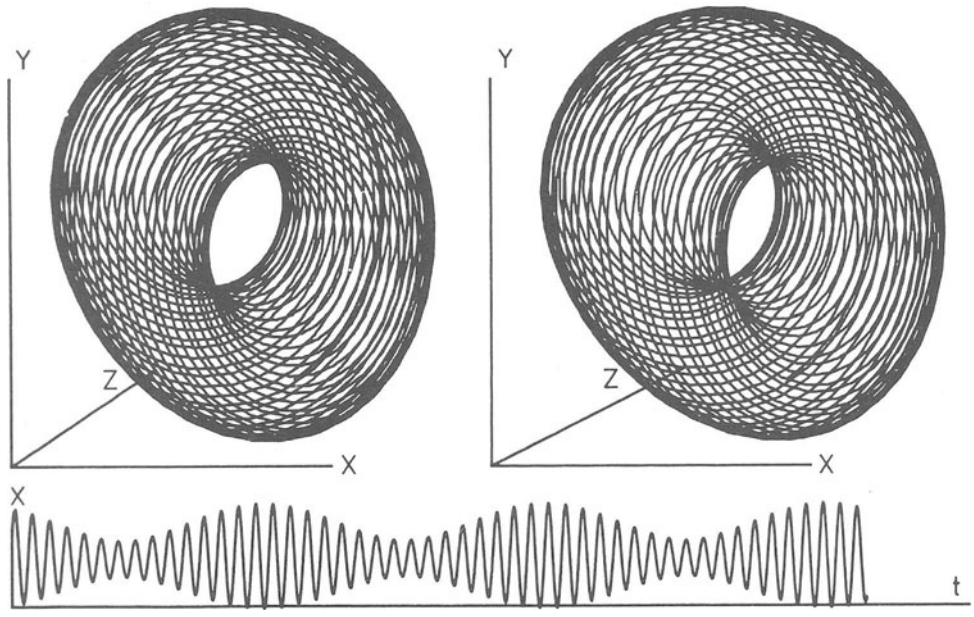

Fig. 2 A trajectory hugging an invariant torus in Eq. (1). Parameters as in Fig. 1. Initial conditions: 1, -1.4, -0.4, respectively. Axes as in Fig. 1 except 0 to 350 for t.

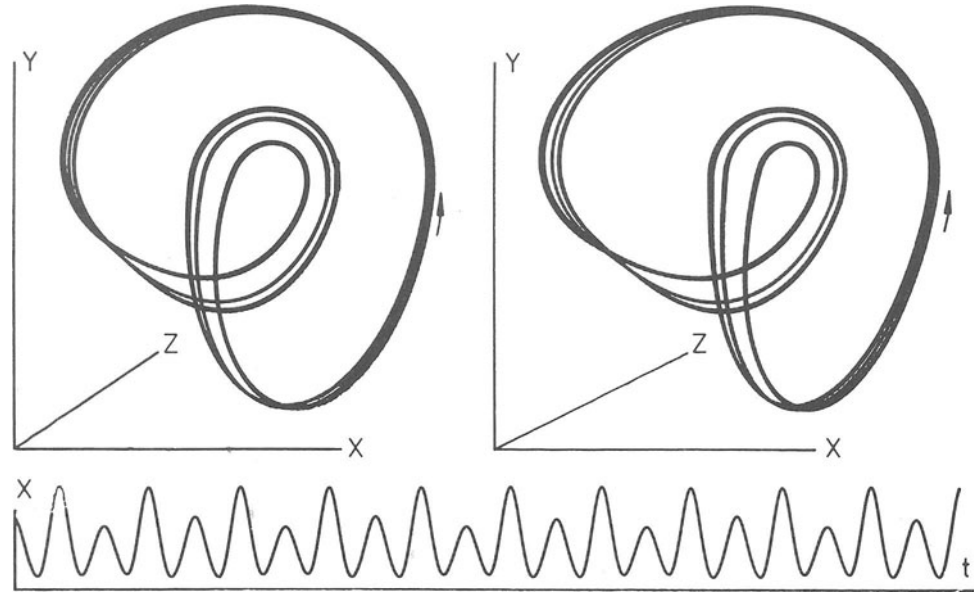

Fig. 3 A first attracting chaotic regime in Eq. (1). Parameters: a = 0.54178, b = 0.03. Initial conditions: 0.887, 0.147, 0.121, respectively. Axes as in Fig. 1 except 0 to 130 for t.

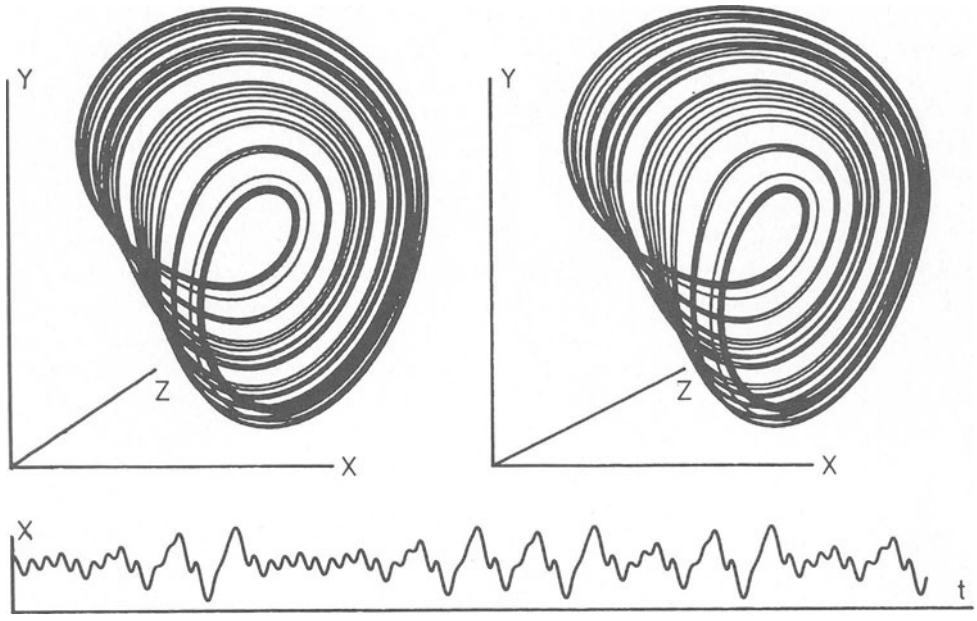

Fig. 4 A second attracting chaotic regime in Eq. (1). Parameters: a = 0.6, b = 0.2. Initial conditions: 1.8, 0, 0, respectively. Axes as in Fig. 1 except -1.5 to 1.5 for z, 0 to 200 for t.

4. A GENERALIZATION

The principle underlying the design of Eq. (1) can be generalized. Eq. (1) can be understood as consisting of a linear oscillator (in x and y) whose time-averaged amplitude (|y|) is part of another 2-variable oscillator (having z, which *sees* only |y|, for the second variable). Another level can therefore be added in a straightforward manner (cf. RÖSSLER [9]), in which the new *second variable* sees only a time-averaged amplitude (|z|) of the last-mentioned oscillator:

$$\begin{aligned} \dot{x} &= -y - z - w \\ \dot{y} &= x \\ \dot{z} &= a(1-|y|) \\ \dot{w} &= c(0.5-|z|) \end{aligned} \qquad (2)$$

This equation does indeed produce a periodically growing and shrinking (*breathing*) torus - that is, hypertorus - if the same projection is chosen as in Fig. 2 and the parameters and initial conditions of Fig. 2 are complemented by c = 0.01 and w(0) = 0.05. For other initial conditions, hyperchaotic transients, analogous to those of Fig. 1 but exponentially diverging in two directions, can be expected. With non-zero damping terms added, hyperchaotic attractors should develop (cf. RÖSSLER [9,4]).

Eq. (2) as written, thus constitutes a candidate for a better understanding of much higher-dimensional (globally 6- and locally 5-dimensional) Hamiltonian systems (cf. ABRAHAM & MARSDEN [6]). Its close to toroidal *hyperchaotic attractors* (yet to be found for the right damping values), on the other hand, may be of interest as a metaphor for dissipative *turbulent* systems.

5. DISCUSSION

It seems as if Eq. (1) were the simplest autonomous system with chaotic solutions so far. Being piecewise linear, it is moreover specially amenable to analysis. A first autonomous C^1-system, almost as simple but without any toroidal solutions, was proposed in RÖSSLER, GÖTZ & RÖSSLER [10] and analyzed in SPARROW [11] and UEHLEKE & O.E. RÖSSLER [12]. A third single-threshold C^1 example was just found by T. MATSUMOTO, Waseda University, Tokyo. (Leon Chua, personal communication, June 1984).

The method of choice in the analytic study of piecewise-linear systems is that of Poincaré half maps, UEHLEKE & RÖSSLER [12, 13]. An implicit algebraic equation (a map that is diffeomorphic and invertible almost everywhere) is obtained for successive puncturings of the separating plane. A complete classification of chaotic piecewise-linear systems with a single planar threshold, no matter whether C^0 or C^1, is within analytical reach, KAHLERT [14].

The further study of low-dimensional O.D.E.s may be useful for a better understanding of turbulent phenomena in fluids, OERTEL [15]. The recent revival in part of the Landau-Hopf multiple-incommensurate-frequency picture of turbulence generation (SREENIVASAN [3]) indicates that simple continuous systems such as Eq. (1), which generate *both* tori and chaos, may be particularly useful.

6. CONCLUSIONS

A new piecewise-linear autonomous 3-variable ordinary differential equation is proposed which may be written in the simple form $\dddot{y}+\ddot{y}+\alpha(1-|\dot{y}|)+\dot{y}+y=0$. This system produces a one-parameter family of invariant tori known as KAM tori. When a linear damping term (by) is added on the left-hand side, the system produces chaotic attractors of different types. A 4-variable generalization (involving two absolute-value functions) analogously produces hypertori and hyperchaos. The new hierarchy can be studied further by means of the analytic technique of Poincare half maps.

ACKNOWLEDGEMENT

O.E. Rössler thanks Len Pismen, Ralph Abraham and Bruce Stewart for discussions. C. Kahlert acknowledges support by the Studienstiftung and the DFG.

REFERENCES

[1] U. DALLMANN: Structural stability of 3-dimensional vortex flows. (These proceedings).

[2] O.E. RÖSSLER, C. KAHLERT: Chaos as a limit in a boundary value problem. (Submitted).

[3] K.R. SREENIVASAN: Transitional and turbulent wakes and chaotic dynamical systems. (These proceedings).

[4] O.E. RÖSSLER: The chaotic hierarchy. Z. Naturforsch. 38 a, 788-801 (1983).

[5] J. MOSER: Stable and Random Motions in Dynamical Systems. Princeton, N.Y.: Princeton University Press (1973).

[6] R. ABRAHAM, J.E. MARSDEN: Foundations of Mechanics. Reading, Mass.: Benjamin/Cummings (1978).

[7] O.E. RÖSSLER: Chaotic behavior in simple reaction systems. Z. Naturforsch. 31 a, 259-264 (1976).

[8] A. CHENCINER: There are more good saddle-node families of invariant curves than could be expected. In: "Dynamical Systems and Bifurcations" (B.L.J. Braaksma, H.W. Broer and F. Takens, eds.), Springer Lect. Not. Math. (to appear).

[9] O.E. RÖSSLER: Continuous chaos - four prototype equations. In: "Bifurcation Theory and Applications in Scientific Disciplines" (O. Gurel and O.E. Rössler, eds.), Ann. N.Y. Acad. Sci. 316, 376-392 (1979).

[10] R. RÖSSLER, F. GÖTZ, O.E. RÖSSLER: Chaos in endocrinology. Biophys. J. 25, 216a (1979) (Abstract); O.E. RÖSSLER: The gluing-together principle and chaos. In: "Nonlinear Problems of Analysis in Geometry and Mechanics" (M. Atteia, D. Bancel and I. Gumowski, eds.), 50-56. Boston-London: Pitman (1981). sd

[11] C. SPARROW: Chaos in a 3-dimensional single-loop feedback system with a princip linear feedback function. J. Math. Anal. Appl. 83, 275 (1981).

[12] B. UEHLEKE, O.E. RÖSSLER: Analytical results on a chaotic piecewise-linear O.D.E., Z. Naturforsch. 39 a, 342-348 (1984).

[13] B. UEHLEKE, O.E. RÖSSLER: Complicated Poincare half-maps in a linear system. Z. Naturforsch. 38 a, 1107-1113 (1983).

[14] C. KAHLERT: Infinite nonperiodic wave-trains in a class of reaction-diffusion systems (in German). Ph. D. Thesis, University of Tübingen (1984).

[15] H. OERTEL: Temporal and Spatial Structures in Fluid Mechanics. (These proceedings).

TRANSITIONAL AND TURBULENT WAKES AND CHAOTIC DYNAMICAL SYSTEMS

K.R. SREENIVASAN

Recent studies of the dynamics of simple nonlinear systems with chaotic solutions have produced very interesting and (perhaps) profound results with several implications in many disciplines. However, the interest of fluid dynamicists in these studies stems primarily from the expectation that they will help us better understand the process of transition and turbulence in fluid flows. At this time, much of this expectation remains untested, especially in 'open' or unconfined fluid systems. This work is aimed at filling some of this gap.

We have measured in the wake behind a circular cylinder, chiefly about 5 diameters behind it, the spectral density of streamwise velocity as a function of the Reynolds number. If the free stream turbulence is low and devoid of any discrete frequency, the signal/noise ratio is large (as in our experiments where the peak signal/noise ratio is of the order of 10^6 or more), and the FFT has adequate resolution, it can be seen that the transition to chaotic state (broad-band spectrum) is characterized by the following stages. As the Reynolds number is increased:

(a) there is first only one basic frequency f_1 (and its harmonics) arising from vortex shedding;

(b) this is followed by the appearance of a second frequency f_2, incommensurate with the vortex shedding frequency and the various combinations of the two frequencies;

(c) a third incommensurate frequency appears (with several combinations of the three frequencies);

(d) at a slightly higher Reynolds number, the spectrum has a broad-band character, although the peak corresponding to the vortex shedding remains.

Phase diagrams and Poincaré sections, as well as calculations of the dimension of the attractor, confirm the existence of these stages, which are much like those indicated by the Ruelle-Takens-Newhouse picture.

However, with further increase in Reynolds number, there is a re-emergence of order, appearance of a fourth independent frequency, and a return to chaotic state; we emphasize that there is a stage in which there are four independent degrees of freedom with no chaos. From this second chaotic state, one can discern the re-emergence of order and return to chaos once again; we suspect that there are many windows of chaos and order - much as in several dynamical systems. It appears that the discontinuity in the vortex shedding frequency at Reynolds numbers of about 80 and 130 is related to the appearance of chaos and order. We have shown that the dimension of the attractor is truly representative of the number of degrees of freedom in the early stages of transition characterized by discrete frequencies. If this same interpretation of the dimension is true also in the chaotic state, then the relatively low dimension of the attractor even at Reynolds number up to about 10^4 suggests that the number of degrees of freedom in turbulent flows far past transitional stages is not high, and some kind of slaving principle or renormalization theory ought to be brought to bear in the reformulation of the "turbulence problem".

1. INTRODUCTION

The equations governing the (incompressible) motion of fluids are

$$\frac{\partial u_i}{\partial x_i} = 0 \tag{1.1}$$

$$\frac{\partial u_i}{\partial t} + u_j \frac{\partial u_i}{\partial x_j} = -\frac{\partial p}{\partial x_i} + \frac{1}{Re} \frac{\partial^2 u_i}{\partial x_j \partial x_j} \tag{1.2}$$

where we have restricted ourselves to body-force-free situations and used suitably normalized quantities, and Re is the Reynolds number. Observations have shown that for the given boundary conditions (and external forces, if applicable), the flow is unique and steady for $Re < Re_{cr}$, where Re_{cr} is a certain critical value of Re; this is the steady laminar motion. As Re increases, the fluid motion may first become periodic, quasi-periodic, etc., and "eventually" chaotic and irregular such that the details of this state of motion are not reproducible. This state is not necessarily "turbulence" as generally understood - whatever this precisely means - but it is believed that the turbulent state is reached if the Reynolds number is high enough. The traditional goal of the stability theory is to describe the evolution from the laminar to the turbulent state, and the goal of all turbulence theories is to understand the (fully) turbulent state itself.

In the recent past, claims have been made that autonomous dynamical systems with small number of degrees of freedom, typified by

$$\frac{db_i}{dt} = f(b_i; \varepsilon_i) \ , \tag{1.3}$$

where i is small and ε_i are the control parameters, help us towards attaining both of the goals mentioned above.

Several questions arise immediately. One natural question is to what degree dynamical systems with small number of degrees of freedom are relevant to fluid flows. To elucidate the concept of "degrees of freedom in fluid flows", let us approximate

$$u_i = \sum_{\underset{\sim}{k}} a_i(\underset{\sim}{k};t) e^{i\underset{\sim}{k}\cdot\underset{\sim}{x}} \tag{1.4}$$

which, with (1.1) and (1.2), yields equations of the type

$$\frac{\partial a_i}{\partial t} = F(a_i; Re), \quad i = 1, N \ (\text{large}). \tag{1.5}$$

The number of the coefficients a_i, which, for given boundary conditions for the fluid flow, are capable of variation in time, can now be called the degrees of freedom of the fluid flow governed by (1.1) and (1.2). Since the laminar flow is uniquely specified by the boundary (and external force) conditions, this number is zero. If Re increases past Re_{cr}, only a finite number of degrees of freedom are excited, and hence it appears that, at least in the transcritical regime, consideration of a small number of degrees of freedom is adequate.

An interesting hypothesis, which we shall examine in this paper, is that the number of degrees of freedom (not necessarily in the sense described above) remains small even in high Reynolds number turbulence.

Assuming that the number of degrees of freedom excited in the neighbourhood of the critical state is indeed small, we must ask if the behaviour in the transcritical regime is independent of the precise nature of the right-hand side of equations (1.3) and (1.5). The reason most often cited in support of the belief that the detailed structure of f_i in (1.3) is immaterial in understanding the evolution of chaotic state in dynamical systems, is the RUELLE-TAKENS theorem [1], which states that chaos (or strange attractor) sets in abruptly, following a few HOPF bifurcations, and that this behaviour is "typical". (In a later paper, NEWHOUSE, RUELLE & TAKENS [2] consider motion on a three-torus (i.e., quasi-periodic motion with three incommensurate frequencies) and introduce a small nonlinear coupling among the three oscillators. They argue that to produce a broad-

band spectral density, it is enough to have a weak coupling among the three oscillators.). Whether or not fluid flows are "typical" in the sense that RUELLE & TAKENS discuss is not clear at all, and one should attempt to answer this question by looking at the specific form of F in (1.5) and by observing the actual bifurcations in experiments on laminar-turbulent transition.

Finally, one must mention the predominant role played by spatial chaos (and order!) in turbulent flows of fluids. Autonomous dynamical systems, on the other hand, do not contain any space information. While spatial order and chaos in fluid turbulence may in some way be related to temporal chaos and order, it is clear that there is little that (autonomous) dynamical systems can say directly about the former.

Several beautiful experiments that have been carried out in the Taylor-Couette flow (e.g., Refs. 3,4) and the convection box (Refs. 5,6) have lent support to the idea that fluid flows bear a close correspondence to dynamical systems. This in itself is undoubtedly remarkable, but it should be remembered that these two flows are special in the following sense. In all "closed flow" systems - of which the convection box and the Taylor-Couette flow are popular examples - each value of the control parameter (for example, the rotation speed of the inner cylinder in the Taylor-Couette problem) characterizes a given state of the flow globally. At least in principle, one can follow the various stages of transition to turbulence in as much detail as possible by exercising infinitely fine control over the control parameter. This is not necessarily true for another class of flows, which we may call "open systems", e.g., channel flows, wakes, jets, boundary layers, etc.. Consider the channel (or the plane Poiseuille) flow. For a given value of the control parameter Re, the flow can be laminar at one location, transitional at another, and turbulent at yet another (downstream) location; the same is true of jets, wakes, for example. As a result, at least two complications arise. First, in open systems, observations cannot be made with such exactitude as in closed flow systems. Second, there could in principle be a strong coupling between different phenomena in different spatial locations in a way that is peculiar to the particular flow in question.

On balance, all these considerations suggested to us that it is desirable to look at some open flows to determine the extent to which (low-dimensional) dynamical systems can assist us in our goals of understanding transition and turbulence in fluid flows. This is the motivation for the work described in this paper, which is to be viewed more as a progress report than as a complete account; obviously much more remains to be done. Our approach is to select well-known flows and follow the bifurcations as closely as possible. Surprisingly, while much work has been done on these flows in the past, an amazing amount of new information can still

be acquired that will facilitate clarifying the relation between chaotic dynamical systems and fluid flow transition and turbulence.

2. EXPERIMENTS

Our first attempts were (for historical reasons) on flow in a coiled pipe, SREENIVASAN & STRYKOWSKI [7]. Spectral measurements indicated that transition to turbulence occurred somewhat similarly to the RUELLE-TAKENS picture; that is, with increasing Re, the power spectral density of the streamwise velocity fluctuation shows essentially a single peak, two peaks and then three peaks immediately followed by the onset of a broad-band component. This behaviour might suggest the presence of a strange attractor. Our subsequent evaluation of the "dimension" (see section 4) of the attractor indicated that this quantity was small (not greater than about 6), at least at Reynolds numbers not too far from the transition value. Our calculations at much higher Re were inconclusive, due to various computational and instrumentation resolution problems; it was also displeasing that spectral peaks were not as sharp or as narrow as desired. A further problem seemed to be the somewhat unusual flow configuration, which itself led to many physically unfamiliar behaviours, making interpretations of results somewhat difficult. Although our further work has led to a better understanding of that flow, it seemed necessary to make measurements in other less unfamiliar flows of common occurrence. We decided to make measurements in a two-dimensional wake, covering a Reynolds number range from the onset of vortex shedding to an "essentially turbulent" state.

All experiments were done in a 70 cm × 50 cm suction-type wind tunnel with speed control obtained by varying the armature current of the d.c. motor driving the fan. At the speeds of the experiments, the free-stream turbulence level (including the wind tunnel unsteadiness) was less than about 0.2 % - neither very small nor very large in comparison with most existing facilities. The spectral density of the streamwise velocity fluctuation u in the free-stream showed no discrete peaks. Three wake generators were used. Two of them were nylon threads stretched across the width of the wind tunnel, 0.024 cm and 0.036 cm in diameter, giving aspect ratios of about 2000 and 1500 respectively; the third was an aluminum tube 4 mm in diameter (aspect ratio ≈ 175).

A large part of the data to be presented below is in the form of power spectral densities of u. For nearly all the signals, digitization was done at sufficiently high frequency (60 kHz or more) to ensure that whenever the signal was periodic, at least 30 digitized points were contained in one period of the basic frequency (so that it was a good representation of the

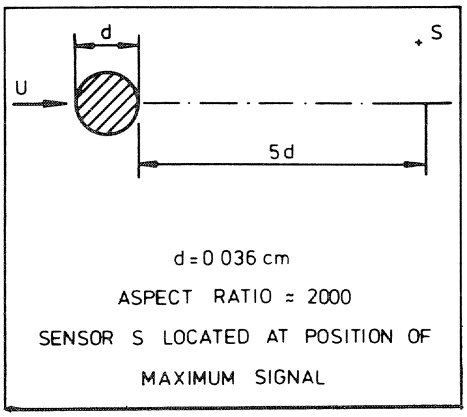

Fig. 1

Schematic of experimental conditions.

analog signal). Further, the entire length of the signal, which contained at least 100 cycles of the basic frequency, was Fourier transformed at once, using the Cooley-Tukey FFT algorithm. The overriding criterion was that the spectral resolution should be as good as possible (here, about 0.9 Hz compared with shedding frequencies of the order of 2000 Hz or more) and must not miss any low frequency modulations.

All velocity signals were obtained with a hot-wire operated on a DISA 55M01 constant temperature anemometer. The speed of the tunnel was monitored with a Pitot tube connected to a calibrated MKS Baratron with adequate resolution (and an averager). The hot-wire and the Pitot tube were mounted on a specially-made slim holder. Most measurements were made approximately 5 diameters downstream from the cylinder and about a diameter or so off the centerplane where the signal was the largest (see Figure 1).

3. RESULTS

Figure 2 shows the logarithm (to base 10) of the normalized power spectral density of the hot-wire signal at a Reynolds number Re (based on the free stream velocity and the diameter of the vortex shedding cylinder) of about 36, which is just about the onset value for vortex shedding. Notice that the general noise level is around 10^{-8}, while the peak of the spectrum (marked f_1), corresponding to the basic vortex shedding frequency behind the cylinder cylinder, is at around $10^{-0.5}$, about 7 1/2 orders of magnitude higher than the noise level! The sharpness is excellent, which also holds for the other peaks to the right of f_1, which are the harmonics of f_1.

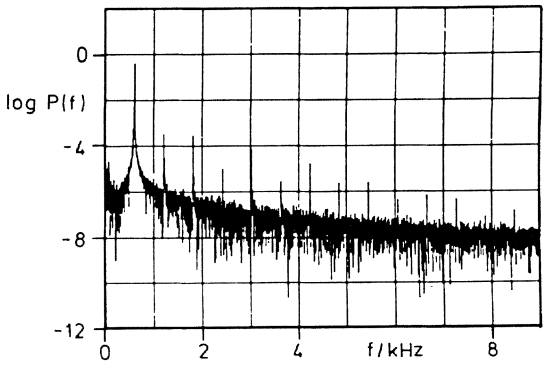

Fig. 2 Frequency spectrum of streamwise velocity fluctuations at Re ≈ 36. Note that the power is plotted on a logarithmic scale. The peak at f_1 = 590 Hz corresponding to vortex shedding, and the subsequent strong peaks above the noise level are simply harmonics of f_1. Notice that the background noise is not white.

At a somewhat higher Reynolds number of 54, there appear a number of peaks in the spectrum (Figure 3a). As shown in the expanded version (Figure 3b), all the peaks can be identified precisely in terms of the interaction of the two frequencies - the basic vortex shedding frequency f_1 and another incommensurate frequency f_2. That it contains only two frequencies can be seen also from a combination of the phase plot and its Poincaré section (Figures 4 and 5). Figure 4, which is a computer plot of the time derivative $\dot{u}$ of the signal against the signal u itself, is seen to be a complicated structure; the Poincaré section (Figure 5), which is simply $\dot{u}$ vs u sampled at the frequency f_2, is essentially a circle - as it ought to be if the signal contained only frequencies f_1 and f_2. At a slightly higher Reynolds number of 62, the second frequency becomes much weaker (Figure 6); that it has not disappeared can be seen clearly from the corresponding phase plot (Figure 7). At Re = 76, several peaks can be seen in the spectral density (Figure 8) and, as shown in detail in Figure 9, these peaks can all be identified with great precision (actually 5 decimal places) as arising from the interaction of three irrational frequencies. After a finite (though small) increase in Reynolds number, one can see about an order of magnitude increase in broad-band frequency content to the left of f_1 (Figure 10). In the language of dynamical systems, we may now consider chaos to have set in.

This progression towards chaos - underlying the possible presence of a strange attractor - proceeds more or less according to the prescription given by NEWHOUSE, RUELLE & TAKENS [2]. There are deviations! These include the conspicuous weakening at Re = 62 of the second frequency after its strong appearance at Re = 54, as well as the moderate and finite increase in Reynolds number that is required between the appearance of the third frequency (Re = 76) and the onset of chaos (Re = 93). It is still

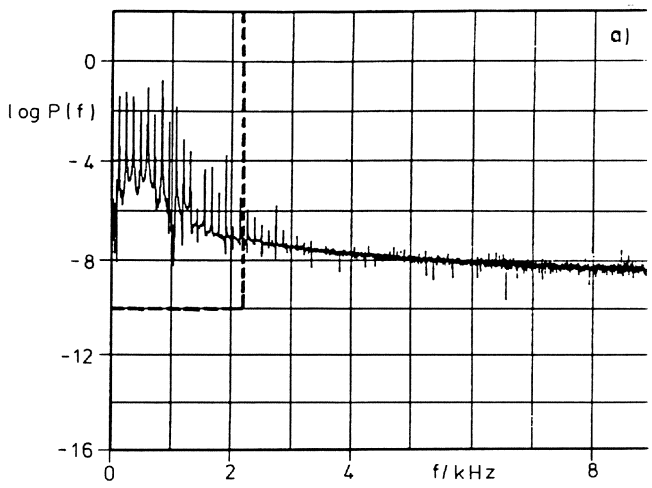

Fig. 3a Frequency spectrum at Ré ≈ 54. f_1 ≈ 835 Hz.

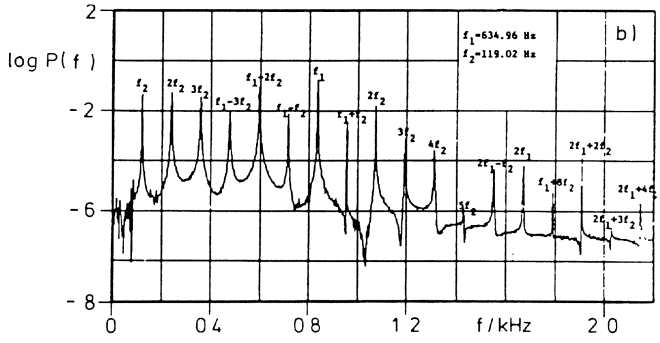

Fig. 3b Expanded version of Figure 3a in the frequency range 0 - 2200 Hz. Note that all significant peaks in Figure 3a are simply linear combinations of f_1 and another incommensurate frequency f_2 ≈ 119 Hz.

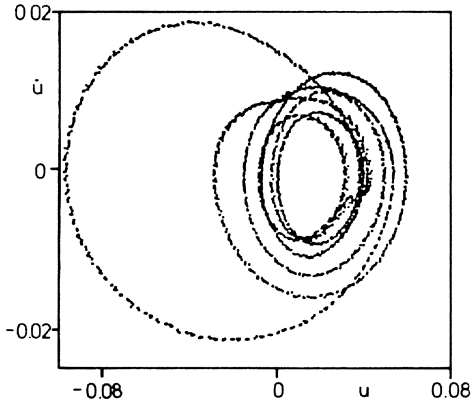

Fig. 4

A phase plot from the velocity signal u at Re ≈ 54. The ordinate is simply the time derivative u̇ of the abscissa u. Number of data points ≈ 3000.

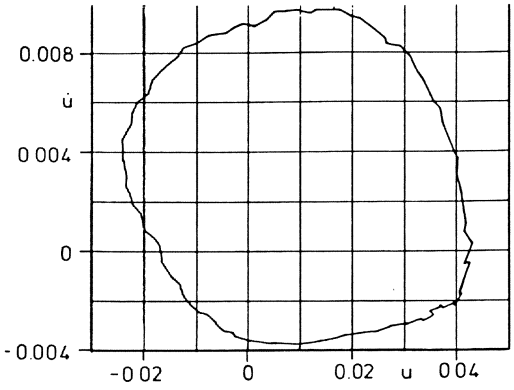

Fig. 5

Poincaré section for the phase plot of Figure 4. This is simply a plot of u̇ vs u sampled exactly at the frequency f_2.

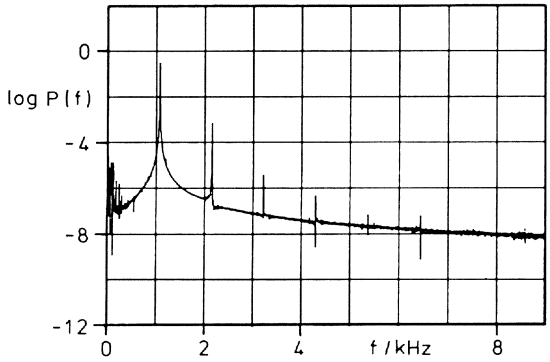

Fig. 6 Frequency spectrum at Re = 62. Notice that the second frequency has diminished in importance.

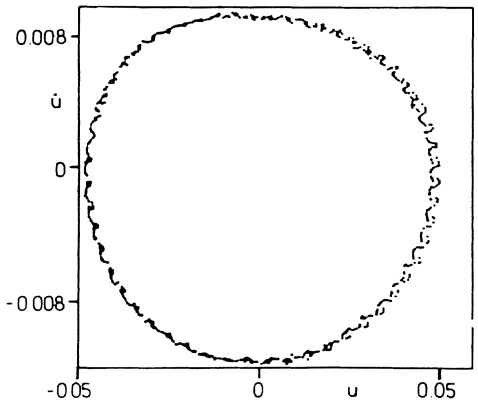

Fig. 7

Phase plot for Re = 62; all details as in Figure 4.

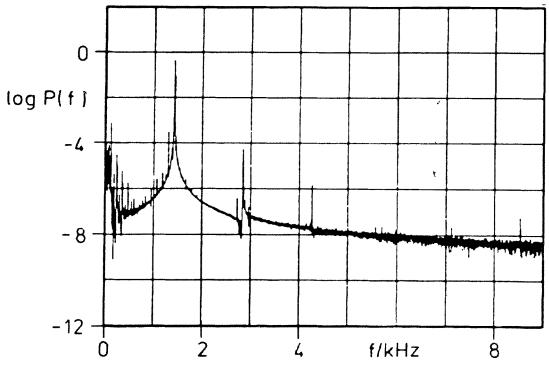

Fig. 8

Frequency spectrum at Re = 76.

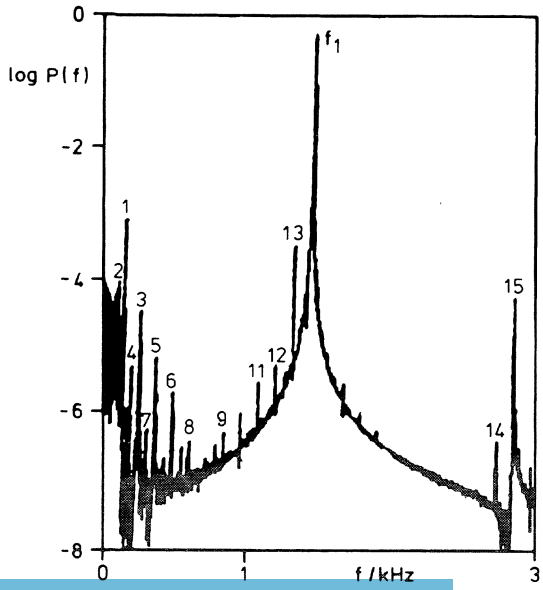

$f_1 = 1422.73$ Hz $\quad f_2 = 119.02$ Hz

$f_3 = 29.30$ Hz

$1 = f_2$	$2 = f_2 - f_3$
$3 = 2f_2$	$4 = 2f_2 - 2f_3$
$5 = f_1/3 - f_2$	$6 = f_1/3$
$7 = f_1/3 - 10f_3$	$8 = f_1/3 + f_2$
$9 = \frac{2}{3}f_1 - f_2$	$10 = \frac{2}{3}f_1$
$11 = f_1 - 3f_2$	$12 = f_1 - 2f_2$
$13 = f_1 - f_2$	$14 = 2f_1 - f_2$
$15 = 2f_1$	

Fig. 9 Expanded version of Figure 8 in the frequency range 0 - 3 kHz. All significant peaks are combinations of three frequencies f_1, f_2, and f_3.

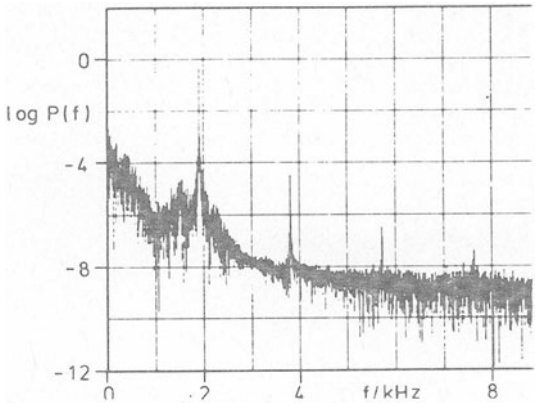

Fig. 10 First appearance of chaos at Re = 93. Notice that in comparison with Figure 8, the broadband "noise" level in the 0 - 2000 Hz range has gone up by an order of magnitude or so.

extraordinary that the "typical" behaviour indicated by RUELLE & TAKENS for a highly idealized mathematical system should have a nontrivial bearing on a rather complicated system.

It should be emphasized that the state we have recognized as chaotic is still far away from being turbulent. In fact, *most* of the energy is still contained in the discrete shedding frequency. Thus further increase in Reynolds number is in order.

With further increase in Reynolds number, the flow evolves into a much better organized state (Figure 11) at Re = 102, and the signal itself looks more periodic. We believe that there are *at least* two basic frequencies present in the system, although, because of the their low amplitude, we have been unable to recognize them precisely or to establish their connection to the frequencies occurring before the onset of chaos at Re = 93.

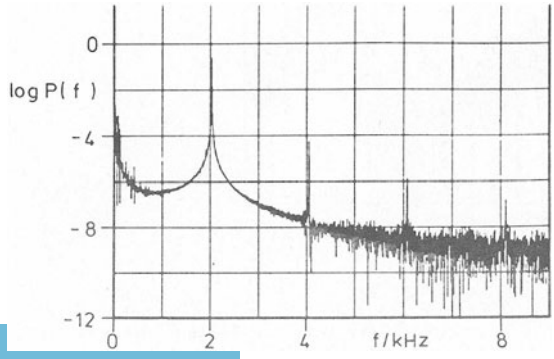

Fig. 11 "Reordering" at Re = 102.

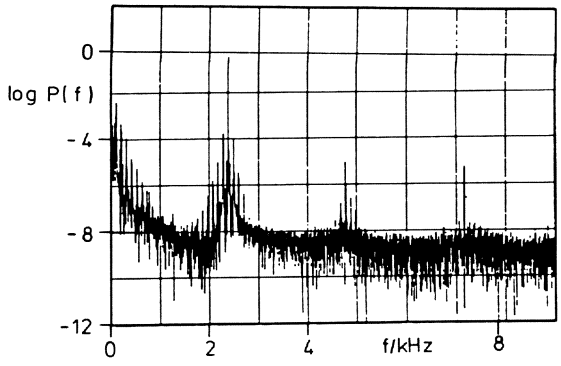

Fig. 12a Discrete frequencies at Re = 115.

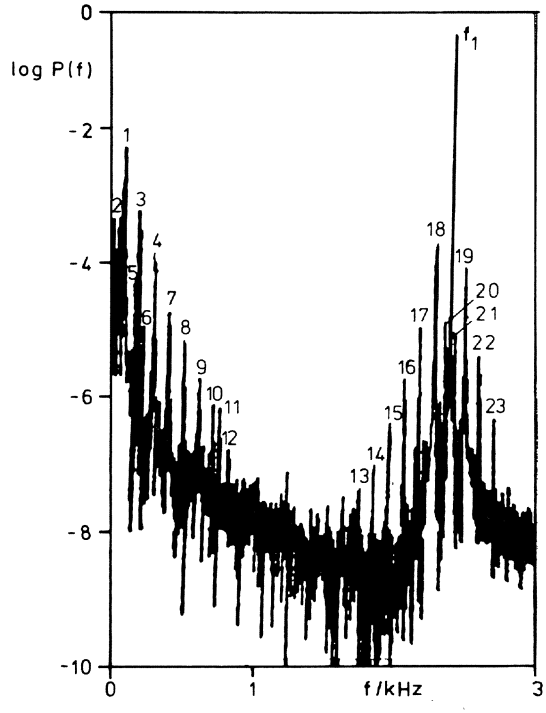

f_1 = 2387.70 Hz f_2 = 106.20 Hz
f_3 = 34.79 Hz f^* = 29.30 Hz

$1 = 3f_3$
$2 = f_2$
$3 = f_2 + 3f_3$
$4 = f_2 + 6f_3$
$5 = 6f_3 - f^*$
$6 = 3f_3 + f_2 + f^*$
$7 = f_2 - 9f_3$
$8 = f_2 + 12f_3$
$9 = 2f_2 + 12f_3$
$10 = 2f_2 + 15f_3$
$11 = 2f_2 + 18f_3 - 2f^*$
$12 = 2f_2 + 18f_3$
$13 = f_1 - 2f_2 - 12f_3$
$14 = f_1 - f_2 - 12f_3$
$15 = f_1 - f_2 - 9f_3$
$16 = f_1 - f_2 - 6f_3$
$17 = f_1 - f_2 - 3f_3$
$18 = f_1 - f_2$
$19 = f_1 - 3f_3$
$20 = f_1 - f_3$
$21 = f_1 + f_3$
$22 = f_1 + f_2 + 3f_3$
$23 = f_1 + f_2 + 6f_3$

Fig. 12b Expanded version of Figure 12a in the range 0 - 3 kHz. Notice that four frequencies are required to account for all dominant peaks above the noise level.

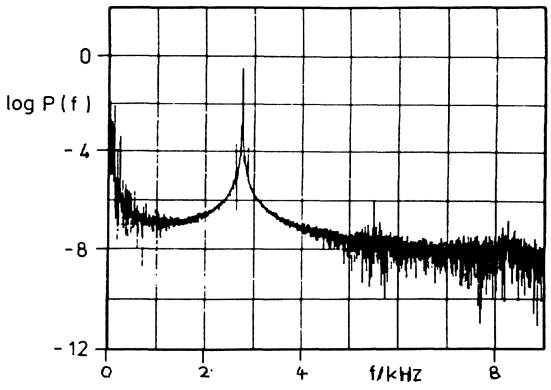

Fig. 13 Frequency spectrum at Re = 127. Notice the reduced relative dominance of the discrete frequencies f , f , and f* in comparison with f .

With further increase in Re, there is a reappearance (Re = 115) of relatively strong discrete components (Figure 12a); and, as outlined in detail in Figure 12b, there is a definite need for four frequencies and their various combinations to identify all the dominant peaks. Further increase in Re results in the weakening (but not the disappearance) of the discrete components at Re = 127 (Figure 13) and a reappearance of chaos at Re = 135 (Figure 14), as indicated by the broadband component in the power spectral density. This second appearance of chaos is marked by a larger fraction of energy content in the broadband component than was the case when chaos set in the first time at Re = 93.
Further increase in Re results in a return to a more ordered state (Figure 15), but this return to "order" is somewhat less convincing than the previous instance at Re = 102. As Re increases further, one sees the reappearance of chaos (Figure 16) at Re = 168; presumably, greater resolution in our measurements would reveal steps similar to those preceeding the appearance of chaotic states at Re = 93 and 135. This reappearance of chaos is also marked by a much higher fraction of energy in the broadband component of motion (or "background noise", as it is often labeled).

Two remarks should be made: First, we note that there is a well-defined state with four discrete frequencies (and their linear combinations) without the presence of a strange attractor - a statement we shall justify later (section 4). This is in contradiction to the NEWHOUSE-RUELLE-TAKENS projection, and to the popular - and as far as we know unproven - statement that "period three means chaos". Second, the complicated appearance and reappearance of ordering and chaos is not unusual in other dynamical systems, either.

The sequence of events described above is summarized in Figure 17. Even though these precise details have not been noted before, we believe that

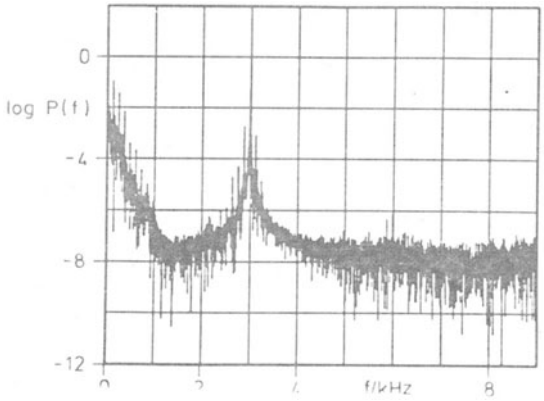

Fig. 14 Second appearance of chaos at Re = 135. Notice that the general noise level in the 0 - 1000 Hz range has gone up significantly.

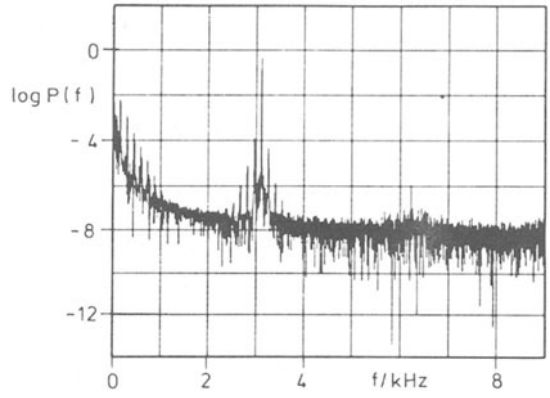

Fig. 15 "Reordering" at Re = 144.

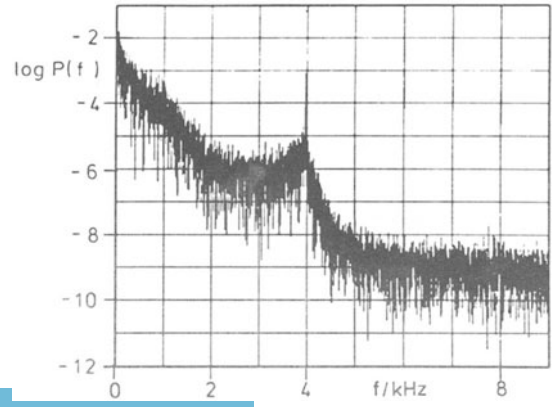

Fig. 16 Chaos at Re = 168. Notice the persistence of the votex shedding frequency.

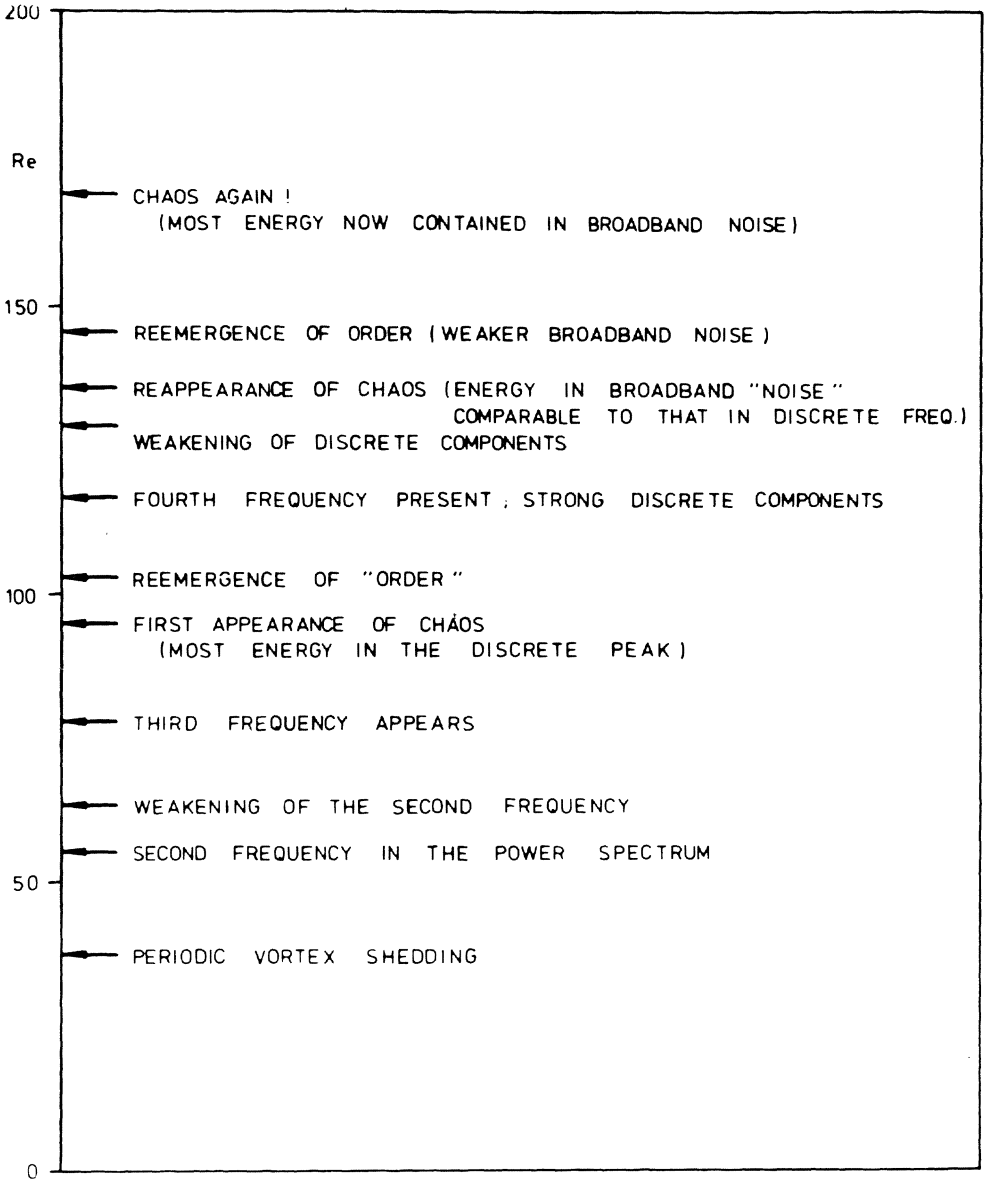

Fig. 17 Summary of the events.

related observations in wakes have in fact been made by previous researchers. For example, consider the windows of chaos and order alluded to above. Although we have not made detailed spectral measurements at higher Reynolds numbers, it is our contention that the succession of order and chaos in a wake continues indefinitely even at very high Reynolds numbers. This was noted several years ago by ROSHKO [8], who showed that order reappears in the Reynolds number range of 10^6. More recently, the fluctuating lift force measurements of SCHEWE [9] on a circular cylinder showed that the spectral density of the lift coefficient was broad at Re = 3.7×10^6 (upper end of transition) and became increasingly narrow until, at Re = 7.1×10^6, it was quite sharp, rather like a narrow-band-pass filtered signal. Although the fluctuating lift force can at best be related to the squared fluctuating velocity filtered via the transfer function corresponding to the response of the circular cylinder, its behaviour is nevertheless indicative of the flow itself in the vicinity of the cylinder.

As another example, consider the variation of the vortex shedding frequency with respect to Reynolds number (Figure 18). It can immediately be seen that the frequency does not monotonically increase with Re, but shows (at least) two distinct breaks. These breaks appear whenever there is a transition to chaos and reordering. Such breaks have been noted before [10,11,12], and perhaps most convincingly demonstrated in a beautiful experiment by FRIEHE [13]. Although the appearance of these breaks has been disputed, GASTER [14], our own data tend to support the conclusion that they do indeed appear. In TRITTON's first observations of the phenomena [10], a discontinuity in f_1 vs Re curve was observed in the range $80 \leq\approx Re \leq\approx 90$, While in his later experiments, TRITTON [12], it appeared at around Re ≈ 110. Our conclusion is that they both appear, in agreement with FRIEHE's observation. Friehe varied the Reynolds number continuously at a low rate and obtained on an x-y plotter the frequency-Re variation directly.

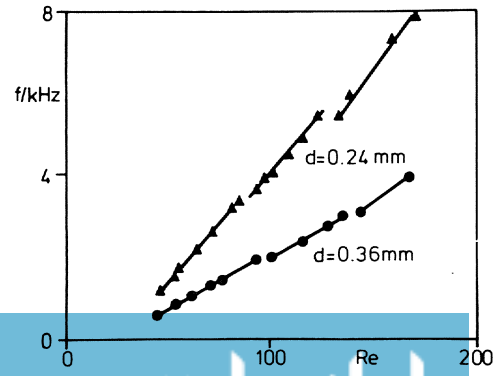

Fig. 18

Variation of the vortex shedding frequency with respect to Reynolds number.

4. DIMENSION OF THE STRANGE ATTRACTOR

It is clearly worth enquiring whether or not there is one single quantity that can successfully describe the many subtle changes that occur in the frequency spectra. There is indeed such a quantity, namely the dimension of the turbulence attractor. The concept of the dimension of the attractor is highlighted in studies of dynamical systems, and we may briefly digress here to discuss its meaning before presenting results of our measurements.

Let us consider that the attractor for turbulent signals is embedded in a (large) d-dimensional phase space. Let $N(\varepsilon)$ be the number of d-dimensional cubes of linear dimension ε required to cover the attractor to an accuracy ε. Obviously, making ε smaller renders N larger, but if the limiting quantity

$$D = \lim_{\varepsilon \to 0} \frac{\log N(\varepsilon)}{\log \left(\frac{1}{\varepsilon}\right)} \tag{4.1}$$

exists, it will be called the dimension of the attractor. An important characteristic of a strange attractor is that D is small even though d is large. We would be interested to see if turbulence has this property.

To see what the dimension means, let us write (4.1) as

$$N(\varepsilon) \sim \varepsilon^{-D}; \tag{4.2}$$

that is, if one specifies D and the accuracy ε to which we need to determine the attractor, we automatically know the number of cubes required to cover the attractor. The only missing information will now be the position of the cubes in the phase space. Thus, D can be considered as a measure of how much more information is required in order to specify the attractor completely; the larger the value of D, the larger is this missing information.

The dimension D, as defined in (4.1), has been called the fractal dimension by MANDELBROT [15], who has contributed a lot to our understanding of the quantity. As defined in (4.1), D is a geometric property of the attractor, and does not take into account the fact that a typical trajectory may visit some region of the phase space more frequently than others. Several measures taking this probability into account have been defined, and are believed to be closely related to the dynamical properties of the attractor. The most well-known among them are:

(a) the pointwise dimension
(b) the Grassberger-Procaccia dimension.

If the attractor is uniform, i.e., if each region in the phase space is as likely to be visited by the trajectory as every other, then the above two measures equal D defined by (4.1). Otherwise, they are generally smaller than D.

Let $S_\varepsilon(x)$ be a sphere of radius ε centered about a point x on the attractor, and let μ be the probability measure on the attractor. Then, the pointwise dimension is defined , FARMER, OTT & YORKE [16], as

$$d_p(x) = \lim_{\varepsilon \to o} \frac{\log \mu[S_\varepsilon(x)]}{\log \varepsilon} \tag{4.3}$$

or

$$\mu[S_\varepsilon(x)] \sim \varepsilon^{d_p} \tag{4.4}$$

GRASSBERGER & PROCACCIA [17] have defined another measure ν that is related to the dimension of the attractor, as well as the information-theoretic entropy. The procedure for computing ν is as follows:

(i) Obtain the correlating sum $C(\varepsilon)$ from:

$$C(\varepsilon) = \lim_{N \to \infty} \frac{1}{N^2} \sum_{\substack{i=j=1 \\ i \neq j}}^{N} H[\varepsilon - |\underset{\sim}{x}_i - \underset{\sim}{x}_j|]$$

where H is the Heaviside step function and $\underset{\sim}{x}_i - \underset{\sim}{x}_j$ is difference in the two vector positions $\underset{\sim}{x}_i$ and $\underset{\sim}{x}_j$ on the phase space. Basically, what C does is to consider a window of size ε, and start a clock that ticks each time the difference $|\underset{\sim}{x}_i - \underset{\sim}{x}_j|$ lies within the box of size ε. Thus, one essentially has

$$C(\varepsilon) = \lim_{N \to \infty} \frac{1}{N^2} \left\{ \text{number of pairs of points } (i,j) \text{ with } |\underset{\sim}{x}_i - \underset{\sim}{x}_j| < \varepsilon \right\}$$

(ii) Obtain ν from the relation, GRASSBERGER & PROCACCIA [17],

$$C(\varepsilon) \sim \varepsilon^{-\nu} \quad \text{as } \varepsilon \to o \tag{4.5}$$

In practice, not all components of x are known for constructing the phase space, but perhaps only one component, say x_m. One then constructs a d-dimensional "phase space" using delay coordinates

$$\{x_m, x_{m+\tau}, x_{m+2\tau}, \cdots\cdots, x_{m+(d-1)\tau}\}$$

where τ is some interval which is neither too small nor too large. If d is substantially larger than ν itself, reasonable results can be obtained.

Since one does not *a priori* know ν, one constructs several phase spaces of increasingly large values of d and evaluates ν for each of them; ν will first increase with d and eventually asymptote to a constant independent of d. This asymptotic value of ν is of interest to us as a measure of the dimension of the strange attractor.

We have computed both d_p and ν for turbulent velocity signals as described above, using the streamwise velocity fluctuations u and the delay coordinates described above to construct the phase space. Our confidence in the numerical values of these measures of dimension is very good when they are less than about 5 or 6, but becomes increasingly shaky at higher values. However, we do believe that they are reasonable, judging from their repeatability and the several precautions we have taken (such as taking the proper limit as $\varepsilon \to 0$ and using, in a couple of cases, double precision arithmetic in our computations). Figure 19 gives the data on ν and d_p as a function of the Reynolds numbers.

Several observations must be made. Concentrating first on the data at Reynolds numbers with discrete spectral peaks, we may conclude the following. At Re = 36, where there is only one independent degree of freedom (corresponding to the vortex shedding) (see Figure 2), the dimension of the attractor does indeed turn out to be about 1. When only two frequencies are present (Figures 3 and 4, Re = 54 and 62 respectively), the dimension is about 2, independent of the relative magnitude of the second frequency. One must note that at Re = 62, where the second frequency is of smaller amplitude, it is necessary to take the computations of the dimension to fairly small values of ε. At Re = 76, where there are three dominant frequencies, the dimension is about 2.7, not very different from the number of independent frequencies present. Lastly, at Re = 115, where there are four independent frequencies, the calculated ν is not very different from 4. Thus, making some small allowances for the computational uncertainties in calculating the dimension, it is seen to be a reasonable representation of the number of degrees of freedom in the system.

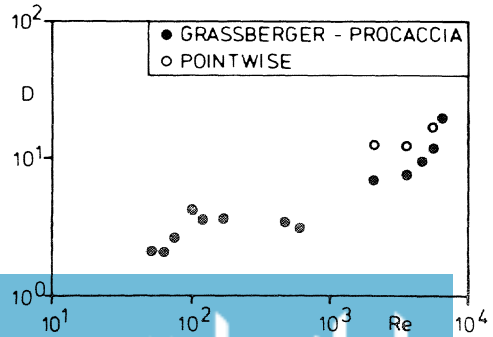

Fig. 19

Variation of the dimension of the attractor with respect to Reynolds numbers. Note that the dimension is about 1 when there is only vortex shedding (Re = 36), about 2 when there are only 2 frequencies (Re = 54), about 3 when there are 3 frequencies, etc..

Now getting back to other Reynolds numbers, it is clear that the first appearance of chaos at Re = 93 is characterized by a jump in the dimension (to about 4.3), whereas a return to "order" at Re = 102 is characterized by a dip in the dimension. We have not computed the dimensions in the Reynolds number range 200 - 500, but calculations in higher Reynolds number range up to about 7000 indicate that it does go up with Re, although not rapidly. In fact, it is about 20 at Re = 7000.

Keeping the above interpretation of the dimension in mind - namely, that it is indicative of the degrees of freedom of the system - it follows that the number of degrees of freedom even at Re = 7000 is of the order of 20. If this is true, it is clear that this information must be used to the best advantage.

It is pertinent to point out that, apart from our own earlier measurements of the dimension of the turbulence attractor, Reference 4 gives such measurements for a TAYLOR-COUETTE flow.

5. DISCUSSION

We have shown that many of the qualitative features of transition to turbulence behind circular cylinders are in essential agreement with the behaviour of dynamical systems. There are some deviations, but it is surprising that the dynamics of fluid motion which we believe to be particularly governed by the Navier-Stokes equations should be represented by extremely simple systems at all. We have shown that during early stages of transition, a strong connection (speculated previously, but never conclusively shown to be true) exists between the dimension of the attractor and the degrees of freedom of the fluid system. Provided that this interpretation is true at higher Reynolds numbers also, our results suggest that the degrees of freedom are not too many, even up to Reynolds number of the order of 10^4. We have several reasons to believe that the dimension of the attractor, as computed according to (4.4) and (4.5), is not very high, even at much higher Reynolds number corresponding to the fully turbulent state (Re $\simeq 10^6$). Most of our data has been at 5 diameters downstream from the cylinder. At least at low enough Reynolds numbers, much the same happens at x/d = 50, for example.

Do we then conclude that the key to understanding transition and turbulence lies completely in the study of dynamical systems? We think that such statements are optimistic at best and misguided at worst, even though there is much that we can learn from dynamical systems. Consider our own experiments. Dynamical systems theory can correctly tell us that chaos occurs after 3 bifurcations, but does not at all tell us what those bifur-

cations are! The origin and physical structure of these bifurcations can be discovered only by looking at the particular form of F in (1.5). For the same reason, it will perhaps never be possible to predict C_D vs Re curve for the circular cylinder without worrying about the special form of F in (1.5). Furthermore, the spatial structure of the wake is an important element completely outside the scope of dynamical systems theory - at least as as it stands today.

What do we make of the fact that the dimensions of the attractor is not too high even at high Re? If the attractor is sufficiently low-dimensional, a clever projection of it can perhaps be used to our advantage. If the attractor dimension is even as high as 20, no matter what projection one devises, it will look uniformly dark. So it is unclear at this stage how this information could be used, except in the hope that it lends credence to concepts embodied in renormalization group theory or slaving principle, etc.. Perhaps it is appropriate to remind ourselves that some excellent fluid dynamicists have for many years toyed with the idea of a relatively small number of degrees of freedom in turbulence, and have not gone very far!

ACKNOWLEDGEMENT

I would like to thank Dr. H. Oertel for inviting this contribution, and for his help in preparing the manuscript according to the format of this volume. A more complete account of this work will appear in "Fundamentals of fluid mechanics" (eds. S.H. Davis & J.L. Lumley), to be published by Springer.
This research was sponsored by a grant from the Air Force Office of Scientific Research.

REFERENCES

[1] D. RUELLE, F. TAKENS: Commun. Math. Phys. 20, 167 (1971).

[2] S. NEWHOUSE, D. RUELLE, F. TAKENS: Commun. Math. Phys. 64, 35 (1978).

[3] J.P. GOLLUB, H.L. SWINNEY: Phys. Rev. Lett. 35, 927 (1975).

[4] A. BRANDSTÄTER, J. SWIFT, H.L. SWINNEY, A. WOLF: Phys. Rev. 51, 1442 (1983).

[5] A. LIBCHABER, J. MAURER: J. De Physique 41, C3-57-C3-56 (1980).

[6] A. LIBCHABER: Proc. of the IUTAM Conference, Kyoto (1983).

[7] K.R. SREENIVASAN, P.J. STRYKOWSKI: Proc. of the IUTAM Conference, Kyoto (1983).

[8] A. ROSHKO: J. Fluid Mech. 10, 345 (1961).

[9] G. SCHEWE: J. Fluid Mech. 133, 265 (1983).

[10] D.J. TRITTON: J. Fluid Mech. 6, 241 (1959).

[11] E. BERGER: Z. Flugwiss. 12, 41 (1964).

[12] D.J. TRITTON: J. Fluid Mech. 45, 749 (1971).

[13] C.A. FRIEHE: J. Fluid Mech. 100, 237 (1980).

[14] M. GASTER: J. Fluid Mech. 38, 565 (1969).

[15] B. MANDELBROT: Fractals: Form, Chance and Dimension, Freeman & Co., San Francisco (1977).

[16] J.D. FARMER, E. OTT, J.A. YORKE: Physica 7D, 153 (1983).

[17] P. GRASSBERGER, I. PROCACCIA: Phys. Rev. Lett. 50, 346 (1983).

FLUID MECHANICAL STRUCTURES

STRUCTURAL STABILITY OF THREE-DIMENSIONAL VORTEX FLOWS

U. DALLMANN

1. INTRODUCTION

In fluid dynamics, we intuitively use the notion *structure* in connection with features of flow fields that are qualitatively quite different. For instance, we recognize an evolution of well-organized flow structures on various scales caused by various kinds of flow instabilities. We also talk about large-scale separated vortex structures. Coherent structures are all of a sudden being identified in a variety of flows. On the other hand, we use terms like vortex, eddy, and turbulent spot as synonyms for some unknown, i.e., undefined structures that appear in velocity or pressure signals. Finally, loosely speaking, the strange attractors exhibit some strange structures of trajectories in phase space, which we would like to relate to small-scale turbulent flow structures in real physical space and time.

Any discussion of *structures* observed in flow fields should be based on a definition of the term structure, in order to describe an essential characteristic, a qualitative property of a flow.

Nevertheless, even on the basis of pure intuition we recognize flow structures only because of apparent qualitative, i.e., structural changes that occur due to changes of initial and/or boundary conditions. In order to define equivalence of structures in otherwise different flow fields, we have to compare flows qualitatively, although comparisons between two flows are mostly based on quantitative data sets. Very often we compare two experimental observations or the result of an experiment with a theoretical prediction, or we are interested in the comparison of two numerical solutions of the same set of equations that have been obtained by use of different numerical methods. Finally, correct physical modelling may be checked by comparing the behavior of the solutions of different approximations to the same basic set of equations of motion. Whatever we may compare, the question remains as to what constitutes qualitative agreement between two flow fields. The answer, equivalent structures and

equivalent structural changes, again calls for definitions rather than intuitive and imprecise arguments.

In addition, we have to ask why nature prefers distinct structures and structural changes. This question then leads us to the hypothesis that the manifold flow structures, sometimes visualized as flow patterns, might be constrained by some kind of structural stability mechanism hidden in the equations of motion. Some flow patterns might be stable; others might be structurally unstable, i.e., they will change into stable ones. In the following, we will summarize some of our previous topological considerations (DALLMANN [1],[2]) showing that we may describe three-dimensional, steady flow fields as solutions of a nonlinear dynamical system. Such dynamical system analysis provides the definition we are looking for: "A dynamical system, i.e., a flow field is structurally stable if small perturbations yield topologically equivalent systems (flows)".

Steady topological flow structures can be discussed in physical space. In order to achieve a better understanding of unsteady flow phenomena, such as unsteady flow separation, subsequent flow instabilities and turbulence it will be necessary to study the changes of such topological flow structures in time. Structural changes of some locally measured quantities in the same phase space might then be correlated to changes of topological flow structures as observed in physical space and time.

The aim of our previous work (DALLMANN [1],[2]) was to describe possible sequences of structural changes of flow fields under the constraints given by the fluid dynamical equations of motion. Here, we do not intend to give a rigorous mathematical description of such changes that are due to structural instabilities and bifurcations. We want to explain the topological concept and demonstrate some well-defined discrete structural changes in the topography of three-dimensional steady flows.

2. TOPOLOGICAL FLOW STRUCTURES

The qualitative characteristics of many complex flows can be analyzed on the basis of a geometric understanding, i.e., *the topological flow structure of* (only) *the velocity field*. Two topological structures, which can be described mathematically by their trajectories, are called identical if there exists a topological transformation, i.e., a bijective and continuous map with continuous inverse, that maps the trajectories of one system onto the trajectories of the other. As a consequence, we may call two flow fields topologically identical if they show qualitatively the same distribution and connection of critical points (i.e., saddle points, nodes, and foci) and possible closed loops in the streamline patterns.

Furthermore, with the definition given above we may vary the shape of any flow field as if it were made of rubber, contracting at some places and expanding at others. These principles will enable us to draw the geometric representations of rather complicated structured flow fields.

2.1 Two-dimensional flow structures

In the following, we will summarize some basic features of two-dimensional flow topology in order to apply to fluid dynamics some definitions well-known in phase-space analysis and bifurcation theory.

The topological structure, or to be more precise, the topography of steady, incompressible, two-dimensional flows is based only on saddle points, centers, and degenerate nodal points in the streamline patterns. The elementary topological structure of the so called sectional streamlines is always given by separatrices, i.e., streamlines connecting saddle points and thus trapping a center point. Some typical examples of separated flows and of Rayleigh-Bénard flow are shown in Figs. 1 - 3. The degenerate nodes mentioned above can be seen along the whole separation and attachment line sketched in Fig. 1.

The topography of complex two-dimensional flows can be easily obtained by the use of such elementary structures connecting the saddles.

Structural changes may occur in two ways in two-dimensional flows. A *local bifurcation* may create a new elementary structure, such as for instance a separation bubble (Fig. 4). The structurally unstable pattern thereby shows a multiple critical point. So-called *global bifurcations* may change saddle-to-saddle connections globally. The principal phenomenon, which is also well-known in dynamical systems analysis, is sketched in Fig. 5. Such structural changes of vortex flows, concatenation and individualization of vortices (DALLMANN [1]), can be observed in a variety of flow situations.

The formation of a travelling vortex in an unsteady flow will also, in a certain frame of reference, show a multiple critical point, i.e., a saddle-center as a local cusp on a certain instantaneous streamline (Fig. 6). Structural changes due to local as well as global flow bifurcations can be observed in the instantaneous streamline patterns of vortex shedding behind bluff bodies (Fig. 7). Since any such "structurally unstable" situation is dependent on the frame of reference, it is immediately clear that the qualitative character of an unsteady flow field cannot be represented completely in terms of instantaneous streamlines (See also Chapter 4).

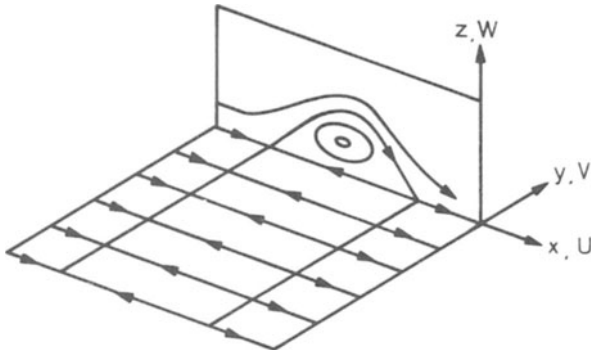

Fig. 1 Topological structure of steady two-dimensional flow separation.

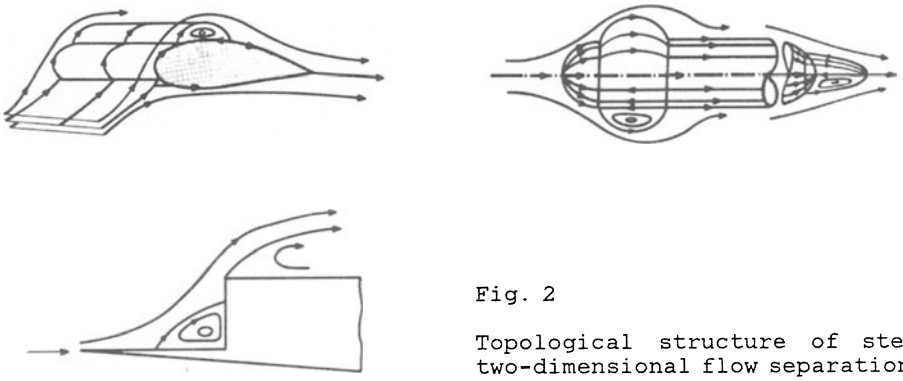

Fig. 2

Topological structure of steady two-dimensional flow separations.

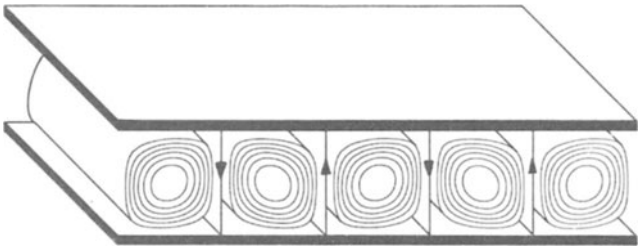

Fig. 3 Topological structure of steady two-dimensional Rayleigh-Bénard convection between two plates.

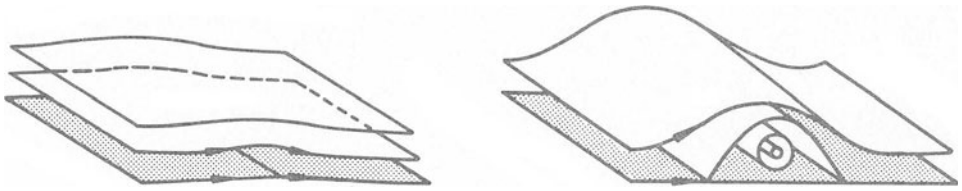

Fig. 4 Structural change through local flow bifurcation creating a so-called separation bubble.

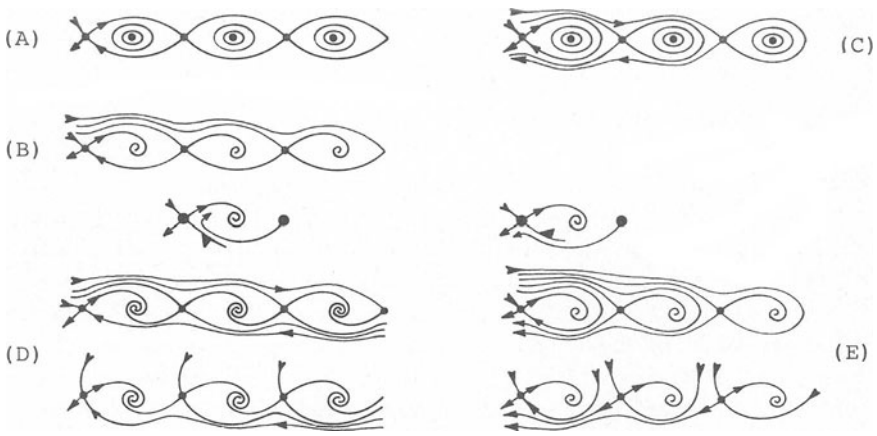

Fig. 5 Concatenation and individualisation of vortices. Saddle-to-saddle connexion appears in a structurally unstable bifurcating situation and will break up to create either concatenated vortices or single structures which may follow each other in a leap-frog fashion. (A, C: two-dimensional flows; B, D, and E: three-dimensional flows)

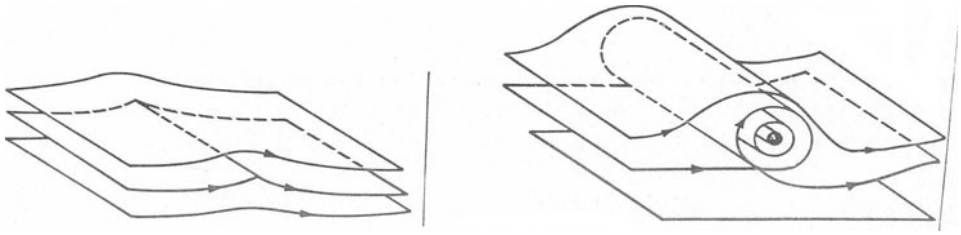

Fig. 6 "Structural change" (relative to a moving observer) of unsteady vortex motion.

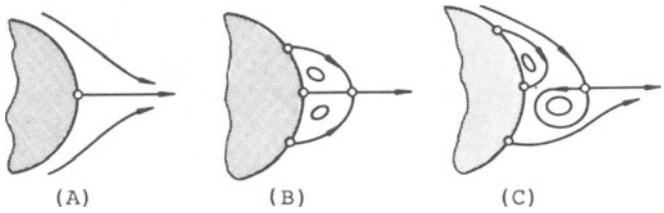

Fig. 7 Structural changes of the flow behind a bluff body.
Local bifurcation: (A) → (B) (steady flow)
Global bifurcation: (B) → (C) (unsteady vortex shedding, instantaneous streamlines)

2.2 Three-dimensional steady flow structures

Concentrating on the flow separation phenomenon we have shown in DALLMANN [1],[2] that a two-dimensional flow is a structurally unstable, transient state of qualitatively different three-dimensional flows. Arbitrary small deviations from perfect two-dimensionality (also axial symmetry) will allow topologically different flows to develop; different separated vortex systems will be created. In generic, three-dimensional flows, no closed region of recirculating fluid will be able to survive if small perturbations occur; therefore, a closed separation bubble will break up and either unsteady vortex shedding or three-dimensional, steady or unsteady vortex separation will occur.

Many experimental observations have shown that a variety of topologically different flow structures may appear in the streamline pattern on the surface of a body submerged in a flow. Extensive topological analysis of experimentally observed separated flows has been reported by TOBAK & PEAKE [3]. BIPPES & TURK [4] have shown that different elementary topological structures can be made visible in the wall streamline pattern on a hemisphere-cylinder by varying the angle of attack, Reynolds number and Mach number, and by altering the flow condition between being laminar or turbulent. Some of BIPPES' oil-flow visualizations are shown in Fig. 8 and the corresponding separatrix patterns in Fig. 9. HORNUNG & PERRY [5] called these surface patterns owl-faces because of the visual impression and they also discussed a "vortex skeleton model" in order to describe the different three-dimensional separated vortex flows above the surface.

In DALLMANN [1],[2], we have pointed out that flow patterns cannot be distinguished on the basis of wall streamline patterns or sectional streamline patterns only. There is no unique relationship between the flow pattern on the surface of a body, the pattern in a certain section through

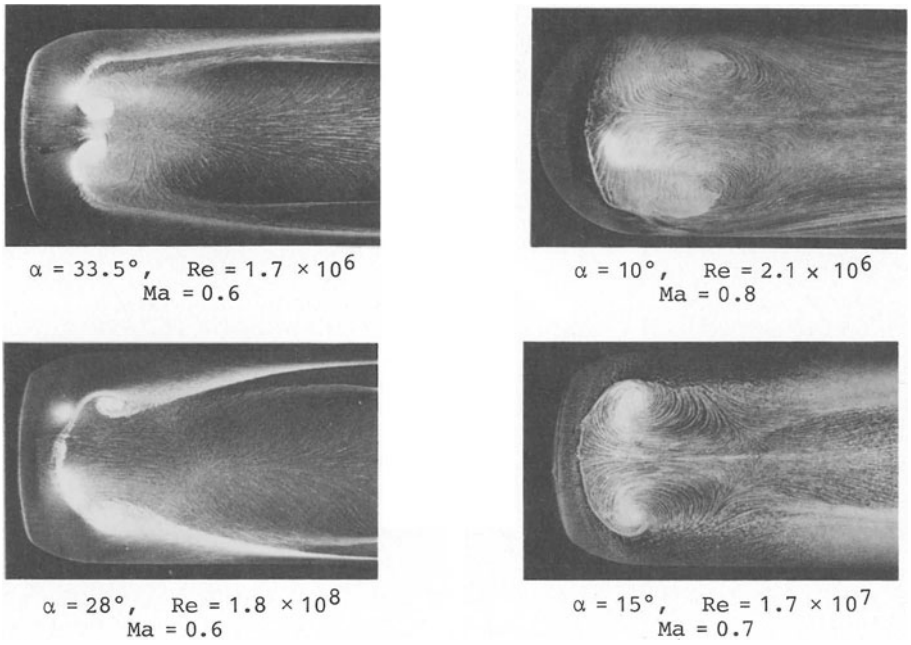

Fig. 8 Surface flow patterns on a hemisphere-cylinder for different angles of attack α, Reynolds number Re and Mach number Ma (from BIPPES & TURK [4]).

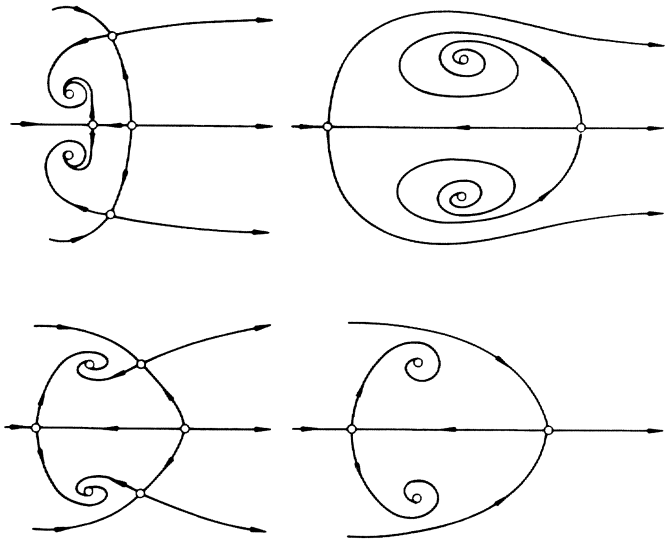

Fig. 9 Separatices defining the topological structures of the surface flow patterns given in Fig. 8.

the flow field, and the topological structure of the whole three-dimensional flow. Flow separation and flow (re-)attachment are merely selected observations associated with the general phenomenon of spatial vortex formation in the vicinity of a body.

In the following, we will sketch some of our results to show how a steady three-dimensional flow field can be analyzed in terms of a nonlinear dynamical system. We will demonstrate some transitions between elementary topological structures and their bifurcations.

3. STRUCTURAL CHANGES OF STEADY VELOCITY FIELDS

3.1. Formation of elementary topological structures

Consider the incompressible steady flow in the vicinity of a point $P(x_0, y_0, z_0)$. Let this point P lie in a symmetry plane of the flow and let it be on the surface of a body. Let us choose a Cartesian coordinate system (x,y,z) such that z = 0 represents the surface of the body in the vicinity of P, and let y = 0 represent the plane of flow symmetry (Fig. 10). The velocity Q = (U,V,W) is thereby assumed to exhibit the following symmetry near P:

$$\begin{aligned} U(x,y,z) &= U(x,-y,z) \\ V(x,y,z) &= -V(x,-y,z) \\ W(x,y,z) &= W(x,-y,z) \end{aligned} \qquad (1)$$

Let us now analyze structural changes of the velocity field near P by looking for the conditions that yield a critical point at P and that will in addition generate topologically different critical point ensembles in the vicinity of P. Such a study is different from other authors' previous

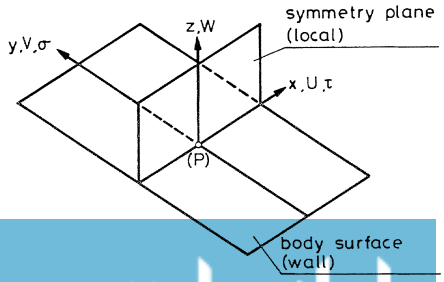

Fig. 10

Coordinate System.

works analyzing local flow behavior in the vicinity of a single critical point only, (PERRY & FAIRLIE [6], LEGENDRE [7], OSWATITSCH [8]).

The velocity field is assumed to be expandable into a formal Taylor series centered at P. Due to the no-slip boundary condition on the wall and the symmetry condition (1), it takes the following form:

$$\begin{aligned} U \cdot z^{-1} &= a_0+a_1x+a_3z+a_4x^2+a_6y^2+a_7xz+a_9z^2+a_{10}x^3+a_{12}xy^2+ \\ &\quad +a_{14}x^2z+a_{15}xz^2+a_{16}y^2z+a_{18}z^3+\ldots \\ V \cdot z^{-1} &= b_0+b_2y+b_5xy+b_8yz+b_{11}x^2y+b_{13}y^3+b_{17}yz^2+b_{19}xyz+\ldots \\ W \cdot z^{-1} &= c_0+c_3z+c_7xz+c_9z^2+c_{14}x^2z+c_{15}xz^2+c_{16}y^2z+c_{18}z^3+\ldots \end{aligned} \tag{2}$$

With a_i, b_i, c_i being constants, the streamline pattern can be derived from

$$dx : dy : dz = U : V : W \tag{3}$$

The introduction of an arbitrary parameter t and a scalar function $\Lambda(x)$ allows us to write

$$\dot{\vec{x}} := \frac{d\vec{x}}{dt} = \Lambda(\vec{x}) \cdot \vec{Q}(\vec{x}) := z^{-1}\vec{Q}(\vec{x}) \tag{4}$$

Owing to the introduction of the velocity components U,V,W from equ. (2), the system (4) is a nonlinear dynamical system describing steady streamline behavior near P. The hyperplane t = const. may be called the phase space; however, the solution of equ. (4) will be obtained in physical space $\vec{x}$.

Because of our assumption that the flow represents a generic situation of the steady equations of motion of an incompressible flow, and because of the no-slip boundary conditions, there are some intrinsic relationships between some of the coefficients a_i, b_i, c_i. On the other hand, any change of Reynolds number and of geometry, i.e., of boundary condition, will change some other relationships among the members of the set (a_i, b_i, c_i).

In order to describe possible structures and structural changes by a qualitative analysis of equ. (4), we have to satisfy only those intrinsic relationships mentioned, allowing an otherwise continuous variation of the set (a_i, b_i, c_i). Such a variation might change one structurally stable system into another structurally stable one. A structurally unstable system will appear for a so-called bifurcation set of coefficients (a_1,

b_m, c_n). A local bifurcation will appear, for instance, whenever a new critical point is generated at P. This causes a non-unique direction field at P, where streamlines may now leave or reach the surface. A necessary condition for such a generation of a single critical point is that the wall shear stress drops to zero, being non-zero in the vicinity of P (OSWATITSCH [8]).

Since the wall shear stress components (τ,σ) can easily be related to the coefficients a_0 and b_0, the bifurcation set obeys the conditions for vanishing wall shear stress components as follows

$$\begin{aligned} a_0 &= 0 \\ b_0 &= 0 \end{aligned} \qquad (5a)$$

but for the wall shear stress gradients we have in general

$$\begin{aligned} a_1 &= 0 \\ b_2 &\neq 0 \end{aligned} \qquad (5b)$$

which by continuity equation div $\vec{Q} = 0$ also yields

$$\begin{aligned} c_0 &= 0 \\ c_3 &\neq 0 \end{aligned} \qquad (5c)$$

Therefore, the qualitative analysis of equ. (4) has to include at least second order terms of the velocity expansion (2). Higher order terms will influence the solution behavior near P only in higher order structurally unstable situations. Lower order terms have to be introduced again to stabilize the system. The so-called unfolding of the second-order system to be analyzed yields

$$\begin{aligned} \dot{x} &= a_1x+a_3z+a_4x^2+a_6y^2+a_7xz+a_9z^2 \\ \dot{y} &= b_2y+b_5xy+b_8yz \\ \dot{z} &= c_3z+c_7xz+c_9z^2 \end{aligned} \qquad (6)$$

Since we know that there must be trajectories of the system (6), i.e., streamlines on the surface z = 0 and in the plane of flow symmetry y = 0, we can simplify the analysis of equ. (6) by studying the second-order subsystems for the wall streamlines

$$\dot{x} = a_1 x + a_4 x^2 + a_6 y^2$$
$$\dot{y} = b_2 y + b_5 xy \qquad (7)$$

and for the plane-of-symmetry streamlines

$$\dot{x} = a_1 x + a_3 z + a_4 x^2 + a_7 xz + a_9 z^2$$
$$\dot{z} = c_3 z + c_7 xz + c_9 z^2 \qquad (8)$$

For these second-order systems the intrinsic relationships between a_i, b_i, c_i due to the equations of motion and the no-slip boundary condition on the wall are

$$2c_3 + a_1 + b_2 = 0$$
$$2c_7 + 2a_4 + b_5 = 0$$
$$3c_9 + a_7 + b_8 = 0 \qquad (9)$$
$$6a_9 + 4a_4 + 2a_6 + b_5 = 0$$

These relationships can be easily obtained (also for higher-order systems locally approximating the equations of motion) by imposing the boundary conditions onto the continuity, momentum, vorticity and higher order vorticity transport equations (DALLMANN [1, 9]).

It is evident from the relationships (9) that only certain combinations of streamline patterns on the surface and in the plane of symmetry will be possible solutions of both systems (7) and (8).

Detailed analysis of equ. (7) (DALLMANN [1], [9]) shows that only the dimensionless ratios $b_2/a_1 = (\sigma_y/\tau_x)_P$ and $b_5/a_4 = 2(\sigma_{xy}/\tau_{xx})_P$ determine the changes of surface flow structure. Two possible sequences of structurally changing wall streamline patterns are given in Fig. 11, the complete bifurcation diagram will be discussed in DALLMANN [9].

Streamline patterns for the plane of flow symmetry, that are similar to those given in Fig. 11, exist. But since there is no symmetry restriction for the symmetry plane streamlines, these may in general leave or reach the surface z = 0 at the critical points in a non-orthogonal direction.

Some possible combinations of streamline patterns on the wall and in the symmetry plane are shown in Fig. 12.

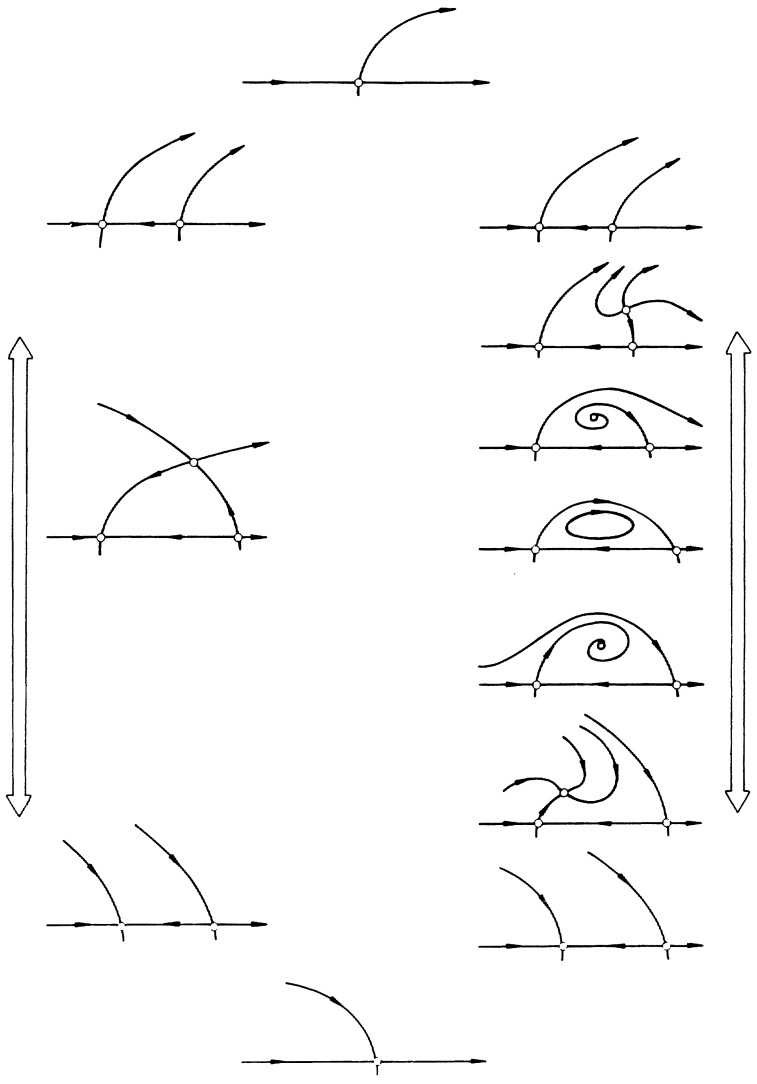

Fig. 11 Two sequences of elementary topological structures on the surface of a body where the no-slip condition holds. Each structure appears in a certain domain defined by $(\tau_x+\sigma_y)/\tau_x$ and σ_{xy}/τ_{xx} as a solution of equ. (7).

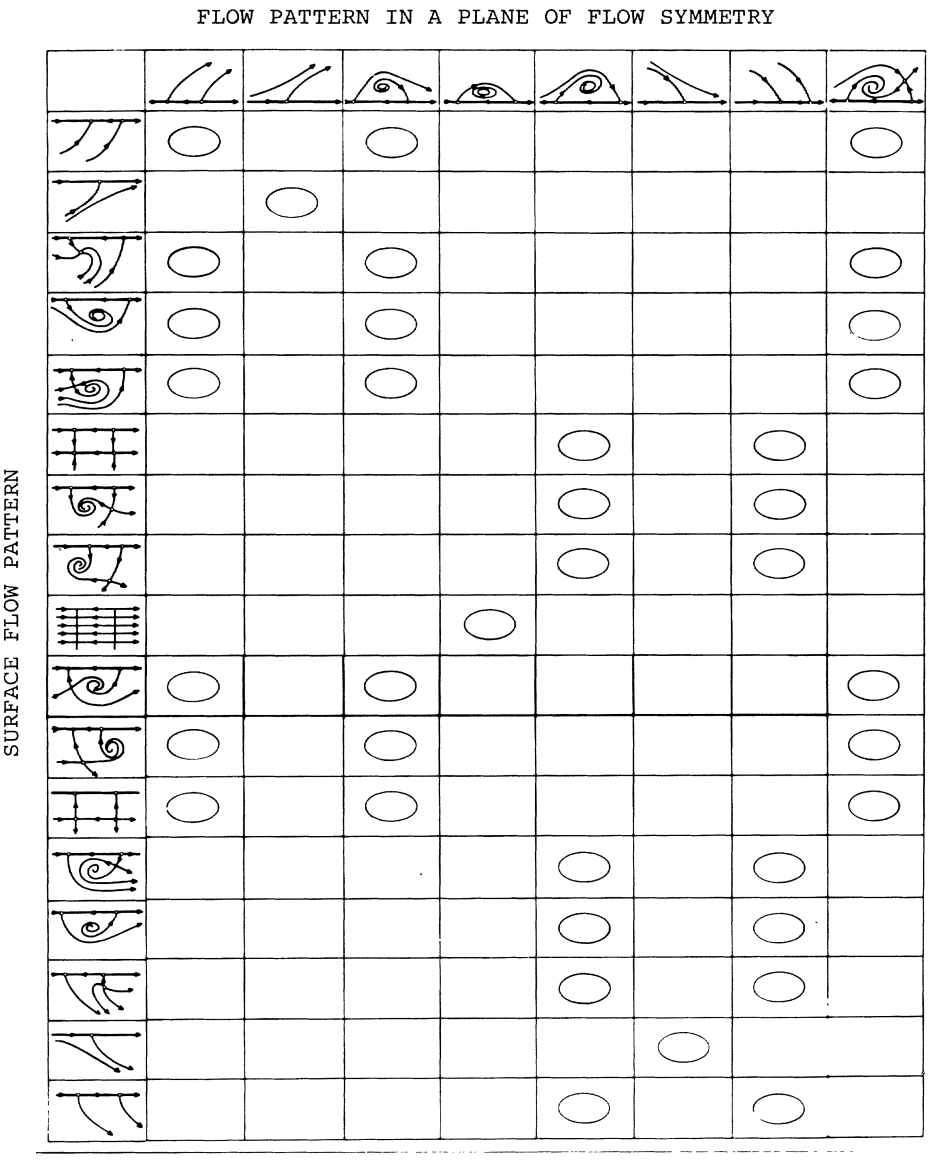

Fig. 12 Kinematically possible combinations of elementary structures of flow patterns on the surface (wall) and above (plane of flow symmetry) (Admissible combinations are indicated ⬭).

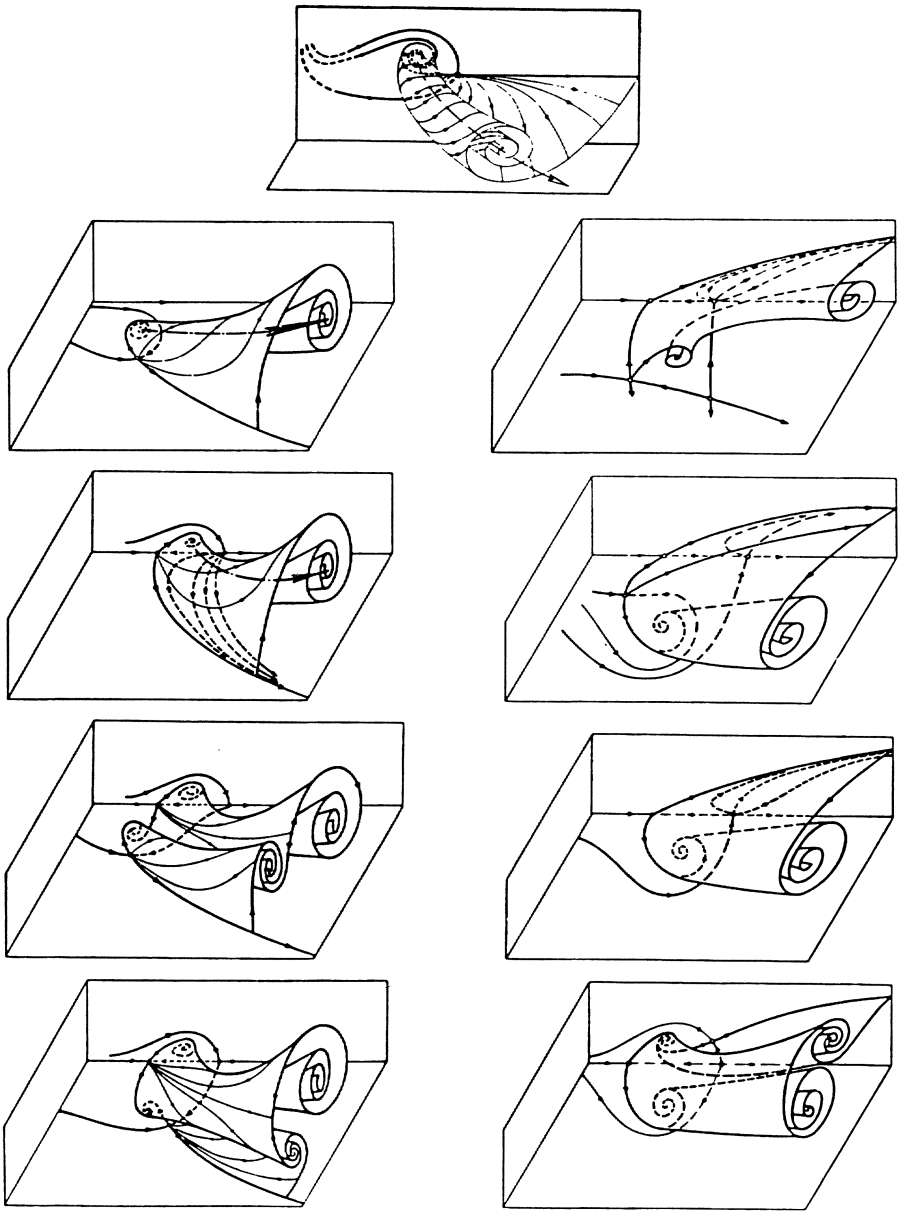

Fig. 13 Streamsurface representations of some separated, three-dimensional flows.

Although the mathematical analysis of systems like (6), (7), and (8), taking into account higher order perturbations and bifurcations, is by no means complete, the results sketched above are sufficient for the so-called elementary topological structures of steady vortex flows to be drawn; some of these are given in Fig. 13.

One result of the analysis is that it is thus proved that a three-dimensional point of separation (see Figure 13) is a special so-called Poincaré saddle, from where all the streamlines leave the surface and finally wind around and converge to a single streamline that has left a nodal point (usually a focus) somewhere else. These streamlines form a special streamsurface within a three-dimensional flow, which we called a singular streamsurface, (DALLMANN [1]). Only these need to be sketched in order to give a geometric representation of the topography of a steady flow field.

According to the results shown in Fig. 11, structural changes occur for distinct values of the coefficient set (a_i, b_i, c_i). These values will be reached only for certain Reynolds numbers Re, angles of attack α, etc.. Therefore, certain regimes of different topological structures will exist in such characteristic dimensionless parameter spaces (Re, α, etc.), for instance for the flow around a blunt body.

In the following, we have chosen the convection flow within a finite container heated from below to demonstrate the usefulness of the topological considerations, not only in analyzing experimental observations, but also in accompanying and guiding numerical flow analysis.

4. CHANGING TOPOLOGICAL STRUCTURES IN RAYLEIGH-BÉNARD CONVECTION

Thermal convection of a fluid that is confined to a container is different from classical Rayleigh-Bénard convection, where an infinite layer of fluid heated from below is considered, and where the appearance of longitudinal convection rolls as shown in Fig. 3 is well understood.

Three-dimensional experiments and numerical calculations using a box with length : depth : height of 4 : 2 : 1, have been reported in OERTEL [10], KESSLER & OERTEL [11], and JÄGER & OERTEL [12]. It turned out that the confinement puts new constraints on the flow evolution, i.e., a great number of possible bifurcation solutions that are dependent on the initial and boundary conditions appear.

In contrast to the case of thermal convection in an infinite layer of fluid, convection in a finite box is characterized by discrete changes of wavelength, i.e., the number of appearing "rolls" changes. Such discrete changes certainly have to be accompanied by a complex structural instability of the flow. The bifurcation at a critical parameter set of Rayleigh number and Prandtl number (Pr) leads to a change in the topological structure.

A decreasing number of "rolls" can be seen in the differential interferogram or by a light sheet visualization technique when the Rayleigh number is increased. Increasing the Prandtl number causes a shift of those sudden transitions towards higher Rayleigh numbers. It thus turns out that Prandtl number changes have a strong influence on the onset of oscillations in the convection flow (i.e., the critical Rayleigh number) as well as on the qualitative behavior, i.e., the structure of the unsteady convection. The oscillations for air are completely different from those for water. For Pr = 0,71 the calculations of KESSLER [13] exhibit large periodic contractions of the rolls, while for Pr = 7 the maximum amplitude of oscillation moves along the otherwise almost permanent rolls.

In order to obtain a clue to a better understanding of different oscillatory behavior for high and low Prandtl number convection flows, we analyzed the possiblity of having topologically different flow structures for a given number of rolls in a finite container just before the onset of oscillation (KESSLER & DALLMANN & OERTEL [14], and DALLMANN & KESSLER [15]). Qualitatively different steady flows might undergo different bifurcations into the unsteady oscillatory regime.

Fig. 14 exhibits the different streamline behavior in the three-roll regimes for air (Pr = 0,71) and water (Pr = 7).

In contrast to two-dimensional considerations, not all the streamlines of three-dimensional convection are confined to a single roll. There are some very complicated successive traverses of streamlines between different rolls.

Inertial end effects and thermal end effects caused by the boundary conditions at the side walls are responsible for the fact that the topological structure of the steady convection is highly dependent upon the Prandtl number.

Let us now assume that we establish from experimental observation that three roll-like structures plus some corner-eddies appear in the container for given Rayleigh number, Prandtl number, and boundary conditions.

Let us study possible bifurcations, i.e. structural changes, from a structurally unstable situation. We initially assume two-dimensional roll

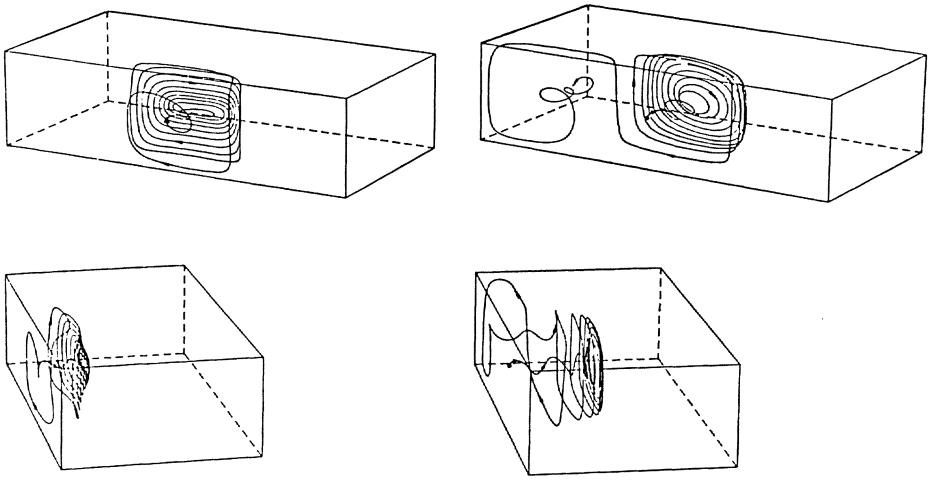

Fig. 14 Different streamline behavior of three-dimensional, steady convection (3 "rolls", adiabatic side walls, left: Pr = 7.00, right: Pr = 0.71), KESSLER [13], KESSLER, DALLMANN & OERTEL [14].

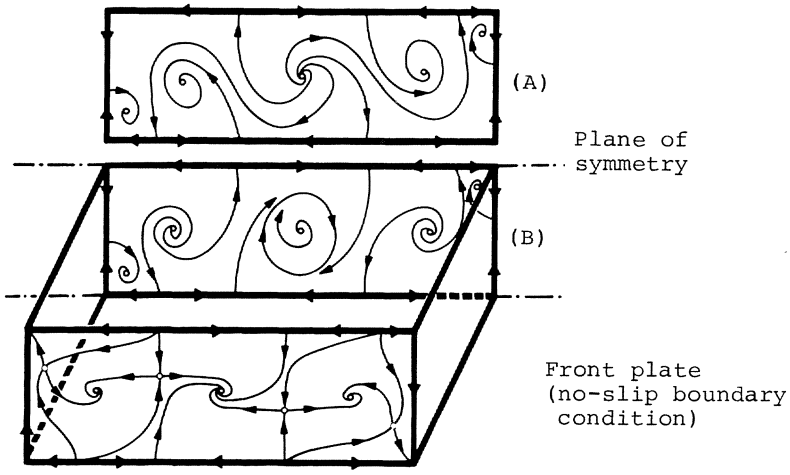

Fig. 15 Convection flow patterns on the front plate and in the plane of symmetry of a rectangular container.

structures with closed cells showing closed streamlines around centers, as well as multiple saddle-to-saddle connections separating one roll from another. Due to the no-slip boundary conditions at the walls, no such degenerate two-dimensional pattern can survive. A spiralling motion towards foci will set in at the side walls (Fig. 15) and, due to continuity, the flow will have to propagate into the interior of the container. If we now assume flow symmetry, a spiralling motion away from the axis will set in as we approach that plane of symmetry. Global bifurcations will split the multiple saddle-to-saddle connections (under certain symmetry conditions) into the two different patterns indicated in Fig. 15 as (A) and (B). As a result, we now discern an interesting feature. The flow following Fig. 15, case (A), in a plane of symmetry indicates mass transfer from the inner roll to the outer rolls. In contrast, we can see in case (B) mass transfer from the larger outer rolls towards a kind of a limit cycle, i.e., a single closed streamline in the plane of flow symmetry. Based on KESSLER [13] we analyzed in DALLMANN & KESSLER [15] a numerical solution of the complete three-dimensional equations of motion for this convection flow in terms of topological structures and structural changes. After having carefully enlarged the numerically obtained streamline trajectories, we were able to confirm that exactly these two different structures appeared for low Prandtl number convection (Fig. 15, case (A)) and high Prandtl number convection (Fig. 15, case (B)), respectively.

In order to complete the topography of such a convection flow in a container, we have to sketch the singular streamsurfaces by sketching separatices that connect critical points. Here we use all the information derived above about the elementary topological flow structures.

In Fig. 16 we present as an example a topological description (with appropriate stretching of streamline trajectories) for the low Prandtl number case. It yields the surprising result that critical points exist not only on the side walls but also appear in the interior of the container (see saddle-foci F). As a consequence, streamline integration performed in order to provide a geometrical (intuitive) picture of a flow field is tedious work; the resulting geometric appearance of the steady convection flow is highly dependent on the initial condition (the starting point of the streamline integration near S, Fig. 17). There are some very complicated toroidal surfaces within such flows where streamlines make successive traverses between different rolls. Detailed checks indicate that in such a three-dimensional configuration, no closed streamlines appear within the container (with the possible exception of closed streamlines in a plane of flow symmetry).

The concept of topological flow structures based on the elementary structures and structural changes discussed above enables us to confirm the existence of qualitatively, i.e., topologically different convection flow fields. Therefore, such a difference between high and low Prandtl number

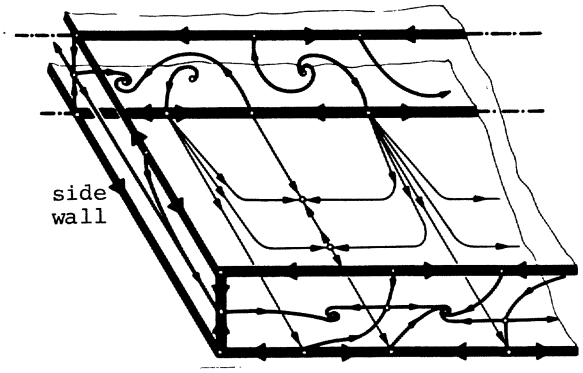

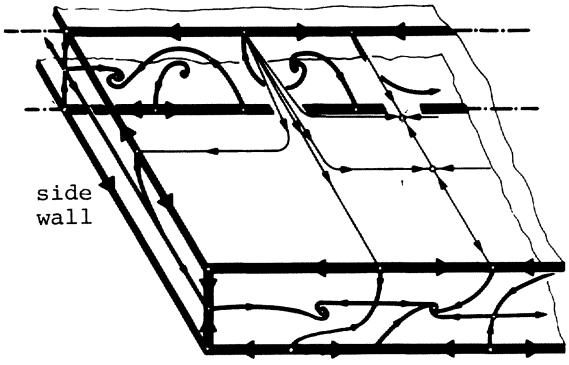

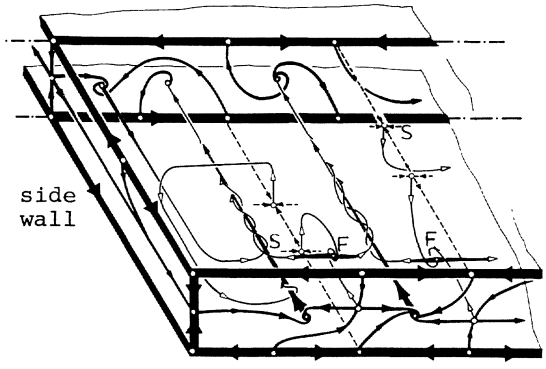

Fig. 16 Topological structure of Rayleigh-Bénard convection in a finite container (section shown only; Pr = 0.71, adiabatic side walls and front plates).

convection even within the steady flow regimes is likely to lead to the observed qualitative difference in the oscillatory convection flow regime.

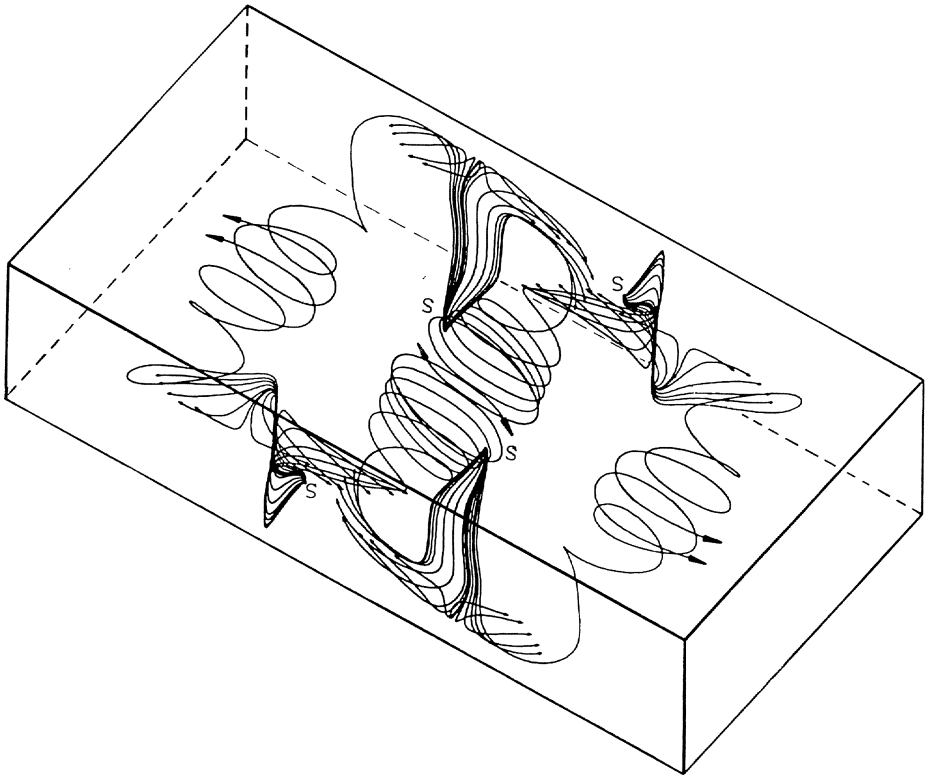

Fig. 17 Calculated streamlines for Rayleigh-Bénard convection in a finite container in full agreement with predicted topological structures sketched in Fig. 16. Streamline integration has been started at Poincaré-saddles S in order to exhibit the streamline behavior near the saddle-foci F (see Fig. 16). Streamline integration exhibits the sensitivity on the starting point chosen arbitrary close to S in full agreement with a priori topological considerations (Figs. 15 and 16).

5. CONCLUDING REMARKS

We hope that we have been able to show that, at least for steady flows, *it is an advantage to apply the well-defined topological description of structure*. We may drop any intuitive idea of steady, three-dimensional vortex flows. Even the representation of flow fields in terms of sectional streamlines turns out to be misleading.

Since the qualitative property of a flow that we call structure changes only at discrete values, i.e., bifurcation parameter values (Reynolds number, Mach number, etc.) it is possible to predict structural changes prior to any calculation or experimental variation of those parameters.

Although the concepts of topological structure analysis and structural stability of flow fields have been proven to be very useful when applied to steady flows, it is clear that any structures defining the topography of the velocity field are not Galilean invariant. Such a dependence on the frame of reference might lead us to analyze the qualitative properties of flows in terms of vorticity structures. In doing so, we have to keep in mind that we are looking for qualitative features of flows and not for quantative comparisons. Such a characterization should be possible and should remain significant for two-dimensional flows, too. But structural changes of the vorticity field can by definition not take place in two-dimensional flows. A description of iso-vorticity lines given in certain sections cutting the flow field would be a quantative and not a qualitative representation of the flow. Therefore, vorticity does not seem to be the best candidate for explaining structural changes of unsteady flows. In addition, the patterns of iso-vorticity lines, instantaneous streamlines, and pathlines may undergo completely different topological changes in unsteady flows, (ALLEN [16]).

It is also possible to examine the nature of an evolving flow field in velocity space rather than in physical space. The singularities of such a mapping, i.e., the points, lines, or surfaces where the Jacobian of the mapping vanishes, may then be analyzed (NYE [17]). The topology of these singularities may undergo a structural instability in time as well as in parameter space of Reynolds number, Mach number, etc. The characterization of these events and their relationship to topological changes of the flow in physical space might provide another language for explaining and comparing some qualitative properties of flow fields.

In order to compare results of nonlinear dynamical systems analysis based on ordinary differential equations with some qualitative features of a time-evolving flow in fluid dynamics, we still have to look for invariant equivalence properties, such as topological equivalence of structures and of structural changes of some invariant flow quantity.

6. REFERENCES

[1] U. DALLMANN: Topological Structures of Three-Dimensional Flow Separation. DFVLR-IB 221-82 A 07 (1982).

[2] U. DALLMANN: Topological Structures of Three-Dimensional Vortex Flow Separation. AIAA-83-1935 (1983).

[3] M. TOBAK, D.J. PEAKE: Topology of Three-Dimensional Separated Flows. Ann. Rev. Fluid Mech. 14, pp.61-85 (1982).

[4] H. BIPPES, M. TURK: Oil Flow Patterns of Separated Flow on a Hemisphere Cylinder at Incidence. DFVLR-FB 84-20, 1983.

[5] H.G. HORNUNG, A.E. PERRY: Some aspects of three-dimensional separation. Part I: Streamsurface bifurcations. Z. Flugwiss. Weltraumforsch. 8, 77-87 (1984),
see also A.E. PERRY and H.G. HORNUNG, Part II: Vortex skeletons. Z. Flugwiss. Weltraumforsch. 8, 155-160 (1984).

[6] A.E. PERRY, B.D. FAIRLIE: Critical Points of Flow Patterns. Advances in Geophysics, 18b, pp.299 (1974), Academic Press, New York - San Francisco - London.

[7] R. LEGENDRE: Regular or catastrophic evolution of steady flows depending on parameters. Rech. Aerosp. 1982-4, pp.41-49 (1982).

[8] K. OSWATITSCH: Die Ablösebedingung von Grenzschichten. IUTAM Symposium on Boundary Layer Research, Freiburg (1957).

[9] U. DALLMANN: (to be published).

[10] H. OERTEL jr.: Natural Convection in Enclosures. HTD - Vol. 8, 11-16 (1980).

[11] R. KESSLER, H. OERTEL jr.: ZAMM 63 (1983).

[12] W. JAEGER, H. OERTEL jr.: DFVLR-IB 221-82 A 04 (1982).

[13] R. KESSLER: Oszillatorische Konvektion. DFVLR-FB 84-14 (1984).

[14] R. KESSLER, U. DALLMANN, H. OERTEL: Nonlinear Transitions in Rayleigh-Bénard Convection. IUTAM-Symposium on Turbulence and Chaotic Phenomena in Fluids, Kyoto/Japan (1983).

[15] U. DALLMANN, R. KESSLER: (to be published).

[16] G.A. ALLEN: Transition and Mixing in Axisymmetric Jets and Vortex Rings. Thesis, Stanford University, Dept. of Aeronautics and Astronautics. SUDAAR 541 (1984).

[17] J.F. NYE: Events in evolving vector fields. J. Phys. A.: Math. Gen. Vol. 13, pp.1-14 (1980).

FLUID MECHANICAL STRUCTURES

SELF SIMILARITY, CRITICAL POINTS, AND HILL'S SPHERICAL VORTEX

G.A. ALLEN JR.

Hill's spherical vortex, a classical solution dating from 1894, is examined in a new perspective. The axisymmetric vorticity transport equation is taken to its low Reynolds number limit (no convective term) and cast into a form that is self similar in time. The subsequent equation is solved by separation of variables and shown to have two linearly independent solutions. One of these two solutions satisfies the Navier-Stokes equation exactly for all Reynolds numbers. However, to satisfy boundary conditions for the unbounded problem, both of these solutions as well as irrotational components are required. The results are represented by self similar particle paths. The flow topology is examined in the context of critical points of the self similar particle paths. It is shown that this result undergoes two transitions in topological structure with changing Reynolds number. Also shown is that the creeping flow (low Reynolds number) solution has three possible topological states in the axisymmetric case.

1. INTRODUCTION

The fluid considered is assumed to be incompressible and Newtonian. The solution method assumes axisymmetry and low Reynolds number. The low Reynolds number vorticity transport equation may be written in spherical polar coordinates as

$$\frac{\partial \omega}{\partial t} = \nu\left[\nabla^2\omega - \frac{\omega}{r^2 \sin^2\theta}\right] \qquad (1)$$

where

θ = coordinate angle with $\theta = 0$ being the axis of symmetry
t = time
ν = kinematic viscosity
$\omega(r,\theta,t)$ = vorticity in the ϕ direction

Equ..(1) may be cast into a self similar form by employing the following self similar transformations which were derived from group theory, (see ALLEN and CANTWELL [1]).

$$\xi = \frac{r}{\sqrt{2\nu t}} \tag{2}$$

$$\omega(r,\theta,t) = H\nu^{-2}t^{m-1}W(\xi,\theta) \tag{3}$$

where

ξ = similarity coordinate
H = characteristic strength of the momentum of the jet in question
$W(\xi,\theta)$ = dimensionless self similar vorticity
m = jet type index

Equations (2) and (3) are inserted into (1), which yields a new partial differential equation in which time does not appear explicitly. This new differential equation may be solved by separation of variables, using the following substitution:

$$W(\xi,\theta) = CP_{\ell}^{1}(\cos\theta)J_{m}^{\ell}(\xi) \tag{4}$$

where

$P_{\ell}^{1}(\cos\theta)$ = first order associated Legendre polynomial
ℓ = integer index indicating order of the pole,
(i.e. ℓ=1, dipole; ℓ=2, quadrupole, etc.)
$J_{m}^{\ell}(\xi)$ = jet function radial solution
C = constant for boundary conditions

The first order associated Legendre polynomial satisfies the following ordinary differential equation

$$\frac{1}{\sin\theta}\frac{d}{d\theta}\left[\sin\theta\frac{dP_{\ell}^{1}}{d\theta}\right] + \left[\ell(\ell+1) - \frac{1}{\sin^{2}\theta}\right]P_{\ell}^{1} = 0 \tag{5}$$

A general analysis of the jet function can be found in Appendix A of ALLEN & CANTWELL [1]. The ordinary differential equation for the jet function is

$$\frac{d^{2}J_{m}^{\ell}}{d\xi^{2}} + (\xi+\frac{2}{\xi})\frac{dJ_{m}^{\ell}}{d\xi} - 2\left[\frac{\ell(\ell+1)}{2\xi^{2}} + m - 1\right]J_{m}^{\ell} = 0 \tag{6}$$

Relations describing the polynomial solutions to equ. (6) were developed for the cases of $\pm m = 0, \frac{1}{2}, 1, \frac{3}{2}, 2, \frac{5}{2}, 3, \ldots$. Some of the solutions from this

infinite set, which have smaller values of m, represent classical flows and have already been investigated. For example, the round jet (m = 0) is well known for its steady Navier-Stokes form first discovered by LANDAU [8] and later independently by SQUIRE [11]. The creeping form of this solution satisfying equ. (1) was found by SOZOU [10] and further investigated by CANTWELL [3]. The vortex ring creeping-flow solution, m = -1, was found by CANTWELL & ALLEN [4]. A previously unexplored flow, the ramp jet (m = 1) was also examined by CANTWELL & ALLEN [5]. One fortunate side effect of this creeping-flow analysis has been the solution formulation in terms of the index m which provides a simple unambiguous means of classifying the different types of jet flows as well as serving as a signpost for examining unexplored flows, e.g. m = ±1/2. Once a value of m has been selected, one may readily calculate the vorticity field, either from the formulas derived in Appendix A of ALLEN & CANTWELL [1] or directly from equations (3) - (6).

The stream function is found by using the following self similarity transformation:

$$\psi(r,\theta,t) = H\nu^{-1/2} t^{m+1/2} G(\xi,\theta) \tag{7}$$

where

$\psi(r,\theta,t)$ = stream function
$G(\xi,\theta)$ = dimensionless self similar stream function

From the definition of the stream function and of the vorticity, one may write

$$-r\omega = \frac{1}{\sin\theta}\frac{\partial^2\psi}{\partial r^2} + \frac{1}{r^2}\frac{\partial}{\partial\theta}\left(\frac{1}{\sin\theta}\frac{\partial\psi}{\partial\theta}\right) \tag{8}$$

The combination of (3), (7) and (8) gives:

$$-2^{3/2}\xi W = \frac{1}{\sin\theta}\frac{\partial^2 G}{\partial\xi^2} + \frac{1}{\xi^2}\frac{\partial}{\partial\theta}\left(\frac{1}{\sin\theta}\frac{\partial G}{\partial\theta}\right) \tag{9}$$

One can show by direct substitution that the correct separation of variables form for this problem is:

$$G(\xi,\theta) = C \sin\theta \, P_\ell^1(\cos\theta) R_m^\ell(\xi) \tag{10}$$

where $R_m^\ell(\xi)$ = radial component of the stream function.

The relationship between the radial component of the vorticity and the stream function is given by

$$J_m^{\ell} = -2^{-3/2}\xi^{\ell-1}\frac{d}{d\xi}\left[\frac{1}{\xi^{2\ell}}\frac{d}{d\xi}(\xi^{\ell}R_m^{\ell})\right] \tag{11}$$

One may simply integrate equ. (11) to generate the radial component of the stream function (the two resulting constants of integration represent the irrotational components of the velocity field for the particular value of ℓ).

The self similar transformations for velocity are:

$$u(r,\theta,t) = H\nu^{-3/2}t^{m-1/2}U(\xi,\theta) \tag{12}$$

$$v(r,\theta,t) = H\nu^{-3/2}t^{m-1/2}V(\xi,\theta) \tag{13}$$

We can combine the definition of stream function with (12) and (13) to give the self similar form:

$$U = \frac{1}{2\xi^2\sin\theta}\frac{\partial G}{\partial\theta} \tag{14}$$

$$V = \frac{-1}{2\xi\sin\theta}\frac{\partial G}{\partial\xi} \tag{15}$$

where

$U(\xi,\theta)$ = self similar velocity in the ξ direction

$V(\xi,\theta)$ = self similar velocity in the θ direction

$u(r,\theta,t)$ = velocity in the r direction

$v(r,\theta,t)$ = velocity in the θ direction

It was shown by CANTWELL [3] that an impulsively started jet from a point source of momentum must satisfy the following integral constraint:

$$\frac{2}{3}\frac{I}{\rho} = \int_0^{\pi}\int_0^{\infty}(u\cos\theta - v\sin\theta)2\pi r^2\sin\theta\, dr\, d\theta \tag{16}$$

where

$$\frac{I}{\rho} = \int_0^{t} f(t)\,dt \tag{17}$$

is the total impulse applied to the fluid. This is where the characteristic jet strength H re-enters the development, for if we define the following:

$$f(t) = Ht^m \tag{18}$$

then the integral constraint (17) is satisfied and the self similarity is retained for most values of m, (two known examples where equ. (18) is not true are the cases of m = 0, which requires a Heaviside step, and m = -1, which requires a Dirac delta function). f(t) is proportional to the momentum being injected into the fluid at the origin. From equations (17) and (18) and the particle path equations we may define a Reynolds number. The particle path equations in physical space are

$$\frac{dr}{dt} = u(r,\theta,t) \quad ; \quad \frac{d\theta}{dt} = \frac{v(r,\theta,t)}{r} \tag{19}$$

If equations (19) are cast into a self similar form we find that the self similar particle path equations are

$$\frac{d\xi}{d\tau} = Re^2 U - \frac{\xi}{2} \tag{20}$$

$$\frac{d\theta}{d\tau} = Re^2 \frac{V}{\xi} \tag{21}$$

where

$$\tau = \ell n(t) \tag{22}$$

$$Re = \left[\frac{Ht^m}{\sqrt{2}\nu^2}\right]^{1/2} \tag{23}$$

Equ. (23) defines our Reynolds number. However, one should be careful in comparing this Reynolds number to others since it is based on a point momentum source and does not contain an explicit length.

There are three boundary conditions that must be satisfied by a physical flow. Two of them represent the same physical condition:

1. The vorticity must die off in a manner dominated by a Gaussian function based on the distance from the origin of the jet.

2. The far-field stream function must behave as an irrotational dipole, which in the self similar coordinate used is

$$\dot{G}_\infty(\xi,\theta) = \frac{\sqrt{2}\sin^2\theta}{8\pi\xi} \tag{24}$$

3. The stream function must be of finite value in the entire flow field.

The boundary condition of (24) is rather interesting, since it can be shown that for the creeping-flow approximation only the jet function solutions for $\ell = 1$ will satisfy (24). The higher-order poles of $\ell \geq 2$ are (in the case of the unbounded jet) entirely a consequence of the convective term. Without the convective term, all of the different orders of poles decouple, and there is no mechanism for a pole of lower order to excite a higher order pole. For this reason, in examining creeping-flow solutions in the unbounded case, we restrict ourselves to $\ell = 1$ where

$$P_1^1(\cos\theta) = \sin\theta \tag{25}$$

2. DERIVATION OF THE LOW REYNOLDS NUMBER SOLUTION FOR HILL'S SPHERICAL VORTEX

In examining the properties of jet functions, it was discovered that for the case of $m = 3/2$, the vorticity equation for Hill's spherical vortex was produced.

The jet function for $m = 3/2$ is

$$J^1_{3/2}(\xi) = c_1\xi + c_2\left(\left[1 - \frac{1}{\xi^2}\right]\sqrt{\frac{2}{\pi}}\, e^{-\xi^2/2} - \xi\,\mathrm{erf}\left(\frac{\xi}{\sqrt{2}}\right)\right) \tag{26}$$

where c_1 and c_2 are constants of integration.

It was recognized that the independent solution corresponding with c_1 in equ.(26) would generate the same vorticity equation for Hill's spherical vortex given by LAMB [7] or by BATCHELOR [2] (which are cast in cylindrical coordinates). When the equations and boundary conditions described in the introduction are applied, the following results:

$$W(\xi,\theta) = \frac{5\sin\theta}{32}\sqrt{\frac{2}{\pi}}\left[\xi\left(1-\mathrm{erf}\left(\frac{\xi}{\sqrt{2}}\right)\right) - \left(1-\frac{1}{\xi^2}\right)\sqrt{\frac{2}{\pi}}\, e^{-\xi^2/2}\right] \tag{27}$$

$$G(\xi,\theta) = \frac{\sin^2\theta\sqrt{2}}{16\pi}\left[\left(1-e^{-\xi^2/2}\right)\frac{2}{\xi} + \left(4\xi+\xi^3\right)e^{-\xi^2/2} - \right.$$

$$\left. - \left(1-\mathrm{erf}\left(\frac{\xi}{\sqrt{2}}\right)\right)\left(\xi^4+5\xi^2\right)\sqrt{\frac{\pi}{2}}\right] \tag{28}$$

The first term in the square bracket of (27) represents a classical vorticity solution. The ξ^4-term in (28) represents the classical stream function, with the ξ^2- and $1/\xi$-terms being the irrotational components. The singular behaviour of the vorticity at the origin is expected, since the momentum source injects vorticity into the fluid from a single point. What has made the classical Hill's spherical vortex so interesting is that it satisfies the Navier-Stokes equation exactly. It does this by simply setting the convective term to zero identically while satisfying the creeping-flow equation. One may write down the classical solution in physical coordinates as

$$\omega(r,\theta) = -\alpha 10\, r \sin\theta \tag{29}$$

$$\psi(r,\theta,t) = \alpha r^4 \sin^2\theta + \sum_{\ell=1}^{\infty} \left[\beta_\ell(t) r^{-\ell} + \gamma_\ell(t) r^{\ell+1}\right] \sin\theta\, P_\ell^1(\cos\theta) \tag{30}$$

where

α = constant of the rotational component,
$\beta_\ell(t)$ and $\gamma_\ell(t)$ are two sets of coefficients for the irrotational component which can be functions of time.

Usually only the dipole $\ell=1$ component appears in the literature, with the higher-order pole coefficients set to zero. Typically the stream function is represented as

$$\psi(r,\theta) = \alpha r^2 \sin^2\theta \left[r^2 - a^2\right] \tag{31}$$

where a is some fixed radius, and the problem is assumed to be steady. The typical description of equ. (31) requires that an irrotational uniform flow be matched to the flow at r = a. This approach has been the standard method with the classical solution of dealing with the embarrassment of the vorticity's becoming infinite for large radius. It should be emphasized that if one requires that the radius r = a be fixed, then equation (31) cannot be cast into a self similar form. However, equ. (31) is self similar if radius a is proportional to $t^{1/2}$. Equ. (31) can probably not be physically realized with its discontinuous vorticity in an unbounded flow. The second independent solution of equ. (26) (in its Navier-Stokes form) would have to manifest itself in some way. Also one would anticipate the appearance of higher-order poles and nonaxisymmetric effects at higher Reynolds numbers.

3. THE TOPOLOGY OF HILL'S SPHERICAL VORTEX

The importance of critical points in flow topology has been discussed in many papers. The work of PERRY & FAIRLIE [9], which is often cited, has provided the basis for our own interest in this topic. CANTWELL [3] applied critical point theory to the low Reynolds number round jet, m = 0. This same technique was later applied to the Navier-Stokes solution of the round jet in ALLEN & CANTWELL [1].

The following analysis was derived from CANTWELL's paper. A viscous critical point in physical space would be analogous to a stagnation point. However, in our unsteady problem there are no stagnation points except at infinity. But if one transforms the flow field into self similar space, one will find the analogues of stagnation points. These critical points can be found by using the particle path equations (20) - (21). When combined with (14), (15), and (28) the particle path equations for the creeping-flow spherical vortex are:

$$\frac{d\xi}{d\tau} = \frac{Re^2 \cos\theta\sqrt{2}}{16\pi\xi^2}\left[\left(1-e^{-\xi^2/2}\right)\frac{2}{\xi} + \left(4\xi+\xi^3\right)e^{-\xi^2/2} - \right.$$
$$\left. - \left(1-\mathrm{erf}\left(\frac{\xi}{\sqrt{2}}\right)\right)\left(\xi^4+5\xi^2\right)\sqrt{\frac{\pi}{2}}\right] - \frac{\xi}{2} \qquad (32)$$

$$\frac{d\theta}{d\tau} = \frac{Re^2 \sin\theta\sqrt{2}}{16\pi\xi^2}\left[\left(1-e^{-\xi^2/2}\right)\frac{1}{\xi^2} - \left(3+2\xi^2\right)\ e^{-\xi^2/2} + \right.$$
$$\left. + \left(1-\mathrm{erf}\left(\frac{\xi}{\sqrt{2}}\right)\right)\left(2\xi^3+5\xi\right)\sqrt{\frac{\pi}{2}}\right] \qquad (33)$$

A critical point is found whereever $d\xi/d\tau$ and $d\theta/d\tau$ are both equal to zero. $d\theta/d\tau$ will be zero for all Reynolds numbers when $\theta = 0$ or when the expression in brackets (the radial component) is zero. The expression in brackets can be cast into the following form, which is iteratively convergent.

$$\xi = \left[2\ell n\left[\frac{3\xi^2+2\xi^4+1}{1+\sqrt{\frac{\pi}{2}}\left(1-\mathrm{erf}\left(\frac{\xi}{\sqrt{2}}\right)\right)\left(2\xi^5+5\xi^3\right)}\right]\right]^{1/2} \qquad (34)$$

The solution of this equation is:

$$\hat{\xi}_c = 0.8117236 \qquad (35)$$

Therefore $d\theta/d\tau$ will be zero for all Reynolds numbers if $\theta = 0$ or $\xi = \hat{\xi}_c$ for $\theta \neq 0$. If $d\xi/d\tau$ is set equal to zero, then the following results:

$$Re^2 = \frac{8\pi\xi^4}{\sqrt{2}\cos\theta\left[2+(4\xi^2+\xi^4-2)e^{-\xi^2/2}-(1-\mathrm{erf}(\frac{\xi}{\sqrt{2}}))(\xi^5+5\xi^3)\sqrt{\frac{\pi}{2}}\right]} \tag{36}$$

As in the case of equ. (33), we find from (36) that $d\xi/d\tau$ is also zero on the $\theta = 0$ axis at discrete points whose location is a function of Reynolds number. For example, at $Re = 0$ we find from (36) that $\xi = 0$. Therefore we know that for zero Reynolds number there is one critical point at the origin, (see Fig. 1a). As Reynolds number increases, this critical point moves away from the origin with increasing ξ but remains at $\theta = 0$ because of the requirement of (33), (see Fig. 1b). At $Re = 2.54857$, the value of ξ is equal to $\hat{\xi}_c$. At this Reynolds number the critical point becomes degenerate, from which the original single critical point bifurcates into three critical points, (see Fig. 1c). One of the three critical points continues on the $\theta = 0$ axis with $\xi > \hat{\xi}_c$. However the other two critical points retain values of $\xi = \hat{\xi}_c$ but satisfy the off-axis angular dependence based on equ. (36) of

$$\theta_c = \pm \mathrm{Arccos}\left[\left(\frac{Re_1}{Re}\right)^2\right] \tag{37}$$

where

$$Re_1 = 2.58857 \tag{38}$$

The Reynolds number Re_1 can be viewed as a transition Reynolds number since it marks a point of topological change. Since the flow is assumed to be axisymmetric about the $\theta = 0$ axis, the two off-axis critical points actually represent a critical line forming a ring of radius $\hat{\xi}_c \sin\theta_c$ that is growing with Reynolds number.

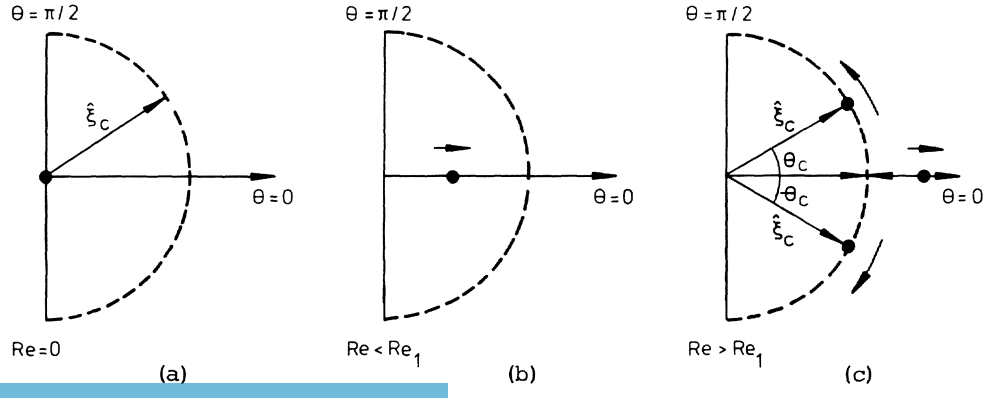

Fig. 1 Bifurcation of critical points.

For infinite Reynolds number one can see from (37) that the critical point angle will be 90°. This aspect, however, is only of academic interest since the assumption of low Reynolds number and probably that of axial axisymmetry will have failed. From equ. (23) we see that the Reynolds number for Hill's spherical vortex is

$$Re = \left[\frac{Ht^{3/2}}{\sqrt{2}\nu^2}\right]^{1/2} \tag{39}$$

Therefore, the Reynolds number is zero for t = 0 (and zero for t < 0 because the flow is unstarted). The Reynolds number will increase with time as $t^{3/4}$. Therefore, there will only be a short time after starting during which the creeping-flow approximation will be valid. We go beyond this region of validity primarily to understand the mathematics of the topological transitions.

4. PROPERTIES OF THE CRITICAL POINTS

One may anticipate the topology of a self similar autonomous solution for an axisymmetric jet prior to actual solution of the momentum equation. This is achieved by performing a first order analysis on the particle paths using continuity and boundary conditions. If, as is assumed here, the solution is regular in space and time, one can represent the particle paths to first order in self similar space coordinates as

$$\frac{d\xi}{d\tau} = a(\xi-\xi_c) + b(\theta-\theta_c) \tag{40}$$

$$\frac{d\theta}{d\tau} = c(\xi-\xi_c) + d(\theta-\theta_c) \tag{41}$$

where a, b, c, d are constants independent of time and ξ_c, θ_c define the location of the critical point.

(40) and (41) can be recast into a single second-order equation. The characteristic equation of (40) and (41) is written as

$$\lambda^2+p\lambda+q = 0 \tag{42}$$

where λ is the secular variable

$$p = -(a+d) \tag{43}$$

$$q = ad-bc \tag{44}$$

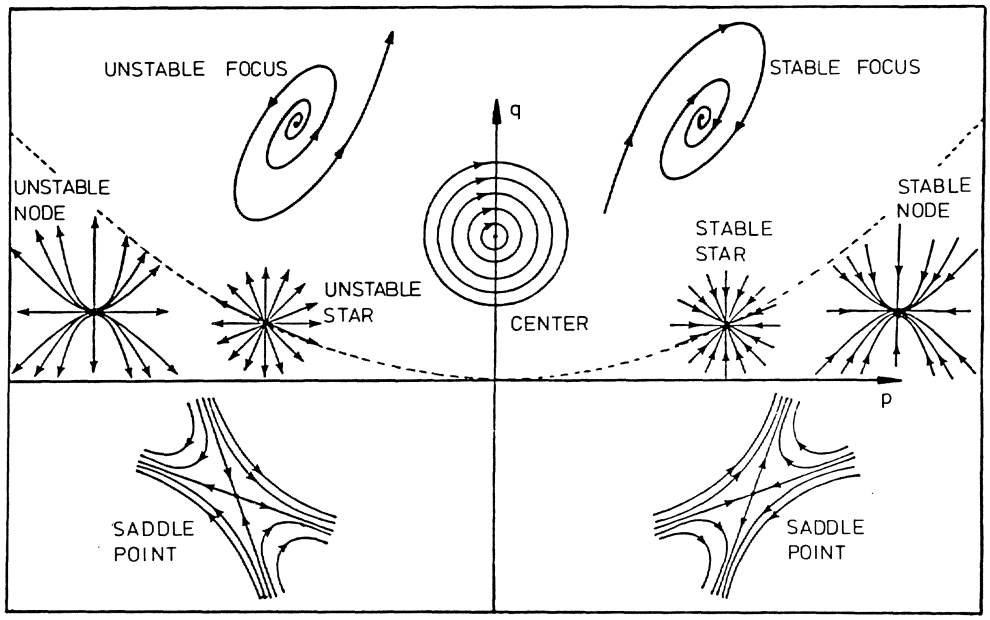

Fig. 2 Critical Point Topologies in p,q Space.

The quantities p, q can be represented as coordinates in a state space, which is shown in Fig. 2. The dashed parabola in Fig. 2 is defined by

$$q = \frac{p^2}{4} \tag{45}$$

The parabola defines a region where the eigenvalues of (42) are single-valued. This parobola and the axis q = 0 along with the p = 0 axis are regions where critical points are degenerate (i.e. two different topological regions occur simultaneously).

As can be seen in Fig. 2, critical points can have many different topological structures based on their p,q value. For example, negative q critical points are always saddle points, and for positive p with q above the parabola the critical points are stable foci. (The terms stable and unstable were inherited from control theory and have nothing to do with hydrodynamic stability). If we combine equations (40), (41) with (20), (21), we find that

$$U = \frac{1}{Re^2}\left[\frac{\xi}{2} + a(\xi-\xi_c) + b(\theta-\theta_c)\right] \tag{46}$$

$$V = \frac{\xi}{Re^2}\left[c(\xi-\xi_c) + d(\theta-\theta_c)\right] \tag{47}$$

We may convert the continuity equation into self similar form giving

$$2U+\xi\frac{\partial U}{\partial \xi}+\frac{\cos\theta}{\sin\theta}V+\frac{\partial V}{\partial \theta}=0 \tag{48}$$

Combining (46) - (48) gives

$$\xi+2a(\xi-\xi_c)+2b(\theta-\theta_c)+\frac{\xi}{2}+a\xi+\frac{\cos\theta}{\sin\theta}c\xi(\xi-\xi_c)+$$

$$+\frac{\cos\theta}{\sin\theta}d\xi(\theta-\theta_c)+d\xi=0 \tag{49}$$

We need to consider two cases:

Case 1 The critical point is off-axis: $\theta_c \neq 0$.
Let $\xi \to \xi_c$, $\theta \to \theta_c$.
Equ. (49) becomes

$$p=-(a+d)=3/2 \tag{50}$$

Case 2 The critical point is on-axis: $\theta_c = 0$.
We can apply the boundary condition that
$V(\xi,\theta_c)=0$.

From this boundary condition and from (47) we find that $c = 0$. Now let $\xi \to \xi_c$, $\theta \to \theta_c$, and equ. (49) becomes

$$p=d+\frac{3}{2} \tag{51}$$

Now combine (51) with (43) and (44), giving

$$q=\left[p-\frac{3}{2}\right]\left[\frac{3}{2}-2p\right] \tag{52}$$

We can now place the trajectory defined by (50) and (52) on the p, q chart of Fig. 2 (see Fig. 3).

The trajectory of Fig. 3 describes all autonomous self similar axisymmetric jets. For the problem of HILL's spherical vortex only a piece of the total trajectory is useful. One can determine the relevant piece as follows. For the fluid at rest there is a single critical point (an on-axis stable star point) at (p,q) = (1, 1/4) that just touches the parabola. Since the spherical vortex will roll up (form a stable focus), we know that the critical point goes initially in the direcion of increasing p, where it would become an on-axis stable node. At (p,q) = (3/2, 0) the critical point becomes degenerate and is capable of following two different paths. It is at this point that bifurcation occurs. Since the spherical vortex

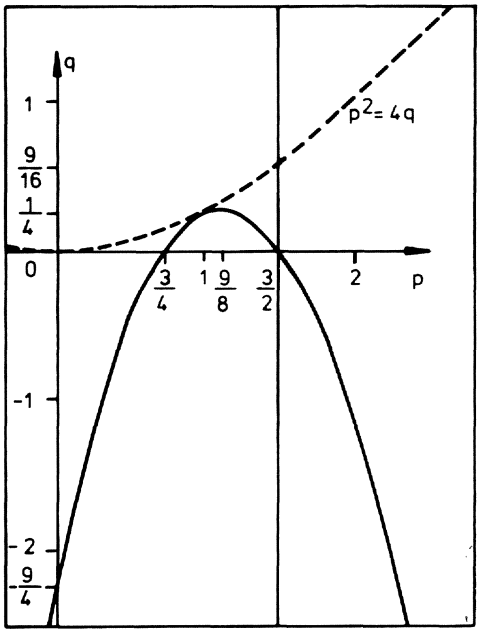

Fig. 3

State space with axisymmetric trajectory.

must form a stable focus, at least one critical point must go up the p = 3/2 trajectory. This bifurcation could occur in many different ways. If the total number of nodes minus the total number of saddle points is to be a constant, and if the flow geometry is to assume the simplest state allowed, then the bifurcation will yield two off-axis nodes going up the p = 3/2 axis together and one on-axis saddle point with negative q. The critical points remain stable nodes until they reach the parabola at (p,q) = (3/2, 9/16). At this point they are again degenerate. If the assumption of axial symmetry were not imposed, it is quite possible that bifurcation might again occur. The imposition of axial symmetry forces the critical points to simply undergo a topological transformation from a stable node into a stable focus. From this point on, the stable focus will increase in q with no further topological change. We can calculate the ultimate p,q value of the single on-axis saddle point by examining the dipole boundary condition. One can calculate a, b, c, d with the following equations:

$$a = \frac{\partial}{\partial \xi}\left[\frac{d\xi}{d\tau}\right]\Bigg|_{\substack{\xi=\xi_c \\ \theta=\theta_c}} \tag{53}$$

$$b = \frac{\partial}{\partial \theta}\left[\frac{d\xi}{d\tau}\right]\Bigg|_{\substack{\xi=\xi_c \\ \theta=\theta_c}} \tag{54}$$

$$c = \frac{\partial}{\partial \xi}\left[\frac{d\theta}{d\tau}\right]\Bigg|_{\substack{\xi=\xi_c \\ \theta=\theta_c}} \tag{55}$$

$$d = \frac{\partial}{\partial \theta}\left[\frac{d\theta}{d\tau}\right]\Bigg|_{\substack{\xi=\xi_c \\ \theta=\theta_c}} \tag{56}$$

If one takes the dipole boundary condition of (24) and then through (14), (15), (20), (21), (53), (56), (43), (44), one can calculate a boundary condition value of (p,q) = (1/4, -1/2). This (p,q) value is on the on-axis saddle point trajectory and defines that critical point's ultimate location. The deductive analysis can be verified by taking the stream function of equ. (28) and performing the same analysis used for the dipole boundary condition. The equation for the value of p is:

$$p = \frac{1}{2}\left[\frac{(1-e^{-\xi^2/2})-(3\xi^2+2\xi^4)e^{-\xi^2/2}+(1-\mathrm{erf}(\frac{\xi}{\sqrt{2}}))\,(2\xi^5+5\xi^3)\sqrt{\frac{\pi}{2}}}{2(1-e^{-\xi^2/2})+(4\xi^2+\xi^4)e^{-\xi^2/2}-(1-\mathrm{erf}(\frac{\xi}{\sqrt{2}}))\,(\xi^5+5\xi^3)\sqrt{\frac{\pi}{2}}}\right]+\frac{3}{2} \tag{57}$$

This equation is useful primarily for the on-axis critical points. For the off-axis points, the result of $\xi = \hat{\xi}_c$ causes the bracket term of (57) to go to zero, leaving p = 3/2. For the on-axis points one calculates ξ for a given Re via equ. (36) with $\theta = 0$. With ξ one can calculate p from (57) and q from (52). For $\xi \to \infty$, a (p,q) value of (7/4, -1/2) is found, which is consistent with the dipole solution. For $\xi \to 0$, the (p,q) of (5/4, 1/4) is found, which is a surprising result. For a critical point to be located at $\xi = 0$, the Reynolds number must be equal to zero (stagnant flow). A stagnant flow normally has a value of (p,q) = (1, 1/4). This paradoxical result is not only obtained for the spherical vortex (m = 3/2) but also for the

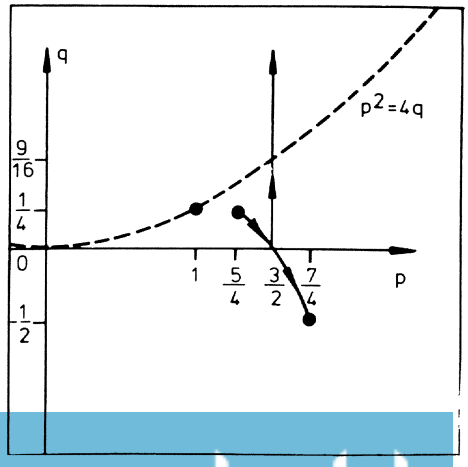

Fig. 4

State space with creeping spherical vortex trajectory.

ramp jet (m = 1) and round jet (m = 0). (It does not occur for the vortex ring (m = -1), for which (p,q) does go to (1, 1/4)). A possible explanation for this observation is that at Re = 0 the spherical vortex, round jet, and ramp jet are being started impulsively. This starting transient that occurs in zero time is manifested by a jump from (1, 1/4) to (5/4, 1/4). The vortex ring (m = -1) goes to zero Reynolds number after infinite time, which is why it ends with a truly stagnant flow. Fig. 4 is drawn from Fig. 3, showing the corresponding trajectory for the spherical vortex creeping-flow solution.

An aspect that remains to be explored is the condition at which the off-axis critical point changes from a stable node into a stable focus. This occurs at the point of degeneracy (p,q) = (3/2, 9/16). Since it is always true that p = 3/2 for the off-axis critical points, we must derive the q-equation using equations (53) - (56) and (44). This equation is greatly simplified when ξ is replaced by the numerical value of $\hat{\xi}_c$, giving

$$q = 2.7002 \times 10^{-3} Re^4 - 0.113915 \tag{58}$$

The transition occurs at q = 9/16, so we may compute the transition Reynolds number from (58):

$$Re_2 = 3.59014 \tag{59}$$

The angular position of the critical point at this transition Reynolds number is

$$\theta_c = 59.7\ ^\circ \tag{60}$$

We can now see that, based on this theory, Hill's spherical vortex has three possible topological states (not including the degenerate states).

State one: $0 < Re < 2.58857$
The topological structure contains one on-axis stable node.

State two: $2.58857 < Re < 3.59014$
The topological structure contains one on-axis saddle point and two off-axis stable nodes.

State three: $3.59014 < Re$
The topological structure contains one on-axis saddle point and two off-axis stable foci.

Since Reynolds number is increasing as $t^{3/4}$, it would be very difficult to see states one and two in an experiment. They would pass by quickly and would probably be masked by starting transients not modelled by the theory. In another flow, that of the round jet (m = 0), the Reynolds number is

not a function of time. In this flow, the three states can be fully developed. Examples of these states from a Navier-Stokes solution are shown in Figs. 5, 6, 7. In these three flows that are presented in physical space, the momentum source is marked by a cross and the critical points by asterisks. The two time lines depicted were initially straight and could be thought of as marking a line of particles in their initial rest positions. The state one flow will never exhibit the sharp corners in the time lines that occur in the state two flow. The state one and state two flows will never roll up like the state three flow. Because the round jet solution is autonomous, (i.e. Reynolds number does not change with time), the p,q theory just described works quite well. However, for nonautonomous flows such as the spherical vortex, the time dependence of the Reynolds number causes

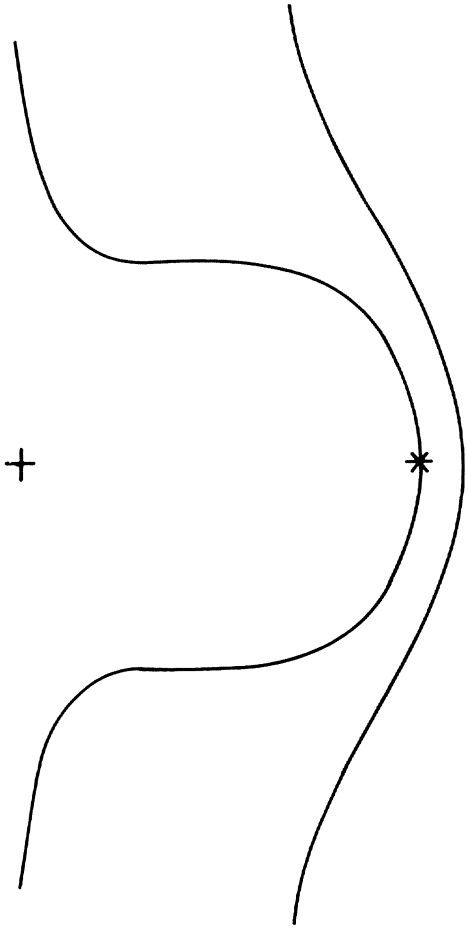

Fig. 5

State one for the round jet (Re = 4).

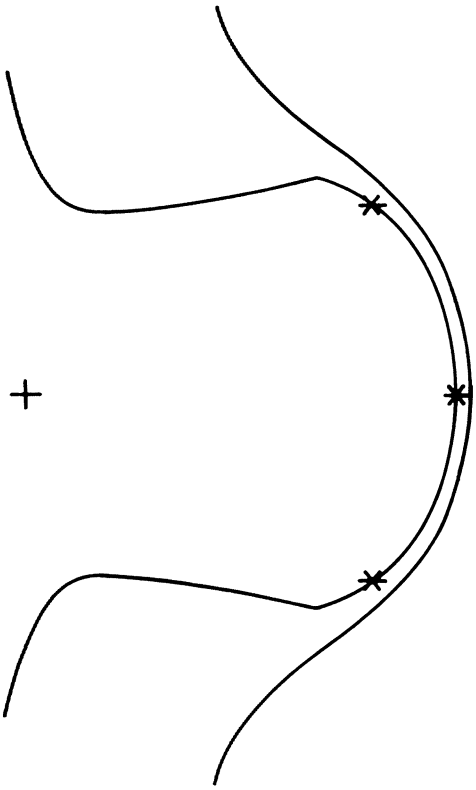

Fig. 6

State two for the round jet (Re = 6).

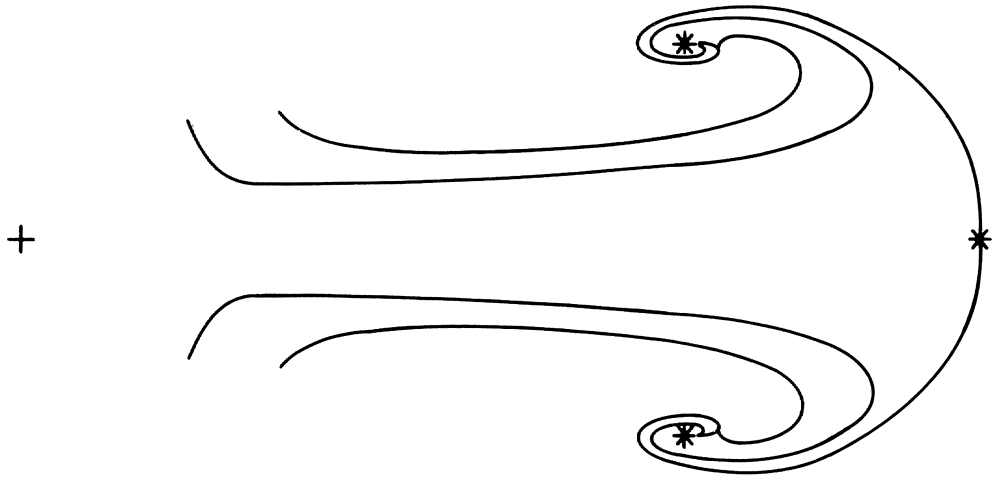

Fig. 7 State three for the round jet (Re = 30).

some difficulties. It has been found that the state three flow does not begin rolling up in physical space until a Reynolds number greater than Re_2 has been reached. This is due to the time dependence of a, b, c, d. A possible interpretation of Re_2 for the nonautonomous flow is that it represents transition in the instantaneous particle paths in self similar space. Since in nonautonomous problems the particle path slopes are constantly changing with time, transition in this space need not mean transition in physical space. In autonomous flows such as the round jet, the particle paths in self similar space do not change with time and are therefore not subject to this difficulty.

CONCLUSIONS

A theory was developed for calculating analytically the flow fields of viscous unsteady jets at low Reynolds number. This theory was applied to Hill's spherical vortex describing an analytic solution for both the vorticity and stream function in the unbounded fluid. It was found that the classical Navier-Stokes solution is only a midfield component of the complete Stokes solution and that vorticity is continuous in the complete solution. The particle path equations were calculated, from which it was found that Hill's spherical vortex has critical points. These critical points arrange themselves into one of three topological states depending on Reynolds number. The transformation from one topological state to

another is regarded as a form of transition. The two Reynolds numbers associated with this transition were calculated.

ACKNOWLEDGEMENT

The author would like to express his thanks to Professor BRIAN CANTWELL for his assistance in developing this theory.

REFERENCES

[1] G.A. ALLEN, B.J. CANTWELL: Transition and Mixing in Axisymmetric Jets and Vortex Rings. Ph. D. Thesis, Stanford University, Department of Aeronautics and Astronautics Report, SUDAAR541, May 1984; NASA Contractors Report (to be published also).

[2] G.K. BATCHELOR: An Introduction to Fluid Dynamics. Cambridge University Press, p.526, (1967).

[3] B.J. CANTWELL: Transition in the Axisymmetric Jet. J. Fluid Mech., 104, 369-386 (1980).

[4] B.J. CANTWELL, G.A. ALLEN: Entrainment Diagrams for Viscous Flows. Proceedings Third Symposium on Turbulent Shear FLows, 17.12-17.18 (1981).

[5] B.J. CANTWELL, G.A. ALLEN: Transition and Mixing in Axisymmetric Jets and Vortex Rings. Proceedings IUTAM Symposium on Turbulence and Chaotic Phenomena in Fluids, 80-89 (1983).

[6] M.J.M. HILL: On a Spherical Vortex. Phil Trans. A, clxxxv (1894)

[7] H. LAMB: Hydrodynamics. Dover Publications, 245-246 (1932).

[8] L. LANDAU: A New Exact Solution of Navier-Stokes Equations. C.R. Acad. Sci. Dok. 43, 286-288 (1944).

[9] A.E. PERRY, B.D. FAIRLIE: Critical Points in Flow Patterns. Adv. Geophysics, 18, 299-315 (1974).

[10] C. SOZOU: Development of the Flow Field of a Point Force in an Infinite Fluid. J. Fluid Mech., 91, 541-546 (1979).

[11] H.B. SQUIRE: The Round Laminar Jet. Quart. J. Mech. Appl. Math. 4, 321-329 (1951).

TRANSITION AND TURBULENCE

THREE-DIMENSIONAL PROCESSES IN LAMINAR-TURBULENT TRANSITION

L. KLEISER

1. INTRODUCTION

The transition of a laminar flow into a turbulent state is a classical problem of fluid mechanics that has been investigated for more than a hundred years. Numerous types of flows have been considered, and a great variety of phenomena and of factors affecting transition have been discovered. Despite the enormous progress achieved, transition to turbulence remains a challenge for many disciplines from mathematics to practical engineering design. Many technologically important properties of flows, such as drag or heat and mass transfer, change drastically during transition. There is therefore an urgent need for improved knowledge, prediction, and possible control of transition. In addition to this practical aspect, there has always been a fundamental interest in the transition phenomenon as a clue to understanding the origin of turbulence. Generally, transition to turbulence occurs via a sequence of increasingly complex but still laminar intermediate stages. These are usually connected with flow instabilities. Flow patterns generated during transition often remain visible far into the turbulent region. The past ten years have seen an explosive growth in a novel direction of research in this field, namely the investigation of low-dimensional dynamical systems and their possible relation to transition and turbulence (OTT [52], ECKMANN [12], TATSUMI [61]).

In order to clarify the basic mechanisms of the transition process and to isolate the influencing factors, one studies purified model flows (HERBERT & MORKOVIN [29]), which are more amenable to theoretical analysis. One such prototype for a class of wall-bounded shear flows is the plane Poiseuille flow, which develops in a parallel plate channel under a constant pressure gradient. The transition process in plane Poiseuille flow will be considered in the present contribution, though occasionally we will comment on the Blasius boundary layer case, where quite similar phenomena can be observed.

During the last five years important progress has been made in understanding the three-dimensional stages of the transition process. This has been achieved through the combined results of experiments, numerical simulation, and stability analysis. The present paper surveys some of these developments and presents results of our own work on the simulation of transition.

The paper is organized as follows. Section 2 introduces the basic definitions and summarizes the present knowledge of plane Poiseuille flow transition. In section 3, the mathematical model and the numerical discretization used in our simulations are discussed. Section 4 studies the two-dimensional finite amplitude waves underlying the transition process. In section 5, three-dimensional transition mechanisms and spatial flow structures are discussed. Section 6 presents remarks on chaotic solutions appearing after the breakdown of regular oscillations, and section 7 concludes the paper.

2. TRANSITION IN PLANE POISEUILLE FLOW

Transition in plane Poiseuille and boundary layer flow has been treated in several review papers, so we will here restrict ourselves to a survey of the main aspects. We mention the works by TANI [60], MORKOVIN [41], and HERBERT & MORKOVIN [29]. Of particular relevance here is the article by HERBERT [22] which reviews the state of the art up to 1981. A very recent and complete account of transition in boundary layers has been given by ARNAL [2] in the AGARD Report 709 [1], while HERBERT [27,28] reviews the latest theoretical progress. See also the proceedings volumes EPPLER & FASEL [13] and [54].

2.1 Problem definition and notation

We consider the transition process in a channel flow driven by a constant pressure gradient (Fig. 1). We use non-dimensional variables based on

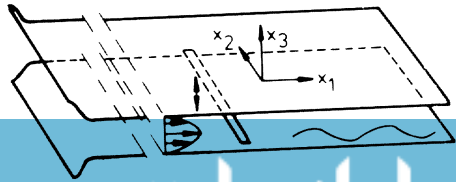

Fig. 1

Experimental setup for investigation of transition (schematic).

channel half-width $\tilde{h}$ and undisturbed laminar centerline velocity $\tilde{U}_{max}$. $\tilde{\nu}$ is the kinematic viscosity of the fluid. The following notation is introduced:

$Re = \tilde{h}\tilde{U}_{max}/\tilde{\nu}$	Reynolds number
$U(x_3) = 1-x_3^2$	basic plane Poiseuille flow velocity
$\underline{u}(\underline{x},t)$	disturbance velocity
$\bar{u}_1$	streamwise mean disturbance
$u_1'' = u_1-\bar{u}_1$	streamwise fluctuation
$u_1' = (\overline{u_1''^2})^{1/2}$	streamwise rms fluctuation
$u_1'_{max} = \max_{x_3} u_1'$	maximum of u_1'
$L_1 = 2\pi/\alpha_1$	streamwise (Tollmien-Schlichting) wavelength
$L_2 = 2\pi/\alpha_2$	spanwise wavelength.

Note that the disturbance $\underline{u}$ is defined as the deviation of the instantaneous total velocity from the laminar basic flow and thus has a nonzero mean $\bar{\underline{u}}$. We study the spatial and temporal evolution of $\underline{u}$ when the mean pressure gradient is kept fixed at its laminar value -2/Re.

For the theoretical analysis of transition, plane Poiseuille flow presents several advantages over the boundary layer. First, the basic flow is strictly parallel and an exact solution of the Navier-Stokes equations for all Reynolds numbers and transition can be studied at a fixed Re. Second, the finite extent of the flow in the normal direction facilitates the numerical analysis of linear and nonlinear stability problems. Third, there exists a strictly periodic two-dimensional secondary flow as an asymptotic state of finite-amplitude waves (see below). Nowadays also a substantial body of experimental information on the transition process in this flow is available (FELISS et al. [15], NISHIOKA et al. [43-47], KOZLOV & RAMAZANOV [38,39]).

2.2 The transition process

Fig. 2 shows the regions where laminar and turbulent channel flow is observed in the experiment (FELISS et al. [15]) depending on the Reynolds number and the turbulence level at the channel entrance. At very low disturbance levels, laminar flow can be maintained up to the critical Reynolds number Re_{cr} = 5772 (DRAZIN & REID [10]) of linear stability theory.

With large inlet disturbances, turbulence is observed down to a Reynolds number Re_{min} of order 1000 (see HERBERT [22] and KLEISER [33] for a review of experiments). The experimental breakthrough in the investigation of the transition process in plane Poiseuille flow has been achieved by NISHIOKA et al. [43]. These investigations have been extended in a series of papers, NISHIOKA et al. [44-47]. Using the vibrating ribbon technique, these authors observed a sequence of events that is quite similar to boundary layer transition (KLEBANOFF et al. [32], HAMA & NUTANT [20], KOVASZNAY et al. [37], WORTMANN [64], WILLIAMS et al. [63]). Characteristic phenomena observed in subsequent stages are summarized schematically in Fig. 3. *Peak* and *valley* refer to spanwise positions where $u_1'(x_2)$ develops a local maximum and minimum, respectively, during the early stages. In accordance with linear stability theory (DRAZIN & REID [10]), the transition process begins with spatially amplified two-dimensional Tollmien-Schlichting (TS) waves

$$\underline{u}_{TS}(\underline{x},t) = \left\{ \hat{\underline{u}}_{TS}(x_3) \exp\left[i(\alpha x_1 - \omega_{TS} t) \right] \right\}_r \qquad (2.1)$$

where $\{\ \}_r$ denotes the real part of a complex number. Fig. 4 shows a typical set of measured instantaneous inflectional velocity profiles with high-shear layers around $x_3 \approx -0.6$. In flow visualizations, a discrete downstream travelling Λ-(or horse shoe-) vortex structure appears periodically at the frequency ω_{TS} of the Tollmien-Schlichting instability wave (a very illustrative movie on this phenomenon has been produced by Wortmann and Strunz, see WORTMANN [64]). In the meantime, such visualizations have also been made in plane Poiseuille flow (KOZLOV & RAMASANOV [38]).

The transition process described so far is now referred to as *peak-valley splitting* or *K-type* breakdown (after Klebanoff). Here the Λ-vortices appearing periodically in streamwise and spanwise direction form a *regular* pattern where one Λ-vortex follows the other at a distance of one TS wavelength. In recent years, a different type of transition has been detected both in boundary layers (SARIC & THOMAS [56], KACHANOV & LEVCHENKO [30], SARIC et al. [57]) and in plane Poiseuille flow (KOZLOV & RAMASANOV [39]). This type is characterized by a *staggered* Λ-vortex pattern and, accordingly, the appearance of the subharmonic frequency $\omega_{TS}/2$. Moreover, in the boundary layer case two different subharmonic transition modes are known, referred to as C-type and H-type, SARIC & THOMAS [56], SARIC et al. [57]. The C-type is explained by the resonant-triad model of CRAIK [8], while the H-type is described by the secondary instability theory of HERBERT [25,26] (as is the classical K-type, see 2.3 below). Which one of these three different types will appear in a particular experimental situation depends on the TS wave amplitude and the disturbance background. In the boundary layer the C-, H-, and K-types appear typically at wave amplitude ranges $u_1' \approx 0.3\%$, $u_1' \approx 0.3\%$-0.6%, and $u_1' \gtrsim 0.6\ \%$, respectively (SARIC & THOMAS [56]).

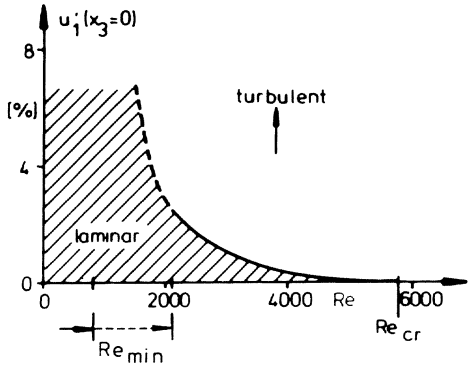

Fig. 2

Regions of laminar and turbulent channel flow, FELISS et al. [15].

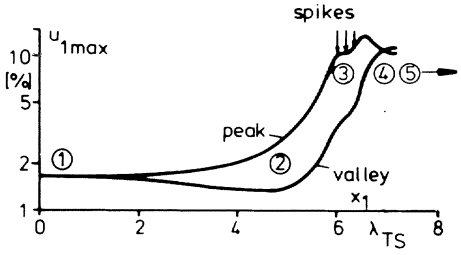

Fig. 3

Development of u'_{1max} and phenomena characterising subsequent stages of laminar-turbulent transition process (K-type)

① 2D Tollmien-Schlichting wave
② 3D distored wave, spanwise peak-valley structure, mean longitudinal vortices, Λ structure
③ spikes, inflection point profiles, high-shear layer
④ turbulent spots
⑤ fully developed turbulence

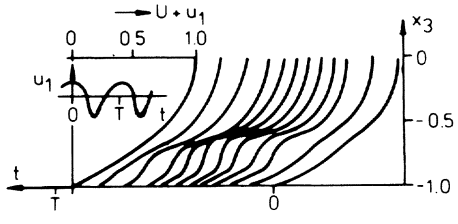

Fig. 4

Instantaneous velocity profiles at peak over one period of oscillation, shortly before the appearance of spikes, NISHIOKA et al. [45].

2.3 Theoretical analysis of transition

Theoretical analysis of transition starts from the Navier-Stokes equations, using the mathematical tools of linear and nonlinear stability theory and of bifurcation theory, DRAZIN & REID [10]. In recent years computer simulations have in addition been contributing substantially to the theoretical understanding of transition, (WRAY & HUSSAINI [65], ORSZAG & KELLS [48], ORSZAG & PATERA [49,50], KLEISER [33,34], KLEISER & SCHUMANN [36]). Here we only sketch the main theoretical results and refer to HERBERT [22,27,28] and ORSZAG & PATERA [50] for details and further references.

Fig. 5 shows the neutral curve of linear stability theory. The nonlinear behavior of finite amplitude disturbances near the neutral curve has been investigated by means of bifurcation theory. In general, bifurcation at Re_{cr} may be either supercritical or subcritical, see Fig. 6. Plane Poiseuille flow bifurcates subcritically. This implies that finite-amplitude equilibrium solutions exist for a certain Reynolds number range $Re_{NL} < Re < Re_{cr}$. Fig. 7 shows the neutral surface of this equilibrium flow in the (Re, α, E') parameter space where E' is the normalized integral energy of the fluctuation (HERBERT [21])

$$E' = \frac{15}{8L_1} \int_0^{L_1} \int_{-1}^{1} \frac{1}{2} (u_1''^2 + u_3''^2) \, dx_1 \, dx_3 \qquad (2.2)$$

The neutral surface in Fig. 7 extends down to a nose point at $Re_{NL} = 2935$, $\alpha = 1.32$. L indicates the neutral curve of Fig. 5, NL the projection of the neutral surface onto the plane E' = 0. The asymptotic behavior of finite amplitude disturbances in time is also indicated in Fig. 6. As the subcritically bifurcating lower branch in Fig. 6b is unstable, 2D finite amplitude disturbances with $Re_{NL} < Re < Re_{cr}$ either decay to zero or, if their amplitude is large enough, are attracted to the upper branch solution (this time evolution will be discussed in section 4).

The equilibrium solution constitutes a two-dimensional periodic secondary flow $A_{PS}u_{PS}$, which is steady in a certain moving frame of reference $x_1' = x_1 - Ct$. This flow, which corresponds to the convection rolls in the Rayleigh-Bénard problem or to the Taylor vortices in the Taylor-Couette problem, has never been observed in an experiment. Instead, the three-dimensional transition process described above sets in once the wave amplitude exceeds a certain threshold. In 1979 BLACKWELDER [4] and HERBERT & MORKOVIN [29] suggested considering the three-dimensional development as the manifestation of a secondary instability and the later appearance of the high-frequency spikes as the result of a tertiary instability of the localized high-shear layers, which arise from the three-dimensional motion. The work of ORSZAG & PATERA [49,50] and of HERBERT [22-27] has

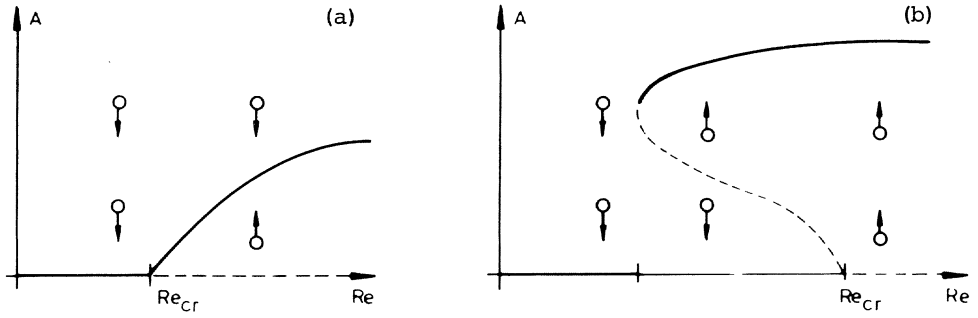

Fig. 6 Schematic representation of (a) supercritical and (b) subcritical bifurcation of basic flow at Re_{cr}. Arrows indicate time behavior of disturbance of initial amplitude A.

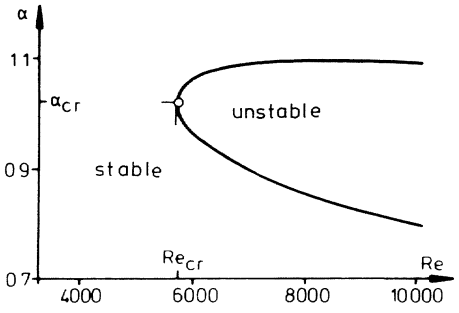

Fig. 5

Neutral curve of linear stability theory for plane Poiseuille flow (HERBERT [21]).

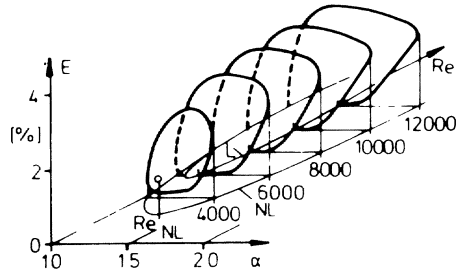

Fig. 7

Neutral surface of 2D periodic secondary flow (HERBERT [21]).

$\underline{U} = (1 - x_3^2, 0, 0)$	LAMINAR BASIC FLOW	
$\underline{U} + \varepsilon \underline{u}_{TS}$	1st INSTABILITY, TSW	
$\underline{U} + A_{2D}\underline{u}_{2D}$	QUASISTEADY 2D FINITE AMPLITUDE WAVE	①
$\underline{U} + A_{PS}\underline{u}_{PS}$	ASYMPTOTIC 2D PERIODIC SECONDARY FLOW	-
$(\underline{U} + A_{2D}\underline{u}_{2D}) + \varepsilon \underline{u}_{3D}$	SECONDARY INSTABILITY	
$\underline{U} + A_{2D}\underline{u}_{2D} + A_{3D}\underline{u}_{3D}$	3D TRANSITION PROCESS	②
⋮	TERTIARY HF INSTABILITY?	③ ④
TURBULENT CHANNEL FLOW		⑤

Fig. 8 Instabilities in plane Poiseuille flow transition. ① - ⑤ associated phenomena according to fig. 3.

confirmed the secondary instability hypothesis. The issue of the tertiary instability is not yet clarified. It will be discussed in 5.3 below. The whole sequence of instabilities is summarized in Fig. 8. The secondary instability is a linear instability of a new basic flow $\underline{U}+\underline{v}_{2D}$, which is steady and periodic in x_1', against small three-dimensional disturbances that are periodic in x_1' and x_2. $\underline{v}_{2D}$ may be the periodic secondary flow $A_{PS}\,\underline{u}_{PS}$ or, as an approximation, a two-dimensional Orr-Sommerfeld eigensolution multiplied by a finite amplitude A_{2D}.

The growth rates of secondary instability are much larger than those of the primary viscous instability. For a given Reynolds number and streamwise wavenumber, they depend on the 2-D disturbance amplitude (A_{PS} or A_{2D}) and the spanwise wavenumber. The physical nature of the secondary instability has been discussed in ORSZAG & PATERA [50]. The instability is considered to be an essentially inviscid type and is caused by the combined effects of vortex stretching and tilting. An investigation of the energy balance shows that the energy is transferred directly from the mean flow to the three-dimensional disturbance, while the two-dimensional wave only mediates (but does not contribute to) the energy transfer.

The secondary instability mechanism is active not only in the two-dimensional equilibrium state of plane Poiseuille flow but already in the time-dependent intermediate state that is slowly evolving towards it. This has been found by numerical simulations (see below) and explains why the equilibrium flow cannot be observed. The secondary instability analysis of HERBERT [23-27] has also been able to explain the subharmonic route of transition (H-type) in both plane Poiseuille flow and boundary layers. Considering its potential for future extensions (e.g. to non-parallel boundary layers with pressure gradients) and applications (e.g. to transition prediction) secondary instability theory constitutes a significant advance in theoretical transition research.

Secondary instability theory successfully describes the onset of the three-dimensional development. It is, however, restricted to small 3D disturbance amplitudes and to cases where the growth rate of the 2D wave is small compared to the 3D growth rate. A theoretical analysis of the highly nonlinear 3D stages of transition arising from secondary instability is very difficult. Numerical simulation seems to be the only means by which results have been obtained outside the laboratory. In 1980 WRAY & HUSSAINI [65] presented a simulation of boundary layer transition and demonstrated excellent agreement of the computed flow fields with measurements of KOVASZNAY et al. [37]. ORSZAG et al. [48-50] have made extensive contributions to the simulation of transition in plane Poiseuille, boundary layer, plane Couette, and pipe flow. More recently BIRINGEN [3] investigated the final stages of transition in plane Poiseuille flow at Re = 1500. In our own earlier work (KLEISER [33,34], KLEISER & SCHUMANN [36]), we have made extensive comparisons with experiments of NISHIOKA et al.

[43-45] and found very satisfactory agreement up to the 1-spike stage. In addition, we have investigated the formation of spatial flow structures and the transition mechanisms in the nonlinear 3D stages. Some of these results are reviewed and extended in section 5.

3. NUMERICAL SIMULATION MODEL

We discuss the mathematical model and the numerical discretization used in our transition simulations. We describe only the main features and refer to KLEISER [33] and KLEISER & SCHUMANN [36] for details.

3.1 Mathematical model

The three-dimensional time-dependent incompressible Navier-Stokes equations are solved in the spatial domain $0 \le x_j \le L_j$ $(j = 1,2)$, $|x_3| \le 1$ (Fig. 9). No-slip conditions are applied at the walls $x_3 = \pm 1$ and periodic boundary conditions in the horizontal directions x_1, x_2. While the assumption of periodicity is natural for the spanwise direction, it requires some explanation for the streamwise direction. The main advantages of the periodic boundary conditions are that they allow the use of Fourier expansions, which lead to a highly accurate and efficient spatial discretization, and that they allow the available numerical resolution to be concentrated in one TS wavelength. Although inflow/outflow boundary conditions can also be treated with spectral methods (PATERA [53]), they lead to a more complicated numerical algorithm and require a considerably larger integration domain. In a vibrating-ribbon experiment a time- periodic TS wave develops downstream. If observed in a frame of reference moving with the phase velocity c_{TS} the wave also experiences temporal growth or decay. So in our simulations we model this situation by downstream-periodic disturbances that develop in time in a reference frame $x_1' = x_1 - c_{TS}t$. According to this model, downstream coordinate and time are

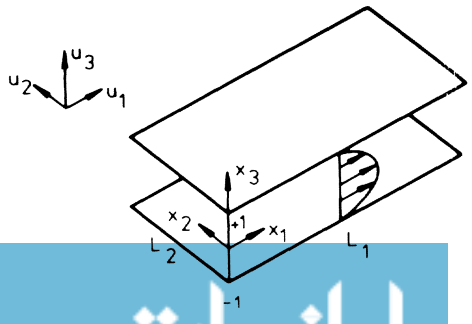

Fig. 9

Integration domain and coordinates.

interchanged to compare numerical and experimental results. It is not known a priori how well this model can describe experimentally observed transition phenomena. Detailed comparisons of simulation results with experiments have in fact demonstrated very close similarity for both boundary layer (WRAY & HUSSAINI [65]) and plane Poiseuille flows (KLEISER [33,34], KLEISER & SCHUMANN [36]).

3.2 Numerical discretization

The spatial discretization is based on a spectral method using Fourier expansions in the horizontal directions,

$$\underline{u}(\underline{x},t) = \sum_{k_1} \sum_{k_2} \hat{\underline{u}}(k_1,k_2,x_3,t)\exp(ik_1\alpha_1 x_1 + ik_2\alpha_2 x_2) \tag{3.1}$$

($\alpha_j = 2\pi/L_j$) and Chebyshev polynomial expansions in the normal coordinate,

$$\hat{\underline{u}}(k_1,k_2,x_3,t) = \sum_{k_3=0}^{N_3} \hat{\underline{u}}(k_1,k_2,k_3,t)T_{k_3}(x_3). \tag{3.2}$$

The sum in (3.1) extends over the domain

$$K = \{(k_1,k_2) : |k_j|<N_j/2, |k_1|/N_1 + |k_2|/N_2 < 2/3\} \tag{3.3}$$

illustrated by Fig. 10. For later reference we define the maximum amplitude of a Fourier mode (referred to as Fourier amplitude)

$$\hat{u}_{jmax}(k_1,k_2) = f(k_1,k_2)\cdot\max_{x_3}|\hat{u}_j(k_1,k_2,x_3)| \tag{3.4}$$

with the normalization

$$f(0,0) = 1, \quad f = 4 \quad \text{if} \quad k_1\cdot k_2 \neq 0, \quad f = 2 \text{ otherwise}. \tag{3.5}$$

Spectral methods (GOTTLIEB & ORSZAG [18], VOIGT et al. [62]) have several advantages over more conventional finite difference or finite element methods. First of all, if used properly they have exponential instead of algebraic convergence rates. Spectral methods do not suffer from numerical damping, as derivatives are obtained by differencing the expansion functions analytically. These properties make them well suited for the investigation of hydrodynamic instability and transition problems.

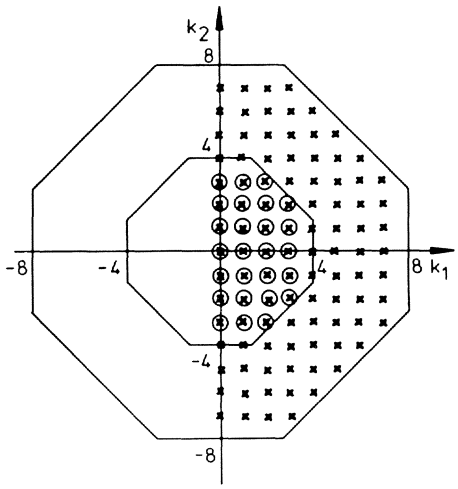

Fig. 10

Wavenumber range K, eq.(3.3), of the Fourier expansion (3.1) for simulations with $N_1 = N_2 = 8$ (o) and $N_1 = N_2 = 16$ (x) grid points.

For time integration we use finite difference methods of second order. Viscous terms are treated implicitly with the Crank-Nicolson method, and nonlinear terms explicitly with the Adams-Bashforth method. As usual, the nonlinear terms are calculated by the pseudospectral approximation, GOTTLIEB & ORSZAG [18]. Errors arising in the Fourier coefficients are reduced by truncating the expansion (3.1) according to (3.3).

The pressure is calculated from a Poisson equation with correct boundary conditions obtained from the condition of vanishing divergence at the boundary, using an influence matrix technique, KLEISER & SCHUMANN [35,36]. The continuity equation and boundary conditions are satisfied exactly by the discretized equations. The solution is obtained by solving sequentially a set of Helmholtz equations. Alternatives to this approach are discussed in ORSZAG & KELLS [48], ORSZAG & PATERA [49], MOSER et al. [42], GOTTLIEB et al. [17], DEVILLE et al. [9], and KESSLER [31]. The numerical algorithm has been implemented in the computer code CHANSON. The code has been checked thoroughly using, for instance, Orr-Sommerfeld eigensolutions, the periodic secondary flow, and a Stokes problem (DEVILLE et al. [9]) as test problems for which analytical or very accurate numerical reference solutions are available.

4. TWO-DIMENSIONAL FINITE AMPLITUDE WAVES

In this section we consider the nonlinear development of two-dimensional Tollmien-Schlichting waves, the understanding of which is important for two reasons. First, the disturbances observed in the initial stage of

transition are approximately two-dimensional over a certain spanwise extent. Second, as we know from secondary instability theory, two-dimensional waves are a necessary prerequisite for the later three-dimensional stages.

The nonlinear time development of downstream-periodic waves in plane Poiseuille flow has been investigated by STUART [59], GEORGE et al. [16], ZAHN et al. [66], and more recently by ORSZAG & PATERA [49,50]. Critical reviews, including older works, have been given by HERBERT [21,22]. FASEL et al. [14] consider the spatially amplified case.

Essential effects of nonlinearity are the production of higher harmonics and of non-negligible Reynolds stress, which in turn lead to a distortion of the fundamental oscillation and of the mean flow. The amplitude growth is limited by nonlinear saturation. The equation for the mean flow $U+\bar{u}_1$ reads

$$\partial_t(U+\bar{u}_1) = 2/Re+\partial_3(\tau_N+\tau_R) \tag{4.1}$$

where

$$\tau_N = \partial_3(U+\bar{u}_1)/Re \tag{4.2}$$

is the Newtonian shear stress and

$$\tau_R = \overline{-u_1" u_3"} \tag{4.3}$$

the Reynolds stress. By definition of U the mean deformation $\bar{u}_1$ obeys

$$\partial_t\bar{u}_1 = \partial_3^2\bar{u}_1/Re+\partial_3\tau_R \ . \tag{4.4}$$

The distortion of the mean flow modifies the energy flux from the mean flow to the fluctuation. The fluctuation energy E', eq. (2.2), evolves according to

$$\partial_t E' = P'-D' \tag{4.5}$$

where production P' and dissipation D' are defined as

$$P' = \frac{15}{8}\int_{-1}^{1} \tau_R\partial_3(U+\bar{u}_1)dx_3 \tag{4.6}$$

$$D' = \frac{15}{8}\frac{1}{Re}\int_{-1}^{1} \overline{(\partial_3 u_1"-\partial_1 u_3")^2}\,dx_3 \ . \tag{4.7}$$

If P' < D' the disturbance decays. If P' > D' > 0, it will increase and possibly settle to an equilibrium state with P' = D'. Such a state corresponds to a point on the neutral surface (Fig. 7).

We illustrate the time-dependent behavior of two-dimensional waves by simulation results (KLEISER [33]) for a typical subcritical case, Re = 3500 and $\alpha = \alpha_1 = 1.3$, near the nose of the neutral surface. The initial velocity field consists of a linear eigensolution multiplied by a finite amplitude, $\underline{u}^o = A_{TS}\underline{u}_{TS}$ (normalized by $\max|u_{1,TS}| = 1$). The oscillation period is $T_{TS} = 15.26$. Fig. 11 shows the results for a set of calculations with different initial amplitudes A_{TS}. After an initial transient on a convective time scale (2 - 3 T_{TS}), the solution arrives at a quasisteady state. The lower branch threshold of the periodic secondary flow is well reproduced (data of periodic secondary flow by TH. HERBERT, private communication). Fig. 12a shows the development of the fundamental and two harmonics on an extended time interval for the case $A_{TS} = 10$ %. The harmonics are one order of magnitude smaller than the fundamental, the energy of which amounts to 99.7 % of E' as $t \to \infty$. Energy production and dissipation are given in Fig. 12b. Production exceeds dissipation by a nearly constant factor of 1.3 in the interval considered. The disturbance grows beyond the equilibrium amplitude, decreasing to this value only on a viscous time scale t = O(Re), ORSZAG & PATERA [49]. The development of the shear stresses is shown in Fig. 13. The relation

$$\tau_N + \tau_R = -2x_3/Re \tag{4.8}$$

for the stationary case that follows from integration of (4.1) is also included in this figure. For the initial Orr-Sommerfeld solution, τ_R changes sign and the production integral (4.6) is negative. At t > 0, τ_N and τ_R are rapidly redistributed and approach their asymptotic shape with P' > 0. The slow evolution after the initial transient on a viscous time scale, in particular in the interior of the flow field, becomes plausible from equations of the type (4.1) or (4.4) where the right-hand sides are of order 1/Re. Additional arguments are given in ORSZAG & PATERA [50] implying that in the area away from the boundaries, vorticity is approximately convected along streamlines.

As mentioned before, the periodic secondary flow is violently unstable against three-dimensional disturbances. This secondary instability is demonstrated in Fig. 14 by numerical simulation results in which small random three-dimensional disturbances have been superimposed on the two-dimensional equilibrium flow (the calculation was done in a frame of reference moving downstream with c = 0.5). While the two-dimensional Fourier modes are initially unaffected, the three-dimensional modes grow rapidly and at t ≈ 50 the strictly periodic motion breaks down into irregular fluctuations. With purely two-dimensional disturbances no such breakdown is observed. In the next section we demonstrate the crucial role

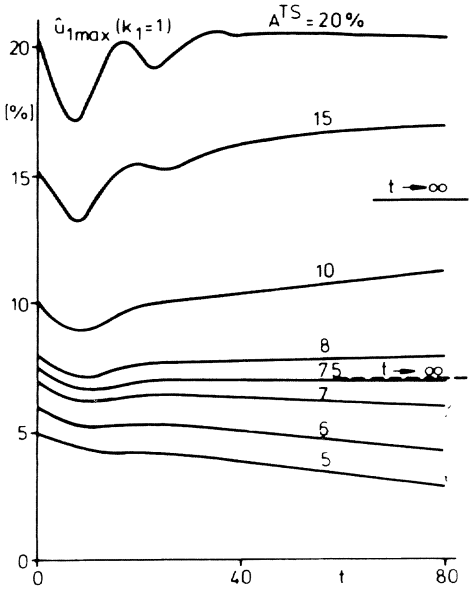

Fig. 11

Nonlinear evolution of fundamental oscillation amplitude for different initial amplitudes A_{TS}. $t \to \infty$ denotes the values for periodic secondary flow.

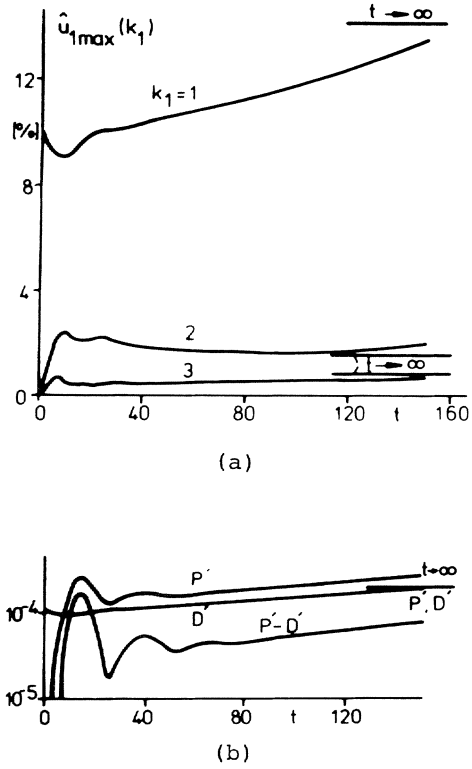

Fig. 12

(a) Development of higher harmonics
(b) Production P' and dissipation D' of fluctuation energy.

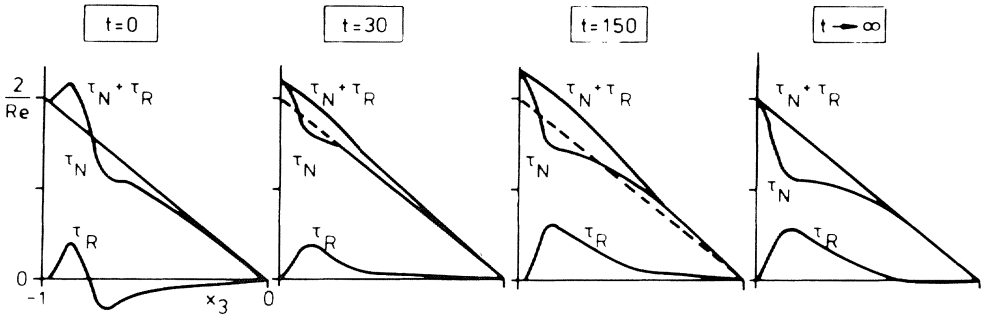

Fig. 13 Viscous shear stress τ_N and Reynolds stress τ_R.

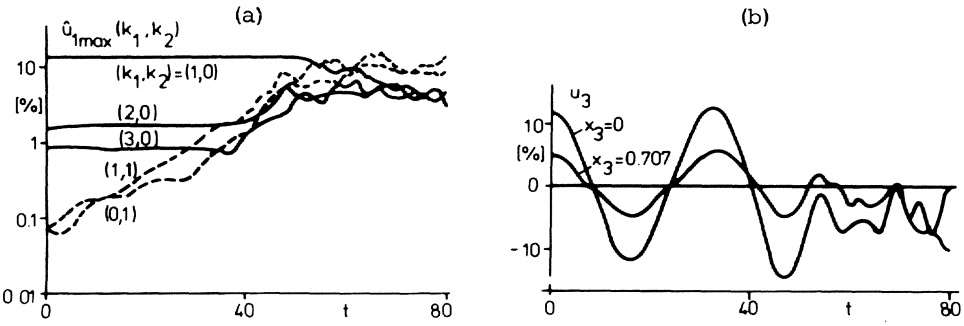

Fig. 14 Instability of periodic secondary flow against small 3D disturbances.
(a) development of 2D —— and 3D --- Fourier amplitudes
(b) normal velocity signal.

of the secondary instability of the quasiequilibria in the transition process.

5. THREE-DIMENSIONAL SIMULATION OF TRANSITION

We now discuss results of three-dimensional transition simulations. As demonstrated in the preceding section, the flow evolution may change drastically if three-dimensional disturbances are introduced. The physical parameters of the simulations to be discussed are adjusted to the experimental conditions of NISHIOKA et al. [45], Re = 5000, $\alpha_1 = 1.12$ and $\alpha_2 = 2.1$. The oscillation period is $T_{TS} \approx 20$ and the phase velocity $c_{TS} \approx 0.28$. In accordance with the experiments, the evolution of a TS wave with superimposed small 3D disturbances is considered. The initial disturbance

$$\underline{u}^0 = A_{TS}\,\underline{u}_{TS} + \varepsilon \underline{u}_{3D} \tag{5.1}$$

consists of a 2D wave with maximum amplitude A_{TS} and a pair of oblique waves with spanwise wavenumbers $\pm\alpha_2$ and amplitude $\varepsilon = 0.1\,\%$. The amplitude distribution $u_1^0(x_3)$ is antisymmetric. The numerical resolution is $N_1 \times N_2 \times N_3 = 8 \times 8 \times 40$, $\Delta t = 0.2$ during the initial stages and is increased to $N_1 \times N_2 \times N_3 = 32 \times 32 \times 40$, $\Delta t = 0.03$ in the late stages of transition considered here.

5.1 Threshold characteristics

First we survey the time evolution of the flow as a function of the initial wave amplitude A_{TS}. Fig. 15a shows the development of the maximum rms fluctuation at a spanwise peak position ($x_2 = 0$). We see the threshold

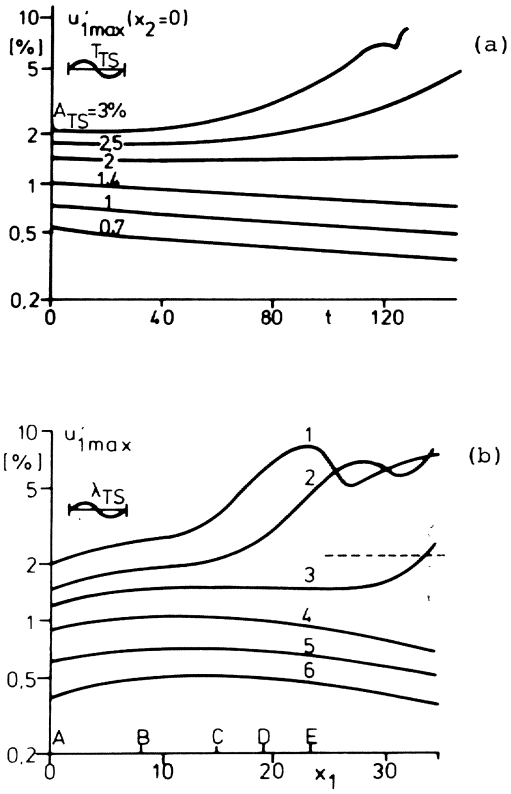

Fig. 15

Development of maximum fluctuation for different initial amplitudes.
(a) numerical simulation
(b) experiment, NISHIOKA et al. [43].

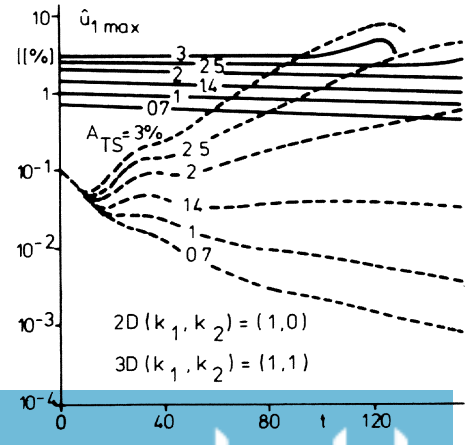

Fig. 16

Development of initially excited Fourier modes in numerical simulations with different initial amplitudes A_{TS}.
—— 2D modes, --- 3D modes.

behavior typical for subcritical transition. At amplitudes below the threshold of $u_1'_{max} \approx 1.5$ %, the disturbances die out and the flow remains laminar. At higher amplitudes transition occurs. The case $A_{TS} = 3$ % has been investigated in detail (KLEISER [33,34], KLEISER & SCHUMANN [36]). Typical transition phenomena of K-breakdown summarized in Fig. 3 have been verified in this simulation. A remarkable agreement with hot-wire measurements (NISHIOKA et al. [44,45]) of mean velocity, rms fluctuation and instantaneous velocity distributions has been found up to the 1-spike stage which occurs at $t \approx 122$. With the present spatial resolution, the simulation is not able to describe the subsequent multi-spike stages accurately. Nevertheless, a similar behavior and a breakdown to a chaotic state not unlike turbulence is obtained if the simulation is continued (see sect. 6).

In Fig. 15b, the corresponding experimental results (NISHIOKA et al. [43]) are shown. Threshold value and time/space scale of development up to the spike stage (station E) are essentially in agreement, $4\ T_{TS}$ in the simulation (not counting the initial transient phase $t \lesssim 40$) and $4\ \lambda_{TS}$ in the experiment).

The development of the initally excited 2D and 3D Fourier modes is shown in Fig. 16. We recognize the threshold character of the secondary instability. The 2D wave amplitude controls the growth of the 3D mode. After the initial transient the growth rates are nearly constant up to some time before breakdown. The growth rate for $A_{TS} = 3$ % has been compared with the result of the linear secondary instability theory and agrees well (HERBERT [22]). In the following we consider the case of $A_{TS} = 3$ %. The development of the higher harmonics will be discussed in 5.3.

5.2 Spatial flow patterns

The growth of the 3D Fourier modes is connected with the evolution of increasingly complicated flow patterns. First we turn to the mean flow. Fig. 17 illustrates the development of the mean secondary flow $(\bar{u}_2, \bar{u}_3)$ in terms of the streamfunction $\bar{\psi}$ (due to an error in calculating $\bar{\psi}$, the streamlines depicted in Fig. 5.23 of KLEISER [33] and in Fig. 6 of KLEISER & SCHUMANN [36] are slightly incorrect). It consists of a system of counterrotating longitudinal vortices, with a second set of vortices appearing at later stages. The whole development is in remarkable agreement with the measurements of KLEBANOFF et al. [32] (Fig. 19) in boundary layer transition. Though the secondary flow is quite weak (about 1 % and 2 % at $t = 110$ and $t = 122$, respectively), it has a considerable effect on the mean profile $U+\bar{u}_1$. Alternating upward movement of low-speed near-wall fluid and downward transport of high-speed fluid induces characteristic spanwise variations as illustrated by Fig. 18. Again the agreement with the experiment is good. In the spanwise region between *peak* and *valley* the

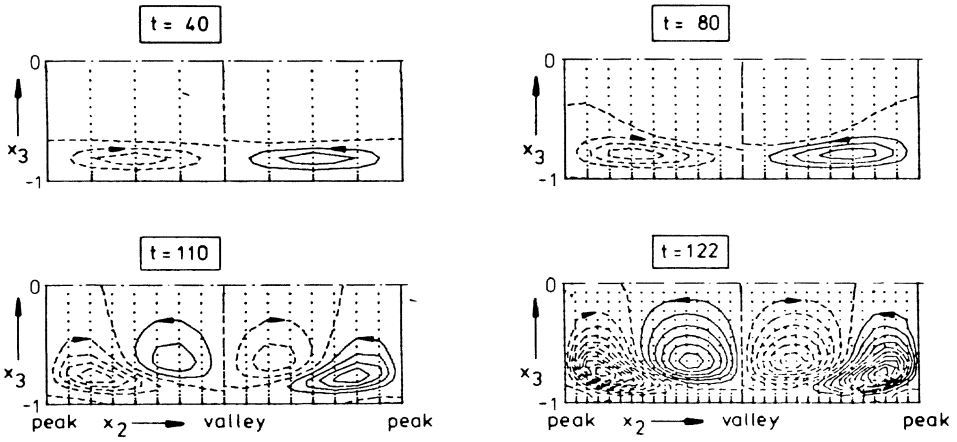

Fig. 17 Streamlines $\bar{\psi}$ = const. for mean secondary flow ($\bar{u}_2$, $\bar{u}_3$). Increments are $10^4 \Delta\bar{\psi}$ = 0.1, 0.5 and 2.5 at t = 40, 80 and t > 110, respectively.

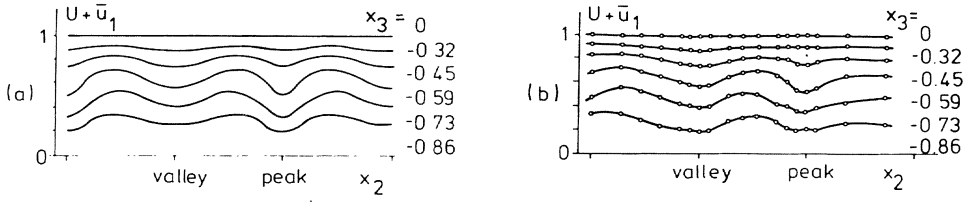

Fig. 18 Spanwise distribution of mean velocity
(a) numerical simulation, t = 122
(b) experiment, NISHIOKA et al. [44], 1-spike stage.

difference between simulation and experimental results is less than 5%.

Instantaneous velocity profiles at peak are shown in Fig. 19. Inflectional profiles and high-shear layers around $x_3 \approx \pm 0.6$ appear at t = 122 as in the experiment (Fig. 4). The development of the high-shear layer in the peak plane $x_2 = 0$ is seen in Fig. 20. While the near-wall shear maximum (connected with the TS wave) does not change much, the detached shear layer undergoes a rapid evolution. At $t \gtrsim 122$, two local shear maxima appear, initiating the later decay into discrete lumps, NISHIOKA et al. [46,47]. At t = 125 (roughly a 2-spike stage, KLEISER [33]), the maximum shear is 4.4, more than twice the maximum (wall) vorticity of the basic flow. The three-dimensional structure of the shear layer at t = 122 is shown in Fig. 21 for two downstream periods. The detached high-shear layer is enclosed

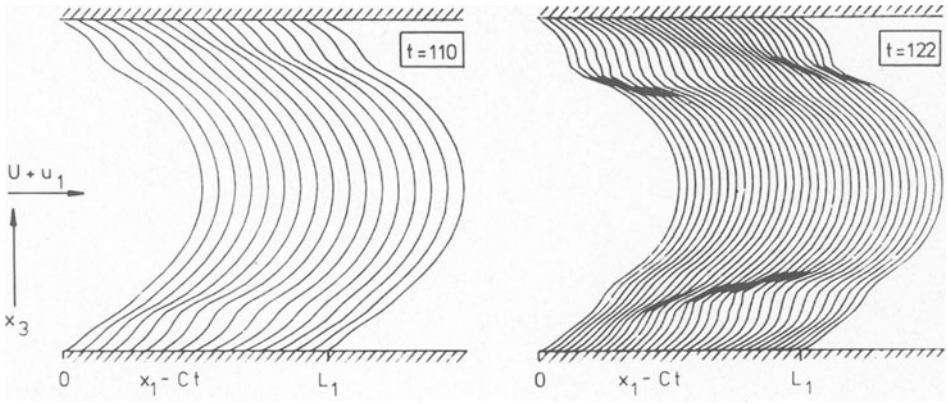

Fig. 19 Instantaneous velocity profiles at peak for one period of oscillation.

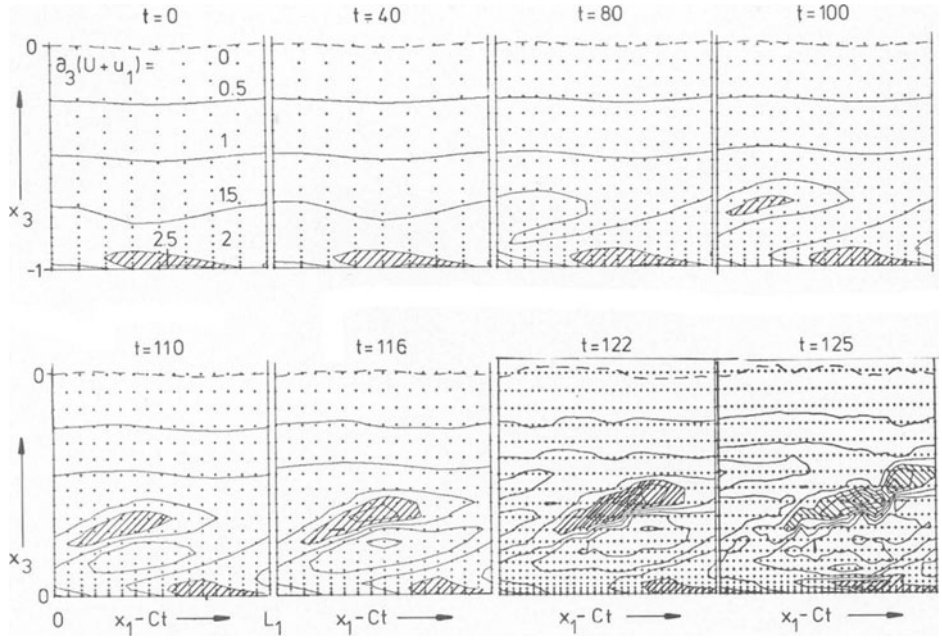

Fig. 20 Development of high-shear layer at peak. Hatched regions indicate $\partial_3(U+u_1) > 2$.

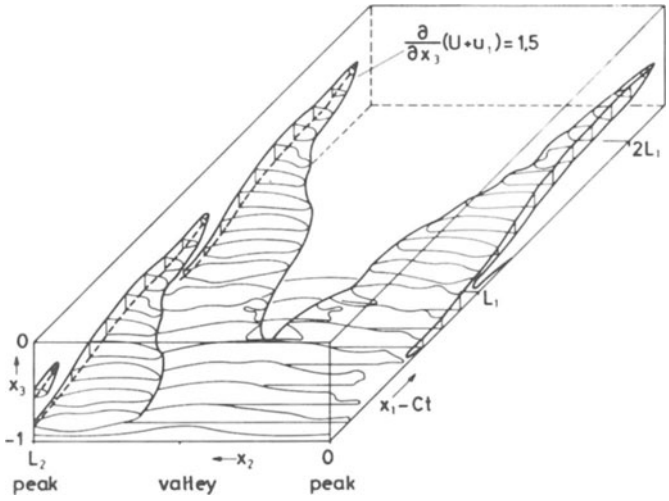

Fig. 21 High-shear layer at t = 122.

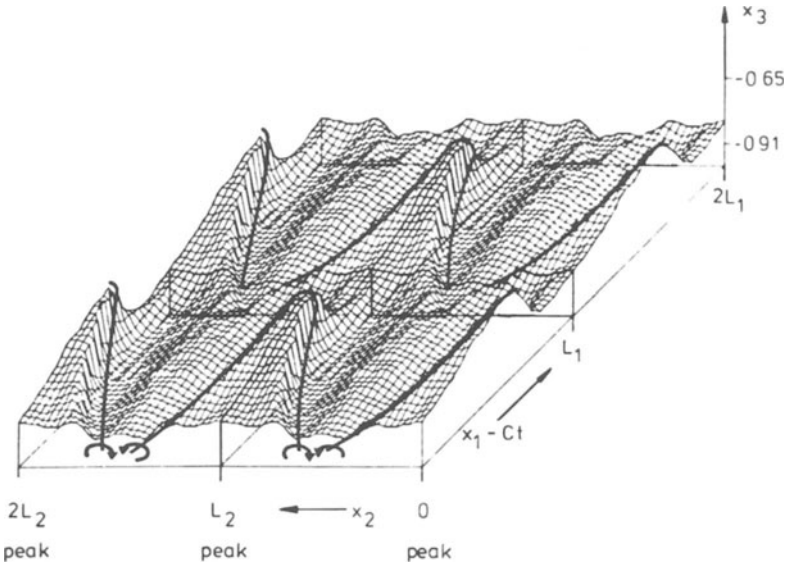

Fig. 22 Isosurface $U+u_1 = c_{TS} = 0.28$ and horseshoe-vortex system at t = 122.

by the downstream elongated tongues and is localized in a narrow region at the peak.

Another visualization of the spatial flow structure is given by the iso-surface of Fig. 22. Points on this surface do not move downstream instantaneously in our moving frame of reference. The ridges of low-speed fluid at the peak are connected with a travelling Λ- (or horse shoe-) vortex system (KLEISER [33]), which induces an upward movement between its legs. The time evolution of several flow patterns, including time lines of fluid markers, has been made visible in a film that conveys a vivid impression of the three-dimensional transition process.

5.3 Nonlinear growth of three-dimensional harmonics

Having understood the linear secondary instability it is natural to investigate the following nonlinear stage where the 3D instability mode has grown to finite amplitude. Does a new discernible tertiary state emerge after the undisturbed basic flow and the secondary 2D (quasi-)equilibrium, and is this again subject to a new, tertiary instability? Before we discuss this question, it is useful to look at the growth of the 3D harmonics. Instead of the maximum amplitude depicted in Fig. 16 an integral measure is used, the *energy amplitude*

$$\hat{E}(k_1,k_2)^{1/2} = \frac{1}{2} f(k_1,k_2) \left[\int_{-1}^{1} |\hat{u}_1(k_1,k_2,x_3)|^2 \, dx_3 \right]^{1/2} \qquad (5.2)$$

where f is defined in (3.5). Fig. 23 shows the energy amplitudes of all wave numbers retained in a simulation with $N_1 = N_2 = 16$ up to $t = 120$ (cf. Fig. 10). First we note that after the initial transient the growth rate $\sigma(k_1,k_2)$ of each mode remains, with few exceptions, nearly constant over most of the time interval. The growth rates are approximated by

$$\sigma(k_1,k_2) = k_1\sigma_{2D} + k_2\sigma_{3D} \qquad (5.3)$$

where $\sigma_{2D} = \sigma(1,0)$ is the growth rate of the 2D fundamental (approximately the TS growth rate at low amplitudes) and $\sigma_{3D} = \sigma(0,1) = \sigma(1,1)$ is the secondary instability growth rate. (5.3) is expected from the quadratic nonlinearity of the Navier-Stokes equations and is also consistent with other simulations, KLEISER [33]. Of course (5.3) cannot be valid for arbitrary large k_j because of viscous dissipation. In the present case, σ_{2D} is slightly negative and $|\sigma_{2D}| \ll \sigma_{3D}$, so the growth rates in Fig. 23 are practically independent of k_1 and proportional to k_2. The increase of the growth rates for the higher k_1 modes at $t \gtrsim 80$ in Fig. 23a marks the end of the 2D stage and may be explained by nonlinear interaction with higher harmonics (of correspondingly higher growth rates) that have grown to this order of magnitude at this stage. While the modes $k_1 > 0$ in Figs. 23a,b

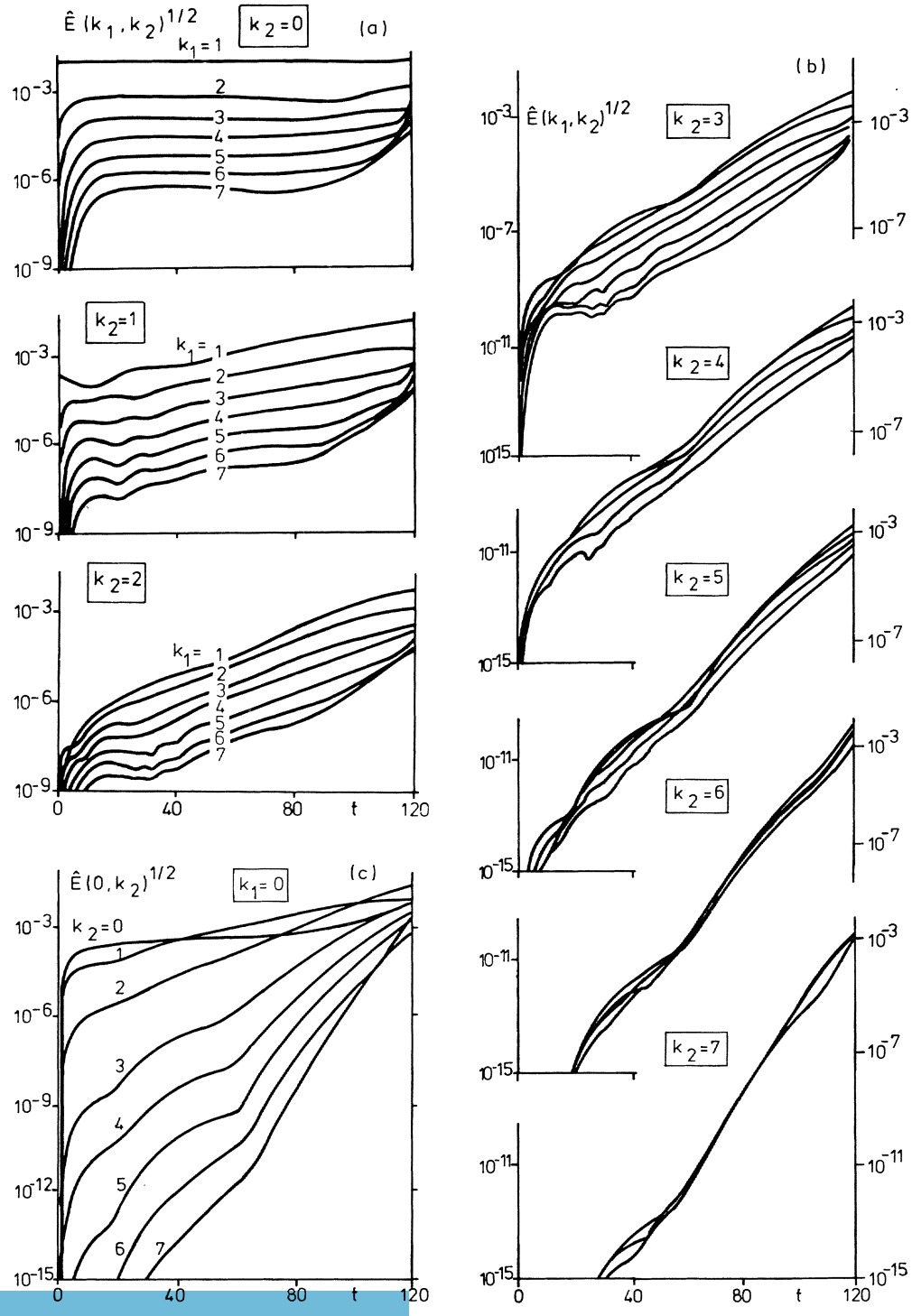

Fig. 23 Development of 2D and 3D harmonics.

contribute to the fluctuation u_1", the modes $k_1 = 0$ in Fig. 23c describe the evolution of the mean deformation u_1 (cf. Fig. 18). In particular we see a considerable growth of the mode $k_2 = 2$ responsible for the doubling of the set of vortices in Fig. 17.

For an investigation of higher harmonics in transition experiments, usually a Fourier analysis of time signals $u_1(t)$ at a fixed spanwise location is made. In our simulation this corresponds to a 1D Fourier analysis of $u_1(x_1)$. We denote these Fourier coefficients by $\hat{u}_{1,HF}$. According to (3.1) in $x_2 = 0$ we have

$$\hat{u}_{1,HF}(k_1,x_3) = \sum_{k_2} \hat{u}_1(k_1,k_2,x_3) \qquad (5.4)$$

The development of the maximum $\hat{u}_{1,HF}$ at $x_2 = 0$ is shown in Fig. 24. The behavior of the fluctuating modes at $t \lesssim 80$ is determined by the 2D modes $k_2 = 0$ (see Fig. 23a). At $t \gtrsim 80$ the growth rates increase and are roughly proportional to k_1 for $k_1 \leq 7$. For higher k_1 (not included in Fig. 24) they decrease again. Magnitude, qualitative behavior, and frequency of maximum growth compare favorably with experiments of NISHIOKA et al. [43,45].

Besides the growth of the amplitudes, the change in the spatial distribution of the Fourier modes is also of interest. The amplitude distribution for the lowest wavenumbers $k_2 \leq 2$ is shown in Fig. 25. The ordinate scale is arbitrary; however, the relative magnitudes in each frame are represented correctly. At $t = 80$ the initially excited modes (1,0) and (1,1) still have not changed much. While the (1,1) mode remains relatively unchanged at later times, the (1,0) mode becomes more localized.

The appearance of significant higher harmonics as transition approaches the spike stage -- with maximum amplification at frequencies one order of magnitude above the TS frequency -- is usually interpreted as a tertiary instability of the high-shear layers which have developed at this stage (Figs. 20, 21). The shear layer instability is a plausible physical explanation and has in fact been supported by an inviscid stability analysis of an instantaneous inflectional velocity profile, NISHIOKA et al. [45]. Although this may be a reasonable local approximation, it is probably too drastic a simplification for an explanation of the real highly three-dimensional phenomena. No spanwise gradients are accounted for in this picture. In fact, the instantaneous profiles change quite rapidly in the spanwise direction. The regular growth of all harmonics appearing in Fig. 23 according to (5.3) suggests an alternative interpretation of the observed phenomena (KLEISER [33]). The appearance of the high-frequency disturbances is explained not by a tertiary instability, but by nonlinear production and interaction of harmonics, starting from a 2D TS mode and the secondary instability mode. In fact, Fig. 23 demonstrates that the growth of the harmonics at rates (5.3) already begins with the onset of

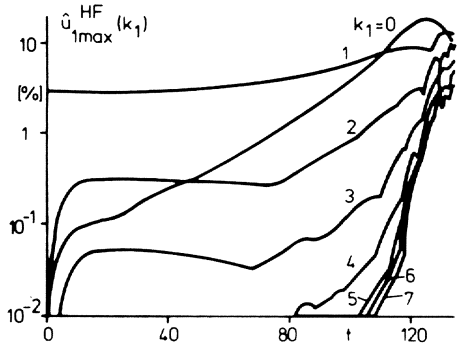

Fig. 24

Development of 1D Fourier amplitudes at peak.

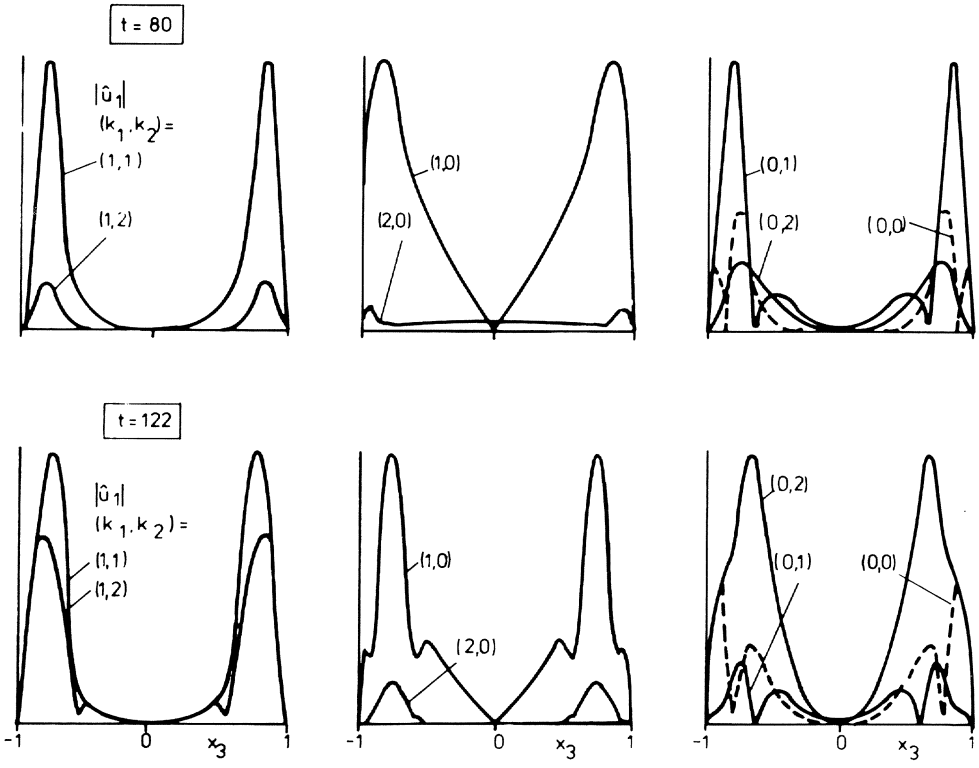

Fig. 25 Amplitude distribution $|\hat{u}_1|$ of Fourier modes (ordinates in arbitrary scale).

secondary instability, where no inflectional profiles and high-shear layers exist (Fig. 20). The overall picture emerging from this interpretation is a regular growth of all 3D harmonics which proceeds up to a point where breakdown of the ordered 3D wave motion into chaotic behavior occurs.

We caution, however, that the data used for support of this interpretation may suffer from limited spatial resolution of the simulation, particularly at late times and for high wavenumbers k_j. Higher resolution simulations and double Fourier decomposition of experimental results (in time and spanwise direction) would be desirable for further clarification. It is reassuring, at least, to note that the facts are essentially in agreement between simulation and experiment and that only their interpretation is an issue. To establish the existence of a tertiary instability in such a manner as has been possible for the primary and secondary instabilities would require the development of an appropriate theoretical framework for both the new basic state and the disturbances. In view of the complexity of the flow at the spike stage, this will not be an easy task.

6. CHAOTIC REGIME

It is natural to ask how the numerical solution behaves if our calculation is extended beyond the 1-spike stage. In the experiment, a multi-spike stage with breakdown of the high-shear layer is observed (NISHIOKA et al. [46,47]), followed by the formation of turbulent spots (CARLSON et al. [6]), which evolve into fully developed turbulent channel flow (ECKELMANN [11]). It is known that direct numerical simulation of turbulence (without Reynolds stress or subgrid modelling) would require computer resources far beyond present capabilities, in particular at higher Reynolds numbers (CHAPMAN [7], ROGALLO & MOIN [55]). Nevertheless, some results have been obtained at low Reynolds numbers. For example, ORSZAG & PATERA [51] verified the universal velocity profile of wall turbulence in a simulation with 64^3 grid points, starting from large-amplitude two-dimensional and three-dimensional initial disturbances. We have continued our transition simulation discussed above, with resolution $N_1 \times N_2 \times N_3 = 32 \times 32 \times 40$, up to $t = 158$. We certainly cannot expect a realistic simulation of turbulent channel flow, yet it is still interesting to look at the results of the numerical model as a solution of a nonlinear dynamical system. The system is given by the equations for the expansion coefficients $\hat{\hat{u}}_j(k_1,k_2,k_3)$ in (3.1), (3.2) and has several ten thousand degrees of freeedom.

Fig. 26 illustrates the development of the downstream-averaged mean velocity profile, which would correspond to a short-time average in an experiment. As expected (ORSZAG & PATERA [51]), we observe a rapid development in the wall region. In the region $0.85 \leq |x_3| \leq 1$, the profile at $t =$

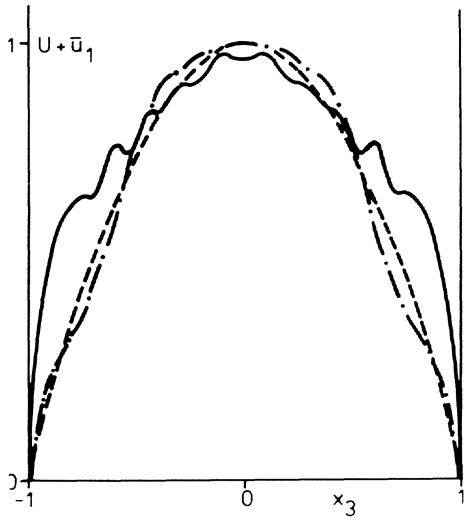

Fig. 26

Downstream-averaged velocity profiles at $x_2 = 0$ after breakdown.
-·-·- t = 134, —— t = 158,
---- parabolic profile.

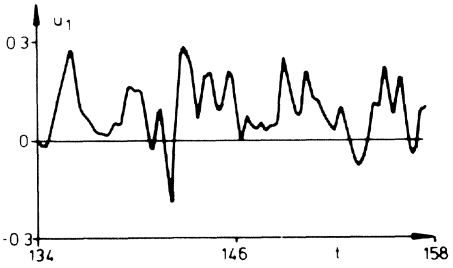

Fig. 27

Instantaneous velocity disturbance signal $u_1(t)$ at $x_1 = x_2 = 0$, $x_3 = -0.6$ seen in moving reference frame.

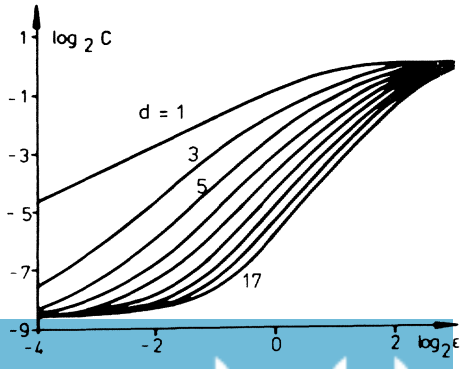

Fig. 28

log C vs log ε: the slope at intermediate ε and large d approximates the "attractor dimension" ν.

158 happens to agree quite closely with that measured by ECKELMANN [11] at a comparable Reynolds number. We stress, however, that the flow is still far from equilibrium, which is attained in the interior only on a viscous time scale $t = O(Re)$ (ORSZAG & PATERA [51]). In Fig. 27 an instantaneous disturbance signal $u_1(t)$ is shown, illustrating the chaotic nature of the solution. In the frame of reference chosen, the u_1 signal is constant for $t \lesssim 80$, thereafter slowly varying and becoming irregular at $t \approx 128$. Chaotic signals may be analyzed by methods developed to characterize attractors of dynamical systems on the basis of a long-time series $\{\underline{X}_1, \ldots, \underline{X}_N\}$ of points on the attractor. A characteristic measure of an attractor is its dimension, which can be defined in several ways (see BRANDSTÄTER et al. [5], and SREENIVASAN [58]). GRASSBERGER & PROCACCIA [19] suggested the use of the correlation exponent ν. This is defined as the exponent in the scaling law $C(\varepsilon) = \varepsilon^{\nu}$ for small ε where the correlation integral $C(\varepsilon)$ is defined as $1/N^2$ times the number of pairs whose distance $|\underline{X}_i - \underline{X}_j|$ is smaller than ε. Some examples are $\nu = 0.63$ for a Cantor set, $\nu = 1$ for a sine wave and $\nu = 2.05$ for the Lorenz attractor. Fig. 28 shows a plot of log C versus log ε of the signal of Fig. 27 for several imbedding dimensions d (GRASSBERGER & PROCACCIA [19]). The slopes $\nu(d)$ at intermediate values of ε tend towards a constant value $\nu \approx 2.3$. This number certainly increases if the simulation is continued, so that more data points are included. Dimensions that have been calculated from experimentally obtained turbulent signals often range from $\nu = 2$ to $\nu = 5$ (e.g. BRANDSTÄTER et al. [5], Taylor-Couette flow) and sometimes up to $\nu = 20$ (SREENIVASAN [58], wake of circular cylinder). They generally increase with Reynolds number. As the dimension of an attractor quantifies the number of relevant degrees of freedom in the dynamical motion of the system, these relatively low dimension numbers -- many orders of magnitude smaller than the dimensions of typical numerical models -- demand that they be utilized in the computation and modelling of turbulent flows.

7. CONCLUDING REMARKS

The past five years have seen important progress in the understanding of three-dimensional processes of transition in wall-bounded shear flows. Linear secondary instability theory (ORSZAG & PATERA [50], HERBERT [27]) provides for the first time a reliable theoretical tool for describing the onset of three-dimensionality. It also explains both the classical fundamental peak-valley splitting mode (K-type) and the newly discovered subharmonic route (H-type) to turbulence (SARIC et al. [57]). Direct numerical simulations of transition using spectral methods have been applied to several flows. It has now been established that they are capable of reproducing the experimentally observed transition process (WRAY & HUSSAINI [65], KLEISER [34], KLEISER & SCHUMANN [36]). They have been used

to investigate nonlinear and three-dimensional mechanisms of the transition process and the evolution of spatial flow patterns. Numerical simulations offer a considerable potential for future investigations of the late stages of transition, of transition control (LAURIEN & KLEISER [40]) and, using the large eddy simulation technique (ROGALLO & MOIN [55]), for the computation of turbulent flows.

The numerical results presented here have been obtained using the computer code CHANSON developed by the author while at the KARLSRUHE NUCLEAR RESEARCH CENTER. He would like to thank U. Schumann for his advice in the development of the numerical method, and Th. Herbert for many helpful suggestions as well as for providing his Orr-Sommerfeld solver and numerical data of the periodic secondary flow. The author has greatly profited from discussions with K.R. Sreenivasan on nonlinear dynamical systems.

REFERENCES

[1] AGARD Report No.709, Special course on stability and transition of laminar flow (1984).

[2] D. ARNAL: Description and prediction of transition in two-dimensional incompressible flow, in AGARD-R-709 [1] (1984).

[3] S. BIRINGEN: Final stages of transition to turbulence in plane channel flow. To appear in J. Fluid Mech.

[4] R.F. BLACKWELDER: Boundary-layer transition. Phys. Fluids 22, 583-584 (1979).

[5] A. BRANDSTÄTER et al.: Low-dimensional chaos in a hydrodynamic system. Phys. Rev. Lett. 51, 1442-1445 (1983).

[6] D.R. CARLSON, S.E. WIDNALL, M.F. PEETERS: A flow-visualization study of transition in plane Poiseuille flow. J. Fluid Mech. 121, 487-505 (1982).

[7] D.R. CHAPMAN: Computational aerodynamics development and outlook. AIAA J. 17, 1293-1313 (1979).

[8] A.D.D. CRAIK: Nonlinear resonant instability in boundary layers. J. Fluid Mech. 50, 393-413 (1971).

[9] M. DEVILLE, L. KLEISER, F. MONTIGNY-RANNOU: Pressure and time treatment for Chebyshev spectral solution of a Stokes problem. To appear in Int. J. Num. Meth. Fluids.

[10] P. DRAZIN, W. REID: Hydrodynamic Stability. Cambridge University Press (1981).

[11] H. ECKELMANN: The structure of the viscous sublayer and the adjacent wall region in a turbulent channel flow. J. Fluid Mech. 65, 439-459 (1974).

[12] J.-P. ECKMANN: Roads to turbulence in dissipative dynamical systems. Rev. Mod. Phys. 53, 643-654 (1981).

[13] R. EPPLER, H. FASEL (ed.): Laminar-Turbulent Transition. (Proc. IUTAM Symposium, Stuttgart 1979). Springer-Verlag, Berlin 1980.

[14] H. FASEL, H. BESTEK, R. SCHEFENACKER: Numerical simulation studies of transition phenomena in incompressible, two-dimensional flows. AGARD-CP-224, 14-1 - 14-8 (1977).

[15] N.A. FELISS, M.C. POTTER, M.C. SMITH: An experimental investigation of incompressible channel flow near transition. J. Fluids Eng. 99, 693-698 (1977).

[16] W.D. GEORGE, J.D. HELLUMS, B. MARTIN: Finite-amplitude neutral disturbances in plane Poiseuille flow. J. Fluid Mech. 63, 765-771 (1974).

[17] D. GOTTLIEB, M.Y. HUSSAINI, S.A. ORSZAG: Theory and applications of spectral methods. In R.G.Voigt et al.[62], 1-54 (1984).

[18] D. GOTTLIEB, S.A. ORSZAG: Numerical Analysis of Spectral Methods: Theory and Applications. NSF-CBMS Monograph No. 26, SIAM, Philadelphia 1977.

[19] P. GRASSBERGER, I. PROCACCIA: Characterization of strange attractors. Phys. Rev. Lett. 50, 346-349 (1984).

[20] F.R. HAMA, J. NUTANT: Detailed flow-field observations in the transition process in a thick boundary layer. Proc. 1963 Heat Transfer and Fluid Mech. Institute, 77-93 (1963).

[21] TH. HERBERT: Die neutrale Fläche der ebenen Poiseuille-Strömung. Habilitationsschrift, Universität Stuttgart (1978).

[22] TH. HERBERT: Stability of plane Poiseuille flow - theory and experiment. Fluid Dynamics Transactions 11, 77-126 (1983).

[23] TH. HERBERT: Secondary instability of plane channel flow to subharmonic three-dimensional disturbances. Phys. Fluids 26, 871-874 (1983).

[24] TH. HERBERT: Modes of secondary instability in plane Poiseuille flow. Proc. IUTAM Symposium "Turbulence and Chaotic Phenomena in Fluids", Kyoto, Japan (1983).

[25] TH. HERBERT: Subharmonic three-dimensional disturbances in unstable plane shear flows. AIAA Paper No. 83-1759 (1983).

[26] TH. HERBERT: Analysis of the subharmonic route to transition in boundary layers. AIAA Paper No. 84-0009 (1984).

[27] TH. HERBERT: Secondary instability of shear flows. In AGARD-R-709 [1] (1984).

[28] TH. HERBERT: Nonlinear effects in hydrodynamic stability. In AGARD-R 709 [1] (1984).

[29] TH. HERBERT, M.V. MORKOVIN: Dialogue on bridging some gaps in stability and transition research. Proc. IUTAM Symposium Stuttgart, 47-72 (1979).

[30] Y.S. KACHANOV, V.Y. LEVCHENKO: The resonant interaction of disturbances at laminar-turbulent transition in a boundary layer. J. Fluid Mech. 138, 209-247 (1984).

[31] R. KESSLER: Oszillatorische Konvektion. DFVLR-FB 84-14 (1984).

[32] P.S. KLEBANOFF, K.D. TIDSTROM, L.M. SARGENT: The three-dimensional nature of boundary-layer instability. J. Fluid Mech 12, 1-34 (1962).

[33] L. KLEISER: Numerische Simulationen zum laminar-turbulenten Umschlagsprozeß der ebenen Poiseuille-Strömung. Dissertation, Universität Karlsruhe (also report KfK 3271, Kernforschungszentrum Karlsruhe) (1982).

[34] L. KLEISER: Spectral simulations of laminar-turbulent transition in plane Poiseuille flow and comparison with experiments. Springer Lecture Notes in Physics 170, 280-285 (1982).

[35] L. KLEISER, U. SCHUMANN: Treatment of incompressibility and boundary conditions in 3-D numerical spectral simulations of plane channel flows. Proc. 3rd GAMM Conference on Numerical Methods in Fluid Mechanics (ed. E.H. Hirschel), Vieweg-Verlag, Braunschweig, 165-173 (1980).

[36] L. KLEISER, U. SCHUMANN: Spectral simulations of the laminar- turbulent transition process in plane Poiseuille flow, in R.G. VOIGT et al. [62], 141-163 (1984).

[37] L.S.G. KOVASZNAY, H. KOMODA, B.R. VASUDEVA: Detailed flow field in transition. Proc. 1962 Heat Transfer and Fluid Mech. Institute, 1-26 (1962).

[38] V.V. KOZLOV, M.P. RAMASANOV: Development of finite-amplitude disturbance in Poiseuille flow. Izv. Akad. Nauk SSSR, Mekh. Zhidk. i Gaza, 43-47 (1983).

[39] V.V. KOZLOV, M.P. RAMASANOV: Formation of three-dimensional structures in Poiseuille flow by resonant interaction. Preprint No. 11-83 I.T.A.M., USSR Acad. Sci., Novosibirsk (1983).

[40] E. LAURIEN, L. KLEISER: Numerical simulation of active transition control by wave-superposition. GAMM Annual Meeting, Regensburg, April 16 - 19, 1984.

[41] M.V. MORKOVIN: Instability, transition to turbulence and predictability. AGARD-AG-236 (1978).

[42] R.D. MOSER, P. MOIN, A. LEONARD: A spectral numerical method for the Navier-Stokes equations with applications to Taylor-Couette flow. J. Comp. Phys. 52, 524-544 (1983).

[43] M. NISHIOKA, S. IIDA, Y. ICHIKAWA: An experimental investigation of the stability of plane Poiseuille flow. J. Fluid Mech. 72, 731-751 (1975).

[44] M. NISHIOKA, S. IIDA, S. KANBAYASHI: An experimental investigation of the subcritical instability in plane Poiseuille flow (in Japanese). Proc. 10th Turbulence Symposium, Inst. Space Aeron. Sci., Tokyo Univ., 55-62 (1978).

[45] M. NISHIOKA, M. ASAI, S. IIDA: An experimental investigation of the secondary instability. Proc. IUTAM Symposium Stuttgart 1979 (Ref. [13]), 37-46 (1979).

[46] M. NISHIOKA, M. ASAI, S. IIDA: Wall phenomena in the final stage of transition to turbulence. In: Transition and Turbulence (ed. R.E. Meyer), 113-126. Academic Press (1981).

[47] M. NISHIOKA, M. ASAI: Evolution of Tollmien-Schlichting waves into wall turbulence. Proc. IUTAM Symposium on Turbulence and Chaotic Phenomena in Fluids, Kyoto, Japan (1983).

[48] S.A. ORSZAG, L.C. KELLS: Transition to turbulence in plane Poiseuille flow and plane Couette flow. J. Fluid Mech. 96, 159-206 (1980).

[49] S.A. ORSZAG, A.T. PATERA: Subcritical transition to turbulence in plane shear flows. In: Transition and Turbulence (ed. R.E. Meyer), 127-146, Academic Press (1981).

[50] S.A. ORSZAG, A.T. PATERA: Secondary instability of wall-bounded shear flows. J. Fluid Mech. 128, 347-385 (1983).

[51] S.A. ORSZAG, A.T. PATERA: Calculation of von Karman's constant for turbulent channel flow. Phys. Rev. Lett. 47, 832-835 (1981).

[52] E. OTT: Strange attractors and chaotic motions of dynamical systems. Rev. Mod. Phys. 53, 655-671 (1981).

[53] A.T. PATERA: A spectral element method for fluid dynamics: laminar flow in a channel expansion. J. Comp. Phys. 54, 468-488 (1984).

[54] PROCEEDINGS of the Second IUTAM Conference on Laminar-Turbulent Transition, Novosibirsk, July 9-13, 1984. To be published by Springer-Verlag.

[55] R.S. ROGALLO, P. MOIN: Numerical simulation of turbulent flows. Ann. Rev. Fluid Mech. 16, 99-137 (1984).

[56] W.S. SARIC, A.S.W. THOMAS: Experiments on the subharmonic route to turbulence in boundary layers. Proc. IUTAM Symposium "Turbulence and Chaotic Phenomena in Fluids", Kyoto, Japan (1983).

[57] W.S. SARIC, V.V. KOZLOV, V.Y. LEVCHENKO: Forced and unforced subharmonics resonance in boundary layer transition. AIAA paper No. 84-0007 (1984).

[58] K.R. SREENIVASAN: Transitional and turbulent wakes and chaotic dynamical systems. This volume.

[59] J.T. STUART: On the non-linear mechanics of hydrodynamic stability. J. Fluid Mech. 4, 1-21 (1958).

[60] I. TANI: Boundary-layer transition. Ann. Rev. Fluid Mech. 1, 169-196 (1969).

[61] T. TATSUMI (ed.): Proc. IUTAM Symposium on Turbulence and Chaotic Phenomena in Fluids, Sept. 5-10, 1984, Kyoto.

[62] R.G. VOIGT et al. (ed.): Spectral methods for partial differential equations. SIAM, Philadelphia (1984).

[63] D.R. WILLIAMS, H. FASEL, F.R. HAMA: Experimental determination of the three-dimensional vorticity field in the boundary layer transition process. To appear in J. Fluid Mech.

[64] F.X. WORTMANN: The incompressible fluid motion downstream of twodimensional Tollmien-Schlichting waves. AGARD-CP-224, 12-1 - 12-8 (1977).

[65] A. WRAY, M.Y. HUSSAINI: Numerical experiments in boundary-layer stability. AIAA Paper 80-0275 (1980).

[66] J.P. ZAHN, J. TOOMRE, E.A. SPIEGEL, D.O. GOUGH: Nonlinear cellular motions in Poiseuille channel flow. J. Fluid Mech. 64, 319-345 (1974).

RENORMALIZATION GROUP FORMULATION OF LARGE EDDY SIMULATION

V. YAKHOT, S.A. ORSZAG

1. INTRODUCTION

Perhaps the most distinguishing characteristic of high Reynolds number turbulent flows is their large range of excited space and time scales. In homogeneous turbulence, dissipation-scale eddies are of order $R^{3/4}$ times smaller than energy-containing eddies, where R is the Reynolds number. In order to solve the Navier-Stokes equations accurately for such a turbulent flow, it is necessary to retain order $(R^{3/4})^3$ spatial degrees of freedom. Also, since the time scale for significant evolution of homogeneous turbulence is of the order of the turnover time of an energy containing eddy, it is necessary to perform order $R^{3/4}$ time steps to calculate for a significant evolution time of the flow. Even if these calculations require only O(1) arithmetic operations per degree of freedom per time step, the total computational work involved would be order R^3, while the computer storage requirement would be $R^{9/4}$. In this case, doubling the Reynolds number would require an order of magnitude improvement in computer capability. With this kind of operation and storage count, it is unlikely that forseeable advances in computers will allow the full numerical simulation of turbulent flows at Reynolds numbers much larger than $R_\lambda = O(100)$ already achieved (see BRACHET et al. [2]).

This pessimistic operation and storage count for solution of the Navier-Stokes equations is the origin of interest in the so-called large-eddy-simulation method. Here, excitations on scales smaller than those resolvable on the numerical grid are modelled, usually by an eddy viscosity coefficient. Such a subgrid scale (SGS) eddy coefficient represents the dissipative effect of motions on scales smaller than the effective grid on the large eddies (defined as those motions adequately represented on the numerical grid). The most common form for this SGS eddy viscosity coefficient is due to SMAGORINSKY

$$\nu_{eddy} = c\Delta^2 \left| \left[\frac{\partial v_i}{\partial x_j} + \frac{\partial v_j}{\partial x_i} \right]^2 \right|^{1/2} \qquad (1.1)$$

where Δ is the grid scale and v_i is the large-eddy velocity. It has been shown by LILLY [12] that the eddy viscosity (1.1) is consistent on dimensional grounds with the Kolmogorov theory of the inertial range. For the inertial-range spectrum $E(k) = C\varepsilon^{2/3}k^{-5/3}$ with $C = 1.5$, LILLY argued that $c \approx 0.04$ in (1.1).

The basic action of the eddy viscosity (1.1) on large scales seems correct in most respects. However, there are two important qualitative deficiencies in this formulation of large-eddy simulations. First, large-eddy simulations based on (1.1) alone neglect the effect of random forcing of small scales at the subgrid level on large scales at the supergrid level. The eddy viscosity (1.1) is non-stochastic (at the subgrid level, though it is still random due to supergrid fluctuations), while the action of random small-scale eddies is certainly stochastic in character. Thus, it should be expected that in addition to eddy viscous effects of small scales on large scales, there should also be a random forcing effect, giving rise to an eddy diffusion process and production of turbulent energy. This point will be discussed later. Second, the eddy viscosity (1.1) does not properly model interference effects between eddy and molecular viscosity, which is essential in turbulent processes where eddy effects must be inhibited (for example, near rigid walls). The simple superposition of eddy and molecular viscosity near walls does not lead to correct results (see MOIN & KIM [14]).

DEARDORFF [4,6,7] made pioneering studies of turbulent shear flows using the SGS viscosity (1.1). For wall-bounded shear flows, DEARDORFF calculated only up to the edge of the buffer layer between the viscous sublayer and the logarithmic region of the velocity profile. A boundary condition is imposed at this point, based on the von Karman theory of the wall layer, in which the turbulent fluctuating stress is assumed known. Molecular viscosity plays no role in DEARDORFF's calculations, which are performed at least formally, at infinite R. Clearly such a simulation does not give a faithful representation of the wall region and accompanying bursts.

If one is interested in the physics of wall turbulence, neglect of the wall region is unjustified. More recent work by MOIN & KIM [14] integrates up to the rigid wall, the increased sophistication giving a so-called transport-eddy simulation. However, transport-eddy simulations (as currently implemented) are much more severely limited than the earlier large-eddy simulation work of DEARDORFF and SCHUMANN. The point is that, as presently practiced, transport-eddy subgrid scale simulations use uniform horizontal resolution independent of distance from the wall (MOIN & KIM [14]). If such a simulation is to capture scales down to those of turbulent bursts (which must be done to capture the turbulence product properly), the number of required degrees of freedom scales as R_*^3. This estimate is based on the fact that, while the streak structure scales with the inner variables (KLINE et al. [10]), streamwise and spanwise corre-

lations scale with the outer variables, i.e. channel height (COMTE-BELLOT [3]). Transport-eddy modelling does allow simulation of flows at somewhat higher Reynolds numbers than those that can be simulated without modelling (MOIN & KIM [14] achieve $R_* = 640$ ($R = \approx 13000$) by transport-eddy modelling, while the direct numerical simulations of ORSZAG & PATERA [16] are restricted to $R_* = 200$), but bursts at mean-flow Reynolds numbers R of 20000 - 100000 (in plane Poiseuille flow) are beyond subgrid scale models as now implemented in Cray-1 class computers. In other words, if a transport-eddy simulation of a well-bounded flow is to fare significantly better than a direct simulation, the dependence of required degrees of freedom must scale less rapidly than R_*^3 as R_* becomes large. At present, no such method exists.

A second problem with current transport-eddy schemes stems from the way the small scales are modelled in the wall layer. In particular, the application of a VAN DRIEST correction to the subgrid eddy viscosities (MOIN & KIM [14]) is not fully justified. While this correction (VAN DRIEST [17]) was originally intended to model the effect of fluctuations within the viscous sublayer in modulating the interaction of molecular and eddy viscosities, applying it to a subgrid scale model could eliminate or significantly alter fluctuations in the supergrid or resolvable scales. A third problem is that existing schemes rely upon availability of experimental data to fix modelling constants. For example, MOIN & KIM [14] introduce a new term into the equation of motion to obtain the correct mean velocity profile in turbulent channel flow. To achieve agreement with experiment, they chose parameters that differ from those that seem to work best for homogeneous turbulence. Other choices of parameters give unrealistic turbulence decay or growth.

In this paper, we use renormalization group (RNG) methods to address the solution of the latter two difficulties encountered by transport- eddy modelling. The RNG SGS closures obtained below seem to model properly the interaction of turbulent motions in the wall region without ad hoc damping factors, and also appear to account for the generation of random bursts in the buffer layer, without requiring extensive experimental data to fit transport coefficients. The problem of computational work scaling as R_*^3 will be addressed once again in the conclusion of this paper, but remains a subject of current investigation.

2. INFRARED RNG METHOD FOR HOMOGENEOUS TURBULENCE

FORSTER, NELSON & STEPHEN [8] introduced the infrared RNG method to investigate the long-time-large-scale properties of randomly stirred fluids. Their work, as well as the subsequent work of MARTIN & DE DOMINICIS, [13],

FOURNIER & FRISCH [9], and YAKHOT [19], showed that the large-scale spectrum of an incompressible fluid governed by the Navier-Stokes equations subject to a Gaussian random force that is white in time and with energy spectrum proportional to k^{-3} (see (2.2) below), generates the Kolmogorov $k^{-5/3}$ energy spectrum in the infrared ($k \to 0$) limit.

The problem treated by the above authors is:

$$\frac{\partial \vec{v}}{\partial t} + \vec{v} \cdot \nabla \vec{v} = -\frac{\nabla R}{\rho} + \vec{f} + \nu_0 \nabla^2 \vec{v} \tag{2.1a}$$

$$\nabla \cdot \vec{v} = 0 \tag{2.1b}$$

with

$$\langle f_j(\vec{k}\omega) f_j(\vec{k}'\omega') \rangle = 2(2\pi)^4 D_0 k^{-3} \left[\delta_{ij} - \frac{k_i k_j}{k^2}\right] \delta(\vec{k}+\vec{k}') \delta(\omega+\omega') \tag{2.2}$$

In this section, we rework the infrared RNG method for the problem (2.1) - (2.2) in order to demonstrate how RNG ideas may fit into the context of subgrid scale closure. However, before proceeding to this task let us give some further justification for the inclusion of the random force (2.2) as a driving force in the Navier-Stokes equations (2.1).

On the one hand, the random force (2.2) is justified by earlier work on the infrared renormalization group because of its consistency with the $k^{-5/3}$ spectrum at small k. However, for our present purposes this is but weak justification, because we are interested in eliminating only the very smallest scales (highest k) of motion that represent the SGS motions. YAKHOT [19] generalized the RNG methods to the ultraviolet case, in which the largest scales of motion are removed by the RNG procedure, and showed that a high-wave number $k^{-5/3}$-like spectrum is also achieved by imposing the random force (2.2). Also, YAKHOT [19] showed that if a field of homogeneous turbulence is driven by a force confined to a band of wave numbers, then the ultraviolet RNG procedure induces a random force at high wave numbers of the form (2.2). The assumptions leading to the latter conclusions have recently been weakened (YAKHOT, unpublished). In any case, if it is to be assumed that the smallest scales of turbulence are governed by KOLMOGOROV-like laws, then we conclude that it is consistent to include the random driving force (2.2) in the equations of motion for the small scales.

The idea of the infrared RNG method is to eliminate modes from the wavenumber strip near the ultraviolet cutoff Λ. Modes in the band $\Lambda e^{-\ell} < k < \Lambda$ are formally removed, using diagrammatic perturbation theory, the latter being structurally similar to that introduced for homogeneous turbulence theory by KRAICHNAN [11] and WYLD [18]. The system resulting from the

elimination of these modes involves modified interaction coefficients, new nonlinearities, as well as modified viscosities and forces. In the RNG method, the resulting equations are then transformed to look as much as possible like the original system (2.1) - (2.2).

To illustrate the technical details of the RNG method, consider Fourier transform of (2.1):

$$v_\ell(\hat{k}) = G^0 f_\ell(\hat{k}) - \frac{i\lambda_0}{2} G^0 P_{\ell mn}(\vec{k}) \int v_m(\hat{q}) v_n(\hat{k}-\hat{q})\, d\hat{q} \tag{2.3}$$

where $\hat{k} = (\vec{k},\omega)$ and

$$G^0 = (-i\omega+\nu_0 k^2)^{-1}; \quad P_{\ell mn}(\vec{k}) = k_m P_{\ell n}(k) + k_n P_{\ell m}(k) ;$$
$$P_{\ell m}(k) = \delta_{\ell m} - \frac{k_\ell k_m}{k^2} \tag{2.4}$$

The integration on the right side of (2.3) is carried out over the domain $\hat{q} = (\vec{q},\Omega)$ with $-\infty < \Omega < \infty$ and $0 < q < \Lambda$. At this stage, we are interested in the effect of the modes from the strip $\Lambda e^{-\ell} < k < \Lambda$. The velocity field is split into the two components: $v^<(\hat{k})$ with $0 < k < \Lambda e^{\ell}$ and $v^>(\hat{k})$ with $\Lambda e^{-\ell} < k < \Lambda$. In terms of this decomposition, the integral in (2.3) becomes:

$$v_\ell(k) = G^0 f_\ell(k) + \frac{i\lambda_0}{2} G^0 P_{\ell mn}(\vec{k}) \times$$
$$\times \int [v_m^<(\hat{q}) v_n^<(\hat{k}-\hat{q}) + 2v_m^>(\hat{q}) v_n^<(\hat{k}-\hat{q}) + v_m^>(\hat{q}) v_n^>(\hat{k}-\hat{q})]\, d\hat{q} \tag{2.5}$$

In order to eliminate modes from the interval $\Lambda e^{-\ell} < k < \Lambda$, all terms $v_\ell^>(\hat{k})$ in (2.5) should be removed by repeated substitution of (2.5) for $v^>$ back into (2.5). This generates an infinite expansion for $v^<$ in powers of λ_0 in which $v^>$ does not formally appear. Next, averages are taken over the part of random force $f^>$ belonging to the strip $\Lambda e^{-\ell} < k < \Lambda$. This procedure formally eliminates the modes $\Lambda e^{-\ell} < k < \Lambda$ from the problem; the results are represented diagrammatically in Fig.1, where the thick slashed and unslashed lines symbolize modes $v^>(\hat{k})$ and $v^<(\hat{k})$, respectively. The wavy line denotes $2D_0|G^0(\hat{k})|_i^2 P_{ij}(\hat{k})k^{-3}\delta(\hat{k}+\hat{k}')$, while the vertex and cross denote $-\frac{i\lambda_0}{2} P_{\ell mn}(\vec{k})$ and random force $\vec{f}(\hat{k})$, respectively.

It follows from Fig. 1, that after removing the modes $\Lambda e^{-\ell} < k < \Lambda$, the equation of motion for $v^<$ can be written up to second order in λ_0 as:

$$(-i\omega+\nu_0 k^2) v_\ell^<(\hat{k}) = f_\ell(\hat{k}) - \frac{i\lambda_0}{2} P_{\ell mn}(\vec{k}) \int f_n^>(\hat{q}) f_m^>(\hat{k}-\hat{q})\, d\hat{q} -$$

$$-\frac{i\lambda_0}{2} P_{\ell mn}(\vec{k}) \int v_m^<(\hat{q}) v_n^<(\hat{k}-\hat{q}) d\hat{q} + \tag{2.6}$$

$$+ 4D_0 (\frac{i\lambda_0}{2})^2 P_{\ell mn}(\vec{k}) \int |G^0(\hat{q})|^2 P_{m\mu}(\vec{q}) P_{n\mu\rho}(\vec{k}-\vec{q}) q^{-3} G^0(\hat{k}-\hat{q}) v_\rho^<(\hat{k}) d\hat{q} + O(\lambda_0^3)$$

The second term on the right side of (2.6) is an induced random force, denoted by Δf_ℓ, with zero mean if the forces in modes $k^>$ are assumed to be statistically homogeneous.

When the $O(\lambda_0^2)$ term on the right-side of (2.6) is moved to the left side, it gives a correction to the bare viscosity $\nu_0 k^2$:

$$k^2 \Delta\nu P_{\ell\rho}(k) =$$

$$= \lambda_0^2 D_0 P_{\ell mn}(\vec{k}) \int |G^0(\hat{q})|^2 P_{m\mu}(\vec{q}) P_{n\mu\rho}(\vec{k}-\vec{q}) q^{-3} G^0(\hat{k}-\hat{q}) d\hat{q} \tag{2.7}$$

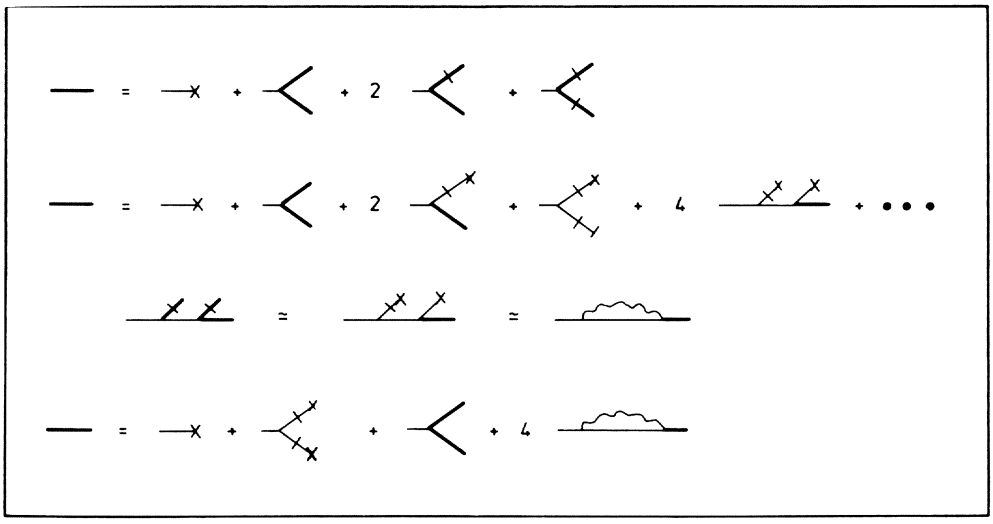

Fig. 1 A diagrammatic representation of the derivative of the renormalized Navier-Stokes equation (2.6).
(a) Diagrammatic representation of the Navier-Stokes equation (2.5).
(b) Irreducible diagram expansion of the equation for $v^<$ with $v^>$ removed.
(c) Second-order correction to propagator, included in (2.6).
(d) Renormalized Navier-Stokes equation (2.6), closed at second-order diagrams as in the quasi-normal approximation, which is asymptotically exact in the limit $\ell \to 0$.

The integration in (2.7) is carried out over $\hat{q} = (\vec{q},\Omega)$ where $-\infty < \Omega < \infty$ and $\Lambda e^{-\ell} < q < \Lambda$. Integration over the frequency Ω gives

$$k^2 \Delta\nu P_{\ell\rho}(\vec{k}) = \frac{\lambda_0^2 D_0}{\nu_0} P_{\ell mn}(\vec{k}) k_\mu \int_{\Lambda e^{-\ell}}^{\Lambda} \frac{P_{m\mu}(\vec{q}) P_{n\rho}(\vec{k}-\vec{q}) q^{-d-2}}{-i\omega+\nu_0(q^2+(k-q)^2)} \frac{d^d q}{(2\pi)^d} \qquad (2.8)$$

where we have now generalized the formula to d dimensions with k^{-3} in (2.2) replaced by k^{-d}.

The correction $\Delta\nu$ to the viscosity is a function of both ω and $\vec{k}$. Since we are interested in behaviour of the system at large scales, we neglect k in comparison and q and ω in comparison with $\nu_0 q^2$ in (2.8). This gives

$$\Delta\nu(\hat{0}) = A_d \frac{\lambda_0^2 D_0}{\nu_0^2 \Lambda^4} \frac{e^{4\ell}-1}{4} \qquad (2.9)$$

where

$$A_d = \tilde{A}_d \frac{S_d}{(2\pi)^d}, \quad \tilde{A}_d = \frac{1}{2} \frac{d^2-2}{d^2+2d} \qquad (2.10)$$

where $S_d = 2\pi^{d/2}/\Gamma(d/2)$ is the area of a unit sphere in d dimensions. Thus, the viscosity resulting from elimination of the modes $v^>$ is:

$$\nu = \nu_0 (1+A_d \lambda_0^{-2} \frac{e^{4\ell}-1}{4}) \qquad (2.11)$$

where the dimensionless coupling constant $\bar{\lambda}_0$ is

$$\bar{\lambda}_0 = \lambda_0 \frac{D_0^{1/2}}{\nu_0^{3/2} \Lambda^2} \qquad (2.12)$$

The elimination procedure just described is accurate in the limit $\ell \to 0$. We conclude that elimination of small scales with $\Lambda e^{-\ell} < k < \Lambda$ affects neither λ_0 nor D_0. The constancy of D_0 under this renormalization follows because, while the second term on the right-hand side of equ. (2.6) gives a zero-mean (averaged over $k^>$) Gaussian random variable with correlation function proportional to k^2, this correction cannot be absorbed in the bare force (2.2) whose correlation function is proportional to k^{-3}. Thus, $D = D_0$, and we must include a new random force with correlation function proportional to k^2 in the renormalized Navier-Stokes equations. The fact that λ_0 is not renormalized is a consequence of Galilean invariance (see FORSTER et al. [8].

It is possible to eliminate a finite band of modes $\Lambda e^{-\ell} < k < \Lambda$ by iterating the above procedure of eliminating an infinitesimally narrow band of modes. The result of this iteration procedure is to generate a renormalized viscosity coefficient $\nu = \nu(\ell)$ and coupling constant $\bar{\lambda} = \bar{\lambda}(\ell)$, while $D(\ell) = D_0$ and $\lambda(\ell) = \lambda_0$ still hold. Whereas the elimination of the infinitesimal band of modes is justified by comparison with second-order perturbation solutions of the Navier-Stokes equations (or by comparing with the direct-interaction approximation for this system), the result of the iteration procedure is no longer justifiable in this way. The nature of the errors incurred by this procedure must be clarified later.

The functions $\nu(\ell)$ and $\bar{\lambda}(\ell)$ are most easily determined by taking the limit $\ell \to 0$ in (2.9) in order to obtain the differential equation

$$\frac{d\nu}{d\ell} = A_d \nu(\ell) \bar{\lambda}^2(\ell) \tag{2.13}$$

where

$$\bar{\lambda}^2(\ell) = \frac{\lambda_0^2 D_0}{\nu^3(\ell)\Lambda^4} e^{4\ell} \tag{2.14}$$

since $\Lambda(\ell) = \Lambda e^{-\ell}$.

The solution of (2.13)-(2.14) is

$$\nu(\ell) = \nu_0 (1 + \tfrac{3}{4} A_d \bar{\lambda}_0^2 (e^{4\ell} - 1))^{1/3} \tag{2.15}$$

and

$$\bar{\lambda}(\ell) = \bar{\lambda}_0 e^{2\ell} (1 + \tfrac{3}{4} A_d \bar{\lambda}_0^2 (e^{4\ell} - 1)^{-1/2} \tag{2.16}$$

In the 'infrared' limit $\ell \to \infty$, the dimensionless coupling parameter $\bar{\lambda}$ approaches the finite limit

$$\bar{\lambda}^* = \sqrt{4/3A_d} \tag{2.17}$$

Pretending that the coupling constant $\bar{\lambda} << 1$ at this "fixed point", so that the nonlinear terms of the renormalized Navier-Stokes equation become negligible as $\ell \to \infty$, we find that the renormalized velocity field is given by

$$v_\ell(\hat{k}) \approx G_R(\hat{k}) f_\ell(\hat{k}) \tag{2.18}$$

where the renormalized propagator $G_R(\hat{k})$ is given by

$$G_R(k) = (-i\omega+\nu(\ell)k^2)^{-1} \tag{2.19}$$

If only modes with wavenumbers larger than $k = \Lambda(\ell)$ are removed by renormalization, then (2.15) gives the k-dependent viscosity:

$$\nu(k) = (\frac{3}{4} A_d D_0)^{1/3} k^{-4/3} \tag{2.20}$$

where we have now set $\lambda_0 = 1$. Noting (2.18), averaging over random force $\vec{f}$ with correlation function k^{-3}, and integrating over ω gives the one-dimensional energy spectrum $E(k)$:

$$E(k) = \frac{1}{2} \frac{S_d}{(2\pi)^{d+1}} \int_{-\infty}^{\infty} G_i(k\omega)\, d\omega = \frac{1}{2(\frac{3}{8}\tilde{A}_d)^{1/3}} (2D_0 \frac{S_d}{(2\pi)^d})^{2/3} k^{-5/3}$$

$$G_{ij}(k\omega) = \frac{\langle v_i(k\omega) v_j(k'\omega')\rangle}{(2\pi)^{d+1} \delta(k+k')\delta(\omega+\omega')} \tag{2.21}$$

Formula (2.21) has also been derived by FOURNIER & FRISCH [9].

It follows from (2.18) that

$$2 \frac{S_d}{(2\pi)^d} D_0 \ell_n \frac{\Lambda(\ell)}{k_0} \simeq \varepsilon_R \tag{2.22}$$

where

$$\varepsilon_R = \frac{1}{2} \nu(\ell) \left(\frac{\partial v_i^<}{\partial x_j} + \frac{\partial v_j^<}{\partial x_i} \right)^2 \tag{2.23}$$

is the (renormalized) rate of energy dissipation per unit mass (see NOVIKOV [15]. Since $\Lambda(\ell) = k$, (2.22) implies that ε_R is a weak function of k, i.e.

$$\frac{\varepsilon_R}{\ell nk/k_0} \simeq 2 \frac{S_d}{(2\pi)^d} D_0 \tag{2.24}$$

independent of k. Substituting (2.24) into (2.21) gives

$$\varepsilon(k) \simeq C_K \varepsilon^{-2/3} k^{-5/3} / [\ell nk/k_0]^{2/3} \tag{2.25}$$

where we identify $\bar{\varepsilon} = \varepsilon_R$ as the rate of energy dissipation and

$$C_K = \frac{1}{2} \frac{1}{(\frac{3}{8}\tilde{A}_d)^{1/3}} \simeq 1.13 \qquad (d = 3) \tag{2.26}$$

Here $(\ell nk/k_0)^{-2/3}$ is a correction to the Kolmogorov $k^{-5/3}$ spectrum caused by the random force (2.2); C_K is the Kolmogorov constant that agrees reasonably well with $C_K \simeq 1.5$ observed experimentally. This result will be used in the next section, where we apply renormalization group ideas to derive a subgrid scale model for finite systems.

It can also be shown that a somewhat more realistic model whose stirring force satisfies:

$$\langle f_i(\hat{k}) f_j(\hat{k}') \rangle \propto \bar{\varepsilon}(\delta_{ij} - \frac{k_i k_j}{k^2}) k^{-d} \delta(k+k') \delta(\omega+\omega') , \qquad k \geq k_c \tag{2.27}$$

for any $k_c > L^{-1}$, also gives the Kolmogorov spectrum in the limit $k \to \infty$. This is easily understood, since all the terms originating from the strip $1/L < k < k_c$ are irrelevant in the limit $k \to \infty$. This result is the key to our treatment of finite systems in section 3. *In particular, we assume that a turbulent fluid in a finite system in which the flow is locally homogeneous, exhibits the Kolmogorov behaviour in the intermediate range* $k_c < k < k_d$ *and can be described by the Navier-Stokes equation (2.1) with the random force (2.27) locally in physical space.*

3. SUBGRID SCALE MODEL FOR INHOMOGENEOUS TURBULENCE

In this section, we describe the application of the infrared RNG method to the development of a subgrid scale closure for inhomogeneous turbulent flows in finite geometries, like pipes and channels. It is well-known experimentally that if the Reynolds number is sufficiently large, one can distinguish three spatial scales in such flows: (i) for wavenumbers $k \lesssim 1/L$ (where L is a scale defining the geometry of the flow), the energy spectrum is anisotropic and is not characterized in any universal statistical way; (ii) for wavenumbers satisfying $1/L << k < k_d \simeq R^{3/4}L^{-1}$, the velocity fluctuations in the turbulent fluid are characterized roughly by the $k^{-5/3}$ spectrum; (iii) in the dissipation range, $k \gtrsim k_d$, the energy spectrum decreases rapidly.

The finite, inhomogeneous systems under discussion here differ from the homogeneous systems discussed in Sec. 2 in that, while it is possible to

drive finite systems by forces like (2.2) to achieve a $k^{-5/3}$ small-scale spectrum, the parameter D_0 characterizing the amplitude of this force is not a free parameter, but rather is determined by the driving mechanism and boundary conditions of the inhomogeneous turbulent flow. In the homogeneous systems under discussion in Sec. 2, D_0 is directly proportional to the energy dissipation rate $\bar{\varepsilon}$, so $\bar{\varepsilon}$ is determined by the random force, and hence is not a renormalizable parameter.

However, in a finite system, the average dissipation $\bar{\varepsilon}$ is a function of the velocity field, boundary conditions, and external driving mechanism. In this case, $\bar{\varepsilon}$ should be determined dynamically from the equations of motion. The dissipative cutoff is no longer an independent parameter but, according to the Kolmogorov theory of small-scale turbulent motions,

$$\bar{\lambda}_0^2 = \frac{\bar{\varepsilon}}{\nu_0^3 k_d^4} \frac{(2\pi)^d}{S_d} \tag{3.1}$$

is dimensionless and typically order 1 in magnitude. In other words, the Navier-Stokes equation with forcing (2.27) is subject to initial and boundary conditions, an element not existing in conventional renormalization group methods applied to infinite systems.

In finite systems, the average rate of energy dissipation per unit mass $\bar{\varepsilon}$ is:

$$\bar{\varepsilon} = \frac{1}{V} \frac{1}{T} \int \varepsilon(x,t) d^3x\, dt \tag{3.2}$$

where

$$\varepsilon(x,t) = \frac{\nu_0}{2}\left(\frac{\partial v_i}{\partial x_j} + \frac{\partial v_j}{\partial x_i}\right) = \nu_0 \frac{\partial v_i}{\partial x_j}\left(\frac{\partial v_i}{\partial x_j} + \frac{\partial v_j}{\partial x_i}\right) \tag{3.3}$$

where $V = L^3$ and T characterizes the time scale for evolution of the flow. Equations (2.1), (2.27), (3.2), (3.3) with the imposed initial and boundary conditions represent a closed set of equations to which we apply the dynamic renormalization group ideas outlined in Sec. 2.

To evaluate $\bar{\varepsilon}$ given by (3.2), (3.3), we eliminate small scales from (3.3) following the technique of Sec. 2. After eliminmation of scales of size of order $V^{1/3}$ and smaller, it is clear that we can neglect the variation of $\varepsilon^<$ in the volume V so that

$$\bar{\varepsilon} \simeq \varepsilon^< \tag{3.4}$$

Here $\varepsilon^{<}(k,t)$ is the inverse Fourier transform of

$$\varepsilon(\hat{k}) = \nu_0 \int [q_\ell (k-q)_\ell v_j(\hat{q}) v_j(\hat{k}-\hat{q}) + \\ + q_\ell v_\ell(\hat{k}-\hat{q})(k-q)_j v_j(\hat{q})]\, d\hat{q}/(2\pi)^{d+1} \tag{3.5}$$

after elimination of small scales.

The integral in (3.5) contains all modes from the domain $0 < k < \Lambda$. Our goal is to evaluate the coarse-grained or renormalized expression for dissipation which does not include the modes $\Lambda e^{-\ell} < k < \Lambda$. As in Sec. 2, we introduce the modes $v^{>}(\hat{k})$ and $v^{<}(\hat{k})$ belonging to the strips $\Lambda e^{-\ell} < k < \Lambda$ and $0 < k < \Lambda e^{-\ell}$, respectively. Then the first term on the right side of (3.5) becomes

$$\varepsilon_1 = \nu_0 \int q_\ell (k-q)_\ell [v_j^{<}(\hat{q}) v_j^{<}(\hat{k}-\hat{q}) + \\ + 2v_j^{<}(\hat{q}) v_j^{>}(\hat{k}-\hat{q}) + v_j^{>}(\hat{q}) v_j^{>}(\hat{k}-\hat{q})]\, d\hat{q}/(2\pi)^{d+1} \tag{3.6}$$

In order to eliminate $v^{>}$ from (3.6), we substitute the formal solution of the equation of motion (2.5) recursively for $v^{>}$ in (3.6). This generates a perturbation expansion for ε_1 in powers of λ_0. The resulting series is then averaged over the part of the random force belonging to the interval $\Lambda e^{-\ell} < k < \Lambda$. In this manner we eliminate the modes $v^{>}$. The procedure is presented in diagrammatic form by Fig. 2. In the renormalization of ε there are two kinds of vertices: the solid circle stands for $\nu_0 q_\ell (k-q)_\ell$ while the open circle stands for $-(i\lambda_0/2)P_{\ell mn}(\vec{k})$. It follows that

$$\Delta\varepsilon_1 = -4\nu_0 \lambda_0^2 D_0 \int q_j (k-q)_j P_{\ell mn}(\vec{q}) P_{\ell\mu\nu}(\vec{k}-\vec{q}) G^0(\hat{q}) G_0(\hat{k}-\hat{q}) \times \\ \times |G^0(\hat{q}-\hat{q}_2)|^2 |\hat{q}-\hat{q}_2|^{-d} P_{\mu n}(\hat{q}-\hat{q}_2) v_m(\hat{q}_2) \times \\ \times v_\nu(\hat{k}-\hat{q}_2)\, d\hat{q} d\hat{q}_2/(2\pi)^{2d+2} \tag{3.7}$$

Here $\Lambda e^{-\ell} < q < \Lambda$ while $0 < q_2 < \Lambda$. The result (3.7) can be simplified in the spirit of the renormalization group: we neglect both k and q_2 in comparison with q for $\Lambda e^{-\ell} < q < \Lambda$. Since $P_{\ell mn}(\vec{q})P_{\ell\mu\nu}(\vec{q})P_{\mu n}(\vec{q}) = 0$, some caution is necessary here to keep the leading order non-vanishing term in the resulting integral. Performing the integration over Ω and neglecting Ω_2 in comparison with Ω, where $\hat{q} = (\vec{q},\Omega)$ and $\hat{q}_2 = (\vec{q}_2,\Omega_2)$, gives

$$\Delta\varepsilon_1 = \frac{\lambda_0^2 D_0}{\nu_0^2} \int \frac{[q_m P_{n\mu\nu}(q) + q_n P_{m\mu\nu}(q)]}{q^9} \times$$

$$\times (q_2)_\mu (q_2)_n v_m^<(\hat{q}_2) v_\nu^<(\hat{k}-\hat{q}_2) \frac{d^3q d^3q_2 d\Omega_2}{(2\pi)^7} \qquad (3.8)$$

Comparing expressions (3.8) and (2.9) gives the result

$$\Delta\varepsilon_1 \simeq \Delta\nu \int (q_2)_n (k-q_2)_n v_m^<(\hat{q}_2) v_m^<(\hat{k}-\hat{q}_2) d\hat{q}_2 / (2\pi)^4 \qquad (3.9)$$

in the limit $k \to 0$.

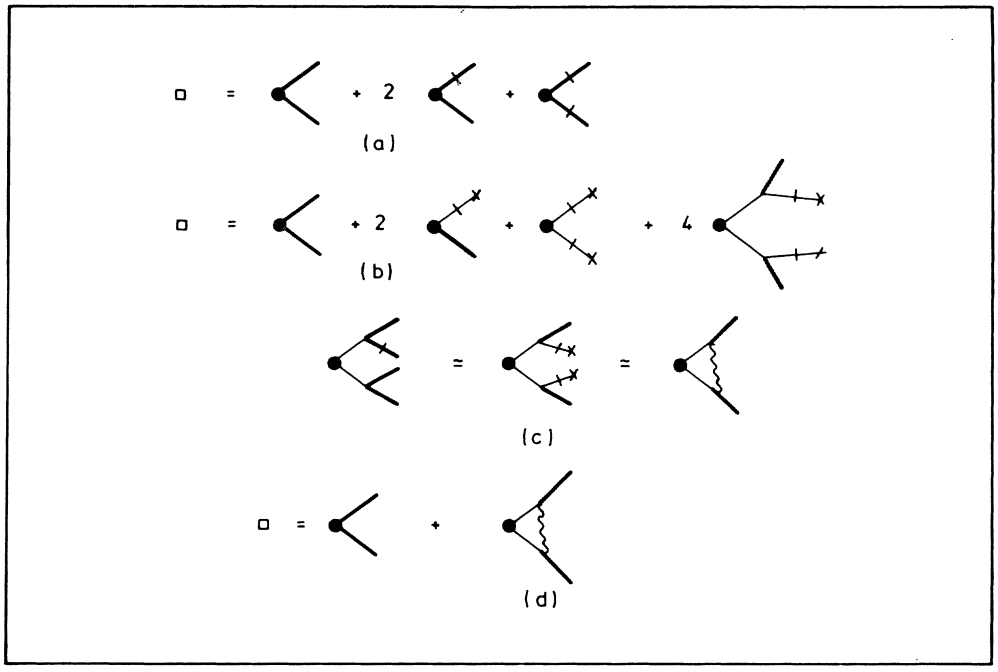

Fig. 2 A diagammatic representation of the coarse-graining (renormalization) of the dissipation rate ε, which is represented by □. The vertex, represented by the solid circle, is $\nu_0 q_i(k-q_i)$, while the dot vertex is $(i\lambda_0/2)P_{\ell mn}(\vec{k})$.
(a) Diagrammatic representation of (3.6).
(b) Irreducible diagram expansion of $\varepsilon^<$.
(c) Second-order correction, included in (3.7).
(d) Diagrammatic representation of (3.7), which is asymptotically exact as $\ell \to 0$.

It follows from (3.9) and the corresponding result for the second integral in (3.5) (which is treated similarly) that, upon using the local homogeneity assumption to transform back to physical space,

$$\varepsilon^{<}(\vec{x},t) = \nu(\ell)\left(\frac{\partial v_i^{<}}{\partial x_j}+\frac{\partial v_j^{<}}{\partial x_i}\right)\frac{\partial v_i^{<}}{\partial x_j} \tag{3.10}$$

where $\vec{v}^{<}(\vec{x},t)$ is defined as the inverse Fourier transform of $\vec{v}^{<}(\hat{k})$. The inverse Fourier transform of $v^{<}$ is defined in the usual way as

$$\vec{v}^{<}(\vec{x},t) = \int_{-\infty}^{\infty} \vec{v}^{<}(\hat{k}) e^{-i\vec{k}\vec{x}} e^{-i\omega t} d\vec{k}\, d\omega \tag{3.11}$$

where the integrals may be taken with infinite range since high modes do not contribute to the Fourier integral.

It can be shown that $\varepsilon^{<}(\vec{x},t)$ given by expression (3.10) is independent of ℓ in the limit of large ℓ. Renormalizing only the subgrid scale motions, we identify $\varepsilon^{<}$ derived above with $\bar{\varepsilon}$, which enters the definition of the random force. Together with (2.15) and (3.10), this implies that

$$\bar{\varepsilon} = \frac{\nu_0}{2}\left[1+\frac{3\tilde{A}_d}{8}\frac{\bar{\varepsilon}}{\nu_0^3\Lambda^4}(e^{4\ell}-1)\right]^{1/3}\left(\frac{\partial v_i^{<}}{\partial x_j}+\frac{\partial v_j^{<}}{\partial x_i}\right)^2$$

Introducing the mesh size $\tilde{\Delta}$ as the smallest unrenormalized scale, i.e. $\tilde{\Delta} = \pi\Lambda^{-1}e^{\ell}$, and recalling that, in the Kolmogorov theory

$$\Lambda \equiv k_d \simeq \alpha(\bar{\varepsilon}/\nu_0^3)^{1/4} \tag{3.12}$$

with $\alpha \simeq 0.2$ we obtain ($\Delta = 2\tilde{\Delta}$ is the half-width of the Gaussian filter, see MOIN & KIM [14]):

$$\bar{\varepsilon} = \frac{\nu_0}{2}\left[1+H\left(\frac{3\tilde{A}_d}{8(2\pi)^4\nu_0^3}\bar{\varepsilon}\Delta^4 - C\right)\right]^{1/3}\left(\frac{\partial v_i^{<}}{\partial x_j}+\frac{\partial v_j^{<}}{\partial x_i}\right)^2 \tag{3.13}$$

where $H(x) = x$ $(x>0)$, 0 $(x<0)$. It follows that the renormalized viscosity is given by

$$\nu_R = \nu_0\left[1+H\left(\frac{3\tilde{A}_d}{8(2\pi)^4\nu_0^3}\bar{\varepsilon}\Delta^4 - C\right)\right]^{1/3} \tag{3.14}$$

Here $C = (3\tilde{A}_d/8(2\pi)^4/\alpha^4 \approx 50$ since $A_3 \approx 0.0118$ (see below) and $\alpha \approx 0.2$. The ramp function H appears in (3.13) because $\ell > 0$ in order for renormalization to be possible. The renormalized equation of motion for $v^<$ is thus

$$\frac{\partial \vec{v}^<}{\partial t} + \vec{v}^< \cdot \nabla \vec{v}^< = -\frac{\nabla p}{\rho} + \vec{f} + \nabla \cdot \nu_R \nabla \vec{v}^< \tag{3.15}$$

where ν_R, given by (3.14), is related to $\bar{\varepsilon}$ by

$$\bar{\varepsilon} = \nu_R \left| \frac{\partial v_i^<}{\partial x_j} + \frac{\partial v_j^<}{\partial x_i} \right| \frac{\partial v_i^<}{\partial x_j}$$

The key assumptions in the derivation of (3.14) - (3.15) are that the renormalized scales are locally homogeneous and isotropic and belong to an inertial range characterized by the Kolmogorov $k^{-5/3}$ spectrum. This implies that the eliminated scales are much smaller than the distance y to the nearest wall, for only such scales can be isotropic. In the derivation of (3.14) - (3.15), we implicitly assume that $\Delta << y$ as well as $\pi/\Delta < k_d$. Thus, Δ must decrease as the distance to the nearest wall y decreases, so it follows from (3.14) that $\nu_R \to \nu_0$ as $y \to 0$.

On the other hand, in the region far from the wall

$$\frac{3\tilde{A}_d}{8(2\pi)^4} \bar{\varepsilon} \frac{\Delta^4}{\nu_0^3} >> C$$

so that the solution to (3.14) is

$$\nu_R = \frac{1}{4} \left| \frac{3\tilde{A}_d}{(2\pi)^4} \right|^{1/2} \Delta^2 \left(\left| \frac{\partial v_i^<}{\partial x_j} + \frac{\partial v_j^<}{\partial x_i} \right|^2 \right)^{1/2} \tag{3.16}$$

which has the form of the classical Smagorinsky eddy viscosity (1.1). The numerical coefficient in (3.16) is evaluated using $\tilde{A}_3 \approx 0.23$ by (2.10). The explicit expression for ν_R far from walls is

$$\nu_R = C_\nu \Delta^2 \left[\left| \frac{\partial v_i^<}{\partial x_j} + \frac{\partial v_j^<}{\partial x_i} \right|^2 \right]^{1/2} \tag{3.17}$$

with $C_\nu \approx 0.0053$.

In contrast to (3.17) the expression used by DEARDORFF [4] is given by (3.17) with $C_\nu \approx 0.0070$. In stratified turbulence, DEARDORFF [5] argued

that $C_\nu \simeq 0.013$ worked better, but this is likely due to neglecting other effects of the stratification on the subgrid turbulence. MOIN & KIM [14] performed their simulations with $C_\nu \simeq 0.003$. However, in order to prevent the turbulence in the wall region from decaying, MOIN & KIM redefined the average dissipation $\bar{\varepsilon}$ as the turbulent dissipation.

$$\bar{\varepsilon} = \frac{\nu_0}{2} \langle (S_{ij} - \langle S_{ij} \rangle)^2 \rangle \tag{3.18}$$

where

$$S_{ij} = \frac{\partial v_i}{\partial x_j} + \frac{\partial v_j}{\partial x_i}$$

and $\langle\ \rangle$ stands for the horizontal average over all scales. They also neglect the effect of the random forcing due to subgrid scale motions. MOIN & KIM [14] pointed out that their calculated turbulent intensities were insensitive to variations of the constant in (3.18) by $\simeq 40$ %. Thus, we conclude that the agreement between calculated and "experimental" data are rather good.

Although the renormalized equation of motion derived in this section is basically the same as used far from the wall by DEARDORFF [4-7] and others, it differs significantly in the wall region where formula (3.16) is not valid. In the wall region the renormalized equations (3.13) - (3.15) do not lead to a turbulent-eddy viscosity proportional to Δ^2. Near the wall, the argument of H( ) in (3.14) is negative, so $\nu_R = \nu_0$.

Another important feature of finite systems is the role of the random force generated by elimination of small scales. This force is Gaussian with correlation function given by the diagrams presented in Fig. 1. The analytic expression for the correlation function corresponding to these diagrams follows from the second term on the right side of (2.6) and is:

$$\langle f_i(\hat{k}) f_j(\hat{k}') \rangle = D' (2\pi)^{d+1} k^2 \left\{ \delta_{ij} - \frac{k_i k_j}{k^2} \right\} \delta(\vec{k}+\vec{k}') \, \delta(\omega-\omega') \tag{3.19}$$

with

$$D' = \frac{D_0^2 \lambda_0^2}{2} \int^{>} \frac{d^d q}{(2\pi)^d} \frac{d\Omega}{2\pi} P_{\ell mn}(\hat{k}) P_{\ell\mu\nu}(\hat{k}) P_{m\mu}(\hat{q}) P_{n\nu}(\hat{k}-\hat{q}) q^{-d} |k-q|^{-d} \times$$

$$\times |G^0(\hat{q})|^2 |G^0(\hat{k}-\hat{q})|^2 \tag{3.20}$$

The integrals in (3.20) are readily evaluated giving

$$D' = \frac{A_d}{9}\frac{\nu_0^3}{k_d}\bar{\lambda}_0^4\,\frac{e^{(d+7)\ell}-1}{d+7} \tag{3.21}$$

A recursion relation for $D'(\ell)$ is derived using (2.15) and (2.16):

$$\frac{dD'}{d\ell} = \frac{A_d}{9}\frac{d}{d\ell}\left(\frac{\bar{\lambda}^4(\ell)\nu^3(\ell)}{k_d(\ell)}\right)$$

$$D'(0) = 0$$

so that

$$D' = \frac{A_d}{9}\frac{\nu_0^3\,\bar{\lambda}_0^4}{k_d}\,\frac{(e^{9\ell}-1)}{1+(3A_d/4)\bar{\lambda}_0^2(e^{4\ell}-1)}$$

$$\doteq \frac{2.09\,\bar{\varepsilon}}{k_d^5}\,\frac{H\{1.5\times10^{-8}(\bar{\varepsilon}/\nu_0^3)\Delta^9 k_d^5-100\}}{1+H(5.5\times10^{-5}(\bar{\varepsilon}/\nu_0^3)\Delta^4-100)} \tag{3.22}$$

It should be emphasized that RNG procedures dealing with infinite systems neglect the induced random force (3.19) in the limit $k \to 0$, because its correlation function is porportional to k^2, which is small in comparison with the correlation $O(k^{-3})$ of the bare force. However, in finite systems where k is bounded from below, the role of the induced force should be reassessed. Far from the wall where $\frac{3}{4}A_d\bar{\lambda}_0^2 e^{4\ell} = \frac{3}{4}A_d\frac{\bar{\varepsilon}}{\nu_0^3\pi^4}\Delta^4 >> 1$ we obtain from (2.25):

$$D' = \frac{\nu_0^3\bar{\lambda}_0^2}{k_d}e^{5\ell} = \frac{\nu_0^3\bar{\lambda}_0^2}{k_d}\left(\frac{k_d}{k_c}\right)^5 \tag{3.23}$$

where $k_c = k_d e^{-\ell}$ is the mode cutoff for the RNG. Thus the condition for the induced force to be small when compared to the bare force is

$$\frac{\nu_0^3\bar{\lambda}_0^2}{k_d}\left(\frac{k_d}{k_c}\right)^5 k^2 < \frac{D_0}{k^3}$$

which holds provided that

$$\left(\frac{k}{k_c}\right)^5 < 1 \quad (k_c << k_d, \quad k \le k_c)\ . \tag{3.24}$$

Thus, far from walls, the RNG induced force is negligible.

However, in the buffer region, defined by the condition

$$1 \lesssim \frac{3}{4} A_d \bar{\lambda}_0^2 e^{4\ell} = O(C) = O(100)$$

the ratio of the RNG induced force to the bare force is

$$\left(\frac{k}{k_d}\right)^5 \frac{\nu_0^3 k_d^3 \bar{\lambda}_0^4}{D_0} \frac{A_d(e^{9\ell}-1)}{1+\frac{3}{4}A_d\bar{\lambda}_0^2(e^{4\ell}-1)} \gtrsim 1 \tag{3.25}$$

provided that

$$\frac{k}{k_d} \gtrsim 0.1 \tag{3.26}$$

noting that $\bar{\lambda}_0^2 = 2D_0/\nu_0^3 k_d^4 = O(1)$.

Thus in the narrow region of scales satisfying

$$0.1\, k_d \lesssim k \lesssim k_c \tag{3.27}$$

with

$$A_d e^{4\ell} = A_d \left(\frac{k_d}{k_c}\right)^4 \simeq 1 \tag{3.28}$$

the induced force is larger than the bare stirring forces and cannot be neglected.

Inequalities (3.28) - (3.29) define the wave vector range in the buffer layer where the induced RNG force cannot be omitted. Without the action of this random force, the turbulence in the buffer layer is likely to decay due to the enhanced (renormalized) viscosity.

4. DISCUSSION AND CONCLUSIONS

In this work we used renormalization-group ideas in order to systematically eliminate small scales and construct a subgrid model. The need for the systematic procedure is demonstrated by the formula (3.14) for the viscosity ν_R which, in the wall region, differs quite substantially from the Smagorinski expression. It has become clear from the recent studies of the large-eddy simulation (MOIN & KIM [14]) that the extrapolation of the Smagorinski formula up to the wall does not lead to satisfactory results, and that additional turbulence modelling is needed to achieve agreement with experimental data. The expression for the turbulent viscosity

derived here agrees well with formulas used by DEARDORFF [4] and MOIN & KIM [14] far from the wall. We expect that this formulation will provide a good description of the entire flow in the channel.

Another outcome of the present theory is the appearance of the random force as a result of small-scale elimination. This result deserves some further comment. BARDINA, FERZIGER & REYNOLDS [1] compared different subgrid models for homogeneous turbulence. They showed that simply using the Smagorinski viscosity results in quite low correlation coefficients of the subgrid scale stresses with those produced in full numerical solutions of the Navier-Stokes equations, especially for homogeneous shear turbulence.

BARDINA et al. [1] also introduced a so-called scale-similarity model in the subgrid scale, which represented the Reynolds stress R_{ij} in the Navier-Stokes equation in terms of filtered scales $u_i' = u_i - \bar{u}_i$ where u_i and $\bar{u}_i$ are the exact and large-eddy velocity, respectively. That is, the subgrid stresses on scales from 0 to Δ are approximated as the filter stresses that involved scales between, for example, Δ and 2Δ. That is

$$R_{ij} \simeq u_i u_j - \bar{\bar{u}}_i \bar{\bar{u}}_j \tag{4.1}$$

where $\bar{\bar{u}}_i$ is the velocity field filtered over 2Δ. BARDINA et al. [1] showed that this model gives a correct representation of turbulence intensities. However, they also showed that this scale-similarity model is not dissipative, so it is unable to describe the decay of turbulence. They showed that a linear combination of these two models is good for a description of both turbulent intensities and dissipative processes, at least in homogeneous turbulence. It is easy to see from (4.1) that $\overline{R_{ij}} = 0$, which implies that $\overline{R_{ij}^2} \simeq O(k^2)$ when $k \to 0$. Thus R_{ij}, as proposed by BARDINA et al. [1], has the properties of the random force that we have derived here. It is an essential result of the present theory that one *must* take into account both the eddy viscosity and the random force since they appear *simultaneously* as a result of the elimination of small scales.

It can be shown (YAKHOT & ORSZAG, to be published) that, when additional physical processes such as rotation, etc. are acting, the equations for the large-eddy simulations based on the present renormalization-group method include many new terms which are usually not taken into account in large-eddy simulations.

This work was supported by the Air Force Office of Scientific Research under Contract No. F49620-83-C-0064, the Office of Naval Research under Contract N00014-82-C-0451, the NASA Langley Research Center under Contract NASI-16977, and the National Science Foundation under Grant ATM8310210.

REFERENCES

[1] J. BARDINA, J. FERZIGER, W.C. REYNOLDS: to be published (1983).

[2] M.E. BRACHET, D.I. MEIRON, S.A. ORSZAG, B.G. NICKEL, R.H. MORF, U. FRISCH: J. Fluid Mech. 130, 411 (1983).

[3] G. COMTE-BELLOT: Eccoulement turbulent entre deux parois paralleles. Publications Scientifiques et Techniques du Ministere de l'Air, no. 419 (1965).

[4] J.W. DEARDORFF: J. Fluid Mech. 41, 453 (1970).

[5] J.W. DEARDORFF: J. Comp. Phys. 7, 120 (1971).

[6] J.W. DEARDORFF: J. Atmos. Sci. 29, 91 (1972).

[7] J.W. DEARDORFF: J. Fluids Eng. 429 (1973).

[8] D. FORSTER, D.R. NELSON, M.J. STEPHEN: Phys. Rev. A16, 732 (1977).

[9] J.-D. FOURNIER, U. FRISCH: Phys. Rev. A28, 1000 (1983).

[10] S.J. KLINE, W.C. REYNOLDS, F.A. SCHRAUB, P.W. RUNSTADLER: J. Fluid Mech. 30, 741 (1967).

[11] R.H. KRAICHNAN: J. Math. Phys. 2, 124 (1961).

[12] D.K. LILLY: in Proc. IBM Sci. Comp. Symp. on Environmental Sciences, White Plains, New York, p.195 (1967).

[13] P.C. MARTIN, C. DeDOMINICIS: Phys. Rev. A19, 419 (1979).

[14] P. MOIN, J. KIM: J. Fluid Mech. 118, 341 (1982).

[15] E.A. NOVIKOV: JETP 47, 5 (1964).

[16] S.A. ORSZAG, A.T. PATERA: Phys. Rev. Letters 47, 832 (1981).

[17] E.R. VAN DRIEST: J. Aero. Sci. 23, 1007 (1956).

[18] H.W. WYLD: Ann. Phys. (N.Y.) 14, 143 (1961).

[19] V. YAKHOT: Phys. Rev. A23, 1486 (1981).

METEOROLOGICAL DYNAMICS

THREE-DIMENSIONAL CUMULUS CLOUD CONVECTION

U. SCHUMANN

1. INTRODUCTION

1.1 Objective

A cloud can be defined as a visible ensemble or aggregate of so-called hydrometers, i.e., minute particles consisting of liquid or frozen water in a wide variety of forms. The processes involved in the formation of clouds range from the very small-scale processes responsible for the nucleation and growth of cloud particles (cloud microphysics) up to the very large-scale dynamical processes that are associated with synoptic weather systems. A large portion of the study of clouds has been focused on their microphysical processes, evidenced by the voluminous material on cloud microphysics, with less attention paid to the dynamics of cloud formation, COTTON, LILLY [1,2]. Much has been learned in recent years about the structure of strong convection, with the help of observational tools, particularly doppler-radar, BROWNING, SCHROTH [3,4]. With the advent of powerful scientific computers such as the CRAY-1, substantial advances in numerical modelling of cumulus convection has been achieved up to now, and even more can be expected in the near future, SCHLESINGER [5].

The objective of this paper is to show the importance and potential of studies of nonlinear fluid dynamics aspects, the need for three-dimensional simulation models together with suitable field observations, and the present state of research in the field.

1.2 Cloud genera

This paper focuses on clouds of convective origin. Meteorologists commonly reserve the word *convection* for vertical flows, while the term *advection* is introduced to indicate horizontal transport.

Three conditions often viewed necessary for cloud formation from a parcel of moist air are 1) a sufficient amount of water vapour, 2) a proper distribution of condensation and ice nuclei, and 3) a process that cools the

air-parcel so that the vapour concentration exceeds its saturation value. This cooling may be due to thermal radiation heat loss (which is typical for formation of fog or certain stratus clouds), turbulent heat loss or mixing with cold and humid air, or due to expansion cooling by lifting the moist air to higher levels with low pressure. This lifting may be due to enforced flow of the air over mountains, due to synoptic effects like cyclonic motion and low level flow convergence, or due to buoyancy-induced convective motion. Synoptic lifting motion is the standard cause for the often observed large-scale stratus clouds. Convective motion, which is often a consequence of heat and humidity supply to the planetary boundary layer from the ground, leads to cumulus clouds. Weak convection results into small cumulus clouds; strong convection may result in big cumulonimbus clouds that may cause large thunderstorms.

1.3 Cloud scales

The *vertical scale* of clouds that occur in the earth's atmosphere are principally confined to the troposphere (the first 10 to 15 kilometers), in which the mean temperature decreases with increasing height up to the tropopause. The troposphere includes the main fraction of the mass of the atmosphere: the integral density height $H = (1/\rho(o))\int_0^\infty \rho(z)dz \approx 8$ km. Vertical motion restricted to the first 1 or 2 kilometers (essentially the planetary boundary layer) represents *shallow convection. Deep convection* on the other hand, extends through heights comparable with H. This distinction has consequences with respect to models: For shallow convection the density variation may be neglected in all but the bouyancy terms (Boussinesq-approximation), whereas for deep convection the density variations have to be taken into account in a more thorough manner.

To first order, the *horizontal* scale of convective motion is equal to or one order of magnitude larger than the vertical scale. According to the meteorological scale definitions, this means that we have to consider the micro-α-scales (250 m - 2.5 km), the meso-ϒ-scales (2.5 km - 25 km), and perhaps the meso-β-scales (25 km - 250 km). For these scales of motion, we may neglect the curvature of the earth's surface, and may assume a negligible Coriolis force. For the larger scales one often assumes hydrostatic equilibrium. This means that deviations from the hydrostatic pressure profile p(z) with $\partial p/\partial z = -\rho g$ are negligible. For motions with vertical scales comparable to or larger than the horizontal scales, non-hydrostatic models have to be applied.

From a fluid dynamics point of view, the cloud scales extend down to the scales of the smallest turbulent eddies. As shown by KOLMOGOROV, the size η of these eddies depends on the amount of turbulent kinetic energy supplied for dissipation ε and the kinematic viscosity ν of air ($\approx 2.10^{-5} m^2/s$), $\eta = (\nu^3/\varepsilon)^{1/4}$. The dissipation rate may be estimated from the root-mean-square

velocity fluctuations u and integral length scale of turbulent motion ℓ to be $\varepsilon = u^3/\ell$. Typical values for strong convection are u = 10m/s, ℓ = 100m, so that $\eta \approx 0.1$mm. GASSMANN et al. [6] have estimated that 95 % of the kinetic energy of a thunderstorm is put into turbulence. This estimate shows that cumulus convection simulation requires proper turbulence models.

The cloud microphysics deals with the behaviour of cloud paritcles. Here the scales range from 10^{-8}m, the size of the smallest aerosol particles which form the condensation nuclei, up to 10cm, which is the size of the largest hail stones observed. Typical rain drops have the size of 0.1 mm to 5 mm. In a cumulus convection model, proper continuum models have to be set up to describe the effect of microphysics on the flow scales. It is noteworthy that the scales of microphysics and turbulence overlap in the range of rain-drop diameters and that the resulting interactions are not yet sufficiently studied.

1.4 Importance of clouds

Clouds have large effects on our weather and climate, both globally and locally on meso-scales.

The importance of understanding the manner in which a change in the cloud amount and distribution may act as a climatic component has been accentuated by concern over the possibility of inadvertent modification of the global climate by human activities. The presence of clouds has profound effect upon the radiation budget of the entire planet. According to different references, about 20-22 % of the solar radiation is reflected from clouds and 26-36 % of the terrestial radiation is transmitted via clouds. Satellite studies indicate that approximately 50 % of the earth is covered by clouds, HOBBS & DEEPAK [7]. From a simple analysis, BOLLE [8, p.266] shows that 1% change in global cloud cover results in 1.2K surface temperature change. Following the same manner of analysis, we have determined that a global mean height increase of all the clouds by 200 m causes an increase of the surface temperature by 1K, mainly because the longwave radiation from the cloud tops is reduced if lifted to higher levels with smaller temperatures. Lifting of low clouds has an opposing effect, HANSEN, JOHNSON, LACIS, LEBEDEFF, LEE, RIND & RUSSELL [9]. Also, the spatial geometry of the clouds is important for radiative transfer in the atmosphere. It has been shown that the outgoing longwave radiation flux can differ as much as 40 % for convective cloud systems from that of stratus type, HOBBS & DEEPAK [7]. Thus changes in cloud cover, height, and structure may counterbalance some of the heating that has been predicted for increasing CO_2-concentration.

On the meso-scale, one of the most severe weather events caused by

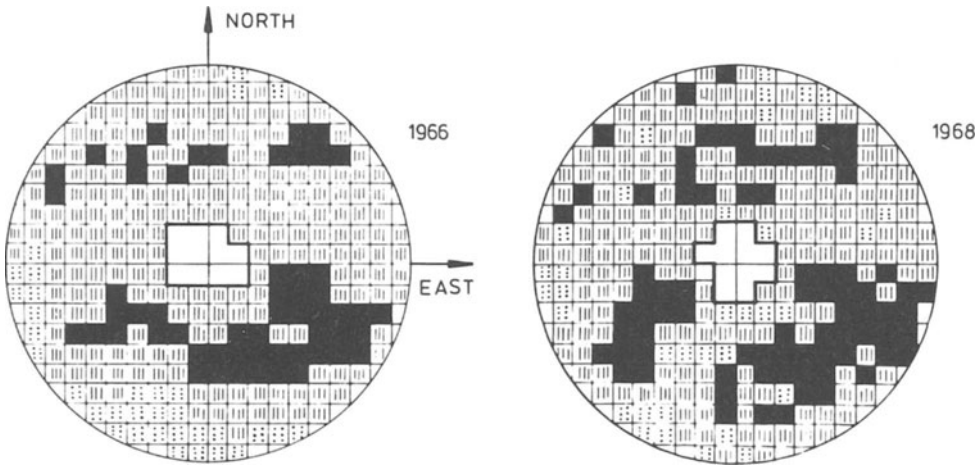

Fig. 1 Frequency of convective precipitating clouds in southern Bavaria in the years 1966 and 1968 as observed by SINGLER [12]. The center of the radar observations is in Riem (1966), 11°45'E 48°8'N, or in Oberpfaffenhofen (1968), 11°16'E 48°5'N. The radius corresponds to about 160 km.

cumulus convection is a strong thunderstorm. Such a storm is produced by a cumulo-nimbus cloud, and always accompanied by lightning and thunder. However, lightning absorbs only about 1 % of the storm energy, GASSMANN, HASCHKE, RUDIN [6]. At least as important are the resultant strong and gusty winds, flash flooding, and occasionally hailstorms, all of which are severe hazards. For example, downdrafts and microbursts produced in thunderstorms and strong showers have been held responsible for aircraft accidents even recently, MELVIN [10].

In Germany, there are up to 35 thunderstorm days annually, with the maximum values in southern Germany, KESSLER [11, p.34]. Convective clouds with precipitation are correlated with orography. For example, SINGLER [12] has measured convective activity in southern Bavaria during two summers with a 3cm-weather-radar (see Figure 1). It clearly shows the increased activity southwest of Munich in the foothills of the Alps.

In the tropics, up to 100 thunderstorms days are observed. Such thunderstorms not only have strong local effects but also a large influence on the global heat and momentum transfer.The basic function of such deep convective clouds is to transfer heat from the lower to the higher levels of the troposphere. For example, the upward transfer of energy by deep convection is the primary driving mechanism for the Hadley cell circulation in the tropics, KESSLER [11, p.548]. This circulation transports the energy excess of the equatorial region towards higher latitudes.

Also, clouds and the resulting precipitation have direct impact on our environment. E.g., chemical compounds are deposited to the ground by *wash-out* or *scavenging*. For example, more than 50 % of SO_2 deposition from the atmosphere is performed by wet processes, IRIBARNE [13].

With respect to weather, prediction of clouds and the resultant precipitation is still very uncertain. Thus the study of cloud physics is important for this purpose also.

1.5 Overview of the paper

The subsequent discussion concentrates on a qualitative description of the conditions (Chapter 2) and flow patterns (Chapter 3) responsible for deep convection that may turn into strong thunderstorms. From the qualitative discussion we will then (Chapter 4) deduce a list of requirements for proper numerical simulation models.

2. CONDITIONS FOR DEEP CONVECTION

2.1 Basic equations

Neglecting the earth's rotation, external heat sources like radiation, diffusion fluxes and all other irreversible processes, the basic equations describe the following conservation laws.

Conservation of mass: $$D\rho/Dt \equiv \partial\rho/\partial t+\mathrm{div}(\rho\vec{v}) = 0 \qquad (2.1)$$

Conservation of momentum: $$D(\rho\vec{v})/Dt = -\mathrm{grad}p-\rho\vec{g} \qquad (2.2)$$

Conservation of entropy: $$D(\rho s)/Dt = 0 \qquad (2.3)$$

Conservation of total water mass: $$D(\rho(m^1+m^2+m^3))/Dt = 0 \qquad (2.4)$$

Here, ρ is the density, $\vec{v}$ is the velocity vector, p is pressure, $\vec{g}$ is the vector of gravity, s is entropy, and m^i are the mass concentrations for dry air (i = 0), water vapour (i = 1), liquid (i = 2), and ice water (i = 3), respectively. The pressure satisfies to a good approximation the equation of state for an ideal gas

$$p = \rho RT,\ R = m^0R_0+m^1R_1 \qquad (2.5)$$

where R is the effective gas constant of the air-vapour mixture. The relationship between temperature T and entropy s can be defined differentially by

$$ds = c_p dT/T - R dp/p + s_k dm^k \tag{2.6}$$

where $c_p \equiv c_{pk} m^k$ is the effective specific heat for constant pressure and s_k are the specific entropies of the components (for equilibrium: $s_1 > s_2 > s_3$) which can be related to the heat of evaporation and freezing. The sum Σdm^k (k = 0,1,2,4) is zero because of mass conservation. Consequently, this equation shows the expected behaviour: that a parcel of air undergoing an isentropic and isobaric process exhibits an increased temperature if water is condensed or frozen.

Convection is driven by horizontal differences in density. The total buoyancy $-\text{grad}p - \rho\vec{g} = -\text{grad}p' + \vec{b}$ can be expressed in terms of a net buoyancy $\vec{b} = \rho'\vec{g}$ where we refer to a dry reference state $(p(z), T(z), \rho(z))$ and denote deviations by $f' \equiv (f - f(z))$. Then for $\rho' \ll \rho(z)$ one can deduce from the above equations:

$$\vec{b} = \rho\vec{g}(\theta'/\theta + 0.61 m^1 - m^2 - m^3 - p'/(\rho c^2)) \tag{2.7}$$

$$1/c^2 \equiv (1 - R/c_p)\rho/p \quad (c = \text{speed of sound}) \tag{2.8}$$

where we have introduced the value $(R_1/R_0 - 1) \approx 0.61$; θ is the *potential temperature* which is defined by

$$d\theta/\theta = dT/T - (R/c_p) dp/p. \tag{2.9}$$

For constant material properties we have

$$\theta = T(p_0/p)^{R/c_p}. \tag{2.10}$$

This is the temperature that an air parcel of temperature T and pressure p assumes if it is compressed adiabatically without phase changes to the reference pressure p_0.

From (2.7) it is evident that positive increments in potential temperature and water vapour produce upward acceleration, while positive liquid and solid water increments produce downward acceleration. The latter effect may be quite substantial in a thunderstorm. Liquid water contents greater than 10 g per kg of air occur, which are equivalent to a cooling of more than 3K in their effect on buoyancy. This effect adds to evaporation cooling in downdrafts. The term $p'/(\rho c^2)$ is small for small Mach number flows.

2.2 Stability criterion

For a horizontally homogeneous layer of air, the stability of the fluid depends upon its vertical temperature gradient or lapse rate $\gamma = -\partial T/\partial z$. The criterion of stability of such a layer is determined from the method of

assuming virtual displacements of a parcel of air and studying whether the consequences of such displacements will be a restoring force - in which case the stratification of the atmosphere is stable - or a force tending to further increase the displacement - in which case the stratification of the atmosphere is unstable, IRIBANE & CHO [13].

For an incompressible fluid, the stratification is neutrally stable if the vertical temperature gradient $\partial T/\partial z$ is zero. For a gas one has to account for the temperature change due to variable pressure and perhaps due to phase changes. For dry air - and to good approximation also for unsaturated moist air - the vertical temperature gradient for a parcel undergoing a virtual displacement is $\Gamma_d = g/c_p \approx 10K/km$. This corresponds to $d\theta/dz = 0$. For saturated air this lapse rate is only $\Gamma_s \approx 7K/km$. It is less because lifting causes condensation heat to become available for heating of the air.

Thus if the actual vertical temperature gradient is $\gamma = -\partial T/\partial z$, we have five possible states of stability for moist air (see also Figure 2): Here the

$$\begin{array}{rl} \gamma < \Gamma_s & \text{absolutely stable} \\ \gamma = \Gamma_s & \text{saturated neutral} \\ \Gamma_s < \gamma < \Gamma_d & \text{conditionally unstable} \\ \gamma = \Gamma_d & \text{dry neutral} \\ \gamma > \Gamma_d & \text{absolutely unstable} \end{array}$$

Here, "conditionally unstable" means that the air is unstable under the condition that the moist air is saturated.

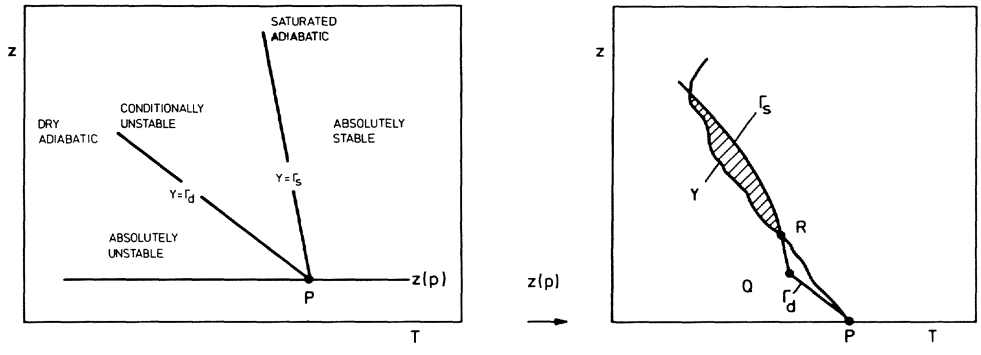

Fig. 2 Stability criteria and latent instability. T = temperature; z = height. γ indicates the temperature stratification of the atmosphere. The shadded area indicates the latent instability.

In certain cases, whole layers of atmosphere can experience lifting. This changes its stability. During lifting, because of decreasing pres- sure, the thickness of the layer grows. This causes an initially stable layer to become less stable. If humidity in the layer decreases with height, then lifting causes the layer to become saturated at the lower level first, and consequently the layer becomes absolutely unstable. This type of instability is called *potential* or *convective instability*.

2.3 Convection indices

So far, we have considered only infinitesimal or homogeneous displacements. Air can be forced to rise even in a stable atmosphere (for instance, if wind blows against a mountain slope) and it may eventually follow a process curve as indicated in Fig.2. Here the curve Γ indicates the actual stratification in the atmosphere. The parcel considered follows Γ_d until saturation at point Q (*lifting condensation level*) and then the saturated adiabatic Γ_s. At R (*level of free convection*) the net buoyancy becomes positive. From R on, the parcel is accelerated upwards. The shaded region above is the region of *latent instability*. It may extend over considerable vertical portions of the troposphere, and its upper limit controls the limit to upward acceleration of the convective motion. In this type of instability, the parcel has to be lifted over a relatively large distance, during which mixing with the environment can be large, so that the given picture can be only qualitative.

Nevertheless, this type of analysis may be taken to define an index that measures the likelihood of convection resulting in thunderstorms. For example, the "lifted index", EAGLEMAN [14, p.57], is computed by taking the average specific humidity through the layer from surface to 1km and the maximum forecast temperature for the day as parameters for a parcel of air starting to rise. This parcel is assumed to be lifted and cooled under adiabatic conditions until the 500 mb level (about 5.5 km) is reached. The temperature of the theoretically lifted parcel of air is compared with the measured temperature at the 500 mb level, and the difference between the measured and computed temperature is taken as definition of the lifted index. The measured temperature is available from weather balloons carrying radiosondes that are sent up twice a day by the weather services. A negative lifted index means that the temperature inside the parcel of air is greater than that of the surrounding atmosphere; thus, the parcel tends to rise further, the atmosphere is unstable, and a severe thunderstorm is likely.

2.4 Effect of inversions and synoptic scale motion

A factor that may both inhibit convection and favour strong thunderstorms is inversions. Inversions are layers in the atmosphere where the temperature increases with height, in contrast to the normal decrease in the troposphere. We distinguish between the inversion that is formed at the top of the planetary boundary layer and upper-air inversions, EAGLEMAN [14]. The former is due to radiation cooling at night and convective mixing during the day. The upper-air inversion layer may be formed if dry and warm air is forced to flow over moist and initially cool air due to synoptic weather events, and is located at levels of the order 800 mb (2-3 km).

Such an inversion layer suppresses cloud development until a thermal, or small cloud, acquires sufficient vertical momentum to break through the inversion layer. This delay frequently allows the resulting convection cell to grow much larger than ordinary because the stable inversion layer prevents premature mixing by a series of smaller convection events.

Of course, it is very difficult to predict whether or not there will be a disturbance strong enough to penetrate the inversion. This is an example where weather prediction may fail dramatically.

This effect is illustrated by a result of SCHUSTER & JOCHUM [17] (see Figure 3). On a summer afternoon in southern Bavaria, a single convective cloud was observed. There was no cloud of comparable size over the whole region. The single cloud persisted for more than two hours. The radiosonde

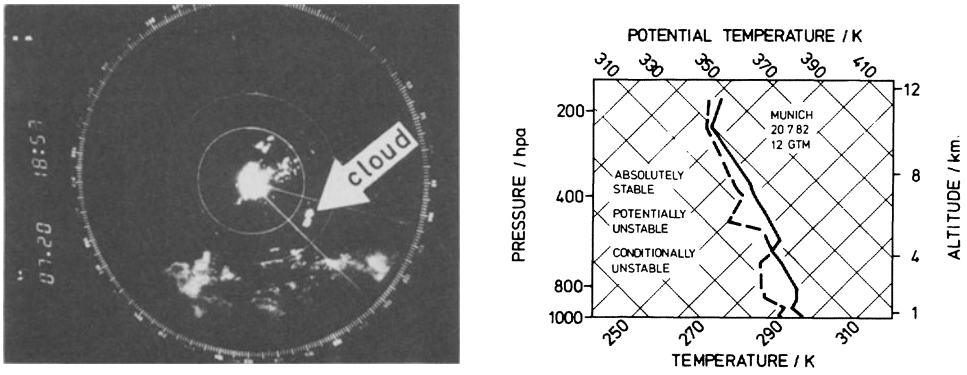

Fig. 3 Single convective cloud observed with weather radar for 20.7.82, 16.57 GMT and temperature and dew-point profile of the same day. The radar picture shows a single isolated convective cloud 45 km southeast of Oberpfaffenhofen (screen radius 160 km). The echos in the center stem from the city of Munich and those in the lower part from the Alps. The cloud was observed for more than two hours. The radiosonde shows a stable layer of very dry air above a height of 5 km.

of Munich shows a strongly stable layer above 5.5 km height. The cloud, however, extended up to a height of 10 km.

It seems reasonable that this cloud was the only one that had enough initial impulse to penetrate the stable upper inversion. It sucked up all humid and warm air from the surroundings in the lower layer like a chimney and prevented the creation of other cells in the surrounding area. Without the strong inversion many more cells of smaller height would have formed.

Cumulus convection may be initiated by lifting potentially unstable layers of air, which is induced by synoptic motion. Thus, low level flow convergence and high level flow divergence are indicative of convection. Also a cold front of a midlatitude cyclone may trigger strong and deep convection. Of course, the proper vertical wind profile also contributes to the development of strong convection, as will be discussed later.

3. FLOW PATTERN WITH DEEP CONVECTION CELLS

Depending on the geometrical complexity of the cloud forming process, one can describe clouds in Lagrangian or Eulerian frames and in terms of different numbers of independent variables. With respect to space variables we distinguish zero- to three-dimensional (OD to 3D) models (see Figure 4). Our subsequent description follows this hierarchy of dimensions.

3.1 Zero-dimensional models

In a OD-model we follow a single parcel of air as it develops as a function of time in a Lagrangian manner along a curve in space. In the simplest case this curve is characterized by the height $z_p(t)$. Thus the only independent variable is t or equivalently z_p, which is determined by integrating the upward parcel velocity. The parcel velocity is determined from the momentum balance as a function of inertia, drag relative to the environment, buoyancy and entrained momentum. Advection and pressure gradients cannot be taken into account in such a OD-model. The parcel mass changes according to entrainment from the environment. Similarly, energy and water mass balances are treated.

With such a model we can investigate the effect of entrainment of ambient air into the cloud parcel for a given mixing rate. The driving force for upward motion comes from the released condensation heat, which grows in proportion to the cloud volume while the entrainment of dry and cool air dilutes the cloud; this effect is related to the cloud surface. Thus there should exist a critical value for the minimum radius required for deep

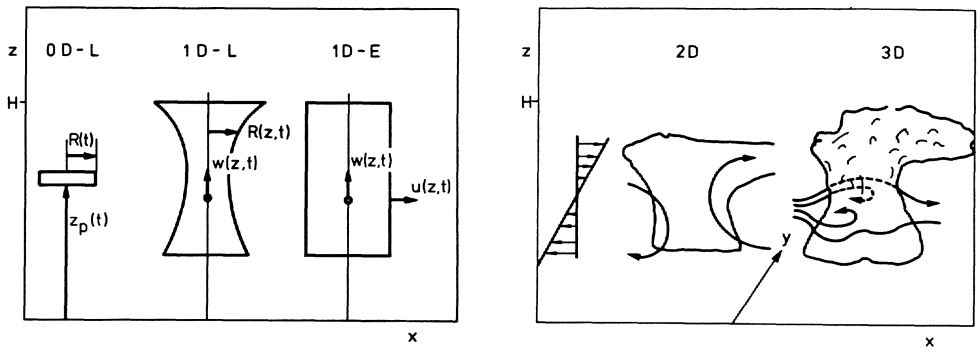

Fig. 4 Dimensional classification of cumulus cloud models.

cumulus convection. In order to estimate this radius we need a simple model for entrainment. The amount m_e of mass entrained per unit time and height depends upon the circumference of the cloud, $2\pi R$, and the turbulent velocity fluctuations. The latter are assumed to be proportional to the vertical velocity w. Thus, dimensional analysis gives $m_e = \alpha\rho wR$, where α is an empirical parameter. Laboratory experiments show that $\alpha \approx 0.1$ [11, p.507]. Using such models, it has been found, GASSMANN & HASCHKE & RUDIN [6], that the minimum critical radius for deep convection must be of the order of 1km at the top of the cloud and 2km at the lower level of the cloud to result in deep convection.

3.2 One-dimensional models

In a 1D-model we describe the dynamics of a cylinder of cloud air that encompasses the whole height of the troposphere. The radial extent of the cloud can be treated either in an Lagrangian manner (R =R(z)) or in an Eulerian manner (R = const., radial velocity u(z) describes flow over the boundary of the cylinder). In comparison to the 0D-model we can now treat vertical advection of mass, momentum, and energy. The model can be stationary or time-dependent. An example for a stationary 1D-Lagrangian model is that of HÖLLER [15]. An example for a non-stationary 1D-Eulerian model is that of NELSON [16,17].

Zero- and one-dimensional models are efficient test-beds for complex microphysics models. The process which produces rain drops, for example, involves a wide spectrum of hydrometeors of different radii. Simple cloud models assume a spectral distribution that can be described by one or two parameters. Such models cannot, for example, describe the effect of new condensation nuclei that are entrained from the side into a cloud, form new small cloud droplets and thus cause a bimodal droplet spectrum. There-

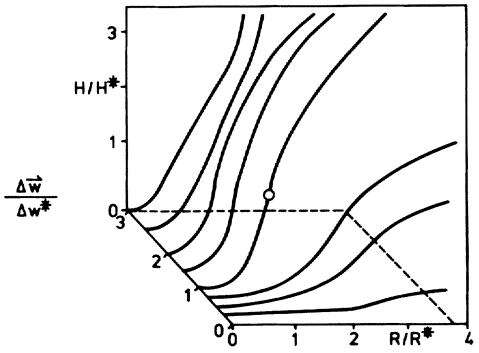

Fig. 5

Result of a sensitivity study with the Nelson-model as obtained from JOCHUM [17]. H, Δw, and R denote the computed cloud height, the input for the initial velocity, and the selected cloud radius, respectively. The results are normalized with the values for reference case, which is marked by a circle.

fore, models have been developed that resolve the spectral resolution for example by set of discrete subclasses of different sizes (typically 75 subclasses are used). HÖLLER [15] has used such a model in order to develop and test more simple cloud microphysics parametrizations. He has deduced a parametrization that treats cloud and rain water separately and describes the spectral distribution in terms of a log-normal distribution that depends upon the zeroth, first and second moments, i.e., the number of particles, the mass content, and a measure of the radar reflectivity. Higher dimensional models are more or less restricted to such simplified descriptions of the hydrometeor spectra.

The time-dependent 1D-Eulerian model of NELSON [16] treats about 50 size-classes of hydrometeors in the water and ice-phase. JOCHUM [17] applied the model in order to simulate observed isolated cumuli. Figure 5 shows the results of a sensitivity study with this model. The main conclusion is that the computed cloud height is highly sensitive to the estimated cloud radius (which controls the entrainment) and the vertical velocity at the cloud basis. This as well as the temperature excess at the basis have to be prescribed as boundary values. Thus the model result is highly dependent upon parameters which can be determined only if we proceed to higher dimensional models.

3.3 Two-dimensional models

Effects that are very difficult to treat in 1D-models but amenable to 2D-models are:

- turbulent entrainments from the sides and the top simultaneously.
- influence of lateral motion and shear.
- tilting of the convection plume.

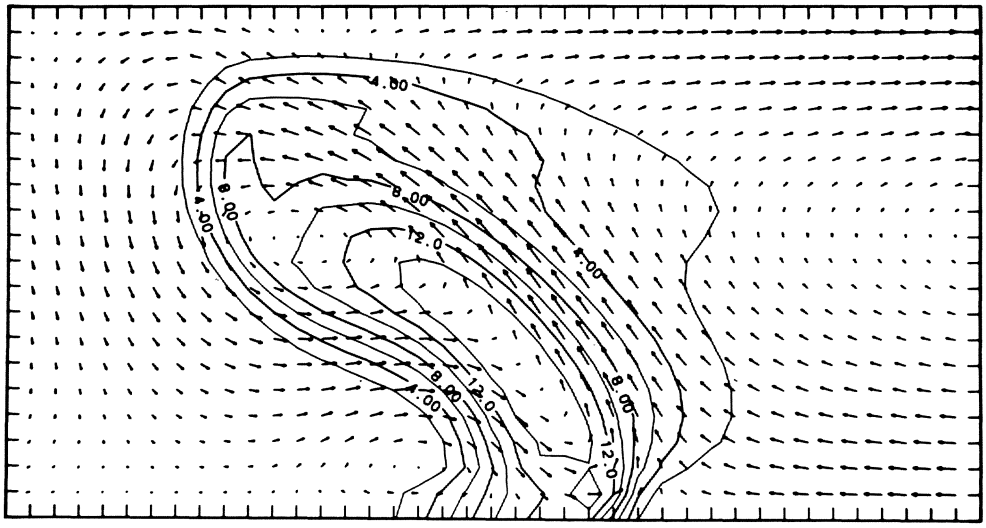

Fig. 6 Result of a two-dimensional model simulation performed by SEITTER [18]. Model circulation after 50 min. The storm is moving from left to right, all vectors are storm relative with the maximum vector equalling 28 m/s. Contours are liquid water content in g/m^3.

With respect to entrainment SQUIRES (1958) [see 11,p.519] has pointed out that the mixing of moist and dry air at the top of a cumulus may cause a considerable cooling due to evaporation, thus resulting in strongly negative buoyancy. Such mixed parcels could conceivably penetrate downwards through the plume for a considerable distance. If this occurs, then the 0D- and 1D-models are seriously incomplete. From studies of TELFORD (1975) [11, p.511], it has been concluded that the effect of top entrainment is large for shallow convection but smaller for deep convection since high-level air is simply too cool to absorb much water vapor, whereas dry, mid-level air has a tremendous capacity to absorb water vapor.

Without tilting, cumulus cells have a limited life cycle, due apparently to the effect of downdrafts of cutting off the moist low level inflow. Such tilting is certainly influenced by shear, and simulation of this effect is not possible in 1D- or in axisymmetric 2D-models.

Lateral motion of the whole convection cell brings it into regions where moist, warm air is available at the ground to further feed the convection. The lateral motion is generally induced by sheared winds. The strong winds at high levels push the storm forward, thus causing relative inflow at the lower levels.

It has been observed, BROWNING [3], that shear results in an asymmetry, so that the updraft slopes upshear over the downdraft. This effect is important for strong convection since it allows precipitation formed in the updraft to fall into the downdraft. This unloads the updraft of the weight of the precipitation while driving the downdraft by liquid water loading and evaporation cooling. If the downdraft would be on the other side of the updraft, then it would soon interrupt the flow of warm and humid air into the updraft. SEITTER [18] has explained the observed upshear tilting by the rotation produced by the horizontal gradient in buoyancy, both conceptionally and by means of 2D numerical simulations (see Figure 6).

On the other hand, shear has basically a suppressing effect on convection because it deforms the convection cell. A convective cell in a mean shear tends to lose its energy to the mean flow through upward momentum transport. In fact, as summarized by LILLY [19], TAKEDA (1971) found that strong shear suppressed his 2D-simulated thunderstorm more than did a raining downdraft. ORVILLE and KOPP (1977) were able to maintain a 2D convective cell forced by flow over a mountain only by reducing the wind speed to 1/5 of that seen in an observational comparison. HANE (1973) was able to maintain a convective storm with shear, but at a reduced amplitude in comparison to observation. In addition, the shear produces turbulence in addition to the convective flow forces and this turbulence causes deterrent entrainment. This effect is not yet included in the 2D simulations but adds in reality. It seems that the effect of shear cannot be fully understood without going to three dimensions.

3.4 Three-dimensional models

BROWNING & FOOTE [20] report on a storm in northeastern Colorado with a life-time of more than nine hours. They have coined the term *supercell* for such a storm and described its basic structure. An important question is how to explain that severe thunderstorms may persist for such long times. It is now obvious that there must exist strong internal flow that counterbalance the strong external winds which would otherwise penetrate the storm and tear it apart. Figure 7 shows a double vortex internal flow pattern that is both consistent with Doppler radar observations and numerical simulations. The internal back flow helps to resist the pressure head of the external wind, and the rotation reduces the difference beween external and cloud motions at the sides. These vortices are called *meso-vortices* or *meso-cyclones*.

There are two mechanisms by which the double vortex may be formed: The first mechanism is simply the turbulent momentum transfer between the outer flow and the convection cell. This mechanism can be seen for example above smoke stacks. Another mechanism is the creation of vertical rotation from preexisting horizontal vorticity in the sheared atmospheric flow by

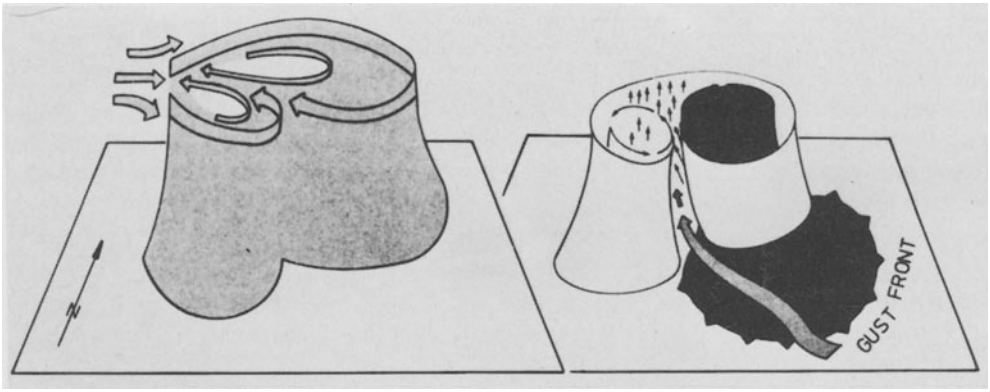

Fig. 7 Double vortex internal flow pattern (left) and gust front and moist inflow air current in a thunderstorm (right) as sketched by EAGLEMAN [14].

convective lifting and tilting of the vortex lines. This effect can be understood from the equations of motion in the simple form for constant density:

$$\partial\vec{v}/\partial t+(\vec{v}.\nabla)\vec{v} = -\text{grad}p/\rho \qquad (3.1)$$

If we take the rotation of this equation, we get an equation for the vorticity $\vec{w} = \text{rot}(\vec{v})$:

$$\partial\vec{w}/\partial t+(\vec{v}.\nabla)\vec{w} = (\vec{w}.\nabla)\vec{v} \qquad (3.2)$$

The right-hand-side term is the so-called *twisting term*. It describes how vorticity is created by shearing or stretching of vortex tubes, and is illustrated in Figure 8. This second mechanism seems to be more important because it works without any fine-scale turbulent mixing.

The double vortex structure also helps to draw additional warm, moist air into the front of the storm at low levels, as shown in Figure 7 (right).

The wind profile is not only sheared in the vertical with respect to the wind speed, but also with respect to the wind direction. Hodographs are used to represent such horizontal velocity fields. At the cold front of a mid-latitude cyclone on the northern hemisphere, the wind at the ground is mainly from the west, while it comes more from the south-west at higher levels. This causes an asymmetry of the resulting convection cells. Most of the rain falls from the northeast section of the storm. Also, due to this asymmetry, the anticyclonic rotation (in the northern part) within

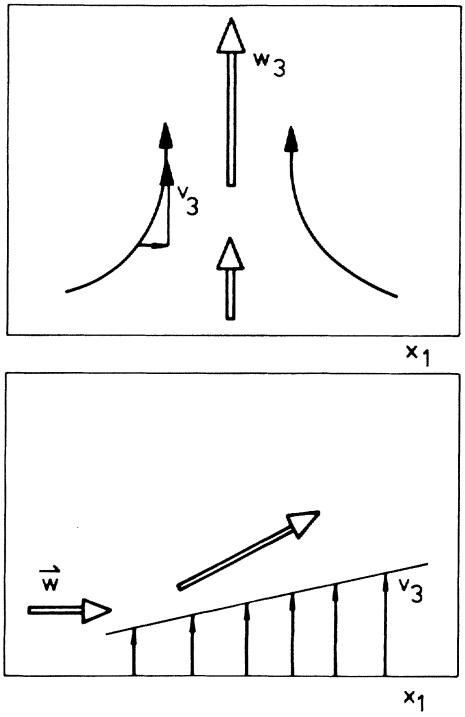

vortex stretching:

$$\partial w_3/\partial t \doteq w_3 \partial v_3/\partial x_3$$

vortex tilting:

$$\partial w_3/\partial t = w_1 \partial v_3/\partial x_1$$

Fig. 8 Illustration of vortex-line stretching and tilting.

the storm does not develop as much strength as the cyclonic vortex. The difference in the strength of the two vortices causes a net non-zero rotation to appear with respect to the surrounding flow. It has been noted by NEWTON & KATZ (1958), (see LILLY, [19]), that some convective storms move at distinctly different speeds and in different directions than the mean flow in which they are embedded. BROWNING [3] established the relationship of this lateral motion with the net rotation of the whole storm from radar observations.

A possible explanation refers to the so-called Magnus-force which deflects the motion of a thunderstorm due to interaction of the net vertical rotation with the surrounding mean flow. Typical deviations of severe thunderstorms are 10 to 30 degrees to the right of the mean winds, EAGLEMAN [14,p.85]. This indicates the existence of a net cyclonic rotation.

Another concept to explain the noted stability and durability of convective storms has been introduced by LILLY [19] in terms of helicity. Helicity, $h = \vec{v}.\vec{w}$, is the scalar product of velocity and vorticity. Convective cells show large helicity because upward motion is connected with upward rotation. If we write the equations of motion (10) in the form

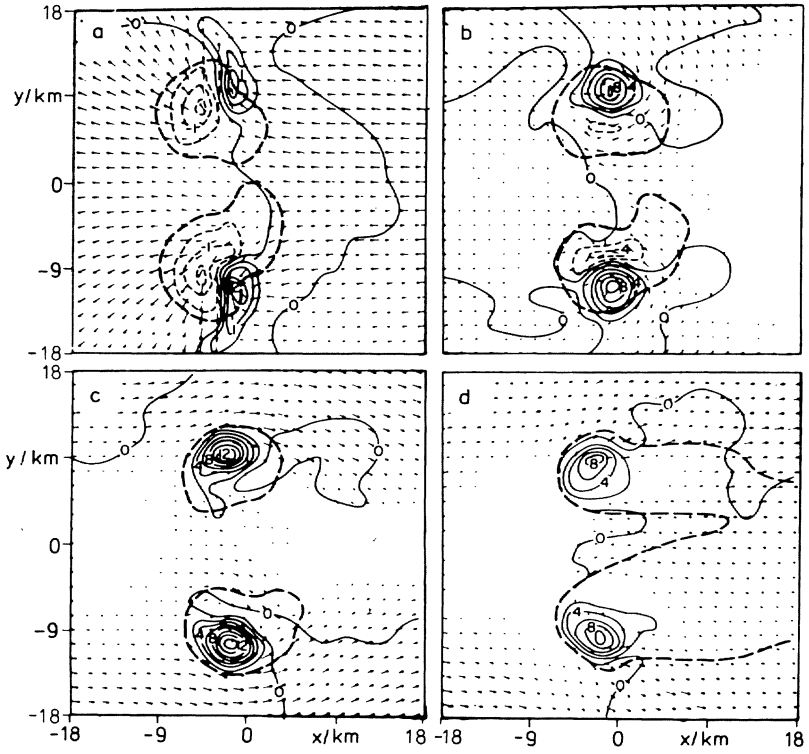

Fig. 9 Result of a three-dimensional cumulus cloud simulation by KLEMP & WILHELMSON [21]. Shown are horizontal vector plots with vertical velocity (m/s) field superimposed at 90 min: (a) z = 0.25 km, (b) z = 2.25 km, (c) z = 3.75 km, (d) z = 5.75 km. Maximum velocity vector corresponds roughly to 13 m/s. The heavy dashed line marks the outer boundary of the rainwater field, except in (d) where it encloses the cloud water field.

$$\partial\vec{v}/\partial t+\vec{w}\times\vec{v} = -\mathrm{grad}(p+\vec{v}^2/2) \qquad (3.3)$$

then we see: If the flow is purely helical it contains rotation, but nevertheless the term $\vec{w}\times\vec{v}$ is zero. This type of flow is called *Beltrami* flow. Although it is not a potential flow, it nevertheless satisfies Bernoullis equation $p/\rho+v^2/2 = \text{const}$. As the term $\vec{w}\times\vec{v}$ is responsible for the twisting term, the effect of stretching and twisting of vortex lines which is typical for turbulence is absent in such a flow. Therefore, the existence of strong helicity in convective storms explains the long life, well-defined organization, and high energy efficiency of these storms. Furthermore, it suggests that such type of flow motion is much more easy to simulate numerically than non-helical convection. In fact, it explains that numerical simulations of convective storms turn out to be rather intensitive to the grid size and subgrid-scale models. Also it provides the chance that

strong convective storm motions - once set up - have a predictable behaviour.

SCHLESINGER [5] and LILLY [2,19] have reviewed the state of 3D numerical modelling. To illustrate the type of results achieved up to now, we refer to the simulation by KLEMP & WILHELMSON [21]. These authors report on results obtained with a 3D model. The model was set up with a unindirectional wind profile with wind of -5 m/s to the east at the ground and +5 m/s to the west at heights of 4-10 km. Thus the corresponding hodograph is a straight curve. The environment is conditionally unstable. The size of the integration domain was 36 km in each horizontal direction, with a mesh interval of 1.5 km, and 10 km in the vertical, with a grid spacing of 500 m. During the simulation the initial updraft set off by a specified low level thermal impulse split into two parts that propagate laterally apart with the rightmoving updraft rotating cyclonically, the leftmoving one anticyclonically. This splitting is illustrated by plots as shown in Figure 9. This figure reveals a structure that is qualitatively very similar to the supercell model of BROWNING (1964) except for the rather early splitting. Further studies have shown that this splitting is delayed if a curved hodograph is taken.

4. REQUIREMENTS FOR A THREE-DIMENSIONAL CUMULUS CONVECTION MODEL

From the description of cumulus convection, the reader should have gained some insight into what is necessary for a proper model. Subsequently, we list some design goals that we have concluded to be important in this respect. Coding of a corresponding model has been started. Further details have been given in HAUF, HÖLLER & SCHUMANN [22].

The model has the following features:

- 3D model (with a 2D version for simplified studies) for moist air with a set of about ten classes of hydrometeors.
- The vertical momentum equation is fully included, i.e. the model is non-hydrostatic.
- Variable density is taken into account to allow for deep convection.
- As prognostic thermodynamic variable we take the entropy s because the balance equation for this quantity reduces to ds/dt = 0 for reversible and adiabatic conditions and nevertheless accounts for pressure work (which would imply extra terms if the enthalpy is used, for example), condensation heating (which would imply extra terms if the potential temperature is used, for example), and because it is more accurate than the potential ice-liquid-temperature proposed by TRIPOLI & COTTON [23]. Furthermore, the conservative properties of entropy make it

a rather smooth function in space and time, which reduces discretization errors. Finally, this concept opens the possibility to include non-equilibrium thermodynamics.

- Sound-filtering, which is important for numerical integration with time-steps that are not restricted by the speed of sound, is performed by either taking div(ρv) = 0 or by integrating the full continuity equation implicitly.
- Variable but smooth orography is represented by a coordinate transformation following CLARK [24] with additional transformations to allow for variable resolution, SCHUMANN & VOLKERT [25].
- Subgrid-scale turbulence is represented by rather simple gradient models because the large eddies are resolved directly.
- The balance equations are discretized by second order finite differences in space and the Adams-Bashforth scheme in time. Special care is taken to ensure full mass, momentum and energy conservation in Cartesian and curvilinear coordinates. Quantities that have to stay strictly positive, such as concentrations, are treated with a second order upwind scheme that guarantees positivity.
- The code is designed to allow for an order 64×64×64 mesh cells. This implies proper data management because fast main memory is at present too small on our CRAY-1, for example, to store all data simultaneously.
- Sound-filtering leads to an elliptic Poisson- or Helmholtz-equation for the pressure field. This equation is solved with fast elliptic solvers that are vectorizable, SCHMIDT, SCHUMANN, VOLKERT & ULRICH [26].
- Special care is taken to develop boundary conditions that allow the prescription inflow and outflow but are nevertheless non-reflective for internally generated gravity-waves.

Ultimately, these studies will contribute to our understanding and prediction capabilities with respect to atmospheric fluid dynamics.

5. ACKNOWLEDGEMENT

I thank Mrs. A. Jochum, Dr. H. Schuster, and Dr. A. Singler of the DFVLR for providing figures showing results of their work that have been included in this paper. Also, several colleagues have read a preliminary version of this paper and their suggestions have been very valuable.

6. REFERENCES

[1] W.R. COTTON: Theoretical cumulus dynamics. Rev. Geophys. Space Phys. 13 (1975), 419-448.

[2] D.K. LILLY: The dynamical structure and evolution of thunderstorms and squall lines. Ann. Rev. Earth Planet. Sci.7 (1979), 117-161.

[3] K.A. BROWNING: The structure and mechanisms of hailstorms. AMS Meteor. Monographs, Vol.16, No.38, 1-44.

[4] A. SCHROTH: Radar meteorology in cloud physics and radio wave propagation research. ESA-TT-808, translation of DFVLR Mitt. 82-09 (1982).

[5] R.E. SCHLESINGER: Three-dimensional numerical modeling of convective storms: a review of milestones and challenges. Proc. 12th Conf. on Severe Local Storms, Jan.11-15, 1982, San Antonio, Texas. American Meteorological Soc., Boston, Mass. (1982), 506-515.

[6] F. GASSMANN, D. HASCHKE, F. RUDIN: Möglichkeiten anthropogener Veränderungen der Gewittertätigkeit. Eidg. Inst. für Reaktorforschung, Würenlingen, Schweiz, EIR-Bericht Nr.500 (1983).

[7] P.V. HOBBS, A. DEEPAK (eds.): Clouds - Their Formation, Optical Properties, and Effects. Academic Press, New York (1981).

[8] H.-J. BOLLE: Radiation and energy transport in the earth atmosphere system. In: Hutzinger (ed.): The Handbook of Environmental Chemistry, Vol.1/ Part B, Springer Verlag Berlin (1982), 131-303.

[9] J. HANSEN, D. JOHNSON, A. LACIS, S. LEBEDEFF, P. LEE, D. RIND & G. RUSSELL: Climate impact of increasing atmospheric carbon dioxide. Science, 213 (1981), 957-966.

[10] W.M. MELVIN: Microbursts. Accident Prevention Bulletin, Vol.39, No.11 (Nov.1982).

[11] E. KESSLER (ed.): Thunderstorms: A social, scientific, and technological documentary, Vol.II. Thunderstorm Morphology and Dynamics. National Severe Storm Lab., Norman, Ok., PB83-124727 (1982).

[12] A. SINGLER: Radar-Echos von Schauern und Gewittern am oberbayerischen Alpenvorrand. DFVLR-FB (1984).

[13] J.V. IRIBARNE, H.-R. CHO: Atmospheric Physics. D. Reidel, Dordrecht (1980).

[14] J.R. EAGLEMAN: Severe and Unusual Weather. Van Nostrand Reinhold Co., New York (1983).

[15] H. HÖLLER: Detaillierte und parametrisierte Modellierung der Wolken-Mikrophysik in einem stationären Wolkenmodell. Diss. Univ. KÖln (1982).

[16] L.D. NELSON: Observations and numerical simulations of precipitation mechanisms in natural and seeded convective clouds. Thesis, Univ. Chicago, Techn. Note 54 (1979).

[17] A. JOCHUM: Numerical simulation and observational analysis of convective clouds in the lower alpine region. Proc. 9th Intern. Cloud Physics Conf., Tallinn, USSR, Aug.21-28, 1984, Vol. II, 539-540.

[18] K.L. SEITTER: The development of an upshear sloping updraft in thunderstorms. Proc. Conf. Cloud Physics, Nov.15-18, 1982, Chicago, American Met. Soc., Boston (1982), 520-523.

[19] D.K. LILLY: The development and maintenance of rotation in convective storms. In: L. Bengtsson & J. Lighthill (eds.): Intense Atmospheric Vortices. Springer-Verlag, Berlin (1982).

[20] K.A. BROWNING, G.B. FOOTE: Airflow and hail growth in supercell storms and some implications for hail suppression. Quart. J.R. Met. Soc. 102 (1976), 499-533.

[21] J.B. KLEMP, R. WILHELMSON: The simulations of three-dimensional convective storm dynamics. J. Atmos. Sci. 35 (1978), 1070-1096.

[22] T. HAUF, H. HÖLLER, U. SCHUMANN: Three-dimensional convective cloud dynamics - a new integration scheme. Proc. 9th Intern. Cloud Physics Conf., Tallinn, USSR, Aug.21-28, 1984, Vol. II, 531-534.

[23] G.J. TRIPOLI, W.R. COTTON: The use of ice-liquid water potential temperature as a thermodynamic variable in deep atmospheric models. Mon. Wea. Rev. 109 (1981), 1094-1102.

[24] T.L. CLARK: A small-scale dynamic model using a terrain-following coordinate transformation. J. Comp. Phys. 24 (1977), 186-215.

[25] U. SCHUMANN,, H. VOLKERT: Three-dimensional mass- and momentum-consistent Helmholtz-equation in terrain-following coordinates. Proc. GAMM-Workshop on Efficient Solvers for Elliptic Systems, Kiel, 27-29 Jan. 1984; Vieweg Series "Notes on Numer. Fluid Mech." (1984, in press).

[26] H. SCHMIDT, U. SCHUMANN, H. VOLKERT, W. ULRICH: Three-dimensional direct and vectorized elliptic solvers for various boundary conditions. DFVLR-Mitt. (1984).

Lecture Notes in Engineering

Edited by C.A. Brebbia and S.A. Orszag

Vol. 1: J. C. F. Telles,
The Boundary Element Method
Applied to Inelastic Problems
IX, 243 pages. 1983.

Vol. 2: Bernard Amadei,
Rock Anisotropy and
the Theory of Stress Measurements
XVIII, 479 pages. 1983.

Vol. 3: Computational Aspects of
Penetration Mechanics
Proceedings of the Army Research
Office Workshop on Computational
Aspects of Penetration Mechanics
held at the Ballistic Research Laboratory
at Aberdeen Proving Ground, Maryland,
27–29 April, 1982
Edited by J. Chandra and J.E. Flaherty
VII, 221 pages. 1983.

Vol. 4: W.S. Venturini
Boundary Element Method in Geomechanics
VIII, 246 pages. 1983.

Vol. 5: Madassar Manzoor
Heat Flow Through Extended
Surface Heat Exchangers
VII, 286 pages. 1984.

Vol. 6: Myron B. Allen III
Collocation Techniques for Modeling
Compositional Flows in Oil Reservoirs
VI, 210 pages. 1984.

Vol. 7: Derek B. Ingham,
Mark A. Kelmanson
Boundary Integral Equation
Analyses of Singular, Potential,
and Biharmonic Problems
IV, 173 pages. 1984.

Vol. 8: Linda M. Abriola
Multiphase Migration of Organic
Compounds in a Porous Medium
A Mathematical Model
VIII, 232 pages. 1984.

Vol. 9: Theodore V. Hromadka II
The Complex Variable Boundary
Element Method
XI, 243 pages. 1984.

Vol. 10: C. A. Brebbia, H. Tottenham,
G. B. Warburton, J. M. Wilson, R. R. Wilson
Vibrations of Engineering Structures
VI, 300 pages. 1985.

Vol. 11: M. B. Beck
Water Quality Management:
A Review of the Development and
Application of Mathematical Models
VIII, 108 pages. 1985.

Vol. 12: In Preparation

Vol. 13: Nonlinear Dynamics
of Transcritical Flows
Proceedings of a DFVLR International
Colloquium, Bonn, Germany, March 26, 1984
VI, 203 pages. 1984.